



VCU

Virginia Commonwealth University
VCU Scholars Compass

Theses and Dissertations

Graduate School

2012

EPID-based Dose Verification for Adaptive Radiotherapy

Joseph Gardner
Virginia Commonwealth University

Follow this and additional works at: <https://scholarscompass.vcu.edu/etd>



Part of the [Health and Medical Physics Commons](#)

© The Author

Downloaded from

<https://scholarscompass.vcu.edu/etd/2941>

This Dissertation is brought to you for free and open access by the Graduate School at VCU Scholars Compass. It has been accepted for inclusion in Theses and Dissertations by an authorized administrator of VCU Scholars Compass. For more information, please contact libcompass@vcu.edu.

EPID-based Dose Verification for Adaptive Radiotherapy

A thesis dissertation submitted in partial fulfillment of the requirements for the degree of Doctor of Philosophy at Virginia Commonwealth University.

by

Joseph K. Gardner
Bachelor of Science, University of Richmond, May 2001
Master of Science, Virginia Commonwealth University, December 2005

Director: Jeffrey V. Siebers, Ph.D.
Professor and Director, Medical Physics Graduate Program
Department of Radiation Oncology

Virginia Commonwealth University
Richmond, Virginia
November, 2012

Acknowledgement

Thanks Dr. Siebers for advising me throughout both my Masters and PhD work. You were a prime motivator, whether through encouragement or fear. I look forward to collaborating with you in the future.

Thanks to my committee members, Drs. Siebers, Williamson, Murphy, Weiss, and Docef. Your insights were quite helpful to improving the quality of this dissertation.

Thanks as well to all of my VCU coworkers, especially the EPID group. Thank you for helping create and modify the family of code that I used for this work. Specifically, thanks to `jsiebers`, `pjkeall`, `mfix`, `ywu`, `mihaylov`, `wli`, `mkowalok`, `jjgordon`, `swang`, `jmoore`, `jververs`, `msharma`. Thanks to Dr. Jian Wu for providing me with his DRR GUI framework. Thanks to Dr. Weiss for contouring the NKI database.

Thanks to the Netherlands Cancer Institute for sharing their prostate fan beam CT data set. Thanks to Dr. Iwan Kawrakow as well as the National Research Council of Canada for allowing us to use VMC++ for dose calculations. Thanks to Dr. Peter Greer for collaboration with his research group. Thanks to Varian Medical Systems for the financial support as well as access to their equipment. Thanks to Chris Barteer for all the times he fixed the equipment that I broke.

And much thanks and love to my family who supported me throughout this endeavor. Thanks Dad for instilling me with a sense of wonder about how things work, and how God designed them. Thanks Mom for my more sensitive side. And, last but not least, thanks Ange for not only emotionally and financially supporting me through the years, but also being willing to start a family before I finished.

Table of Contents

1.	Introduction.....	1
2.	Background and Significance	5
2.1.	Image Guided Adaptive Radiotherapy	5
2.2.	Dose Verification Using Portal Dosimetry	7
2.2.1.	Pretreatment Verification.....	7
2.2.2.	During Treatment Verification.....	14
2.2.3.	EPID-based Verification Tools	20
2.3.	Hypothesis and Goals.....	21
3.	Sources of Exit Fluence Deviations	23
3.1.	Fluence Variation Caused by Machine-related Variability	24
3.2.	Fluence Variation Caused by Patient-related Variability	33
3.2.1.	Monte Carlo System.....	34
3.2.2.	Monte Carlo Calculations	36
3.3.	Comparison of Sources of DPI Deviations	41
4.	Exit Dosimetry for Closing the Loop of Image Guided Adaptive Radiotherapy.....	43
4.1.	Patient Dose Deviation Simulations	43
4.1.1.	Planned Dose – Planning Geometry	43
4.1.2.	Delivered Dose – Time-of-Treatment Geometry	45
4.1.3.	Reconstructed Dose – Planning Geometry	46
4.1.4.	Planned, Actual, and Backprojected Dose Comparisons	48

4.2.	Detection of Implanted Markers	55
4.2.1.	EPID/Calypso Interference.....	58
4.3.	DRR Simulations.....	64
4.3.1.	DRR Calculation.....	65
4.3.2.	Patient Scatter Model.....	70
4.4.	Significance of Findings	74
5.	Dose Verification Graphical User Interface.....	80
5.1.	Current Clinical Practice.....	81
5.2.	GUI-based Tool.....	83
5.2.1.	Clinical Version	83
5.2.2.	Research Version.....	88
5.3.	Future Improvements	91
6.	Conclusion.....	93
7.	References	95
8.	Appendix I.....	100
9.	Appendix II.....	108

List of Tables

Table 1: Maximum pixel standard deviations (over 60 images) and percent differences (between any two images) for the picket-fence MLC test field and a patient test field for beam accelerating potentials of 6 MV and 18 MV, both with and without rigid registration and output normalization..... 33

Table 2: Optimization objectives for the RTOG-0126 protocol. A 0.5 cm margin was added around each structure for optimization. The objectives are listed according to weight..... 37

Table 3: Description of NKI patient database. It included nineteen total prostate cases, ten of which were optimized with 6 MV beam energy. Not counting the first geometry, which was assumed to be the planning geometry, each patient had several more day-of-treatment fan beam CTs. 38

Table 4: DPI variation caused by changes in the patient anatomy between the planning geometry and the day-of-treatment geometry. All differences were calculated with respect to maximum dose in the planning DPI..... 40

Table 5: Mean and maximum per-pixel standard deviations for the scatter component of the exit image. These values were calculated with respect to maximum total dose. The mean scatter variation for each patient was averaged over all beams, while the maximum scatter variation was found over all beams. 71

List of Figures

Figure 1: Flow chart for exit fluence-based delivery verification. For pretreatment verification, the DPI is simulated without the patient geometry present in the beam. For during-treatment verification, the DPI is simulated through an assumed patient geometry.
..... 15

Figure 2: Flow chart for dose reconstruction-based delivery verification. To backproject the exit fluence for dose reconstruction, the best estimate of the patient geometry is assumed. The reconstructed dose is then compared to the planned dose.
..... 17

Figure 3: Dependence of averaged central axis area on averaged size and shape for flood fields. Circular areas of different diameters are shown in the left plot and square areas of different side lengths are shown in the right plot. Maximum variation is less than 0.2%.
..... 25

Figure 4: Relative daily output, as measured by the average of the central axis area of flood field images for a 6 MV accelerating potential. The blue circles correspond to the calibration flood fields, while the red circles correspond to the flood field images, which were normalized to the calibration flood fields.
..... 26

Figure 5: Relative daily output, as measured by the average of the central axis area of flood field images for a 18 MV accelerating potential. The blue circles correspond to the calibration flood fields, while the red circles correspond to the flood field images, which were normalized to the calibration flood fields. 27

Figure 6: Standard deviation (SD) maps for the 6 MV calibration flood field (top left) and flood field image (bottom left), along with corresponding histograms of the SD values. 28

Figure 7: Standard deviation (SD) maps for the 18 MV calibration flood field (top left) and flood field image (bottom left), along with corresponding histograms of the SD values. 29

Figure 8: Fluence variability caused by uncertainty in jaws positioning. The intensity represents the standard deviation (SD) of each pixel over 100 images, between which the jaws were moved to form a 20×20 cm² field and then moved back to the original 10×10 cm² field. The maximum fluence uncertainty (1 SD) at the field edge was 2.3%. The x-jaws are located on the right and left edges, while the y-jaws are located on the top and bottom edges. 30

Figure 9: Fluence variability caused by uncertainty in EPID positioning. The intensity represents the standard deviation (SD) of each pixel over 100 images, between which the imager was retracted and re-extended. The maximum fluence uncertainty (1 SD) at the field edge was 1.3%. 31

Figure 10: Patient test field is shown in the top row, while the picket fence MLC test field is shown in the bottom row. The first column shows the fields themselves, while the second column shows the pixel standard deviations (calculated over 60 images) in the inset with the histogram of the pixel SDs outside. The inset of the third column shows the largest difference between any two images over the 60 images, along with the corresponding histogram of the differences on the outside. 32

Figure 11: Basic setup of our in-house MC system (on left), and the additions I made to it (on right). 35

Figure 12: Patient-geometry-related sources of fluence variability. Panel (a) shows the exit fluence intensity for a beam simulated through the planning geometry. Panels (b) and (c) show the histogram of the pixel SDs and the pixel SD image for this beam simulated through twelve different patient geometries-of-the-day. Panels (d) and (e) show the histogram and image of the largest percent difference between any two DPIs simulated on any two given patient geometries. The deviations present on the left side of the field were caused by the presence or lack of gas in the rectum in each patient geometry. The deviations on the right side of the field were caused by deviations in the patient contour on different patient geometries. 39

Figure 13: Demonstration of how the backprojection assumption could lead to erroneous dose reconstruction. A planning target (red circle) is located inside a water phantom. The planning fluence is incident on both the planning phantom geometry (left) and treatment phantom geometry (center). An air gap which was not present in the planning geometry, has been introduced in the treatment geometry. Due to less attenuation in the treatment geometry, the measured DPI has an area of higher intensity when compared to the expected DPI (estimated using the planning geometry). In the backprojection assumption, the DPI deviation is attributed to the incident fluence. Dose reconstruction will result in a higher estimated target dose, while the reconstructed DPI will agree with the measured DPI. 47

Figure 14: Distribution of GTV D_{95} deviations for each patient. Delivered versus planned deviations are shown by the blue triangles. Backprojected versus planned

deviations are shown by the purple x's. The mean deviations between backprojected and delivered dose are shown by the orange circles..... 50

Figure 15: Deviation in GTV D_{95} versus fraction of DPI pixels that have deviations greater than 5%, for all NKI patients. The diamonds correspond to differences between the delivered and planned doses. The squares correspond to differences between the backprojected and planned doses. The triangles correspond to differences between the backprojected and delivered doses. Respective trend lines are shown. For DPIs, only pixels with dose greater than 20% of maximum dose were analyzed. For each patient pose, the DPI pixel deviation frequency was averaged over all beams..... 52

Figure 16: Coronal slice through the planning pose (left) and a day-of-treatment pose (right). The rectal gas present in the day-of-treatment pose causes DPI deviations greater than 5% from expected. However, the GTV D_{95} deviation is less than 100 cGy. 53

Figure 17: Coronal slice through the planning pose (left) and a day-of-treatment pose (right). The filling of the bladder in the day-of-treatment pose causes the prostate to shift inferior to isocenter, and therefore the GTV D_{95} deviation is greater than 500 cGy. However, there are no large patient attenuation differences caused by bladder filling, and therefore the DPI deviations are less than 5% in all pixels..... 53

Figure 18: ROC curve showing the predictive value of DPI deviations for GTV D_{95} deviations with tolerance criteria of 50 cGy, 100 cGy, 150 cGy, and 200 cGy. The dotted black line is the line $y = x$ 55

Figure 19: Ratio images of DPI with anthropomorphic phantom in the beam and without the phantom in the beam. The left image corresponds to an accelerating

potential of 6 MV, whereas the right image corresponds to an accelerating potential of 18 MV. The gold markers are circled..... 58

Figure 20: Example of a through-patient DPI captured during treatment of a prostate site. The gross artifacts, present both inside and outside the field, were unexpected. It was hypothesized that the artifacts were caused by interference between the Calypso transponders located in the patient's prostate and the readout electronics of the EPID. The gantry angle for this DPI was 180° 59

Figure 21: Ratio of the $10 \times 10 \text{ cm}^2$ field acquired with active Calypso tracking to that without Calypso tracking. The field is marked by the dashed black line. Artifacts as large as an order of magnitude are seen outside the field..... 61

Figure 22: Ratio of the $10 \times 10 \text{ cm}^2$ field acquired with active Calypso tracking and a rudimentary Faraday cage surrounding the EPID to that without Calypso tracking or Faraday cage. Artifacts were reduced by an order of magnitude outside of the field. Deviations along the field edges were due to slight variation in the jaw positions between acquisition of the two DPIs..... 62

Figure 23: Profile along the left-right direction for a $10 \times 10 \text{ cm}^2$ field for a non-Calypso/non-Faraday cage set-up (green line), a Calypso/non-Faraday cage set-up (blue line), and a Calypso/Faraday cage set-up (red line). The green line represents normal acquisition of a DPI. The blue line represents the artifact caused by electronic interference between the EPID readout and Calypso transponder tracking. The red line represents the correction for the artifact by enclosing the EPID in a rudimentary Faraday cage. The "ripples" in the middle of the profile are caused by attenuation of the case containing the transponders on the couch..... 63

Figure 24: Profile along the superior-inferior direction for a 10×10 cm² field for a non-Calypso/non-Faraday cage set-up (green line), a Calypso/non-Faraday cage set-up (blue line), and a Calypso/Faraday cage set-up (red line). The green line represents normal acquisition of a DPI. The blue line represents the artifact caused by electronic interference between the EPID readout and Calypso transponder tracking. The red line represents the correction for the artifact by enclosing the EPID in a rudimentary Faraday cage. 64

Figure 25: Irregular phantom created for geometric validation of the DRR model. The incident beam, directed into the page, is shown in yellow. 67

Figure 26: DRR-generator GUI. The GUI is used to set options describing the geometry of the beam, phantom, and imager, based on a user-selected input file (seen in top left). The “Calculate DRR” button is then pressed, which calls the DRR simulation code to run. The generated DRR is then displayed in the panel on the right. 67

Figure 27: Comparison of DPIs simulated through an irregular water phantom by the primary component of an MC calculation (top left) and by a point-source DRR calculation (bottom left). The difference map, measured in percent with respect to maximum intensity, is shown in the top right panel. Profile intensities along the dashed black line of the images are shown in the bottom right panel. The blue data refers to the MC-generated DPI, while the green data refers to the DRR-generated DPI. 69

Figure 28a: Scatter variation for patient 1, scaled in percentages. The left column shows the per-pixel relative standard deviation of the scatter DPI through a series of eleven patient geometries. The right column shows the same scatter variation, but in relation to the maximum mean total DPI. Only the DPI area within 2 cm of the

beam is included. Gantry angles of 180° , 230° , 280° , and 330° are shown on the following pages. 72

Figure 29: Decision tree showing how to process DPI deviations. If the differences are insignificant, dose reconstruction is performed to achieve delivery verification. If the differences are significant, the source of the differences is determined by comparing the deviation map with a bank of known deviations. This comparison will show whether the differences were caused by changes in the patient geometry, changes in the machine-delivered fluence, or a combination of the two. 77

Figure 30: Sample printout from the l'mRT Matrixx verification system. The expected and measured fields are displayed on the left side, while the right side shows both a user-selected profile across both images, as well as the gamma comparison image. Treatment plan information is displayed at the bottom along with gamma results and appropriate signature lines. 82

Figure 31: EPID-based delivery verification GUI designed for clinical use. The expected image is displayed in the upper left panel, while the measured image is displayed in the upper right panel. The resulting gamma comparison image is displayed in the lower right panel. Buttons in the lower left panel allow for scrolling among all of the fields for a given patient, as well as printing out the QA report for the patient. The table shows the gamma results for each field, as well as whether the field passed or failed the given criteria (in this case, a 3 mm distance-to-agreement and a 3% dose difference). 85

Figure 32: Sample QA printout that is auto-generated by the clinical DPI comparison GUI. The calculated and measured fields are shown, as well as the

corresponding 3 mm / 3% gamma image and a profile comparison image. Field information is shown at bottom as well as a signature line for the verification..... 87

Figure 33: EPID-based delivery verification GUI for research purposes. The two imported images are displayed in the top panels, and the comparison image is displayed in the bottom right panel. Comparison metrics available are a percent difference image, a gamma image, and a pixel intensity deviation (PID) histogram. The result of the comparison is shown in the lower left corner (in this case, the test image passed the accepted tolerance). 90

Figure 34: GTV, rectum, and bladder DVHs for patient poses [01, 02 ...] for patient 1. The planned doses are shown as the bolded black solid lines. For each simulated treatment fraction, both the delivered doses (thin solid lines) and reconstructed doses (dashed lines) are shown. Beam energy for this patient was 6 MV. 108

Figure 35: GTV DVHs for patient poses [01, 02 ...] for patient 1. The planned dose is shown as the bolded black solid line. For each simulated treatment fraction, both the delivered doses (thin solid lines) and reconstructed doses (dashed lines) are shown. Beam energy for this patient was 6 MV. 109

Figure 36: Histograms of the differences between planned, actual, and backprojected GTV dose indices for patient 1. The x-axes represent the dose difference in units of cGy. The numbers in the red/green boxes represent the mean differences. For the D_{95} values, the average delivered dose is 75 cGy greater than the average reconstructed dose. Beam energy for this patient was 6 MV. 110

Figure 37: GTV, rectum, and bladder DVHs for patient poses [01, 02 ...] for patient 2. The planned doses are shown as the bolded black solid lines. For each simulated treatment fraction, both the delivered doses (thin solid lines) and reconstructed doses (dashed lines) are shown. Beam energy for this patient was 6 MV. 111

Figure 38: GTV DVHs for patient poses [01, 02 ...] for patient 2. The planned dose is shown as the bolded black solid line. For each simulated treatment fraction, both the delivered doses (thin solid lines) and reconstructed doses (dashed lines) are shown. Beam energy for this patient was 6 MV. 112

Figure 39: Histograms of the differences between planned, actual, and backprojected GTV dose indices for patient 2. The x-axes represent the dose difference in units of cGy. The numbers in the red/green boxes represent the mean differences. For the D_{95} values, the average delivered dose is 177 cGy greater than the average reconstructed dose. Beam energy for this patient was 6 MV. 113

Figure 40: GTV, rectum, and bladder DVHs for patient poses [01, 02 ...] for patient 3. The planned doses are shown as the bolded black solid lines. For each simulated treatment fraction, both the delivered doses (thin solid lines) and reconstructed doses (dashed lines) are shown. Beam energy for this patient was 6 MV. 114

Figure 41: GTV DVHs for patient poses [01, 02 ...] for patient 3. The planned dose is shown as the bolded black solid line. For each simulated treatment fraction, both the delivered doses (thin solid lines) and reconstructed doses (dashed lines) are shown. Beam energy for this patient was 6 MV. 115

Figure 42: Histograms of the differences between planned, actual, and backprojected GTV dose indices for patient 3. The x-axes represent the dose difference in units of cGy. The numbers in the red/green boxes represent the mean differences. For the D_{95} values, the average delivered dose is 18 cGy greater than the average reconstructed dose. Beam energy for this patient was 6 MV. 116

Figure 43: GTV, rectum, and bladder DVHs for patient poses [01, 02 ...] for patient 4. The planned doses are shown as the bolded black solid lines. For each simulated treatment fraction, both the delivered doses (thin solid lines) and reconstructed doses (dashed lines) are shown. Beam energy for this patient was 18 MV..... 117

Figure 44: GTV DVHs for patient poses [01, 02 ...] for patient 4. The planned dose is shown as the bolded black solid line. For each simulated treatment fraction, both the delivered doses (thin solid lines) and reconstructed doses (dashed lines) are shown. Beam energy for this patient was 18 MV. 118

Figure 45: Histograms of the differences between planned, actual, and backprojected GTV dose indices for patient 4. The x-axes represent the dose difference in units of cGy. The numbers in the red/green boxes represent the mean differences. For the D_{95} values, the average delivered dose is 302 cGy greater than the average reconstructed dose. Beam energy for this patient was 18 MV..... 119

Figure 46: GTV, rectum, and bladder DVHs for patient poses [01, 02 ...] for patient 5. The planned doses are shown as the bolded black solid lines. For each simulated treatment fraction, both the delivered doses (thin solid lines) and

reconstructed doses (dashed lines) are shown. Beam energy for this patient was 6 MV.
 120

Figure 47: GTV DVHs for patient poses [01, 02 ...] for patient 5. The planned dose is shown as the bolded black solid line. For each simulated treatment fraction, both the delivered doses (thin solid lines) and reconstructed doses (dashed lines) are shown. Beam energy for this patient was 6 MV. 121

Figure 48: Histograms of the differences between planned, actual, and backprojected GTV dose indices for patient 5. The x-axes represent the dose difference in units of cGy. The numbers in the red/green boxes represent the mean differences. For the D_{95} values, the average delivered dose is 239 cGy greater than the average reconstructed dose. Beam energy for this patient was 6 MV. 122

Figure 49: GTV, rectum, and bladder DVHs for patient poses [01, 02 ...] for patient 6. The planned doses are shown as the bolded black solid lines. For each simulated treatment fraction, both the delivered doses (thin solid lines) and reconstructed doses (dashed lines) are shown. Beam energy for this patient was 6 MV.
 123

Figure 50: GTV DVHs for patient poses [01, 02 ...] for patient 6. The planned dose is shown as the bolded black solid line. For each simulated treatment fraction, both the delivered doses (thin solid lines) and reconstructed doses (dashed lines) are shown. Beam energy for this patient was 6 MV. 124

Figure 51: Histograms of the differences between planned, actual, and backprojected GTV dose indices for patient 6. The x-axes represent the dose difference in units of cGy. The numbers in the red/green boxes represent the mean

differences. For the D_{95} values, the average delivered dose is 128 cGy greater than the average reconstructed dose. Beam energy for this patient was 6 MV. 125

Figure 52: GTV, rectum, and bladder DVHs for patient poses [01, 02 ...] for patient 7. The planned doses are shown as the bolded black solid lines. For each simulated treatment fraction, both the delivered doses (thin solid lines) and reconstructed doses (dashed lines) are shown. Beam energy for this patient was 18 MV..... 126

Figure 53: GTV DVHs for patient poses [01, 02 ...] for patient 7. The planned dose is shown as the bolded black solid line. For each simulated treatment fraction, both the delivered doses (thin solid lines) and reconstructed doses (dashed lines) are shown. Beam energy for this patient was 18 MV. 127

Figure 54: Histograms of the differences between planned, actual, and backprojected GTV dose indices for patient 7. The x-axes represent the dose difference in units of cGy. The numbers in the red/green boxes represent the mean differences. For the D_{95} values, the average delivered dose is 36 cGy greater than the average reconstructed dose. Beam energy for this patient was 18 MV..... 128

Figure 55: GTV, rectum, and bladder DVHs for patient poses [01, 02 ...] for patient 8. The planned doses are shown as the bolded black solid lines. For each simulated treatment fraction, both the delivered doses (thin solid lines) and reconstructed doses (dashed lines) are shown. Beam energy for this patient was 6 MV. 129

Figure 56: GTV DVHs for patient poses [01, 02 ...] for patient 8. The planned dose is shown as the bolded black solid line. For each simulated treatment fraction,

both the delivered doses (thin solid lines) and reconstructed doses (dashed lines) are shown. Beam energy for this patient was 6 MV. 130

Figure 57: Histograms of the differences between planned, actual, and backprojected GTV dose indices for patient 8. The x-axes represent the dose difference in units of cGy. The numbers in the red/green boxes represent the mean differences. For the D_{95} values, the average delivered dose is 71 cGy greater than the average reconstructed dose. Beam energy for this patient was 6 MV. 131

Figure 58: GTV, rectum, and bladder DVHs for patient poses [01, 02 ...] for patient 9. The planned doses are shown as the bolded black solid lines. For each simulated treatment fraction, both the delivered doses (thin solid lines) and reconstructed doses (dashed lines) are shown. Beam energy for this patient was 6 MV. 132

Figure 59: GTV DVHs for patient poses [01, 02 ...] for patient 9. The planned dose is shown as the bolded black solid line. For each simulated treatment fraction, both the delivered doses (thin solid lines) and reconstructed doses (dashed lines) are shown. Beam energy for this patient was 6 MV. 133

Figure 60: Histograms of the differences between planned, actual, and backprojected GTV dose indices for patient 9. The x-axes represent the dose difference in units of cGy. The numbers in the red/green boxes represent the mean differences. For the D_{95} values, the average delivered dose is 23 cGy greater than the average reconstructed dose. Beam energy for this patient was 6 MV. 134

Figure 61: GTV, rectum, and bladder DVHs for patient poses [01, 02 ...] for patient 11. The planned doses are shown as the bolded black solid lines. For each

simulated treatment fraction, both the delivered doses (thin solid lines) and reconstructed doses (dashed lines) are shown. Beam energy for this patient was 18 MV..... 135

Figure 62: GTV DVHs for patient poses [01, 02 ...] for patient 11. The planned dose is shown as the bolded black solid line. For each simulated treatment fraction, both the delivered doses (thin solid lines) and reconstructed doses (dashed lines) are shown. Beam energy for this patient was 18 MV. 136

Figure 63: Histograms of the differences between planned, actual, and backprojected GTV dose indices for patient 11. The x-axes represent the dose difference in units of cGy. The numbers in the red/green boxes represent the mean differences. For the D_{95} values, the average delivered dose is 57 cGy less than the average reconstructed dose. Beam energy for this patient was 18 MV..... 137

Figure 64: GTV, rectum, and bladder DVHs for patient poses [01, 02 ...] for patient 12. The planned doses are shown as the bolded black solid lines. For each simulated treatment fraction, both the delivered doses (thin solid lines) and reconstructed doses (dashed lines) are shown. Beam energy for this patient was 18 MV..... 138

Figure 65: GTV DVHs for patient poses [01, 02 ...] for patient 12. The planned dose is shown as the bolded black solid line. For each simulated treatment fraction, both the delivered doses (thin solid lines) and reconstructed doses (dashed lines) are shown. Beam energy for this patient was 18 MV. 139

Figure 66: Histograms of the differences between planned, actual, and backprojected GTV dose indices for patient 12. The x-axes represent the dose

difference in units of cGy. The numbers in the red/green boxes represent the mean differences. For the D_{95} values, the average delivered dose is 70 cGy less than the average reconstructed dose. Beam energy for this patient was 18 MV..... 140

Figure 67: GTV, rectum, and bladder DVHs for patient poses [01, 02 ...] for patient 13. The planned doses are shown as the bolded black solid lines. For each simulated treatment fraction, both the delivered doses (thin solid lines) and reconstructed doses (dashed lines) are shown. Beam energy for this patient was 18 MV..... 141

Figure 68: GTV DVHs for patient poses [01, 02 ...] for patient 13. The planned dose is shown as the bolded black solid line. For each simulated treatment fraction, both the delivered doses (thin solid lines) and reconstructed doses (dashed lines) are shown. Beam energy for this patient was 18 MV. 142

Figure 69: Histograms of the differences between planned, actual, and backprojected GTV dose indices for patient 13. The x-axes represent the dose difference in units of cGy. The numbers in the red/green boxes represent the mean differences. For the D_{95} values, the average delivered dose is 137 cGy greater than the average reconstructed dose. Beam energy for this patient was 18 MV..... 143

Figure 70: GTV, rectum, and bladder DVHs for patient poses [01, 02 ...] for patient 14. The planned doses are shown as the bolded black solid lines. For each simulated treatment fraction, both the delivered doses (thin solid lines) and reconstructed doses (dashed lines) are shown. Beam energy for this patient was 18 MV..... 144

Figure 71: GTV DVHs for patient poses [01, 02 ...] for patient 14. The planned dose is shown as the bolded black solid line. For each simulated treatment fraction, both the delivered doses (thin solid lines) and reconstructed doses (dashed lines) are shown. Beam energy for this patient was 18 MV. 145

Figure 72: Histograms of the differences between planned, actual, and backprojected GTV dose indices for patient 14. The x-axes represent the dose difference in units of cGy. The numbers in the red/green boxes represent the mean differences. For the D_{95} values, the average delivered dose is 127 cGy greater than the average reconstructed dose. Beam energy for this patient was 18 MV..... 146

Figure 73: GTV, rectum, and bladder DVHs for patient poses [01, 02 ...] for patient 16. The planned doses are shown as the bolded black solid lines. For each simulated treatment fraction, both the delivered doses (thin solid lines) and reconstructed doses (dashed lines) are shown. Beam energy for this patient was 6 MV. 147

Figure 74: GTV DVHs for patient poses [01, 02 ...] for patient 16. The planned dose is shown as the bolded black solid line. For each simulated treatment fraction, both the delivered doses (thin solid lines) and reconstructed doses (dashed lines) are shown. Beam energy for this patient was 6 MV. 148

Figure 75: Histograms of the differences between planned, actual, and backprojected GTV dose indices for patient 16. The x-axes represent the dose difference in units of cGy. The numbers in the red/green boxes represent the mean differences. For the D_{95} values, the average delivered dose is 5 cGy greater than the average reconstructed dose. Beam energy for this patient was 6 MV. 149

Figure 76: GTV, rectum, and bladder DVHs for patient poses [01, 02 ...] for patient 18. The planned doses are shown as the bolded black solid lines. For each simulated treatment fraction, both the delivered doses (thin solid lines) and reconstructed doses (dashed lines) are shown. Beam energy for this patient was 6 MV. 150

Figure 77: GTV DVHs for patient poses [01, 02 ...] for patient 18. The planned dose is shown as the bolded black solid line. For each simulated treatment fraction, both the delivered doses (thin solid lines) and reconstructed doses (dashed lines) are shown. Beam energy for this patient was 6 MV. 151

Figure 78: Histograms of the differences between planned, actual, and backprojected GTV dose indices for patient 18. The x-axes represent the dose difference in units of cGy. The numbers in the red/green boxes represent the mean differences. For the D_{95} values, the average delivered dose is 60 cGy greater than the average reconstructed dose. Beam energy for this patient was 6 MV. 152

Figure 79: GTV, rectum, and bladder DVHs for patient poses [01, 02 ...] for patient 19. The planned doses are shown as the bolded black solid lines. For each simulated treatment fraction, both the delivered doses (thin solid lines) and reconstructed doses (dashed lines) are shown. Beam energy for this patient was 18 MV..... 153

Figure 80: GTV DVHs for patient poses [01, 02 ...] for patient 19. The planned dose is shown as the bolded black solid line. For each simulated treatment fraction, both the delivered doses (thin solid lines) and reconstructed doses (dashed lines) are shown. Beam energy for this patient was 18 MV. 154

Figure 81: Histograms of the differences between planned, actual, and backprojected GTV dose indices for patient 19. The x-axes represent the dose difference in units of cGy. The numbers in the red/green boxes represent the mean differences. For the D_{95} values, the average delivered dose is 3 cGy greater than the average reconstructed dose. Beam energy for this patient was 18 MV..... 155

Figure 82: Distribution of bladder D_{25} deviations for each patient. Delivered versus planned deviations are shown by the blue triangles. Backprojected versus planned deviations are shown by the purple x's. The mean deviations between backprojected and delivered dose are shown by the orange circles. 156

Figure 83: Distribution of bladder D_{50} deviations for each patient. Delivered versus planned deviations are shown by the blue triangles. Backprojected versus planned deviations are shown by the purple x's. The mean deviations between backprojected and delivered dose are shown by the orange circles. 157

Figure 84: Distribution of rectum D_{17} deviations for each patient. Delivered versus planned deviations are shown by the blue triangles. Backprojected versus planned deviations are shown by the purple x's. The mean deviations between backprojected and delivered dose are shown by the orange circles. 158

Figure 85: Distribution of rectum D_{35} deviations for each patient. Delivered versus planned deviations are shown by the blue triangles. Backprojected versus planned deviations are shown by the purple x's. The mean deviations between backprojected and delivered dose are shown by the orange circles. 159

List of Abbreviations

ART	Adaptive Radiation Therapy
aS, aSi	Amorphous Silicon
CBCT	Cone Beam Computed Tomography
cGy	Centigray
CT	Computed Tomography
CTV	Clinical Target Volume
DF	Dark Field
DGRT	Dose Guided Radiation Therapy
DICOM	Digital Imaging and Communications in Medicine
dMLC	Dynamic Multi-Leaf Collimation
DPI	Dosimetric Portal Image
DRR	Digitally Reconstructed Radiograph
DTA	Dose to Agreement
DVH	Dose Volume Histogram
EBRT	External Beam Radiotherapy
EPID	Electronic Portal Imaging Device
FBCT	Fan Beam Computed Tomography
FF	Flood Field
FN	False Negative
FP	False Positive
GTV	Gross Tumor Volume

GUI	Graphical User Interface
H/N	Head and Neck
IGART	Image Guided Adaptive Radiation Therapy
IGRT	Image Guided Radiation Therapy
IMRT	Intensity-Modulated Radiation Therapy
KF	Kawrakow Fippel
kV	Kilo-Voltage
MC	Monte Carlo
MLC	Multi-Leaf Collimator
MU	Monitor Unit
MV	Mega-Voltage
MVCT	Mega-Voltage Computed Tomography
NIST	National Institute of Standards and Technology
NKI	Netherlands Cancer Institute
PID	Pixel Intensity Distribution
PTV	Planning Target Volume
QA	Quality Assurance
ROC	Receiver Operating Characteristic
RTOG	Radiation Therapy Oncology Group
R&V	Record and Verify
SD	Standard Deviation
SDD	Source to Detector Distance
TG	Task Group

TN	True Negative
TP	True Positive
TPR	True Positive Rate
TPS	Treatment Planning System
VMC	Voxel Monte Carlo
VCU	Virginia Commonwealth University

Abstract

EPID-BASED DOSE VERIFICATION FOR ADAPTIVE RADIOTHERAPY

By Joseph Kingsley Gardner, B.S., M.S.

A dissertation submitted in partial fulfillment of the requirements for the degree of Doctor of Philosophy at Virginia Commonwealth University.

Virginia Commonwealth University, 2012.

Major Director: Jeffrey V. Siebers, Ph.D.
Professor and Director, Medical Physics Graduate Program
Department of Radiation Oncology

Dose verification is a critical component of adaptive radiotherapy, as it provides a measurement of treatment delivery success. Based on the measured outcome, the plan may be adapted to account for differences between the planned dose and the delivered dose. Although placement of an EPID behind the patient during treatment allows for exit dosimetry which may be used to reconstruct the delivered patient dose via backprojection of the fluence, there have not been any studies examining the basic assumption of backprojection-based dose verification: that deviations between the expected and delivered exit fluences are totally caused by errors in the delivered fluence, and not caused by patient geometry changes. In this dissertation, the validity of this assumption is tested. Exit fluence deviations caused by machine fluence delivery errors are measured as well as those caused by interfractional changes in the patient anatomy. Dose reconstruction errors resulting from the backprojection assumption are assessed. Correlations are examined between exit fluence deviations and patient dose reconstruction deviations. Based on these correlations, a decision tree is proposed

detailing when caution should be taken in performing dose reconstruction to achieve delivery verification. Finally, a semi-automated dose verification tool is constructed for both clinical and research purposes.

1. Introduction

When diagnosed with cancer, several treatment options are available to the patient including surgery, chemotherapy, and radiation therapy. One type of radiotherapy, external beam radiotherapy (EBRT), involves the use of a linear accelerator to produce high energy radiation incident on the patient. A standard workflow for EBRT involves imaging the patient with a computed tomography (CT) imager. The physician then identifies the tumor and surrounding normal structures on the CT image and designs a plan that will deliver a tumoricidal dose while minimizing damage to normal structures. This external beam is delivered at several incident angles on the patient to focus dose on the tumor. Also, to take advantage of the differing recovery rates of cancerous and normal tissues, the dose is divided into multiple fractions that are delivered on different days across the span of several weeks.

Simply designing an ideal treatment plan, however, is not sufficient; successful delivery of the plan to the patient is equally critical. Therefore quality assurance (QA) tests are performed on the plan on the linear accelerator without the patient present. Treatment plan QA ensures both that the plan data is successfully transferred from the planning computer to the treatment machine and that the delivered beams are within acceptable tolerance of the planned beams.

Reproducibility of dose delivery over the course of treatment, however, is problematic due to interfractional variation in both patient geometry and the treatment machine output. The treatment plan is optimized on a CT which is acquired several days prior to treatment delivery. Not only is there inherent variation in the patient set-up position for each fraction of delivery, but the internal geometry of the patient is also constantly changing both inter- and intra-fractionally. These variations cause the delivered patient dose to deviate from the planned dose. Furthermore, standard plan designing assumes no variation in machine output, which is not the case; the beam output and positioning involves inherent levels of uncertainty.

Patient positioning uncertainties can be reduced through image guided radiotherapy (IGRT), in which imaging of the patient in the treatment position is used to improve daily patient alignment. Based on time-of-treatment image acquisition, the patient may be shifted in order to reduce deviations between the planned position and treatment position. The radiotherapy is “guided” by the imaging.

Treatment delivery may also be improved through a process termed image-guided adaptive radiotherapy (IGART), in which the treatment plan is adapted to geometric patient changes throughout treatment delivery. IGART allows for adaptation to a changing treatment geometry with the goal of achieving a dose distribution (accumulated over the fractional deliveries) that more closely achieves the planned outcome, compared to delivery of the initial planned treatment for every fraction. For example, if the tumor shrinks as each fraction is delivered, the treatment may be adapted by shrinking the incident beam sizes, thereby sparing dose to the surrounding normal tissue.

IGART necessitates feedback between the patient status during delivery and during planning. IGART also has the potential to correct for deviations between delivered and planned dose, but in order to do so, the delivered dose must be measured. When this measurement is fed back to the planning system, radiation therapy planning and delivery becomes a closed loop system. A judgment may be made on how well the treatment was delivered, and whether or not the treatment should be replanned to account for delivered dose deviations. Direct measurement of the received patient dose (*in vivo* dosimetry) is not feasible; it would require dosimeters to be implanted throughout the patient. Therefore, an indirect method of dose verification is more realistic. This indirect measurement may be achieved with a dosimeter measuring the patient exit fluence (the radiation that transmits through patient), which includes primary incident radiation and the attenuation of the beam by the patient. Based on deviations between expected and measured exit fluences, accuracy of the delivered patient dose may be inferred.

Patient exit fluence measurements have been used in direct comparison with expected fluence predictions for visual verification of treatment delivery (Talamonti, Casati et al. 2006; van Zijtveld, Dirkx et al. 2006; Bailey, Kumaraswamy et al. 2012). While the exit fluence comparison allows for treatment validation, it only provides limited guidance when deviations are observed. Exit fluence measurements have also been used to estimate the delivered patient dose via a technique called patient dose reconstruction (Louwe, Damen et al. 2003; Steciw, Warkentin et al. 2005; Wendling, Louwe et al. 2006; Louwe, Wendling et al. 2007; McDermott, Wendling et al. 2008; Wendling, McDermott et al. 2009; Mans, Wendling et al. 2010). On the surface, this

seems to provide direct verification of the dose received. It does so by backprojecting the measured exit fluence through a presumed patient anatomy and estimating dose. However, the exit fluence is a result of the incident fluence and the patient attenuation. Backprojection implicitly assumes that the patient anatomy is unchanged and therefore, measured exit fluence deviations are only due to deviations in the fluence incident on the patient. Commercial products are being developed based on this backprojection assumption of idealized anatomy.

This dissertation examines exit dosimetry by (a) directly isolating and quantifying sources of exit fluence deviations and (b) assessing the dosimetric consequences of attributing patient-caused exit fluence deviations to incident fluence deviations.

Repeated EPID measurements of test fields were used to evaluate the precision of beam delivery. Exit fluence deviations resulting from patient changes were quantified via computer simulation methods to ensure exact knowledge of the simulated patient anatomies and machine output. Together, these quantifications assess the assumptions of “backprojection” exit fluence-based dose reconstruction. To assist in this analysis, a semi-automated dose verification and comparison tool was created.

This tool is useful not only for this dissertation, but also for efficiency gains in clinical QA.

2. Background and Significance

2.1. Image Guided Adaptive Radiotherapy

Image guided adaptive radiotherapy (IGART) combines image guidance with adaptive radiotherapy (ART). Image guidance not only improves patient positioning throughout the treatment, but also has the potential to update the patient geometry. The updated geometry may then be used for adaptive treatment planning or treatment re-optimization in order to account for differences between the original planning geometry and the updated geometry.

One of the first implementations of ART was proposed by Yan et al. (Yan, Vicini et al. 1997) to account for patient-specific anatomy variability. During the first week of treatment, a fan-beam CT (FBCT) of the patient was acquired each day. Based on the measured distribution of patient geometries, a patient-specific margin was incorporated into the replanned treatment, which was delivered starting in the second week of treatment. Letourneau et al. (Letourneau, Wong et al. 2007) proposed an online IGART system in which, for each treatment fraction, a cone beam CT (CBCT) of the patient was acquired, critical volumes were defined, and treatment was replanned while the patient was on the treatment couch. In this scenario, the only opportunity for delivery QA is during treatment delivery.

Another instance of IGART was developed at the University of California San Francisco: dose-guided radiation therapy (DGRT) (Cheung, Aubry et al. 2009). This scheme involves adaptation of the treatment plan by accounting for daily differences between the dose-of-the-day and the planned dose. In their proposed method, while the patient is on the treatment couch immediately prior to delivery, a megavoltage CT (MVCT) of the patient is acquired. This MVCT is corrected for various artifacts associated with MV imaging. Since the field of view of an MVCT is not as large as an FBCT, any critical missing data from the MVCT reconstructed geometry is assumed using knowledge of the patient geometry from the FBCT acquisition. Critical structures are recontoured, and replanning takes place while the patient remains on the treatment couch. Differences between the original planned dose distribution and the new, adapted dose distribution can be visualized in the control room, and the adapted plan is delivered to the patient. This system was tested on six head-and-neck (H/N) patients as well as two prostate patients. While the DGRT-adapted plan didn't show improvement in target coverage, there was improvement in sparing of the organs at risk surrounding the target.

When IGART is implemented, treatment replanning may result in a change to the delivered fluence. However, quality assurance (QA) of the delivered fluence is needed. One method is exit fluence measurement and comparison with planned exit fluence. This exit fluence comparison method is used in this work, while other methods are also examined.

2.2. Dose Verification Using Portal Dosimetry

The device used to measure the exit fluence must be accurate and reproducible. An electronic portal imaging device (EPID) provides both high resolution (0.4 mm x 0.4 mm) and accurate, precise measurements. The dose-response of three commercially available EPIDs (Siemens, Elekta, Varian) has been characterized (McDermott, Louwe et al. 2004; Nijsten, van Elmpt et al. 2007). In this dissertation, Varian aS500 and aS1000 EPIDs were used. Greer et al. (Greer and Popescu 2003) and Van Esch et al. (Van Esch, Depuydt et al. 2004), found that dose response and dose-rate response were approximately linear for a Varian aS500 EPID. Greer et al. also found that there was a field-size response of -2% for a 4x4 cm² field relative to a 10x10 cm² field and a +2.5% response for a 24x24 cm² field relative to a 10x10 cm² field with respect to ionization chamber measurements in water. This field size response was caused by backscattering from the EPID positional arm and has been reproduced through simulations at our institution. Dosimetric differences due to field-size response are accounted for through backscattering correction factors (Wang, Gardner et al. 2009). Greer et al. also concluded that the buildup effect was insignificant for 6 MV beams.

2.2.1. Pretreatment Verification

For intensity modulated radiotherapy (IMRT), pretreatment delivery of the patient radiation fields to a dosimeter is performed in order to validate transfer of the treatment planning information from the treatment planning system (TPS) to the linac, as well as the deliverability of the treatment (Ezzell, Burmeister et al. 2009). The accelerator output fluence corresponding to each treatment field is measured without the patient in

the field prior to treatment delivery. This fluence can be compared to the expected fluence (Talamonti, Casati et al. 2006; van Zijtveld, Dirx et al. 2006; Bailey, Kumaraswamy et al. 2012) or used to estimate the patient dose distribution corresponding to the delivered fluence in order to verify delivered and planned dose distributions (van Elmpt, Nijsten et al. 2006; van Zijtveld, Dirx et al. 2007; van Elmpt, Nijsten et al. 2008).

The basic goal of pretreatment delivery is to ensure accurate patient treatment dose delivery. The task group (TG) report on IMRT commissioning (Ezzell, Burmeister et al. 2009) recommends that delivered dose be within 5% of planned dose in areas of high dose and low gradient, and within 7% in areas of low dose and low gradient. Also, 90% of delivered dose points should agree within 3% and 3 mm with the expected dose points. Pretreatment verification can detect delivery errors caused by transfer failure of the treatment plan between the planning system and the delivery system. This failure might result from human errors (e.g. selecting the wrong plan to transfer to the delivery machine) or from system errors (e.g. network transmission). Pretreatment verification can also catch errors caused by linac's inability to accurately deliver the planned treatment. This failure potentially could be caused by variation in the accelerator output or the physical limitations of the multileaf collimator (MLC). Either of these deviations could be detected through use of pretreatment verification.

One shortcoming of pretreatment verification, however, is that the during-treatment delivered dose is not verified. There is a critical assumption being made that the treatment machine will reproduce the pretreatment fluence for each treatment. Changes or errors introduced between pretreatment verification and treatment delivery

will escape detection. Therefore during-treatment verification is necessary to validate daily dose delivery.

2.2.1.1. Gamma Comparison Metric

Whether comparing two two-dimensional images, such as fluence maps, or two three-dimensional images, such as patient dose maps, the standard comparison metric for verification is the gamma metric (Low and Dempsey 2003). The gamma metric combines both the dose difference between the same pixel in an evaluated and a reference image as well as the distance-to-agreement (DTA) between the evaluated image pixel and the closest pixel in the reference image that equals that value. The user sets tolerances levels for both metrics—for example, a 3% dose difference tolerance and a 3 mm DTA tolerance. The gamma value for each pixel is calculated using the following formula:

$$\gamma_{r_e, r_r} = \min \left(\frac{r^2_{r_e, r_r}}{\Delta d^2} + \frac{\delta^2_{r_e, r_r}}{\Delta D^2} \right) \quad \forall r_e$$

where r_{r_e, r_r} is the spatial distance between the evaluated and reference dose points, δ_{r_e, r_r} is the difference between the evaluated dose D_{e, r_e} at position r_e and reference dose D_{r, r_r} at position r_r , Δd is the DTA tolerance, and ΔD is the dose difference tolerance. A pixel which fails either the DTA or dose difference tolerances will have a gamma value greater than one. The per-pixel gamma results can be plotted so that areas of failure are evident. TG Report 119 recommends that 90% of pixels pass the gamma metric with tolerances of 3% and 3 mm (Ezzell, Burmeister et al. 2009).

Naïve usage of the gamma metric, however, can lead to misleading results. MC-generated images have abnormally high gamma pass rates since the inherent statistical noise in the simulation yields lower DTAs between the evaluated and reference images. Also, even though the gamma metric is generally accepted as the proper comparison metric, there is poor correlation between gamma passing rates and delivery success (Yan, Liu et al. 2009; Nelms, Zhen et al. 2011; Gordon, Gardner et al. 2012).

2.2.1.2. DPI Comparison

Pretreatment dosimetric portal image (DPI) validation entails comparison of measured DPIs for each treatment beam with DPIs predicted based upon beam information in the TPS. These expected DPIs can be directly predicted by some TPSs (such as Varian's PortalVision software based on Van Esch et. al.) (Van Esch, Depuydt et al. 2004), computed with external analytic programs (Van Esch, Vanstraelen et al. 2001), or computed via Monte Carlo (MC) radiation transport simulations (Siebers, Kim et al. 2004; Parent, Seco et al. 2006). Differences between the actual and predicted fluences ideally can be pinpointed to machine-related variations or treatment plan data transfer failure. Subsequently, these errors can be corrected prior to actual patient treatment.

EPID-based pretreatment fluence verification has been performed at several institutions (Talamonti, Casati et al. 2006; van Zijtveld, Dirkx et al. 2006). At the University of Florence hospital, an aSi EPID was dosimetrically calibrated to match TPS-generated doses over a range of field sizes for beam energy 6 MV. Comparisons between measured and simulated fields for a series of fifteen clinical IMRT fields resulted in an average of 97.6% of pixels passing gamma for criteria of 3% and 3 mm. This agreement was comparable to that achieved when radiographic film was used to

measure the delivered fluence. The EPID was preferred over film for pretreatment verification, due to the greater time and effort required to use film (Talamonti, Casati et al. 2006). Pretreatment verification using DPI comparison had been performed at the Erasmus Cancer Center in Rotterdam for three years by 2006. In 270 patient treatment courses, four clinically relevant errors were caught. One instance involved the wrong plan transmitted to the treatment machine, while the other three involved MLC leaf malfunctions (van Zijtveld, Dirkx et al. 2006).

As arc therapy has become more widespread over the past several years, EPID-based pretreatment verification has been utilized in that modality as well. At the Roswell Park Cancer Institute in Buffalo, two EPID dosimetry systems were compared to a standard diode array for fourteen prostate arcs and twelve head and neck (H/N) arcs. On average, both systems yielded 98% of pixels passing gamma (3%, 3 mm) for the prostate cases, and 95% for the H/N cases (Bailey, Kumaraswamy et al. 2012).

One of the goals of this work is to provide our institution the framework for using DPI-based pretreatment verification. Prior to 2009, in addition to independent MC calculations, our clinic performed IMRT QA through visual inspection of differences between the planned and measured DPIs. Afterwards, this qualitative method was replaced by a quantitative one: using an l'mRT Matrixx (IBA Dosimetry America, Bartlett, TN) two-dimensional array of ionization chambers, and its accompanying comparison software. This comparison outputs the frequency of pixels that pass gamma (i.e. have gamma values less than one) with tolerance levels set to those recommended in TG 119 (Ezzell, Burmeister et al. 2009). Since there are inherent advantages to an EPID-based verification system, the goal is to revert back to that

system, but with added improvements in automation and quantitative assessment (discussed in section 5.1), notably improving upon the potentially misleading gamma metric.

2.2.1.3. Patient Dose Reconstruction

As the true goal of QA processes is to ensure that treatment delivery will result in the planned treatment dose, an enhancement of pretreatment verification is to use the measured DPIs to reconstruct the delivered dose in a planning CT geometry. In this case, instead of determining the success of the delivery based on deviations in the 2-D DPI, a judgment may be made based on deviations between the original planned and reconstructed 3-D patient dose. In a pretreatment context, EPID-based patient dose reconstruction is achieved by backprojecting fluence (as measured by DPIs at the EPID measurement plane) to the exit of the accelerator head, and then utilizing this fluence in a forward calculation of the patient dose (van Elmpt, Nijsten et al. 2006; van Zijtveld, Dirx et al. 2007). Some current commercial pretreatment QA products (MapCHECK, Sun Nuclear) use this method of verification.

At the University Hospital Maastricht, pretreatment patient dose reconstruction was performed on nine 3D conformal lung plans and five IMRT H/N plans (van Elmpt *et al.* 2008). Differences between the planned and reconstructed patient dose DVHs were used for judgment of delivery success. Differences less than 5% were observed in the mean PTV dose for the lung cases, while there were no significant differences in the lung and spinal DVH parameters. For the H/N cases, differences in the mean PTV dose, the mean parotid dose, and the maximum spinal cord dose were about 3%.

In similar work, physicists at Erasmus iteratively estimated the incident fluence required to produce the measured exit fluence, then utilized that fluence in a patient dose calculation (van Zijtveld *et al.* 2007). Their method was demonstrated for ten head-and-neck (H/N) cancer treatment plans and five rectum cases. Gamma analysis (2%, 2 mm) showed agreement in more than 95% of voxels. Differences in DVH parameters were less than 2%. Also, two of the cases which previously failed their earlier DPI-comparison method were re-examined using patient dose reconstruction. In the case of the MLC leaf malfunction, it was observed that DVH comparison resulted in good agreement for the PTV dose. However, the gamma analysis showed local failure in the PTV volume over which the malfunctioning MLC leaf was positioned. It was concluded that simple DVH analysis of the reconstructed patient dose was not a sufficient means to catch significant local errors; however, using a 3-D gamma analysis would detect these errors.

Pretreatment patient dose reconstruction based on measured delivery fluences is useful to detect deviations between dose distributions approved by the physician during the treatment planning process. Similar to pretreatment fluence-based DPI comparisons, pretreatment dose reconstruction inherently cannot detect unintended alterations in the treatment delivery after pretreatment QA is performed. Furthermore, as treatment planning transitions from a once- or twice-per-treatment process to a daily online process, the ability to do pretreatment QA diminishes. When a treatment plan is generated based upon a time-of-treatment image of the patient on the treatment machine, it is neither practical nor desirable to move the patient for the purposes of performing pretreatment QA.

2.2.2. During Treatment Verification

As noted previously, shortcomings of pretreatment verification include its inability to detect intentional changes in the treatment plan or unintentional changes in the delivery, either via changes in the record and verify (R&V) database or equipment failures.

These changes, however, can be detected using *during*-treatment measurements. In this scenario, the imager is extended behind the patient during treatment delivery, and a through-patient image is acquired for each delivered beam. Instead of comparing the planned dose to the expected dose, the planned dose may now be directly compared to the predictions of the delivered dose. Although passive during-treatment QA may not prevent delivery of deviant doses, it will detect deviant dose delivery and can enable treatment delivery adaptations of future fractions to achieve the planned treatment.

Active during-treatment QA, which monitors exit fluence as it is being delivered and compares it with expected fluence delivery, has the potential to prevent gross treatment delivery errors (Mutanga, de Boer et al. 2012). Both determining treatment adaptations and implementation of a closed-loop active delivery QA system are beyond the scope of this work. This work's goal is to detect and classify delivery deviations which would trigger plan adaptation.

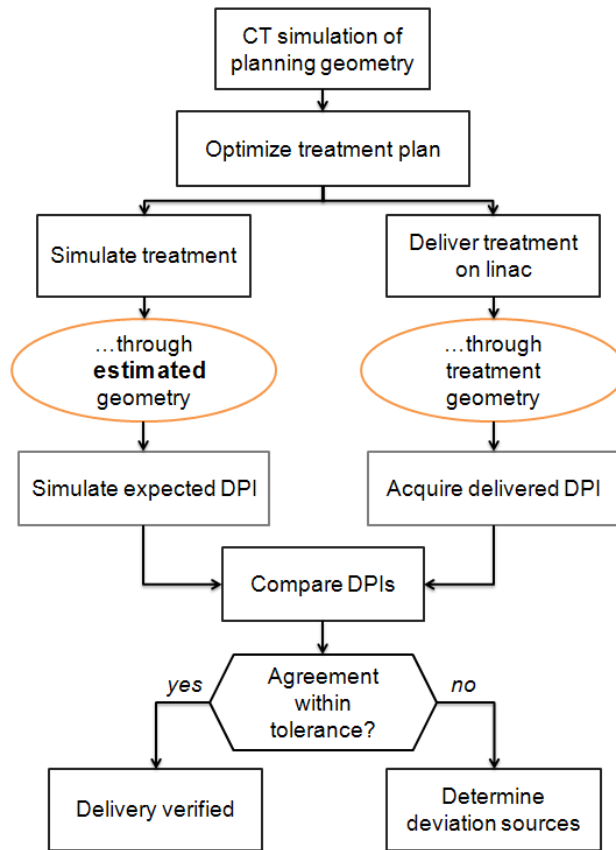


Figure 1: Flow chart for exit fluence-based delivery verification. For pretreatment verification, the DPI is simulated without the patient geometry present in the beam. For during-treatment verification, the DPI is simulated through an assumed patient geometry.

2.2.2.1. DPI Comparison

The information flow for during-treatment DPI acquisition is shown in Figure 1. Similar to pretreatment verification, during-treatment verification can be accomplished via direct comparison of DPIs or by patient dose reconstruction. Simulating during-treatment DPIs requires an estimate of the fluence incident upon the patient as well as an estimate of the patient geometry. The former can be obtained from the TPS or a simulation of the beam delivery, while the latter can be obtained from the treatment planning CT image or a more recent image of the patient anatomy, e.g. from a

pretreatment image of the patient on the treatment machine. Using this input image, simulated DPIs can be generated via analytic or MC methods (Kroonwijk, Pasma et al. 1998; Pasma, Heijmen et al. 1998; McCurdy and Pistorius 2000; McCurdy, Luchka et al. 2001). These simulated DPIs are then compared with the measured DPIs for each field to determine if the treatment was delivered successfully.

Pasma et al.(Pasma, Heijmen et al. 1998) predicted DPIs by ray-tracing the primary fluence through the patient CT and then adding a rotationally-symmetric scatter kernel to account for scatter. McCurdy et al. (McCurdy and Pistorius 2000; McCurdy, Luchka et al. 2001) predicted DPIs by ray-tracing the incident fluence through the patient CT and then adding a MC-calculated scatter portion. Kroonwijk et al.(Kroonwijk, Pasma et al. 1998) were able to detect the presence of air pockets in the rectum in prostate cases due to differences between the simulated and measured DPIs. In all of these studies, the expected exit fluence was calculated based on the patient geometry obtained from the planning CT.

In this work, two different methods were used to simulate during-treatment DPIs: 1) MC simulation and 2) calculation of an attenuation-based primary component combined with an estimate of a scatter component. While the former method should provide accurate DPI estimates, it can be CPU intensive (time consuming). While the accuracy of the latter method is less than that of MC simulation, I hypothesize that it will still be sufficient to detect gross delivery errors.

2.2.2.2. Patient Dose Reconstruction

The measured DPI can also be used to reconstruct the patient dose (Louwe, Damen et al. 2003; Steciw, Warkentin et al. 2005; Talamonti, Casati et al. 2006; Wendling, Louwe

et al. 2006; McDermott, Wendling et al. 2008; Wendling, McDermott et al. 2009; Mans, Wendling et al. 2010). Patient dose reconstruction is more prevalent than comparison of expected and actual DPIs because it allows for dose verification of the three-dimensional patient dose, whereas comparison of DPIs does not provide such a straightforward understanding of delivered dose.

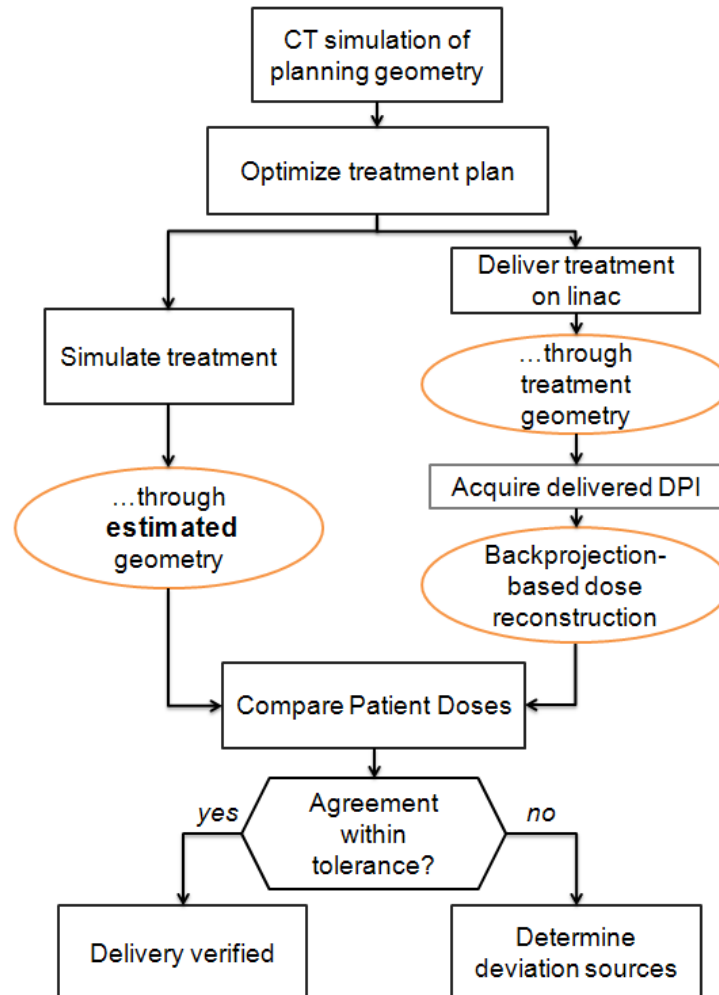


Figure 2: Flow chart for dose reconstruction-based delivery verification. To backproject the exit fluence for dose reconstruction, the best estimate of the patient geometry is assumed. The reconstructed dose is then compared to the planned dose.

Patient dose reconstruction requires backprojection of the measured fluence through the patient geometry. A flow chart of this process is shown in Figure 2. A DPI

is acquired during treatment delivery. The exit fluence is obtained from the DPI by deconvolving the image with kernels which were calculated to match simulated DPIs with measured DPIs. At this point the exit fluence contains both the primary fluence (which transmitted through the patient without interaction) and patient scatter. Backprojection of the patient scatter is inappropriate because the source of each scatter particle inside the patient is unknown. Since an estimate of the patient scatter is obtainable via MC simulation, this estimate may be subtracted from the exit fluence, leaving the primary exit fluence. The primary fluence is then backprojected to achieve dose reconstruction.

One method to reconstruct the dose involves backprojecting the primary fluence through the patient back to its source in the accelerator head. The fluence is then placed incident on the patient and used to calculate the patient dose in a forward manner (Talamonti, Casati et al. 2006). Another method involves backprojecting the primary fluence into the patient to reconstruct the primary dose. The fluence is then convolved with an appropriate kernel to estimate the scatter component of the patient dose (Wendling, Louwe et al. 2006).

One of the leading institutions in backprojection-based patient dose reconstruction is the Netherlands Cancer Institute-Antoni van Leeuwenhoek Hospital (NKI). In their system the measured DPI is backprojected to a plane through isocenter inside the patient which is normal to the beam direction, while accounting for the inverse-square law, beam attenuation, and scatter originating from the patient, the table, and the EPID itself. While single planar dose is not three-dimensional dose reconstruction, the planned and reconstructed planar doses in the patient plane typically

agree within 1% for IMRT fields (Wendling, Louwe et al. 2006). Updates to this method include use of time-of-treatment cone beam CTs (CBCTs) (McDermott, Wendling et al. 2008), expanding dose estimation to 3D (Wendling, McDermott et al. 2009), and arc therapy dose reconstruction (Mans, Wendling et al. 2010). The NKI fluence backprojection essentially reconstructs the dose distribution in the accelerator coordinate system, thereby permitting comparison of the planned and delivered planning target volume (PTV) dose distributions.

A base assumption of patient dose reconstruction is that the patient geometry is equal to that assumed for dose reconstruction. Any changes to the patient geometry between the time of imaging and the time of treatment delivery are ignored. During patient dose delivery, the patient exit fluence is formed from 1) the fluence entering the patient, 2) attenuation by the patient, and 3) scattered radiation from the patient. When the exit fluence is backprojected through the patient geometry for dose reconstruction, any differences between the expected and measured patient exit fluences are attributed completely to deviations in the delivery of the fluence entering the patient independent of whether such deviations are plausible or not.

In this dissertation, I hypothesize that differences between expected and measured patient exit fluences are not completely due to deviations in the fluence incident on the patient. Specifically, this work quantifies fluence delivery errors and analyzes exit fluence deviations caused by changes in the patient geometry.

Furthermore, I conjecture that exit fluence deviations are primarily caused by variations in patient anatomy, and therefore, caution should be used when relying on patient dose reconstruction to achieve delivery verification.

2.2.3. EPID-based Verification Tools

A potentially significant increase in workload for clinicians is required if each measured and expected DPI must be compared visually and presence of any significant differences determined. To avoid the extra time required for comparison, some semi-automatic comparison tools have been implemented which sort out any cases where there are clearly no significant differences between the DPIs (van Zijtveld, Dirx et al. 2006; Mans, Wendling et al. 2010).

Van Zijtveld et al. (van Zijtveld, Dirx et al. 2006) implemented a pretreatment fluence verification system in which visual inspection of the DPIs was avoided in two-thirds of the cases for 270 patients. For automatic approval, each field had to pass three tests:

- The percentage of pixels failing gamma (3% / 3 mm) had to be less than 15%.
- The largest area of gamma failure had to be less than 5 cm².
- If failure areas larger than 1 cm² existed, each area had to have an average gamma less than 1.5 and a maximum gamma less than 2.

If a field failed any of these criteria, then it was flagged for manual review. Their semi-automatic comparison tool was able to catch four cases in which the differences were clinically significant: in three cases a MLC leaf was malfunctioning, and in the fourth case the incorrect patient plan was loaded. The comparison metric they based their decisions on was the gamma index.

Both pretreatment and during-treatment verification systems have been in place at the NKI since 2005. From 2005 to 2009, of the 4337 patient treatment plans verified, seventeen major plan deviations were detected, including deviations caused by patient

anatomy changes (six), transmission failure between the TPS and treatment machine (four), suboptimal tuning of the treatment plan (two), accidental modification of the record-and-verify system immediately prior to treatment delivery (two), an undeliverable plan (one), and the treatment machine skipping a segment of an IMRT delivery (one). Together, these systems show the positive potential of EPID-based treatment verification.

In this dissertation, a semi-automatic comparison tool was created for pretreatment and during-treatment fluence validation. In addition to the gamma metric employed by others, comparison metrics based on dose differences were used. While the DTA component of the gamma metric is useful for accounting for EPID positioning errors, it is also capable of producing false positives and negatives in the presence of fluence deviations caused by changes in the patient anatomy. The developed tool can alert the user when differences between the planned and delivered exit fluences are significant, thereby “closing the loop” of radiation therapy treatment delivery.

2.3. Hypothesis and Goals

The overriding goal of my dissertation is to develop a clinically viable treatment dose validation system utilizing EPID-based fluence verification. In pursuit of this goal, the base assumptions of dose reconstruction were tested. The sizes of fluence deviations caused by the treatment accelerator were experimentally quantified to test the plausibility of attributing measured exit fluence deviations to changes in the input fluence. The impacts of changing patient anatomies on exit fluence were quantified by

developing a Monte Carlo simulation framework which permitted dose computation on multiple patient anatomies both with and without back-projection based fluence adjustments.

In this work it was hypothesized that patient anatomical variations, as opposed to variations in the fluence produced by the accelerator, have a greater likelihood to alter exit fluences. It was hypothesized that dose reconstruction can be erroneous if it is falsely assumed that all exit fluence deviations are caused by machine-related entrance fluence deviations. Furthermore, it was surmised that comparison of predicted and measured exit fluences would be a sufficient means of dose verification, while comparison of planned and reconstructed patient doses should only be performed when minimal exit fluence deviations exist. A QA flow chart was formed to determine when fluence-based or patient dose-based verification should be implemented. To permit implementation of EPID-based QA, a semi-automatic tool was developed to aid treatment delivery verification by comparing the expected and measured exiting fluences.

Comparison of machine- and patient-related sources of exit fluence deviations is covered in section 3 of this work. Examination of delivery verification errors caused by reliance on the backprojection assumption required by patient dose reconstruction is made in section 4. Design and function of the semi-automatic verification tool is reported in section 5. Final discussion and conclusions appear in section 6.

3. Sources of Exit Fluence Deviations

As previously mentioned, during-treatment exit fluence deviations from expected can be caused by changes in the incident fluence or changes in the patient attenuation. While dose backprojection inherently assumes the former, the frequency and plausibility of this assumption has not been confirmed. As a goal of this dissertation is to separate delivery machine related and patient attenuation related sources of exit fluence deviations, this chapter examines these two sources.

Separate experiments were set up to isolate and estimate the machine-related and patient-related sources of exit fluence variability. Machine-related sources were quantified via repeated measurements of fluence delivery without a patient or phantom in the beam. This material is described briefly in Section 3.1 with details published in Physics, Medicine, and Biology (Gardner, Clews et al. 2009) as well as presented at the Electronic Portal Imaging International Workshop in 2008. The journal article is shown in Appendix I. Quantification of patient-related sources of exit fluence deviations required decoupling of the patient-related sources from machine-related sources. To accomplish this, MC radiation transport simulations were employed. In the simulation environment, the entrance fluence could be exactly replicated and placed incident on a series of CT images for a given patient. Therefore all calculated exit fluence deviations

could be attributed to changes in the patient geometry and not to changes in entrance fluence or imager fluctuation. Details of the MC system are given in Section 3.2.1.

3.1. Fluence Variation Caused by Machine-related Variability

The goal of this study was to quantify machine-related source of DPI variability.

Machine-related sources of DPI variability were separated into two broad categories: 1) those related to the generation of the incident beam, and 2) those related to measurement fluctuations inherent in the detection system. Incident fluence sources include linac output fluctuation as well as positioning variance of the linac head components including MLC positions during IMRT delivery. Measurement sources include EPID pixel calibration variations and detector positioning variations.

Measurements were acquired at beam accelerating potentials of 6 MV and 18 MV of the following fields:

- Calibration flood and dark fields
- Full-imager field
- 10×10 cm² field
- Picket fence field, which formed 1 mm-wide regions of high intensity every 3 cm
- Complex prostate dynamic MLC IMRT field

Over the span of two months, sixty images were acquired of each field. The reader is encouraged to review Appendix I for the remaining details of the experimental setup.

Results will be repeated here briefly.

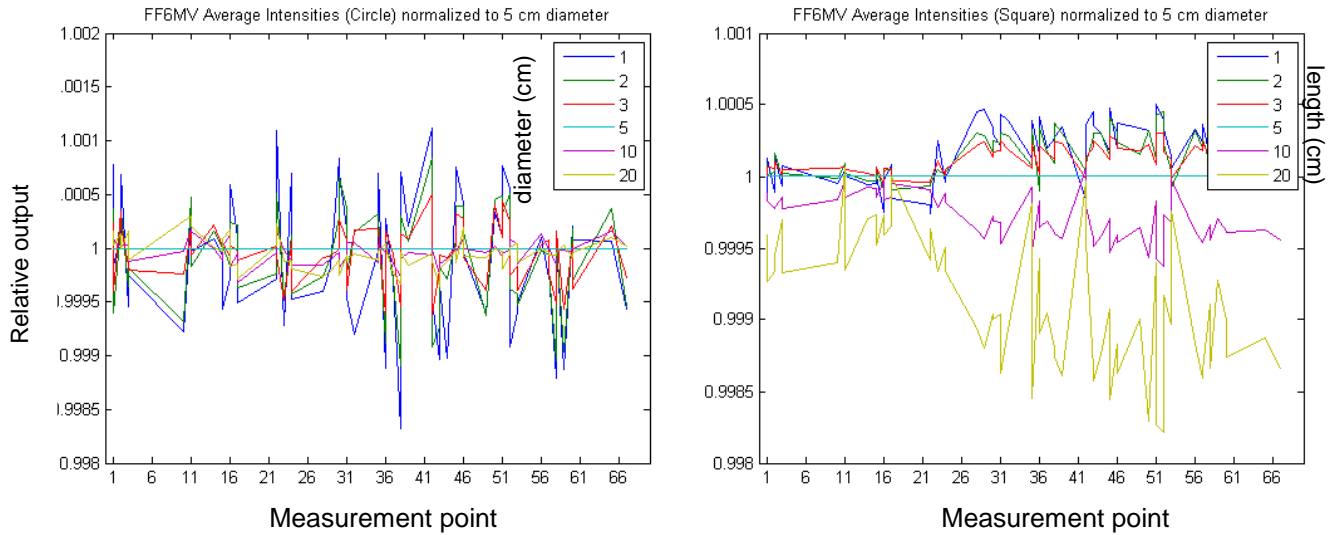


Figure 3: Dependence of averaged central axis area on averaged size and shape for flood fields. Circular areas of different diameters are shown in the left plot and square areas of different side lengths are shown in the right plot. Maximum variation is less than 0.2%.

The calibration variability of the EPID was found to be independent of the size or shape of the averaged central axis area from 1 cm² to 400 cm² (Figure 3). The relative daily outputs as measured by the average of the central axis area are seen in Figure 4 and Figure 5. The standard deviations (SDs) of the central axis area of the calibration flood fields, shown in Figure 6 and Figure 7, were 3.0% and 1.9% for the 6MV and 18 MV accelerating potentials, respectively. These SDs correspond to the combination of accelerator output variation and EPID detection variation. The SDs in the central axis area of the flood field images, which were corrected for daily output variations by daily dark/flood field calibration applied, were 0.2% for both accelerating potentials. Calibrating measured images to daily-acquired calibration fields effectively eliminates fluence variability due to accelerator output variation and EPID response variation.

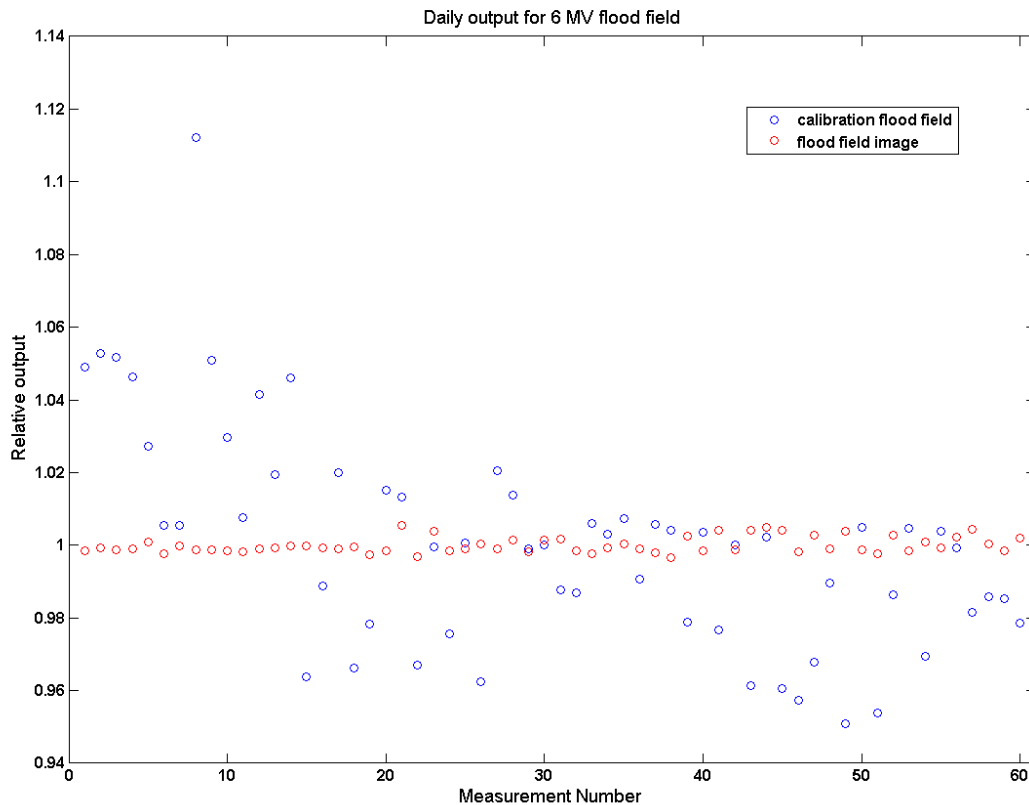


Figure 4: Relative daily output, as measured by the average of the central axis area of flood field images for a 6 MV accelerating potential. The blue circles correspond to the calibration flood fields, while the red circles correspond to the flood field images, which were normalized to the calibration flood fields.

By acquiring repeated measurements of the fields while adjusting the jaws between measurements, I found that the uncertainty in the jaws positioning was less than 0.2 mm (1 SD) at isocenter for each jaw. This uncertainty is less than half the size of an aS1000 pixel. The maximum pixel SD caused by the jaws positioning uncertainty was 2.3%. The pixel SD image is shown in Figure 8.

Repeated measurements while repositioning the EPID between measurements showed that the measured uncertainty in the EPID positioning was also less than half of

a pixel at isocenter. The EPID positioning variation caused a maximum fluence pixel SD of 1.3%, as seen in Figure 9.

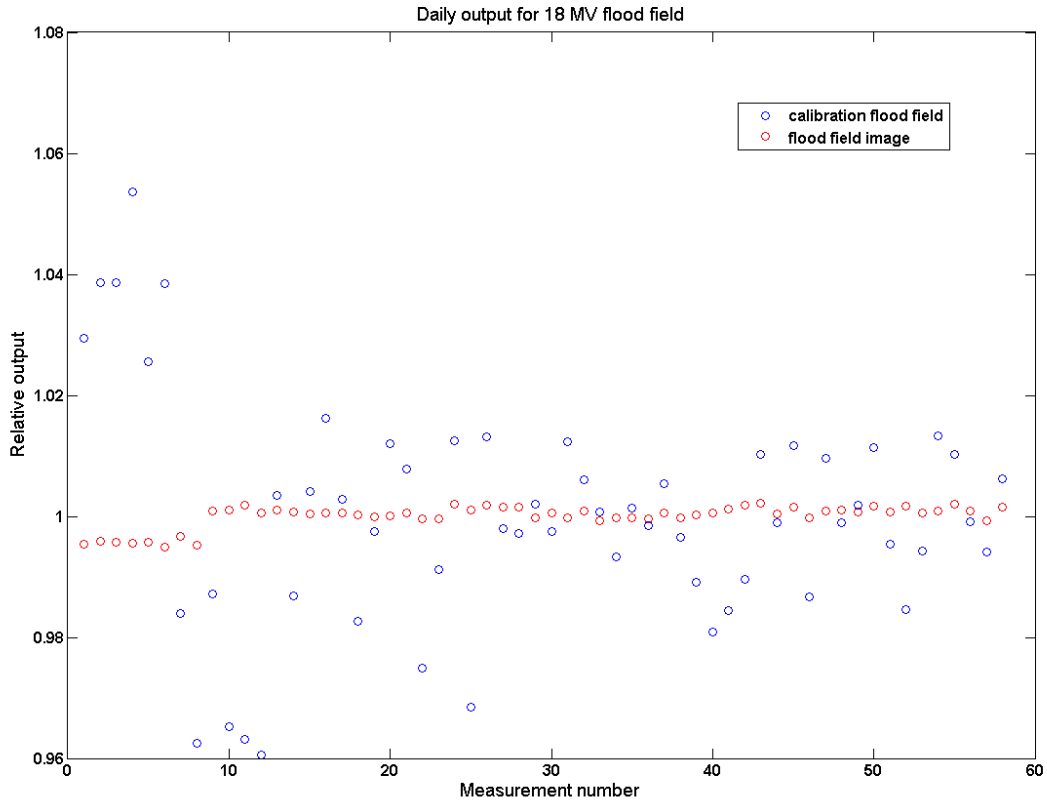


Figure 5: Relative daily output, as measured by the average of the central axis area of flood field images for a 18 MV accelerating potential. The blue circles correspond to the calibration flood fields, while the red circles correspond to the flood field images, which were normalized to the calibration flood fields.

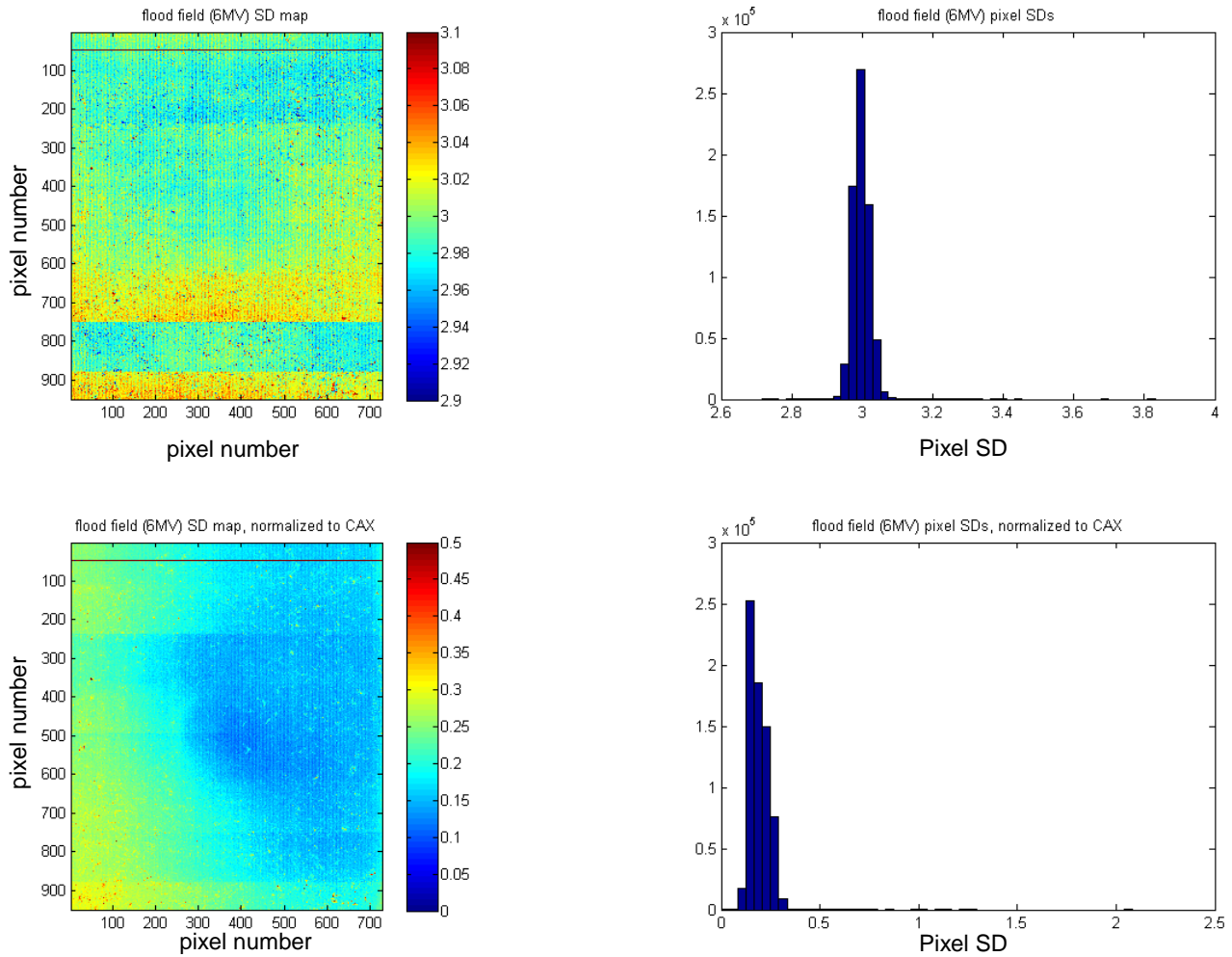


Figure 6: Standard deviation (SD) maps for the 6 MV calibration flood field (top left) and flood field image (bottom left), along with corresponding histograms of the SD values.

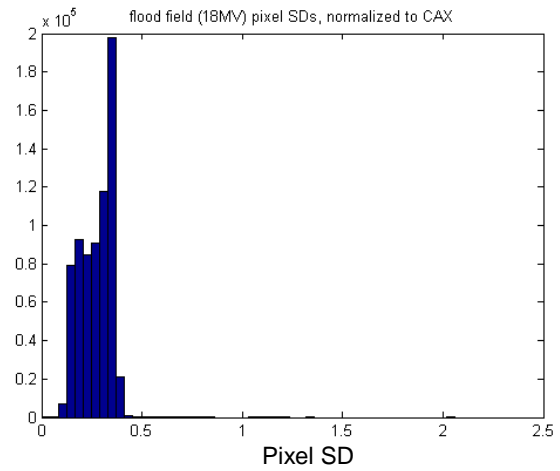
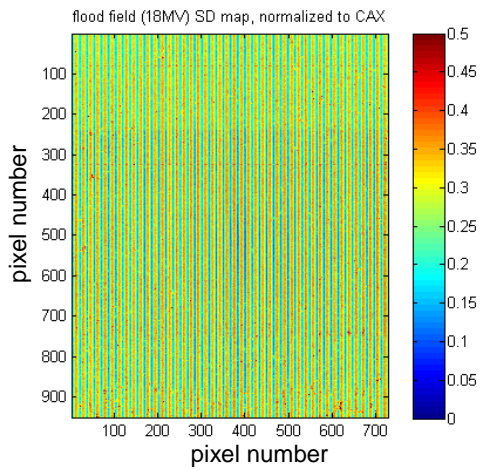
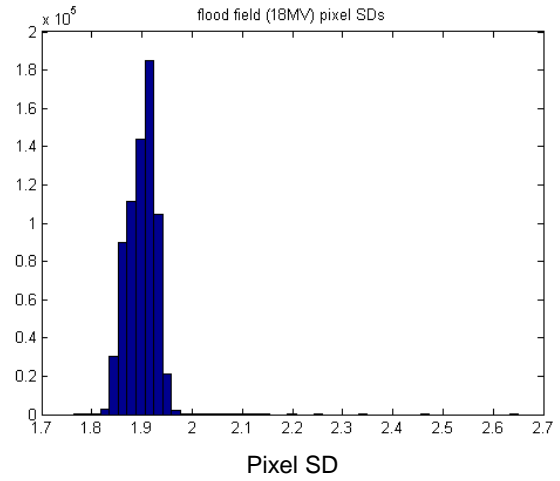
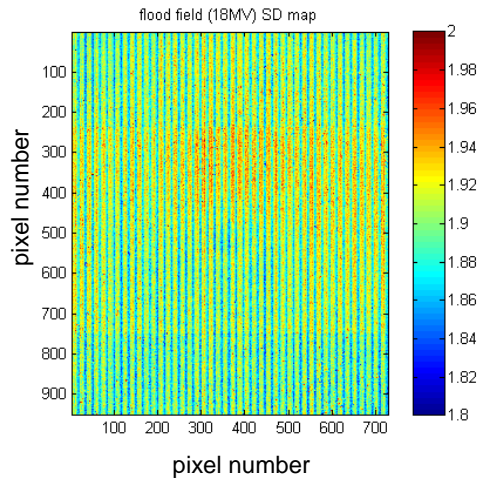


Figure 7: Standard deviation (SD) maps for the 18 MV calibration flood field (top left) and flood field image (bottom left), along with corresponding histograms of the SD values.

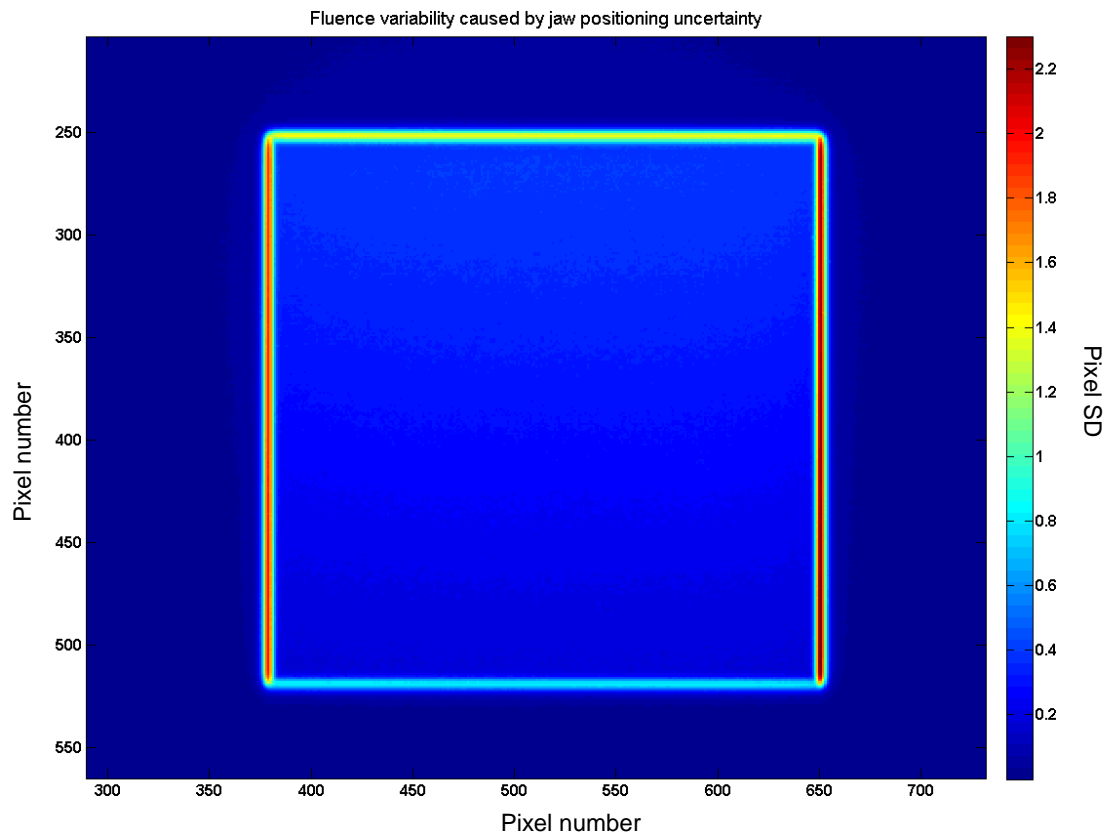


Figure 8: Fluence variability caused by uncertainty in jaws positioning. The intensity represents the standard deviation (SD) of each pixel over 100 images, between which the jaws were moved to form a $20 \times 20 \text{ cm}^2$ field and then moved back to the original $10 \times 10 \text{ cm}^2$ field. The maximum fluence uncertainty (1 SD) at the field edge was 2.3%. The x-jaws are located on the right and left edges, while the y-jaws are located on the top and bottom edges.

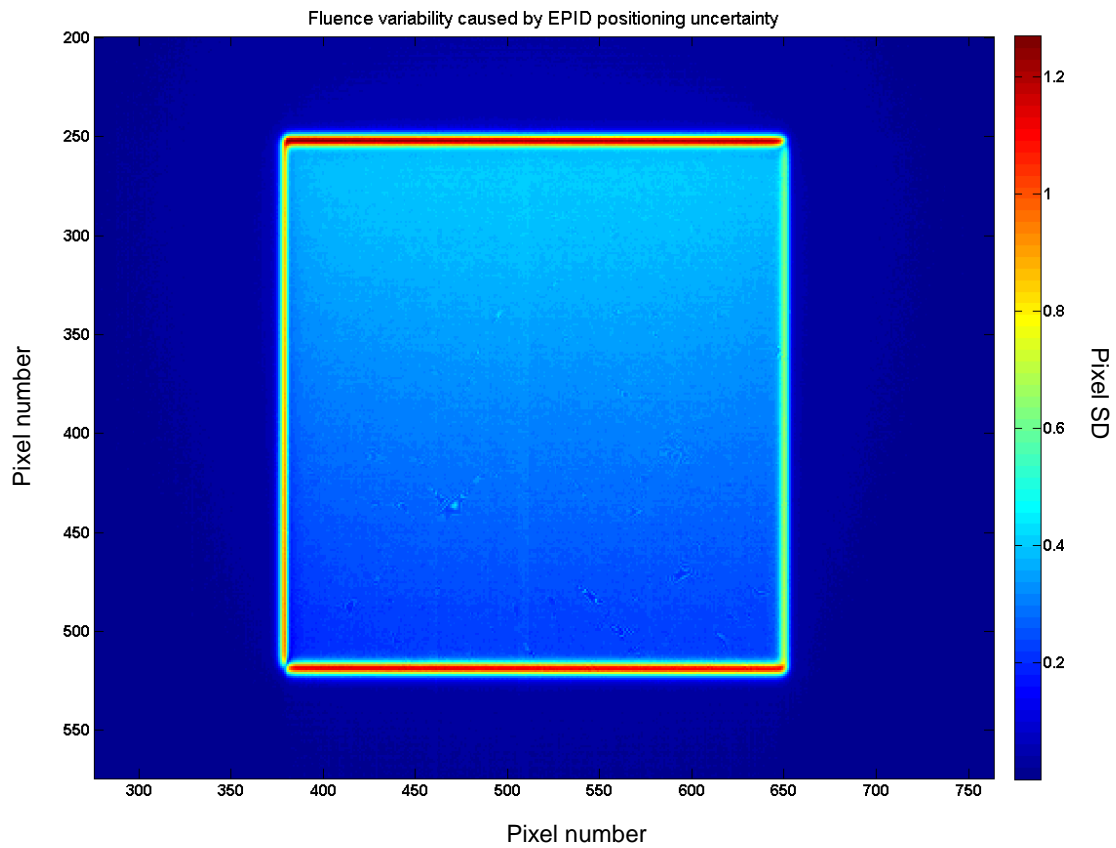


Figure 9: Fluence variability caused by uncertainty in EPID positioning. The intensity represents the standard deviation (SD) of each pixel over 100 images, between which the imager was retracted and re-extended. The maximum fluence uncertainty (1 SD) at the field edge was 1.3%.

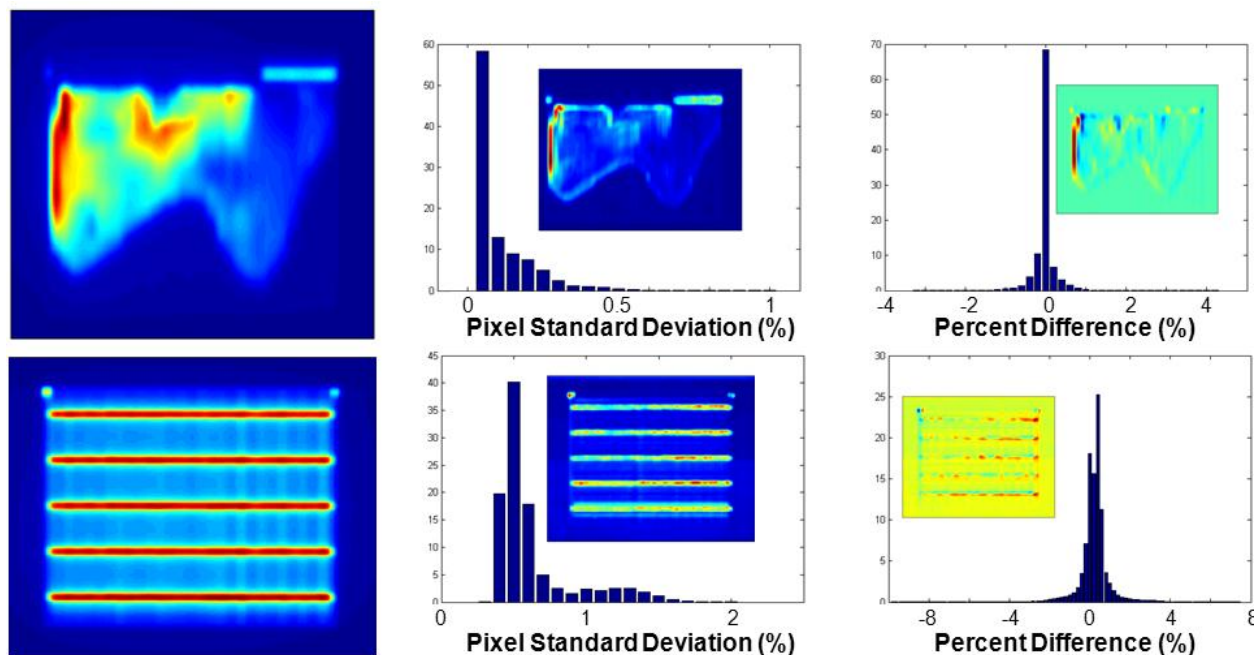


Figure 10: Patient test field is shown in the top row, while the picket fence MLC test field is shown in the bottom row. The first column shows the fields themselves, while the second column shows the pixel standard deviations (calculated over 60 images) in the inset with the histogram of the pixel SDs outside. The inset of the third column shows the largest difference between any two images over the 60 images, along with the corresponding histogram of the differences on the outside.

Images of a 6 MV picket-fence test field and a patient test field are seen in Figure 10, along with their corresponding pixel SD images and the largest difference image between any two measured fields. The largest calculated pixel SD for the picket-fence fields were 2.1% and 2.3% for the 6 MV and 18 MV accelerating potentials, respectively. The largest calculated pixel SD for the patient fields were 1.0% and 1.1% for the 6 MV and 18 MV fields, respectively. The largest percent difference between any two picket-fence fields was 9.8% (6 MV) and 8.4% (18 MV). The largest percent difference between any two patient fields was 4.2% (6 MV) and 3.5% (18 MV).

In addition to comparing raw images, images were compared after registration and normalization. Inclusion of this preprocessing reduced the pixel SDs of the picket-fence field to 1.6% (6 MV) and 1.8 % (18 MV), and the patient field to 0.8% (6 MV) and

0.9% (18 MV). These results are summarized in Table 1. Utilizing registration and normalization therefore improves the detectability of exit fluence deviations (Gordon, Gardner et al. 2012).

Table 1: Maximum pixel standard deviations (over 60 images) and percent differences (between any two images) for the picket-fence MLC test field and a patient test field for beam accelerating potentials of 6 MV and 18 MV, both with and without rigid registration and output normalization.

		Maximum percent difference (%)	Maximum pixel SD (%)	Maximum pixel SD (%) with rigid registration and output normalization
Picket fence	6 MV	9.8	2.1	1.6
	18 MV	8.4	2.3	1.8
Patient field	6 MV	4.2	1.0	0.8
	18 MV	3.5	1.1	0.9

The purpose of this study was to measure the fluence variation caused by machine-related sources, so that the basic assumption of backprojection-based dose reconstruction could be tested: that patient-related sources of fluence variation are negligible compared to machine-related sources. Based on these results, fluence variation caused by machine-related sources is expected to be 1% on average and no greater than 5% in worst-case scenarios while the machine is still operating under tolerances. Gross delivery errors could still happen due to machine-related failures, but these will easily be characterized as machine errors, not variability.

3.2. Fluence Variation Caused by Patient-related Variability

As mentioned, the other possible source of exit fluence deviations is from changes in the patient attenuation and scatter due to variations in the patient anatomy. To investigate this source, a study was designed to quantify exit fluence variability caused

by changes in the patient geometry. I utilized our in-house MC system and coded in additional functions as needed. This system is described in the following section.

3.2.1. Monte Carlo System

The MC system used at our institution gives the user options regarding fluence generation, particle transport through the MLC, patient dose calculation, and DPI generation. The incident fluence may be generated either by a phase space file representative of a full accelerator head simulation or from a source model (Fix, Stampanoni et al. 2001) that has been tuned to match our treatment machine. For IMRT beams, particles are transported through the MLC using Siebers's method (Siebers, Keall et al. 2002). Several patient dose calculation codes are coded into the system, including MCNP (Pacilio, Aragno et al. 2007), DOSXYZnrc (Walters, Kawrakow et al. 2005), and VMC++ (Kawrakow 2001). After transport through the patient, the exit fluence is translated to the EPID location and a DPI is formed either using full MC simulation (Siebers, Kim et al. 2004) or via convolution with energy-dependent kernels (Wang, Gardner et al. 2009). For the studies in this dissertation, the Fix source model was used as well as Siebers's MLC transport to generate the fluence incident on the patient. Since VMC++ dose calculations have been validated against DOSXYZnrc at our institution (Gardner, Siebers et al. 2007; Gardner, Siebers et al. 2007), VMC++ was used for patient dose calculation and formation of the exit fluence. The DPI was then formed via convolution of the fluence with energy-binned kernels.

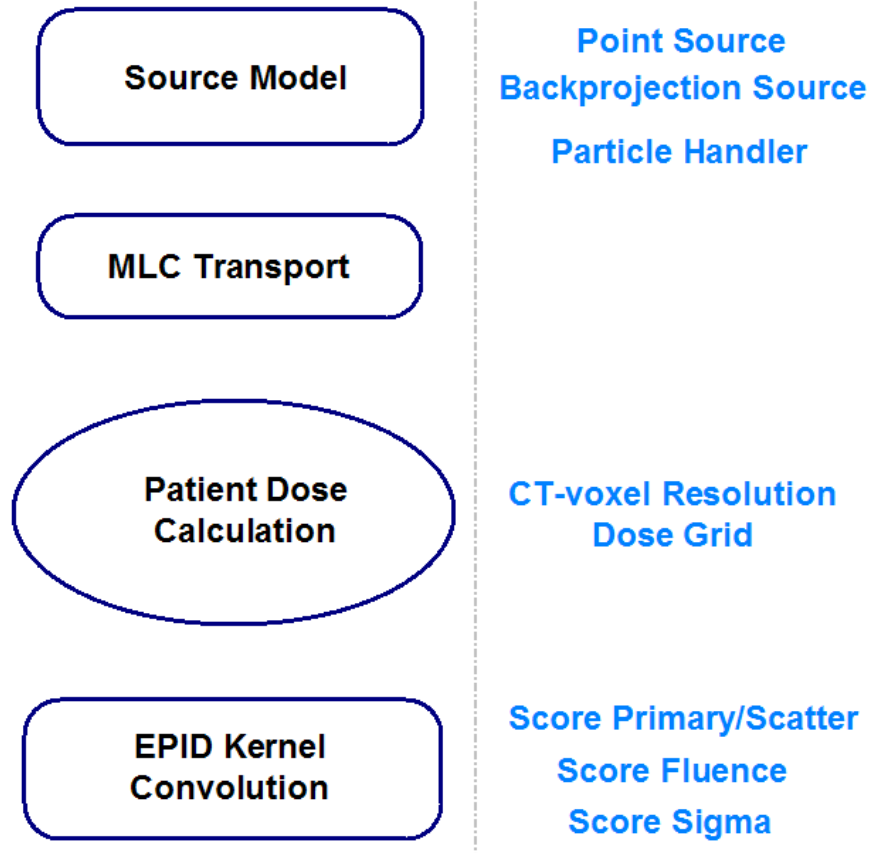


Figure 11: Basic setup of our in-house MC system (on left), and the additions I made to it (on right).

There were several additions I made to the library of codes, shown in Figure 11. I adapted the source model to allow for a simple point source (discussed in Section 4.3.1) as well as a backprojected source (discussed in Section 4.1.3). I also added in a particle handler which was useful for separation of the exit fluence into primary and scatter components. Within the particle handler, upon being sourced, the direction and energy of each particle in the incident fluence was stored in random access memory. After transport through the patient/phantom geometry, the direction and energy of each exit particle was compared to the stored values of the incident particle. If they agreed to within roundoff error, the particle was labeled a primary particle; if not, it was labeled a scatter particle. For patient dose calculation, I scripted in the ability for the dose grid

resolution to be automatically set to the CT voxel resolution. I found that this increase in resolution did not significantly affect the DPI calculation time, since per-pixel DPI uncertainty decreases at a slower rate than per-voxel patient dose uncertainty. Originally, the exit image (i.e. the convolved fluence) was the only output allowed. I added the ability to score the fluence at the imager plane. The fluence and DPI could now also be divided into primary and scatter fluences and images. Finally, I added calculation of the uncertainty for both fluences and DPIs.

3.2.2. Monte Carlo Calculations

To examine the effect that changes in patient geometry have on the exit fluence, MC calculations were performed with identical source particles to ensure that no fluence deviations could be attributable to incident fluence variations. The patient cohort used in this study was a dataset obtained from the NKI, which included nineteen prostate patients. Each patient had from nine to fourteen FBCT acquisitions, which were acquired throughout the course of treatment delivery. The CTs were rigidly registered to each other using bony anatomy landmarks using an in-house algorithm (Fatyga, Sleeman et al. 2012). The first FBCT of each patient was treated as the planning CT, and plans were optimized on this geometry using the RTOG-0126 protocol (see planning objectives in Table 2). A summary of the beam energy for each patient, as well as the number of non-planning geometries is shown in Table 3. In ten patients, the plans were optimized with beam energy of 6 MV. The remaining nine patients had plans optimized with 18 MV beam energy. All plans included seven beams at beam angles of 30° , 80° , 130° , 180° , 230° , 280° , and 330° . The GTV, rectum, and bladder

were manually contoured on each patient image by a single physician. Since this database only involves the prostate site, the GTV was representative of the CTV.

Table 2: Optimization objectives for the RTOG-0126 protocol. A 0.5 cm margin was added around each structure for optimization. The objectives are listed according to weight.

ROI	Constraint Type	Target Dose (cGy)	% Volume	Weight
CTV + 0.5 cm	Min DVH	7920	98	100
CTV + 0.5 cm	Max DVH	8470	2	90
Rectum + 0.5 cm	Max DVH	6000	50	80
Rectum + 0.5 cm	Max DVH	6500	35	80
Rectum + 0.5 cm	Max DVH	7000	25	80
Rectum + 0.5 cm	Max DVH	7500	15	80
Rectum + 0.5 cm	Max Dose	8470		80
Bladder + 0.5 cm	Max DVH	6500	50	80
Bladder + 0.5 cm	Max DVH	7000	35	80
Bladder + 0.5 cm	Max DVH	7500	25	80
Bladder + 0.5 cm	Max DVH	8000	15	80
Bladder + 0.5 cm	Max Dose	8470		80
L Femur + 0.5 cm	Max DVH	3500	50	20
L Femur + 0.5 cm	Max Dose	5000		20
R Femur + 0.5 cm	Max DVH	3500	50	20
R Femur + 0.5 cm	Max Dose	5000		20

Please note that, whereas my journal article detailed a single patient case, this dissertation work has expanded to a greater number of patients. Also, the treatment plan detailed in the article differed in that the pelvic nodes were also included in the optimization process. This led to larger fields, with greater complexity and higher intensity gradients. All seven beams were split into two separate fields. The plan was optimized with 18 MV energy beams.

For each patient, the exit fluence was simulated through each of the patient geometries. For each patient geometry, each beam sampled the exact same particles from the source model by using the same random seeds for source model input. Therefore, all differences in the DPIs could be attributable to patient anatomy changes and not to entrance fluence deviations. For each DPI, 2.5×10^7 particles were sampled, yielding an approximate DPI statistical precision of one percent. Average total calculation time per beam was approximately 25 minutes (distributed over ten processors). Differences were computed between the simulated DPIs generated through each of the patient CTs. The DPI per-pixel SDs (calculated over n patient geometries) were also computed for each beam for each patient.

Table 3: Description of NKI patient database. It included nineteen total prostate cases, ten of which were optimized with 6 MV beam energy. Not counting the first geometry, which was assumed to be the planning geometry, each patient had several more day-of-treatment fan beam CTs.

Patient	Beam energy	Number of geometries
1	6 MV	11
2	6 MV	12
3	6 MV	11
4	18 MV	10
5	6 MV	12
6	6 MV	8
7	18 MV	11
8	6 MV	12
9	6 MV	11
10	6 MV	10

Patient	Beam energy	Number of geometries
11	18 MV	11
12	18 MV	13
13	18 MV	10
14	18 MV	10
15	18 MV	12
16	6 MV	12
17	18 MV	12
18	6 MV	11
19	18 MV	10

For the published study, a sample patient beam is shown in Figure 12, along with its corresponding pixel SDs (calculated over images from twelve patient geometries) and largest percent difference between two DPIs. Per-pixel percent differences greater than 5% (with respect to maximum intensity) existed in 16 out of 154 simulated DPIs for this patient. The largest calculated pixel SD was 2.5%, and the largest pixel percent difference between any two fields was 8.6%. Visual inspection of the patient CT data showed that the primary sources of exit fluence deviations were changes in the patient anatomy that resulted in different radiological pathlengths through the patient for the source particles. In some cases, this change in attenuation was caused by changes in the rectal filling. When gas was present in the rectum, the intensity of the DPI increased behind the rectum. In other cases, particularly in beams at gantry angles of 80° and 280° , the edges of the beams became tangential with the patient's outer skin contour. Therefore, slight changes in the height of the patient's abdomen on the treatment table resulted in significant changes in beam attenuation length.

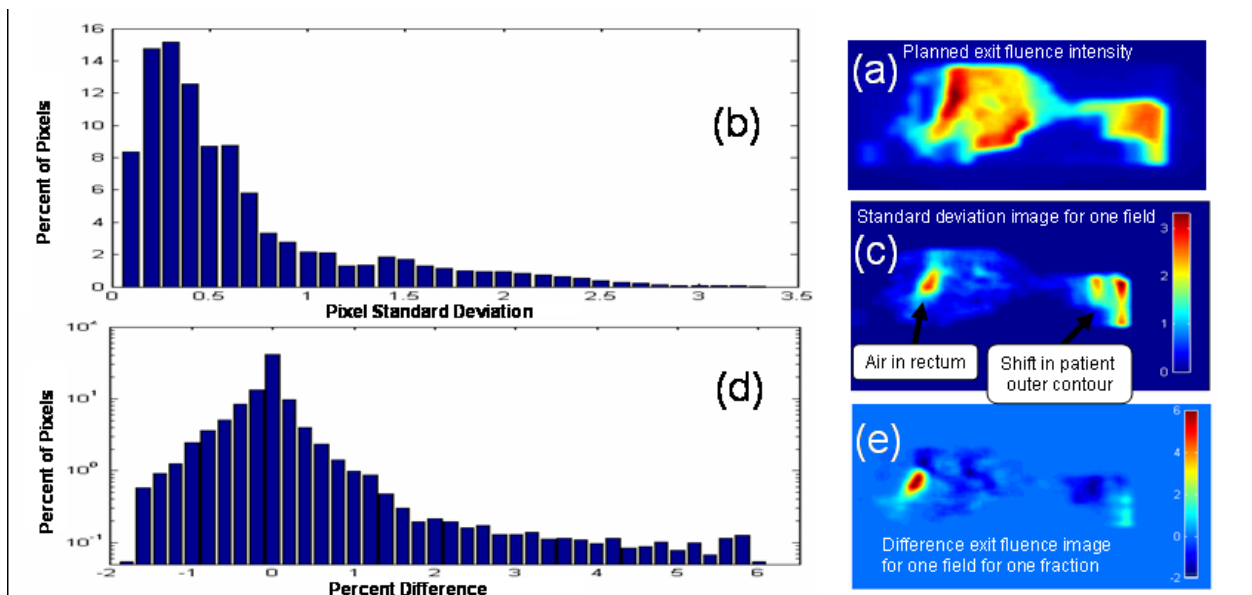


Figure 12: Patient-geometry-related sources of fluence variability. Panel (a) shows the exit fluence intensity for a beam simulated through the planning geometry. Panels (b) and (c) show the histogram of the pixel SDs and the pixel

SD image for this beam simulated through twelve different patient geometries-of-the-day. Panels (d) and (e) show the histogram and image of the largest percent difference between any two DPIs simulated on any two given patient geometries. The deviations present on the left side of the field were caused by the presence or lack of gas in the rectum in each patient geometry. The deviations on the right side of the field were caused by deviations in the patient contour on different patient geometries.

Results are show in Table 4 for the nineteen plans in which pelvic nodes were not included in the treatment plan. Per-pixel differences greater than 5% existed in 935 out of 1,442 simulated DPIs (64% of fields), and greater than 10% existed in 384 fields (26% of fields). Maximum per-pixel SDs for each patient ranged from 1.8% to 12.7%. Differences were most pronounced in patients whose planning CT contained a large amount of rectal gas.

Table 4: DPI variation caused by changes in the patient anatomy between the planning geometry and the day-of-treatment geometry. All differences were calculated with respect to maximum dose in the planning DPI.

Patient	Maximum difference (%)	Maximum SD (%)
1	26.0	7.5
2	36.9	12.7
3		
4	14.0	5.4
5	12.6	4.2
6	17.7	6.3
7	10.5	4.2
8	15.2	4.1
9	18.8	8.0
10	20.6	6.2

Patient	Maximum difference (%)	Maximum SD (%)
11	8.4	3.1
12	14.4	5.7
13	10.4	4.2
14	6.0	1.8
15	8.1	2.2
16	15.7	6.1
17		
18	21.9	8.3
19	8.1	3.4

3.3. Comparison of Sources of DPI Deviations

While machine-related sources of fluence variation resulted in maximum DPI pixel SDs of 1% and maximum deviations of 5%, patient anatomy-related sources resulted in maximum DPI pixel SDs over 12% and maximum deviations of 36%. Exit fluence deviations caused by patient-geometry-related sources were greater than those caused by machine-related sources, within the limits of this study. Tests with our delivery system indicate that per-delivery fluence variations caused by machine-related sources of variation are within the acceptable tolerances expected for patient treatment. For our system, blind application of the backprojection assumption to determine the incident fluence for patient dose reconstruction is not justified. Doing so would likely attribute patient-geometry-related sources of exit fluence deviations to incident fluence deviations—the wrong source.

It should be noted, however, that gross delivery errors could happen as a result of machine failure, such as failure of plan transfer to the treatment machine or failure of MLC leafs to remain in tolerance. Even though these gross delivery errors would exceed the deviations caused by patient anatomy variations, they would easily be characterized as machine-related errors due to the size and shape of the DPI deviation maps. In cases where gross delivery occur due to machine failure, backprojection-based dose reconstruction can be performed since the exit deviations are caused by the entrance deviations (as long as concurrent deviations caused by patient anatomy variations are insignificant in comparison).

This work was limited to a prospective study of detecting and measuring exit fluence deviations. Therefore, several other potential machine-related sources of

fluence variability have perhaps gone unmeasured. These sources include variability caused by gantry and collimator angle variation. For pretreatment verification these sources have not caused any problems in the past, since all measurements were acquired at gantry and collimator angles of zero degrees. However, for through-patient verification, possible gantry sag and collimator rotation must be accounted for.

4. Exit Dosimetry for Closing the Loop of Image Guided Adaptive Radiotherapy

“Closing the loop” of IGART refers to feeding back information from treatment delivery verification for purposes of affecting future deliveries. The two basic methods studied in this work which yield delivery verification are comparison of simulated and measured DPIs, and comparison of planned and actual patient doses. In this chapter, correlations between DPI deviations and patient dose deviations will be examined, and recommendations will be made as how dose verification should be performed.

4.1. Patient Dose Deviation Simulations

An intuitive means of patient dose delivery verification involves comparison of planned and delivered 3D patient dose maps and DVHs. Direct patient dose comparisons circumvent challenges associated with correlating DPI deviations to patient dose deviations. In this section, a method to reconstruct the patient dose is described, as well as its assumptions and limitations. Correlation between DPI deviations and patient dose deviations is also examined.

4.1.1. Planned Dose – Planning Geometry

Standard treatment delivery involves 1) acquisition of a planning CT, 2) plan optimization on the planning CT to some predetermined objectives, and 3) subsequent

delivery of this plan to the patient for all fractions. Between 2) and 3), beam parameters are transferred to the treatment machine's R&V system to ensure that planned beams are delivered throughout the treatment course. The total planned dose to the patient is divided into a fractionation scheme to favor normal tissue sparing, and the summation of the fractional doses is assumed to equal the delivered dose. Throughout delivery, it is assumed that changes in the patient geometry negligibly affect the dose delivered to the patient. Setup uncertainties and patient geometric changes are ideally absorbed by margins placed around the target and other structures of interest. This planned dose to the planning target volume (PTV) is said to be representative of the dose received by the patient's clinical target volume (CTV).

To simulate the offsets of differing fractional patient poses, the nineteen patient NKI prostate database was utilized (a description of the database was given in Section 3.2.2). For this study, each acquired CT was treated as a separate "fraction" of delivery. Each fraction was given equal weighting, and the delivered dose to each patient pose was calculated by:

$$D = (\varphi_P \rightarrow G_F) \times n_f$$

where D is the dose, φ_P is the planning-geometry-optimized fluence incident on the fractional geometry G_F , and n_f is the number of fractional geometries obtained for the patient. Note that the dose was not accumulated over all fractions, but instead each fraction was viewed as representative of a total treatment dose by multiplying it by the number of fractions. For the planned dose, since the patient geometry is assumed to be unchanged, the dose was calculated on the planning CT, and then multiplied by n_f as well.

The treatment plans were optimized to the high dose arm of the RTOG-0126 protocol. The optimization objectives are shown in Table 2. The quality of plan optimization should have little effect on the comparisons made among the different patient poses, since each patient pose used the same plan which was optimized on the planning geometry.

4.1.2. Delivered Dose – Time-of-Treatment Geometry

As shown in chapter 3, the variation in patient geometry over the course of treatment delivery yields non-negligible changes in the exit fluence. To determine the effect of the anatomic changes on the delivered dose, the dose for each image set was computed by impinging the same source particles from the fluence (optimized on the first CT) on each fraction's CT. This was possible with the MC dose calculation system by ensuring that the same random seeds were set for each component of the simulation for each fractional delivery. Using this correlated source model assured that all observed dose differences were caused by differences in the patient's anatomy. These fractional doses were termed the true doses, as they reflected our best estimate of the delivered dose to the patient. For each fraction, the true doses were then compared to the planned dose. Differences between planned and delivered doses were caused by the patient geometry variation throughout the treatment course. Results of this comparison will be shown after the next section as these doses are also compared with backprojected doses as described below.

4.1.3. Reconstructed Dose – Planning Geometry

As shown in Section 3.3, dose delivery through a patient geometry that differs from the geometry used to predict the time-of-treatment DPI will result in differences between measured and predicted DPIs. Even though for this *in silico* study, identical incident fluences were incident upon the differing daily poses, clinically, when deviations between predicted and measured DPIs are observed, several groups backproject the exit fluence through the patient geometry to estimate the patient dose (Steciw, Warkentin et al. 2005; Talamonti, Casati et al. 2006; Mans, Wendling et al. 2010). To quantify the dose as predicted by backprojection, the following procedure was followed.

The exit fluence corresponding with the planning geometry was calculated through the first acquired CT for each patient, as was the exit fluence through each fraction's geometry, termed the actual exit fluence. The backprojection-based reconstructed patient dose was obtained in similar fashion to the true dose, except the incident fluence was multiplied by the ratio of the true exit fluence to the planned exit fluence:

$$D_R = \varphi_P \frac{e_F}{e_P} \rightarrow G_P$$

where D_R is the reconstructed dose, φ_P is the optimized fluence incident on G_P , the planning geometry, e_F is the exit fluence calculated through each fraction's geometry, and e_P is the exit fluence calculated through the planning geometry. The reconstructed dose was then compared to the true dose.

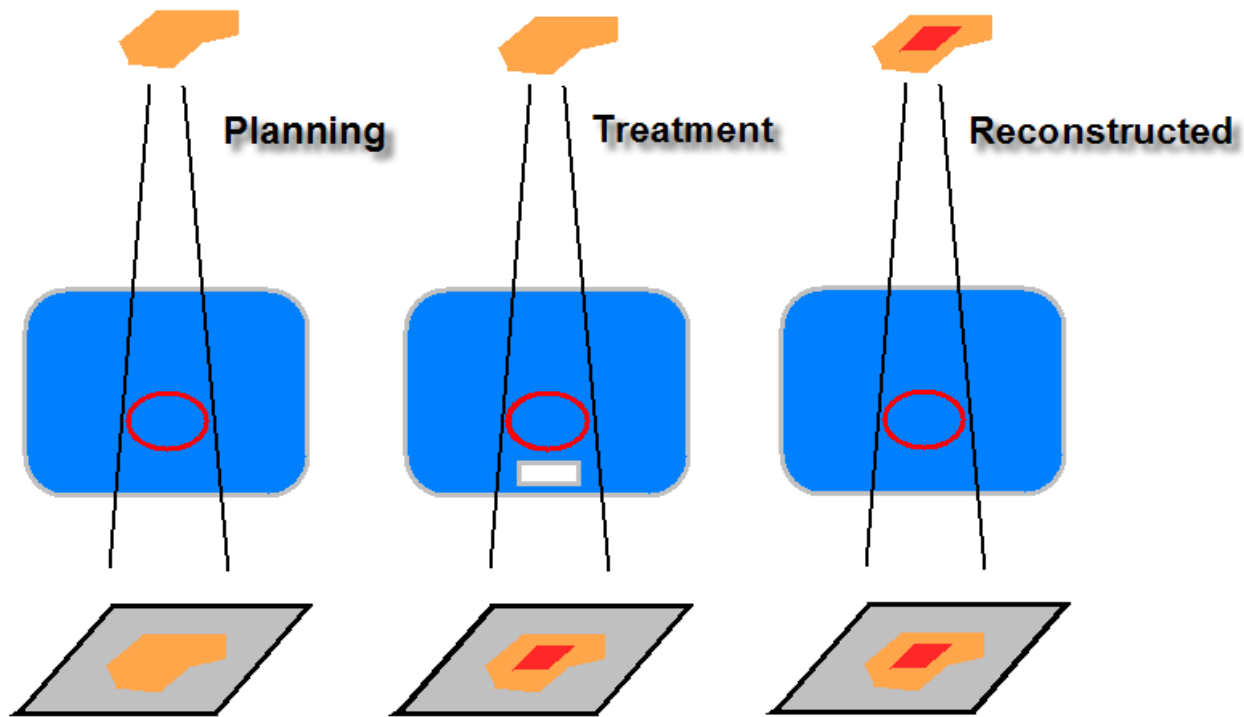


Figure 13: Demonstration of how the backprojection assumption could lead to erroneous dose reconstruction. A planning target (red circle) is located inside a water phantom. The planning fluence is incident on both the planning phantom geometry (left) and treatment phantom geometry (center). An air gap which was not present in the planning geometry, has been introduced in the treatment geometry. Due to less attenuation in the treatment geometry, the measured DPI has an area of higher intensity when compared to the expected DPI (estimated using the planning geometry). In the backprojection assumption, the DPI deviation is attributed to the incident fluence. Dose reconstruction will result in a higher estimated target dose, while the reconstructed DPI will agree with the measured DPI.

It was hypothesized that, for patient cases, deviations between the reconstructed and true doses would be larger than deviations between the planning and true doses. The reasoning for this hypothesis is shown in the following thought experiment (shown in Figure 13). Consider the planning geometry to be a solid water phantom, and the time-of-treatment geometry to be the same solid water phantom, except with a volume of air in the beam-line. The CTV is located directly in front of where the air pocket exists. The time-of-treatment measured exit fluence would be equal to the expected exit fluence except for the area directly behind the air pocket, which would have a higher intensity due to a lower attenuation pathlength through the air pocket. For backprojection-based patient dose reconstruction, this deviation would be attributed

wrongfully to deviations in the incident fluence, which would be assumed to have an area of higher intensity. The reconstructed patient dose uses an incident fluence with an area of higher intensity, and therefore the reconstructed dose would be elevated throughout the patient along the area covered by the higher intensity area. While both the reconstructed and true doses for the CTV are higher than the planned CTV dose, the reconstructed dose also has higher dose in all normal structures along the beam as well. While this is a simplified thought experiment, it indicates that caution must be exercised before blindly using fluence backprojection to achieve dose reconstruction.

4.1.4. Planned, Actual, and Backprojected Dose Comparisons

A simple metric to compare patient plans is the dose-volume histogram (DVH). Indeed, DVH metrics are used as a basis for both plan optimization and plan approval. DVHs for the GTV, rectum and bladder for each patient are shown in Figure 34-82 in Appendix II. Respective zoomed-in GTV DVHs are shown are also shown in Appendix II. Each plot includes the planning DVH as well as each day-of-treatment delivered and reconstructed DVHs. Histograms of several GTV dose indices differences are shown in Appendix II also.

An example of a patient which showed minor deviations is patient 7 (Figure 52-55). The average reconstructed GTV D_{95} is 2 cGy less than the planned D_{95} , while the average actual D_{95} is 38 cGy less than the planned. If the plan were to be adapted to achieve the same exit fluence using dose reconstruction results, 2 cGy more dose would be delivered to the GTV D_{95} . This adaptation would result in the GTV D_{95} absorbing 36 cGy less than the planned dose. This correction would result in a slight improvement to the total target dose.

A typical patient case is patient 13 (Figure 67-70). The average reconstructed GTV D_{95} is 55 cGy greater than the planned D_{95} , while the average actual D_{95} is 82 cGy less than the planned. If the plan were to be adapted to achieve the same exit fluence using dose reconstruction results, 55 cGy less dose would be delivered to the GTV. This adaptation would result in the GTV absorbing 137 cGy less than the planned dose. Instead of improving the treatment, this correction would exacerbate the delivery.

The largest discrepancies between backprojected and actual doses happened in patient 4 (Figure 43-46). The average reconstructed GTV D_{95} is 123 cGy greater than the planned D_{95} , while the average actual D_{95} is 179 cGy less than the planned. If the plan were to be adapted to achieve the same exit fluence using dose reconstruction results, 123 cGy less dose would be delivered to the GTV. This adaptation would result in the GTV absorbing 302 cGy less than the planned dose.

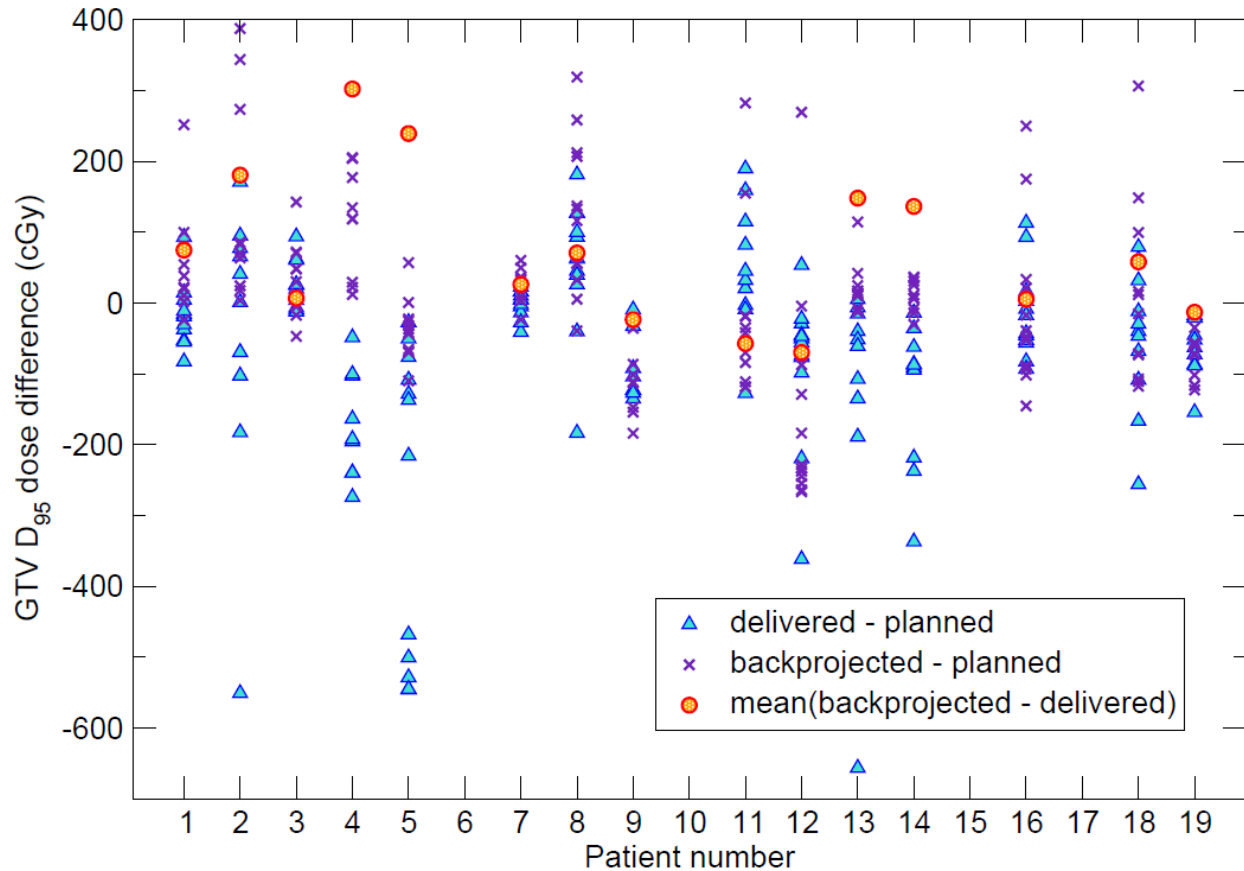


Figure 14: Distribution of GTV D₉₅ deviations for each patient. Delivered versus planned deviations are shown by the blue triangles. Backprojected versus planned deviations are shown by the purple x's. The mean deviations between backprojected and delivered dose are shown by the orange circles.

For each patient, DVH deviation distributions between delivered and planned dose, as well as between backprojected and planned dose were calculated, along with the mean deviation between backprojected and delivered dose. The dose indices examined were GTV D₉₅ (Figure 14), bladder D₂₅ (Figure 82) and D₅₀ (Figure 83), and rectum D₁₇ (Figure 84) and D₃₅ (Figure 85) (only the GTV plot is shown in this chapter; all others are shown in Appendix II). For the GTV D₉₅, in some patients (patients 2 and 12), the backprojected dose deviated more from the planned dose than the delivered dose. In other cases (patients 13 and 14), the opposite held true: the delivered dose deviated more from the planned dose than the backprojected. The backprojection-

versus-delivered deviations show the effect that adaptation of the plan would have on the delivered dose. Once again, in some cases the adaptation would bring the delivered dose closer to the planned dose, but in others it would push it farther away. The bladder and rectum plots show that while the backprojected dose stays within a few hundred cGy of the planned dose, the delivered dose varies up to 6000 cGy. The difference in magnitude is due the fact that dose reconstruction was implemented on the planning geometry—the structures were in the exact same position for calculation of both planning and backprojected dose distributions. The delivered dose, however, was calculated on each patient pose, yielding widely varying bladder and rectum doses due to their positional variance.

The relationship between exit fluence deviations and patient dose deviations was examined. For each beam of each patient pose of each patient, the number of pixels with deviations greater than 5% was determined. Only pixels with dose greater than 20% max dose (i.e. those in the beam) were tabulated. The fraction of pixels with deviations greater than 5% was then calculated for each patient pose of each patient geometry. The deviation between delivered and planned GTV D_{95} 's were plotted against the DPI deviations (shown in Figure 15). For each patient pose, the DPI deviation frequency was averaged over all beams. Lines of best fit were plotted for each set of data (delivered minus planned, backprojected minus planned, backprojected minus delivered), and the null hypotheses was tested: that the slope of each line was equal to zero. The null hypothesis was not rejected ($p = 0.08$) for the delivered-minus-planned data; the slope of the data could be zero. The null hypothesis was rejected for the backprojected-minus-planned data ($p = 3.4 \times 10^{-11}$) and the backprojected-minus-

delivered data ($p = 0.004$). In this instance, DPI deviations were positively correlated to DVH deviations.

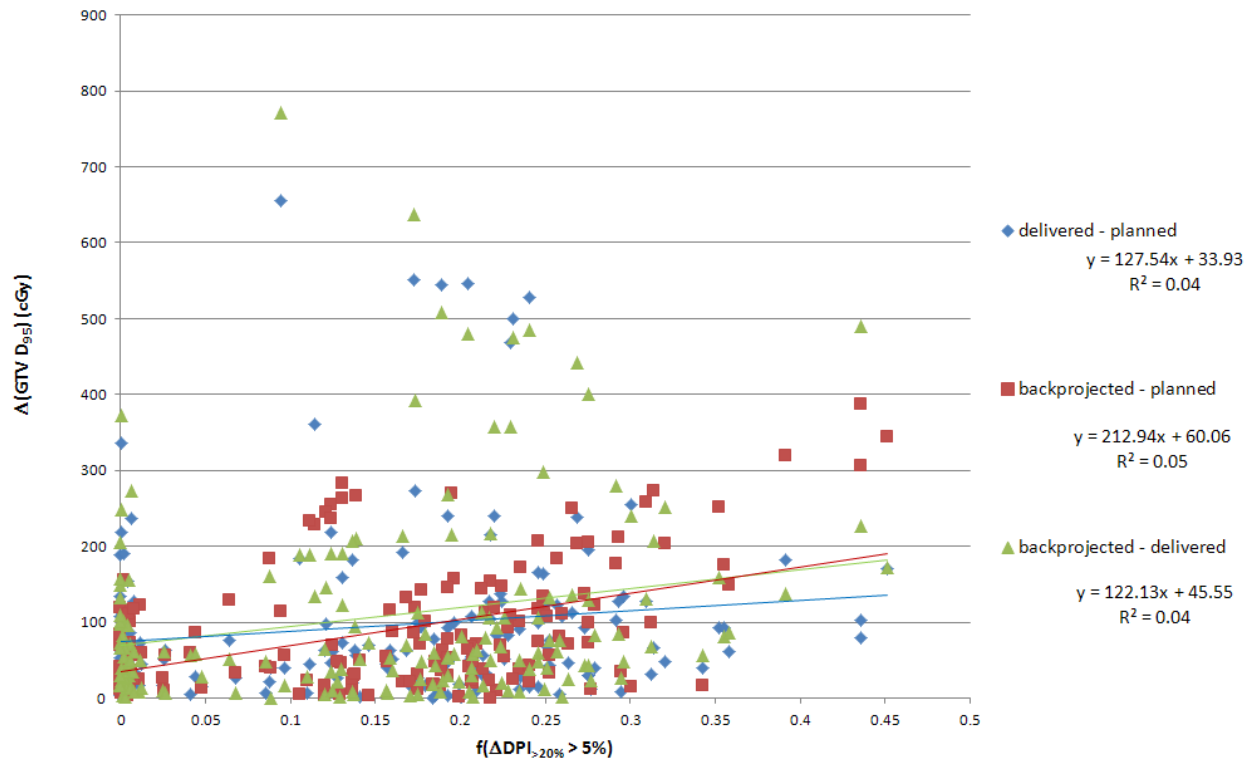


Figure 15: Deviation in GTV D_{95} versus fraction of DPI pixels that have deviations greater than 5%, for all NKI patients. The diamonds correspond to differences between the delivered and planned doses. The squares correspond to differences between the backprojected and planned doses. The triangles correspond to differences between the backprojected and delivered doses. Respective trend lines are shown. For DPIs, only pixels with dose greater than 20% of maximum dose were analyzed. For each patient pose, the DPI pixel deviation frequency was averaged over all beams.

It must be noted that the correlation between DPI deviations and DVH deviations is not always straightforward. As seen in Figure 15, there are some patient poses which result in greater than 40% of DPI pixels having deviations greater than 5%, yet there is less than a 100 cGy GTV D_{95} difference. Further examination of these patient poses reveals that DPI deviations were caused by variations in the amount of gas present in the rectum (see Figure 16). Since beam attenuation through gas is much less than that through tissue, the difference between the planned and delivered DPIs was greater than

5% in the area behind the presence of rectal gas. However, the location of the rectal gas did not cause significant differences between the planned and delivered target dose. In a few observed patient poses, however, the GTV location was shifted past the limits of the PTV due to variation in bladder filling (see Figure 17). In this case, even though the GTV D_{95} deviation was greater than 500 cGy, there were no DPI deviations greater than 5%. In these cases, variation in bladder filling did not significantly affect the patient attenuation.

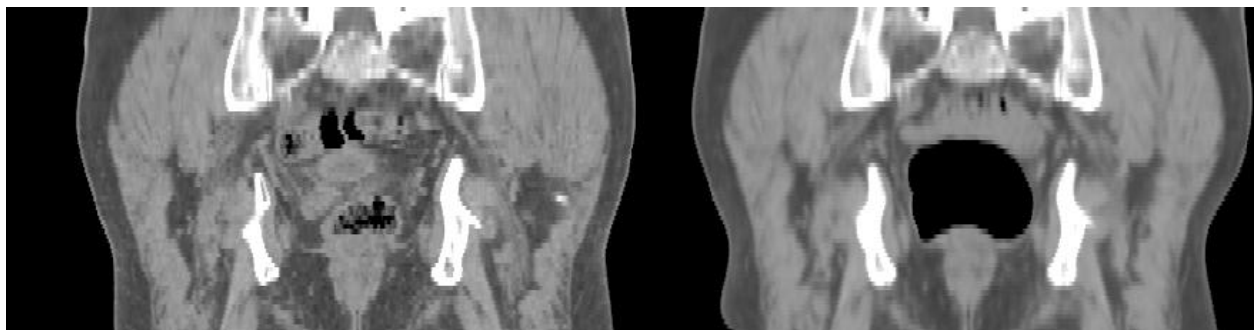


Figure 16: Coronal slice through the planning pose (left) and a day-of-treatment pose (right). The rectal gas present in the day-of-treatment pose causes DPI deviations greater than 5% from expected. However, the GTV D_{95} deviation is less than 100 cGy.



Figure 17: Coronal slice through the planning pose (left) and a day-of-treatment pose (right). The filling of the bladder in the day-of-treatment pose causes the prostate to shift inferior to isocenter, and therefore the GTV D_{95} deviation is greater than 500 cGy. However, there are no large patient attenuation differences caused by bladder filling, and therefore the DPI deviations are less than 5% in all pixels.

To further examine the efficacy of using DPI deviations to predict DVH deviations a receiver operating characteristic (ROC) curve was generated. The percentage of failing DPI pixels (i.e. those with deviations greater than 5%) was used as the independent variable. For each patient pose, the GTV D_{95} deviations were deemed

positive or negative based on whether or not they exceeded doses of 50 cGy, 100 cGy, 150 cGy, and 200 cGy. If the DVH deviation exceeded the dose deviation criterion, it was considered a true or false positive (TP or FP), (true if the DPI deviations were a correct predictor, false if the DPI deviations were an incorrect predictor). If the DVH deviation did not exceed the dose deviation criterion, it was considered a true or false negative (TN or FN). The true positive rate (TPR) and false positive rate, defined as:

$$\text{TPR} = \text{TP} / (\text{TP} + \text{FN})$$

$$\text{FPR} = \text{FP} / (\text{FP} + \text{TN})$$

were plotted against each other to form ROC curves for each dose deviation criterion. The ROC curves are shown in Figure 18. A measure of predictive accuracy was obtained by measuring the area under each curve (AUC)—equaling 0.58 for the 50 cGy criterion, 0.63 for the 100 cGy criterion, and 0.55 for both the 150 cGy and 200 cGy criteria. None of the criteria yielded an acceptable predictive quality, as an AUC of 0.63 was not sufficient.

One method to correct for the false positives (e.g. significant DPI deviations, but insignificant DVH deviations) involves limiting rectal gas via dietary protocol. In fact, the NKI recommends a dietary protocol of mild laxatives two days prior to imaging or treatment (Smitsmans, Pos et al. 2008). This protocol resulted in less random interfraction prostate motion. A method to correct for the false negatives (e.g. insignificant DPI deviations, but significant DVH deviations) would be to use implanted markers in the target. Due to their higher electron density, these markers will alter the attenuation through the patient such that they are visible in the DPI. Thus, the positioning of the target may be monitored with the EPID. Also, other target-monitoring

devices could be used to assure that the target has not significantly shifted between planning and delivery. Detection of implanted markers is discussed in the following section.

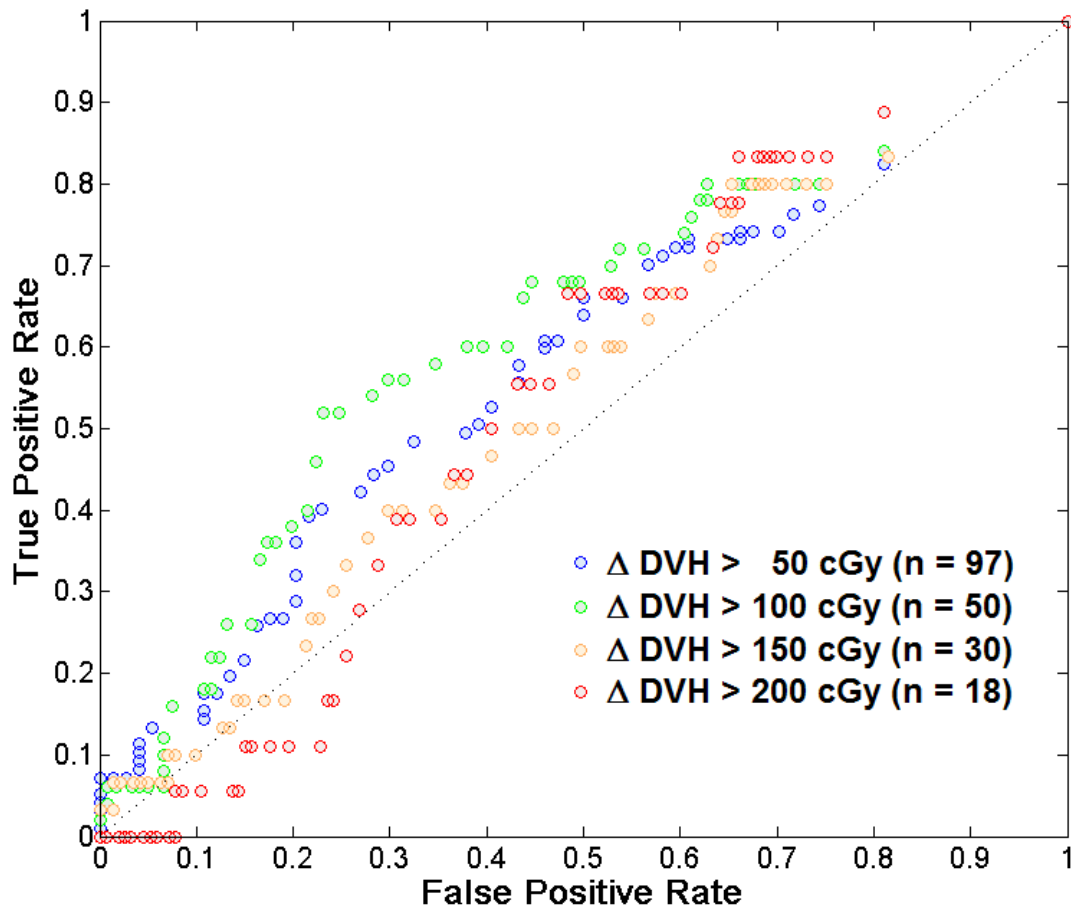


Figure 18: ROC curve showing the predictive value of DPI deviations for GTV D_{95} deviations with tolerance criteria of 50 cGy, 100 cGy, 150 cGy, and 200 cGy. The dotted black line is the line $y = x$.

4.2. Detection of Implanted Markers

The proposal for this work called for both time-of-treatment CTs and DPIs to be acquired for patients at our institution for the prostate site. Only two patients enlisted in the prostate protocol at our institution. This protocol included acquisition of a CBCT while the patient was on the delivery couch, as well as acquisition of DPIs for every

treatment beam. The protocol also called for Calypso (Seattle, WA) marker implants to monitor prostate positioning throughout treatment delivery. Therefore it was of interest as to whether the markers could be detected in measured DPIs for each beam.

Before any patients went through the protocol, an experiment was designed to determine whether the EPID could detect objects of similar size to Calypso transponders. While measured exit fluence images can detect the presence of changes in the patient geometry, they do not necessarily provide a quantitative description of what those changes are. If objects such as fiducial markers are implanted at precise locations within the patient geometry, it may be possible to locate them in the exiting fluence due to their higher attenuation coefficients as compared to the surrounding normal tissue. The detection of these objects in the measured exit fluence image provides insight into target location changes during treatment, which is critical for achievement of dose verification. At our institution, the Calypso system has been installed to monitor patient position variations during treatment delivery.

Electromagnetic transponders are implanted in the patient and transmit safe radiofrequency waves which are detected by the Calypso receptor and processed to determine transponder position. Thus, patient anatomic positional information is gained during treatment delivery. Although these transponders have a lower atomic density than gold fiducial markers, they should still be visible in a DPI due to their higher density as compared to surrounding tissue. If the transponders can be detected in a DPI, then this provides an opportunity to correlate Calypso's positioning measurements with those determined using the DPI. For patient plans which do not employ the Calypso system, implanted gold fiducial markers may be used for patient setup, alignment, and

monitoring. Localization of the markers on the measured DPI will provide knowledge of the patient geometry during treatment.

For IMRT treatments, identification of markers in DPIs is confounded by patient scatter, fluence fluctuations caused by the IMRT delivery, and tissue heterogeneities in the patient. Distinguishing the markers from background becomes difficult due to the widely varying levels of intensity incident on the patient. To obtain a DPI in which the objects may be located, a ratio may be taken between the DPI with the patient present and the DPI without the patient present. With the patient present, the fluence incident on the EPID could be described as:

$$\psi_{patient} = \psi_0 (A_{MLC} A_{patient} + S)$$

where ψ_0 is the fluence exiting the accelerator, A_{MLC} is the attenuation due to the MLC, $A_{patient}$ is the attenuation due to the patient, and S is patient scatter. Without the patient present, the fluence incident on the EPID could be described as:

$$\psi_{no-patient} = \psi_0 A_{MLC}$$

Solving for the attenuation due to the patient, the following equation is obtained:

$$A_{patient} = \frac{\psi_{patient}}{\psi_{no-patient}} - S \frac{\psi_0}{\psi_{no-patient}}$$

To examine whether an object the size of a transponder could be distinguished on a DPI of an IMRT field, two standard gold markers were positioned near the prostate location in a Rando (The Phantom Laboratory, Salem, NY) anthropomorphic pelvic phantom. DPIs of the IMRT field were acquired both with and without the phantom present in the beam at a gantry angle of 0°. A simple ratio (which assumes no scatter) was then calculated between the two images, yielding the attenuation map from the

phantom. As seen in Figure 19, both gold markers were distinguishable in the ratio image in areas of both high and low beam intensity. Future work in this study will be to subtract the estimated scatter from the patient/phantom geometry before the ratio is calculated. The addition of a scatter filter to the algorithm should cause the markers to be much more distinguishable. Also, pre-existent code in our institution that automatically detects markers will be used to automate the detection process (Murphy and Todor 2005).

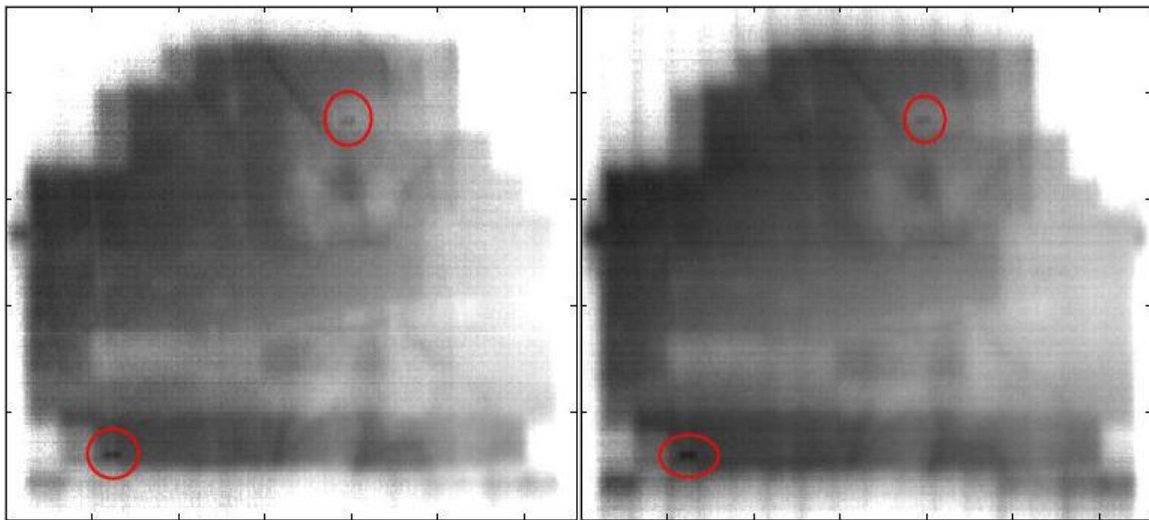


Figure 19: Ratio images of DPI with anthropomorphic phantom in the beam and without the phantom in the beam. The left image corresponds to an accelerating potential of 6 MV, whereas the right image corresponds to an accelerating potential of 18 MV. The gold markers are circled.

4.2.1. EPID/Calypso Interference

Once the DPIs were obtained for the first fraction of the first patient approved for the prostate protocol, it was immediately apparent that a significant artifact existed in the images. The artifact appeared to be caused by an errant readout from the EPID imager due to the presence of vertical stripes through the images (see Figure 20). It was hypothesized that the artifact was caused by electronic interference between the EPID

readout system and the Calypso transponders which were implanted in the patient's prostate. Supporting this hypothesis was the fact that the artifact grew worse when the EPID was closer to the Calypso receiver used for locating the position of the transponders. The artifact was most noticeable when the gantry was at 180° , i.e. when the EPID was at its highest position, and closest to the Calypso detection panel. The artifact was least noticeable when the gantry was farthest from 180° (for treatment beams at gantry angles of 30° and 330°).

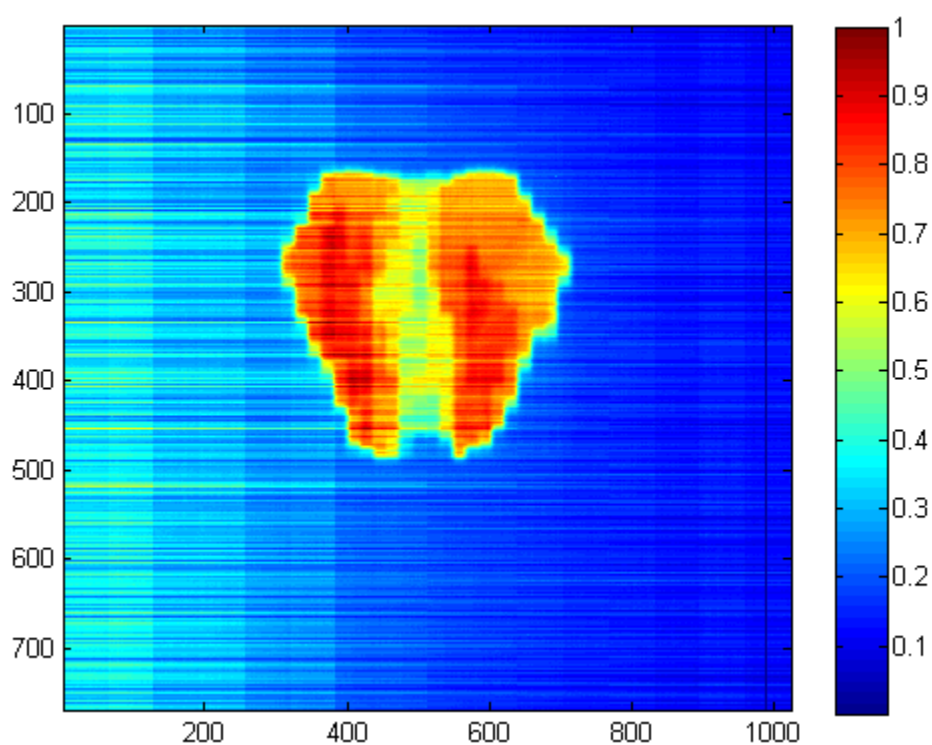


Figure 20: Example of a through-patient DPI captured during treatment of a prostate site. The gross artifacts, present both inside and outside the field, were unexpected. It was hypothesized that the artifacts were caused by interference between the Calypso transponders located in the patient's prostate and the readout electronics of the EPID. The gantry angle for this DPI was 180° .

To test this hypothesis, reproduction of the artifact was attempted in a controlled setting. A set of Calypso transponders was borrowed from our clinic, and placed upon the treatment couch, with the Calypso detection panel in its proper place, located above

the couch. The gantry was rotated to 180°, and the EPID was extended above the Calypso panel at SDDs ranging from 125 cm to 150 cm. Control images of two fields (a flood field and a 10×10 cm² field) were acquired while the Calypso monitoring remained inactive. Test images were then acquired with the Calypso monitoring active. A ratio of the active to inactive Calypso images for the 10×10 cm² field is shown in Figure 21. Differences as large as an order of magnitude were seen outside of the field. An indirect relationship was confirmed between the artifact severity and distance between the EPID and Calypso panel.

It was hypothesized that this artifact could be removed by constructing a Faraday cage around the EPID to remove any electronic interference from the Calypso panel. The same measurements described in the previous paragraph were re-acquired, except with a rudimentary Faraday cage protecting the EPID. The cage was constructed out of overlapping pieces of aluminum foil wrapping around the outer shell of the EPID. As shown in Figure 22, the severity of the artifact was reduced by an order of magnitude. Profiles across the left-right and inferior-superior directions are shown in Figure 23 and Figure 24. Even with the reduction of the artifact, they were still too large to detect the implanted transponders. Therefore, no more measurements were analyzed for the dose verification study.

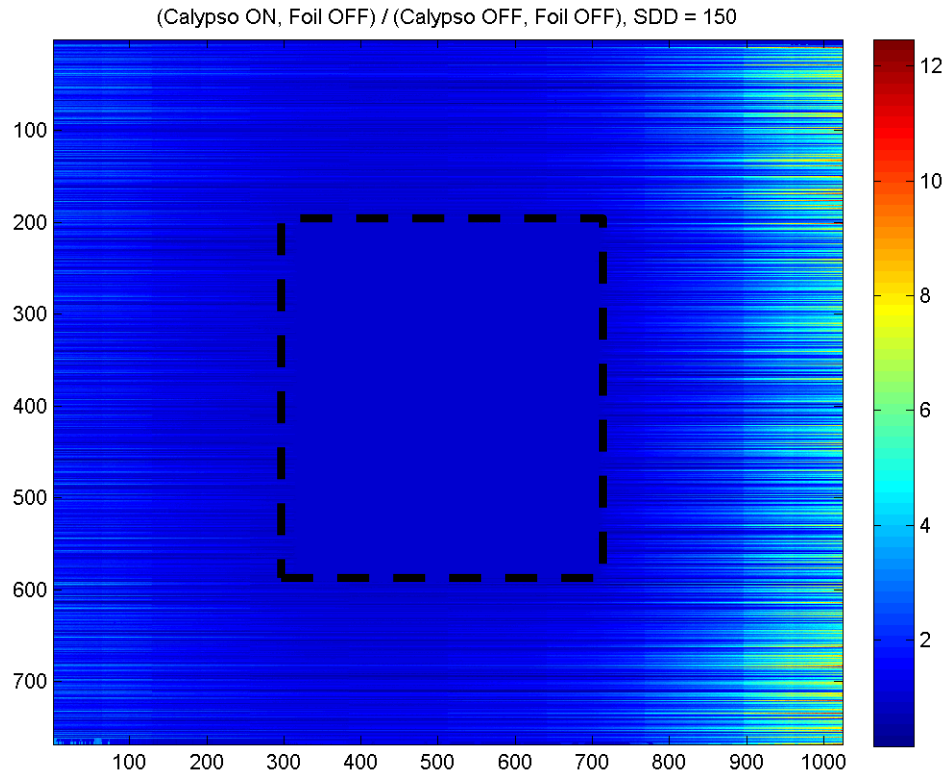


Figure 21: Ratio of the $10 \times 10 \text{ cm}^2$ field acquired with active Calypso tracking to that without Calypso tracking. The field is marked by the dashed black line. Artifacts as large as an order of magnitude are seen outside the field.

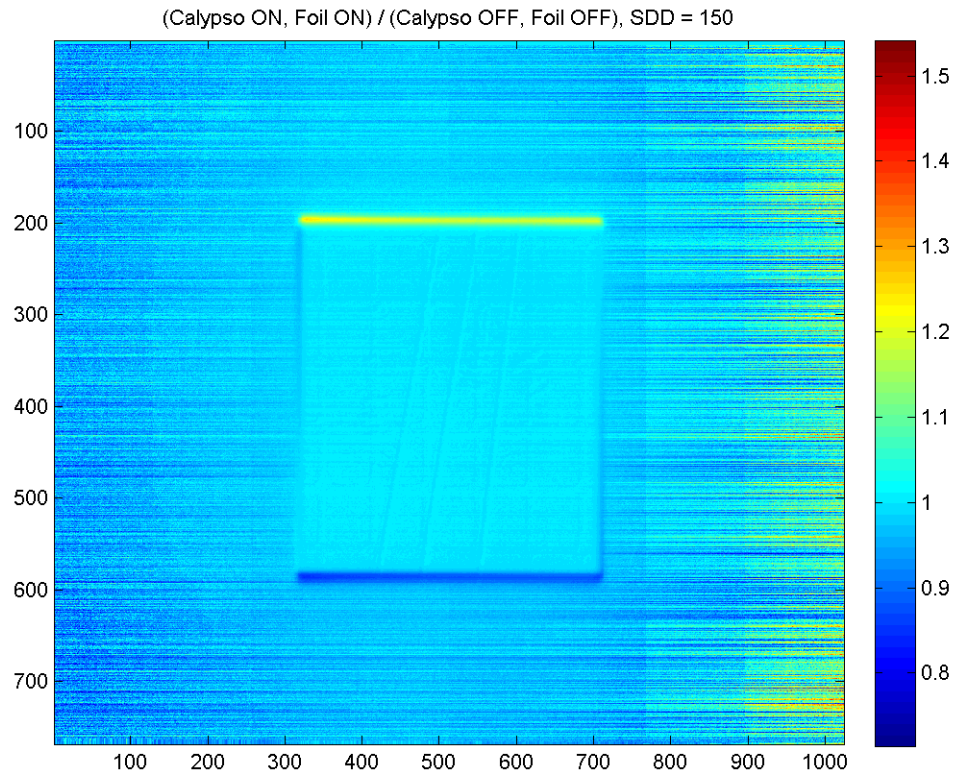


Figure 22: Ratio of the $10 \times 10 \text{ cm}^2$ field acquired with active Calypso tracking and a rudimentary Faraday cage surrounding the EPID to that without Calypso tracking or Faraday cage. Artifacts were reduced by an order of magnitude outside of the field. Deviations along the field edges were due to slight variation in the jaw positions between acquisition of the two DPis.

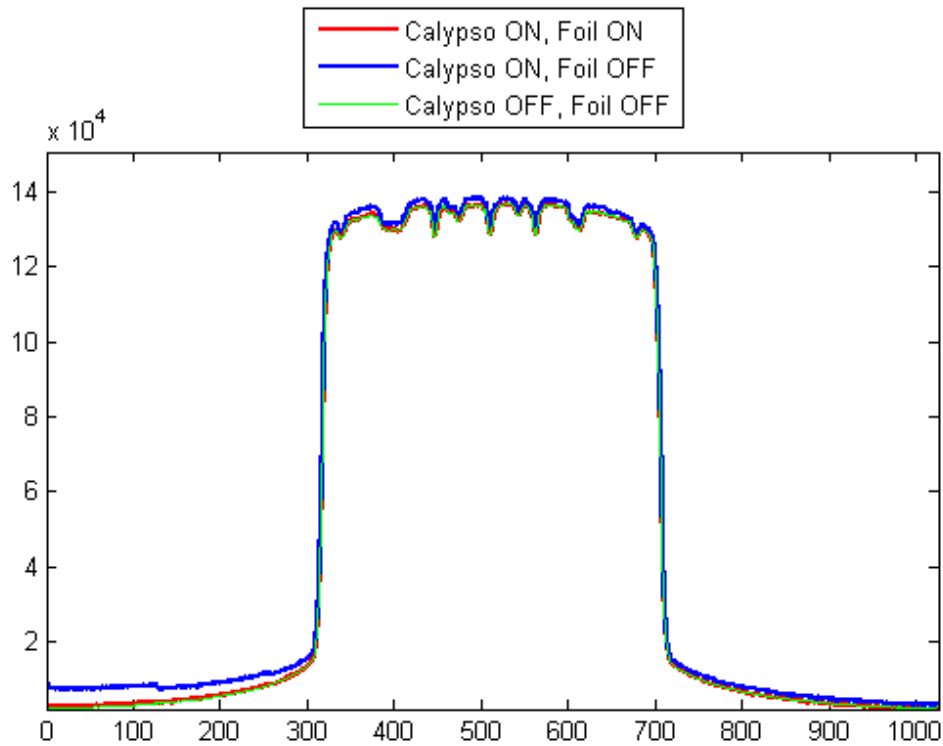


Figure 23: Profile along the left-right direction for a $10 \times 10 \text{ cm}^2$ field for a non-Calypso/non-Faraday cage set-up (green line), a Calypso/non-Faraday cage set-up (blue line), and a Calypso/Faraday cage set-up (red line). The green line represents normal acquisition of a DPI. The blue line represents the artifact caused by electronic interference between the EPID readout and Calypso transponder tracking. The red line represents the correction for the artifact by enclosing the EPID in a rudimentary Faraday cage. The “ripples” in the middle of the profile are caused by attenuation of the case containing the transponders on the couch.

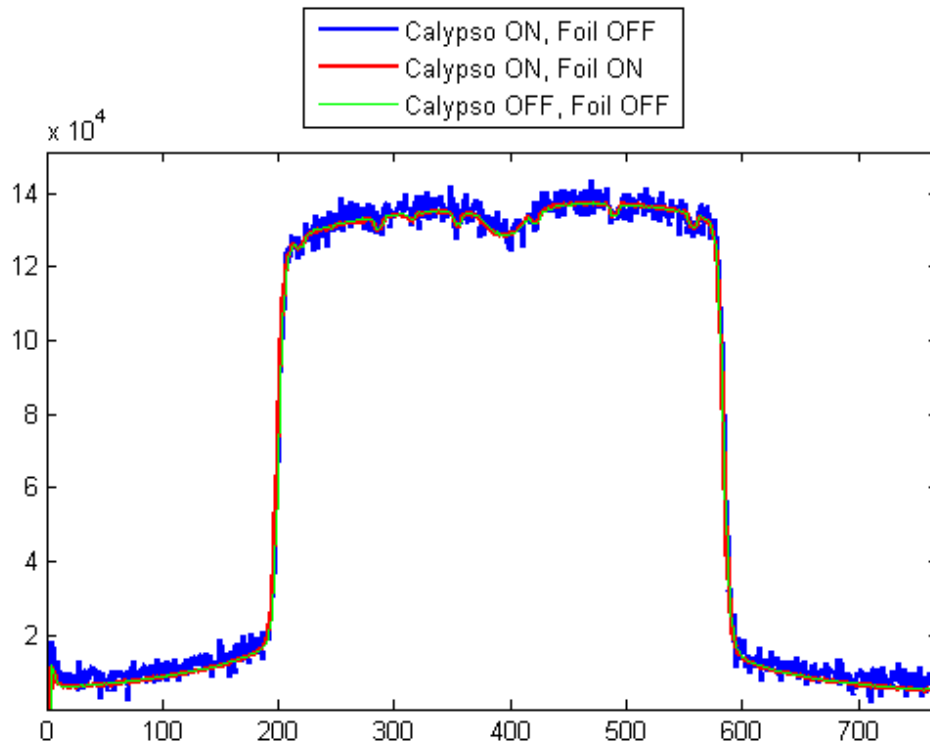


Figure 24: Profile along the superior-inferior direction for a $10 \times 10 \text{ cm}^2$ field for a non-Calypso/non-Faraday cage set-up (green line), a Calypso/non-Faraday cage set-up (blue line), and a Calypso/Faraday cage set-up (red line). The green line represents normal acquisition of a DPI. The blue line represents the artifact caused by electronic interference between the EPID readout and Calypso transponder tracking. The red line represents the correction for the artifact by enclosing the EPID in a rudimentary Faraday cage.

4.3. DRR Simulations

Closing the loop of IGART via DPI comparison requires accurate simulation of the expected DPI. Sensitivity of comparisons should increase as the amount of time decreases between the image used for DPI simulation field and the treatment time DPI measurement as there is less time for the patient to change. Depending on the clinic and patient protocol, the most recent patient geometry could range from the planning FBCT (taken several days in advance) to a CBCT acquired moments before the

treatment delivery begins. Therefore a balance must be struck between the accuracy and the speed of DPI simulation.

In non-time critical situations, MC simulation of radiation transport to simultaneously determine patient dose and the exit fluence DPI provides an accurate method to perform delivery verification. However, dose calculation for online IGART treatment evaluations is not feasible with pure MC techniques due to computation time. Nonetheless, in these cases post-treatment delivery validation can be performed when daily treatment adaptations occur. This process, however, only permits offline closed loop adjustments. Greater speed DPI calculations are required for online IGART.

A through-patient DPI consists of two fluence components incident upon the EPID: 1) the attenuation of the incident fluence through the patient, termed DPI_{att} , and 2) the scattered radiation produced within the patient, termed DPI_{scat} . The DPI calculation is therefore separable, and each component has the potential to be computed using faster techniques. An estimate of DPI_{att} may be obtained by calculating the attenuation along the ray through the patient geometry to each detector pixel. These calculations are called digitally reconstructed radiographs (DRRs). An estimate of DPI_{scat} component may be obtained from MC models, if there is low variation of the component caused by variation in patient anatomy. This section describes development of DRR-based DPI calculations, with MC calculation through the same geometries used as a reference standard.

4.3.1.DRR Calculation

A DRR patient attenuation model was created by modifying an in-house DRR algorithm. Inputs for the original in-house DRR code include 1) the source definition, which is

taken to be a mono-energetic point source, 2) the patient CT geometry through which the incident source fluence is projected, and 3) the detector geometry, which is a simple plane of pixels. The original DRR generator ray traced through the patient geometry from a point source located at the accelerator target location. In performing the ray trace, the provided code simply added pathlengths through the geometry as opposed to computing exponential attenuation. Siddon's technique was used for ray tracing (Siddon 1985).

This in-house DRR code was adapted for calculating the primary transmission of a megavoltage beam through a patient geometry. Three major changes were implemented. First, the code was updated to handle poly-energetic beams as input by using a fluence-weighted sum of mono-energetic calculations. For both 6 MV and 18 MV accelerating potentials, the beam energy spectra were modeled according to Mohan (Mohan, Chui et al. 1985), with energy bins of 0.5 MeV. Secondly, the patient CT was transformed from CT-number information to meaningful attenuation information, i.e. $\mu\rho$, where μ is the mass attenuation coefficient and ρ is the density of the voxel material. Since μ is dependent on beam energy, per-energy-bin instances of the patient geometry were created. The per-energy values of μ were derived using XCOM (Berger, Hubbell et al. 1998), a photon cross sections database provided by the National Institute of Standards and Technology (NIST). Finally, the model for attenuation was updated from an additional to an exponential one.

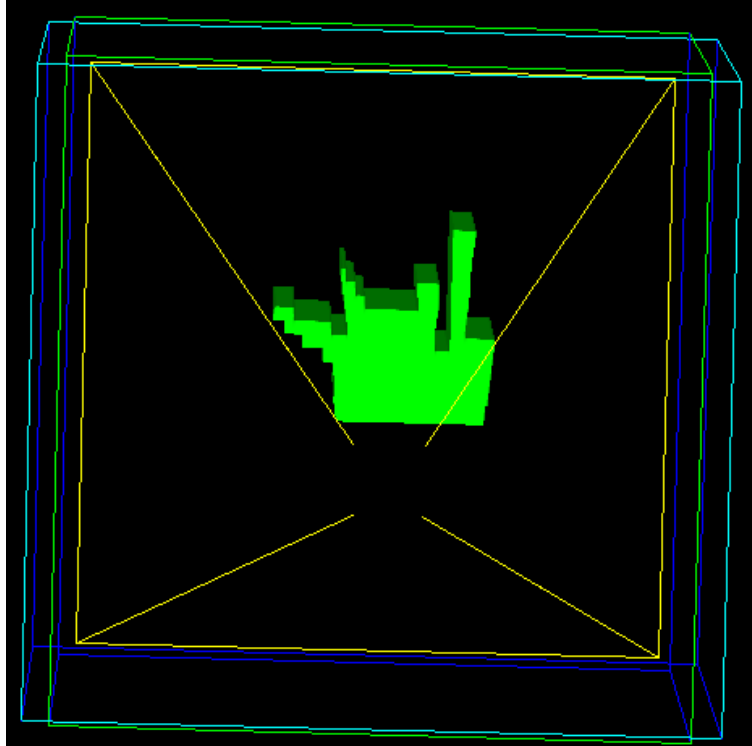


Figure 25: Irregular phantom created for geometric validation of the DRR model. The incident beam, directed into the page, is shown in yellow.

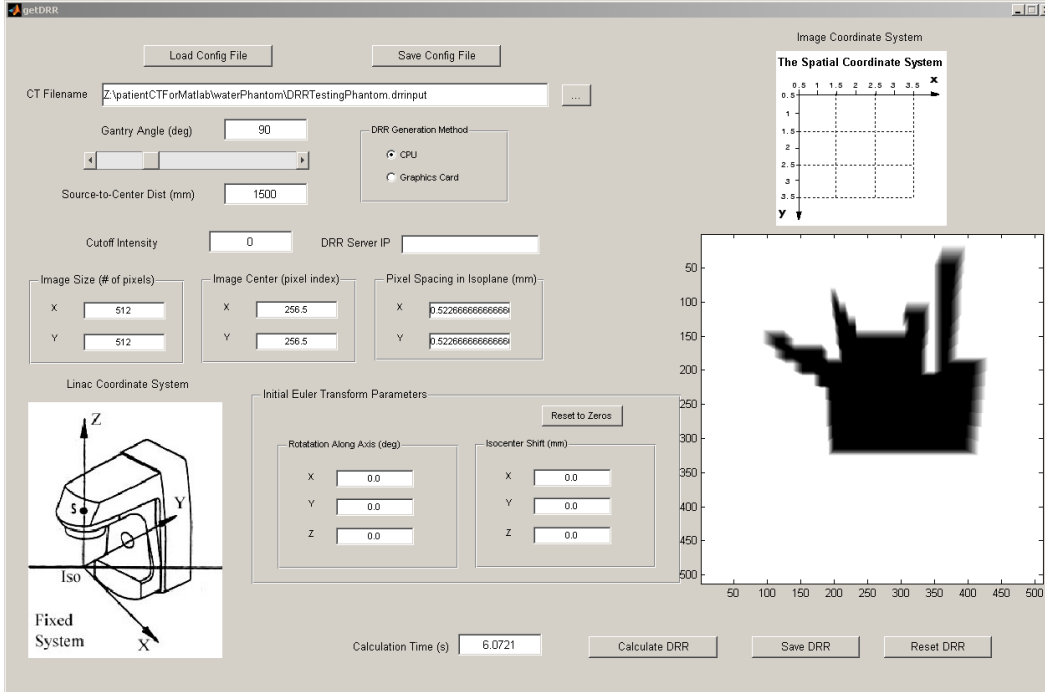


Figure 26: DRR-generator GUI. The GUI is used to set options describing the geometry of the beam, phantom, and imager, based on a user-selected input file (seen in top left). The “Calculate DRR” button is then pressed, which calls the DRR simulation code to run. The generated DRR is then displayed in the panel on the right.

Primary attenuation for the DRR-based DPI-generator was benchmarked via comparison with an MC-generated exit fluence (discussed in Section 3.2.1). I coded in the ability to separate the MC-generated exit fluence into primary and scatter components, permitting this comparison. For the MC calculations, instead of using the full head source model, a simple point source was coded by changing the directional components of each sourced particle and forcing them to have the same origin at the target location (0,0,0), thereby allowing for comparison to the simple DRR point source. To verify that the geometry of the DRR was consistent between the DRR and MC codes (i.e. the patient geometry and scoring plane were in the correct position relative to the point source), an irregular water phantom was created and is shown in Figure 25. Delivery information stored in the TPS was transferred manually to both the DRR and MC codes for input. This information included beam energy, patient/phantom geometry, and imager geometry. One billion photons were simulated incident on the testing phantom for the MC calculation, which required slightly less than three hours of computer time (on a single CPU). DRR-generation required approximately one minute (on a single CPU), of which the majority was spent loading the phantom geometry into the code system. The DRR calculation itself took less than ten seconds. The graphical user interface (GUI) for the DRR generator is shown in Figure 26.

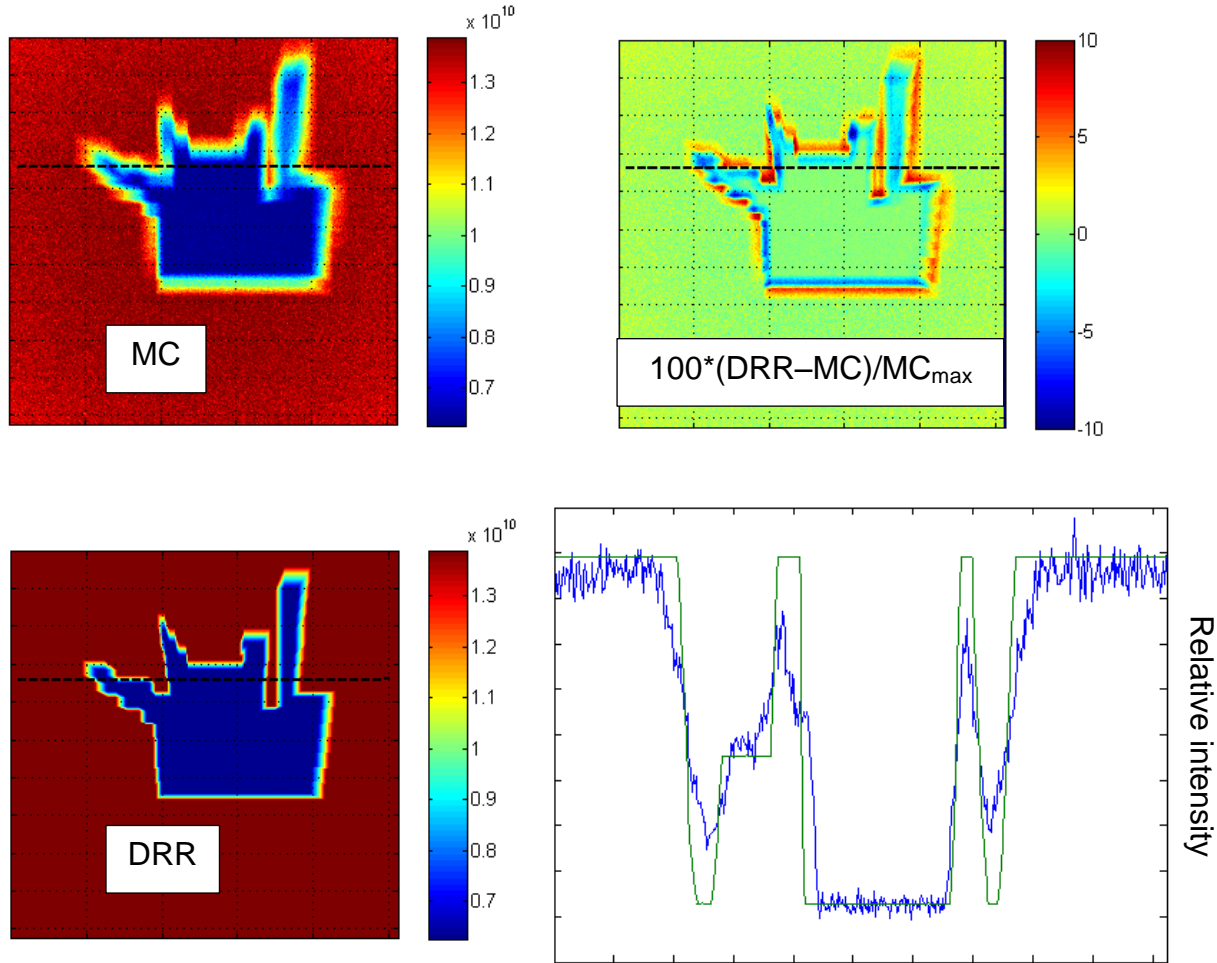


Figure 27: Comparison of DPs simulated through an irregular water phantom by the primary component of an MC calculation (top left) and by a point-source DRR calculation (bottom left). The difference map, measured in percent with respect to maximum intensity, is shown in the top right panel. Profile intensities along the dashed black line of the images are shown in the bottom right panel. The blue data refers to the MC-generated DPI, while the green data refers to the DRR-generated DPI.

The DRR- and MC-generated images are compared in Figure 27. Differences up to ten percent of maximum intensity were observed along the edges of the irregular phantom. While the MC-generated image showed a softer gradient in these areas, the DRR-generated image displayed very sharp edges. In low-gradient areas, however, the DPs agreed within two percent. It was shown that the TPS information was successfully transferred to the DRR system, and that the DRR-generator correctly

modeled the geometry of the beam, patient, and imager. Planned future development of the DRR code includes IMRT capabilities and a more fully automated system.

4.3.2. Patient Scatter Model

It was hypothesized that patient exit scatter variation was insignificant with respect to the total exit fluence, and therefore a single scatter estimate would be valid for all patient poses. An estimate of the patient scatter contribution to the exit fluence was obtained by using MC simulations to compute the scatter contribution to the exit fluence for each image of each patient from the NKI prostate patient database (described in Section 3.2.2). Since the VMC++ MC code used in this study does not have a “latch bit” (which, in other MC codes, defines the geometry of last interaction for each particle), a module was written which enabled separation of primary and scatter components. First, the MC source model was modified to bank particles to an exit particle handler. This consisted of saving the phase space coordinates of the source model particle. Phase space coordinates (u, v, w) of particles exiting the MC patient geometry were compared to those of the source model particle. If the energy and direction differed by less than round-off error, the particle was labeled a primary particle; if not, the particle was labeled as scatter. The exit scatter fluence was then convolved with the EPID fluence-to-dose energy deposition kernels at the imager surface to produce the scatter DPI. The per-pixel standard deviation of these DPIs was then calculated over the set of all geometries for each patient. This scatter variation was then divided by the maximum of the mean total DPI (primary plus scatter), to determine the significance of the variation in the scatter component as compared to the total DPI.

For a single patient case, plots of the scatter variation, both by itself and compared to maximum mean total dose, are shown in Figure 28. For this patient, DPIs were simulated through eleven geometries. The per-pixel relative standard deviation of the scatter component for each beam ranged up to 8% of the scatter DPI imager dose. When compared to the maximum total imager dose for each beam, however, the impact of the scatter variation is minimal: for this patient, it is less than 0.2%. The mean and maximum per-pixel scatter variations (with respect to total imager dose) for each patient are shown in Table 5. The mean per-pixel scatter variation with respect to total dose was averaged over all beams for each patient, while the maximum per-pixel variation was determined over all beams as well. The largest mean scatter variation was on the order of 0.1%, and the largest maximum scatter variation was on the order of 0.6%.

Table 5: Mean and maximum per-pixel standard deviations for the scatter component of the exit image. These values were calculated with respect to maximum total dose. The mean scatter variation for each patient was averaged over all beams, while the maximum scatter variation was found over all beams.

Patient	Mean scatter variation (%)	Max scatter variation (%)	Patient	Mean scatter variation (%)	Max scatter variation (%)
1	0.12	0.41	11	0.07	0.20
2	0.11	0.40	12	0.07	0.21
3	0.13	0.60	13	0.05	0.15
4	0.05	0.15	14	0.06	0.19
5	0.11	0.51	15		
6	0.10	0.33	16	0.11	0.37
7	0.07	0.21	17		
8	0.09	0.25	18	0.14	0.46
9	0.11	0.41	19	0.08	0.23
10	0.14	0.47			

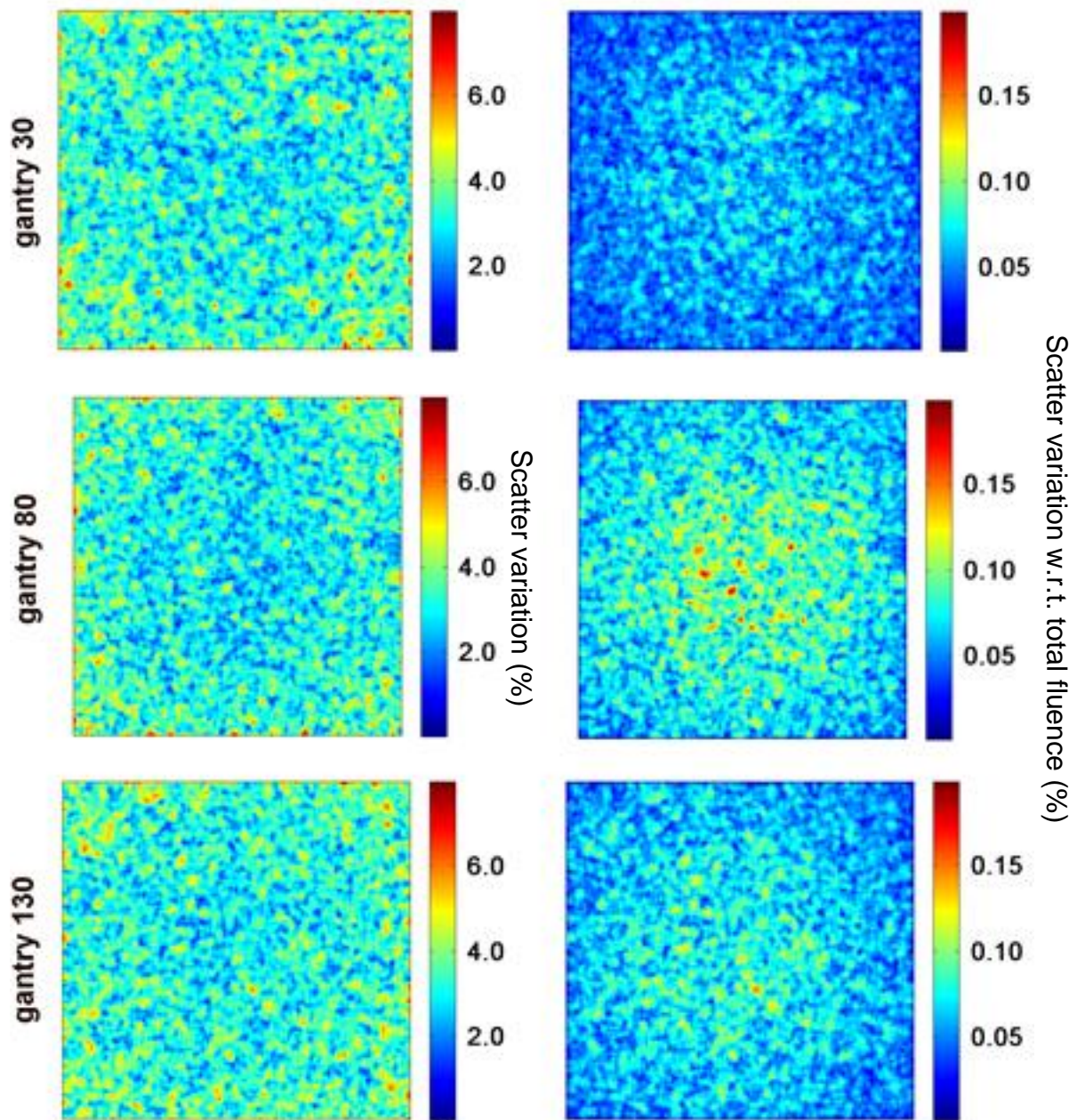


Figure 28a: Scatter variation for patient 1, scaled in percentages. The left column shows the per-pixel relative standard deviation of the scatter DPI through a series of eleven patient geometries. The right column shows the same scatter variation, but in relation to the maximum mean total DPI. Only the DPI area within 2 cm of the beam is included. Gantry angles of 180°, 230°, 280°, and 330° are shown on the following pages.

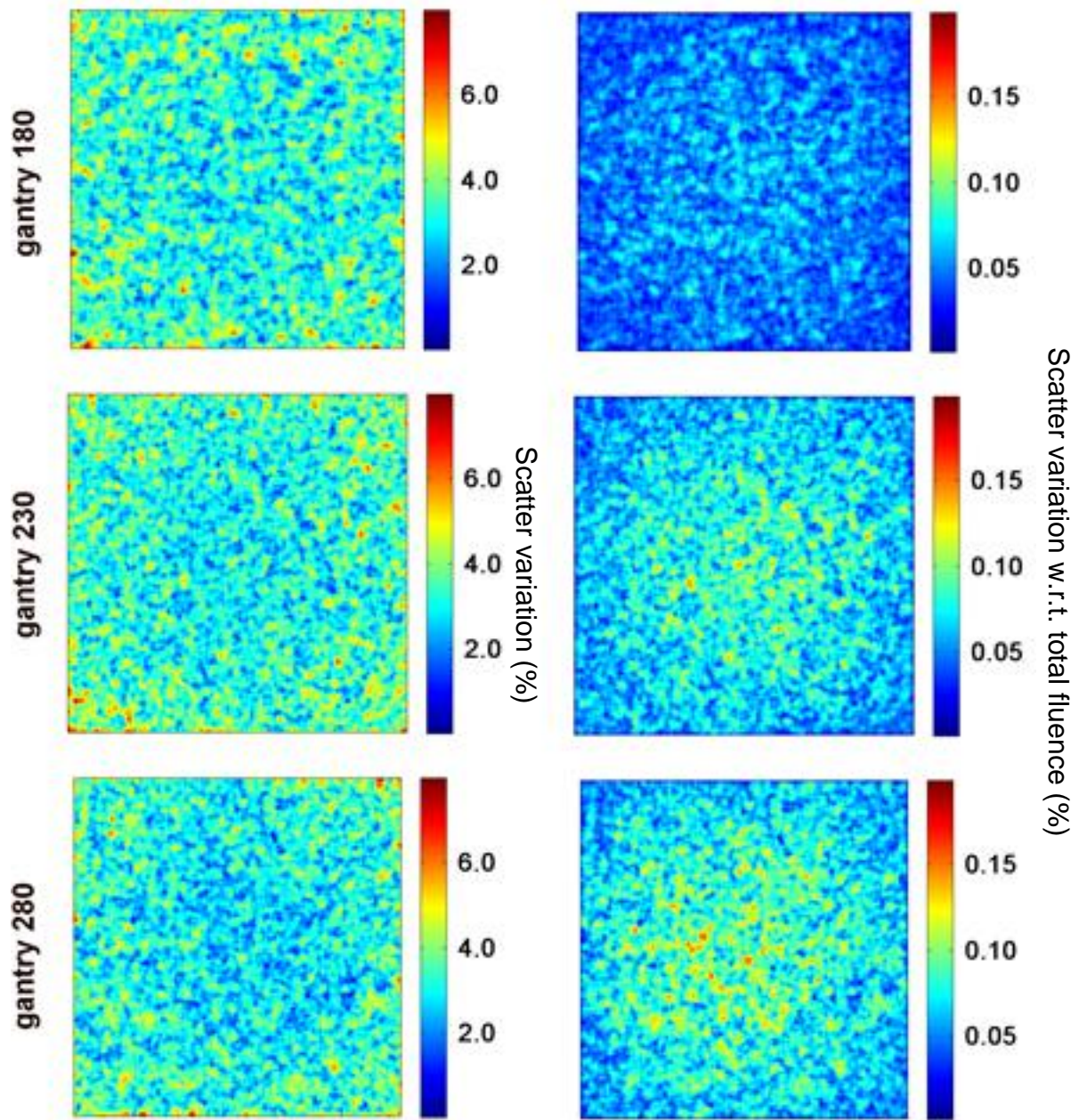


Figure 13b: Scatter variation for patient 1, scaled in percentages. The left column shows the per-pixel relative standard deviation of the scatter DPI through a series of eleven patient geometries. The right column shows the same scatter variation, but in relation to the maximum mean total DPI. Only the DPI area within 2 cm of the beam is included. Gantry angles of 30°, 80°, 130°, and 330° are shown on the previous and following pages.

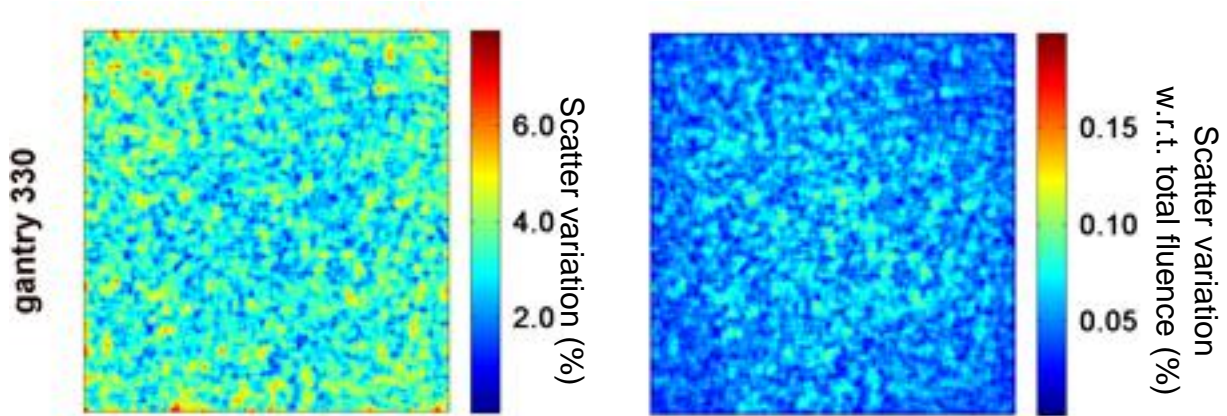


Figure 13c: Scatter variation for patient 1, scaled in percentages. The left column shows the per-pixel relative standard deviation of the scatter DPI through a series of eleven patient geometries. The right column shows the same scatter variation, but in relation to the maximum mean total DPI. Only the DPI area within 2 cm of the beam is included. Gantry angles of 30°, 80°, 130°, 180°, 230°, and 280° are shown on the previous pages.

For all patients, the scatter variation of the DPI was observed to have insignificant impact (less than 0.2%) when compared to the total intensity of the DPI, as shown in Table 5. Therefore, when simulating a DPI by combining a DRR calculation with a scatter component, it is unnecessary to estimate the scatter through each individual patient geometry. Since scatter variation is insignificant with respect to fluence variations caused by changes in the patient geometry, the scatter component of the exit fluence for a patient pose can be estimated by the MC-derived scatter component of the planning geometry exit fluence. Addition of the planning exit scatter fluence to the day-of-treatment DRR-generated primary exit fluence yields an estimate of the expected during-treatment exit fluence, which will be compared to the per-beam DPIs measured during each fraction of treatment delivery.

4.4. Significance of Findings

Since there was positive correlation between the DVH deviations and DPI deviations, there is potential to reduce patient dose reconstruction errors caused by the

backprojection assumption. For this dataset, the amount of time that elapsed between acquisition of the planning CT and day-of-treatment CT images varied from a few days to several weeks. Exit fluence deviations caused by changes in patient geometry should decrease as the time between imaging and treatment decreases. In an ideal situation, the patient would be imaged as the treatment is delivered, thereby giving complete knowledge of the geometry through which dose is delivered and the DPI is acquired. In this case, the delivered dose could be reconstructed with no errors introduced by the backprojection assumption.

Although it is currently unfeasible to image the patient during treatment, it is possible to image them immediately prior to treatment delivery. Some delivery systems have a CBCT system for pretreatment imaging. Acquiring a CBCT of the patient immediately prior to treatment delivery—and using that geometry for backprojection—would reduce the exit fluence deviations caused by assuming the backprojection geometry is the same as the planning geometry. However, exit fluence deviations, although reduced, will persist due to changes in the patient geometry between acquisition of the CBCT and delivery of the treatment immediately thereafter.

One disadvantage of imaging the patient before each fraction of delivery is the extra dose that this CT imaging causes. A daily CBCT would not be necessary for a patient geometry which does not vary significantly from fraction to fraction. In these cases, generating DPIs through previous patient geometry incidences should suffice for treatment verification. A potential application of this work in exit fluence dosimetry is to set tolerance levels for exit fluence deviations such that if deviations exceed the level, then the patient should be re-imaged immediately after treatment delivery.

Differences between expected and measured DPIs will always exist because 1) the patient geometry always deforms both inter- and intrafractionally, and 2) the beam characteristics have an inherent variation. Thresholds theoretically can be determined which will distinguish between clinically significant and insignificant deviations. Based on these tolerances, it will be possible to predict when exit fluence deviations indicate significant deviations between the planned and delivered patient doses. Thus, dose verification will be performed. However, as has been shown by my backprojection-based dose reconstruction, misattributing a source of exit fluence deviation may result in a poorer estimate of the patient dose. Therefore, it is critical to determine the source of DPI deviations to judge not only how delivery verification should be performed, but also whether the delivery was within tolerance.

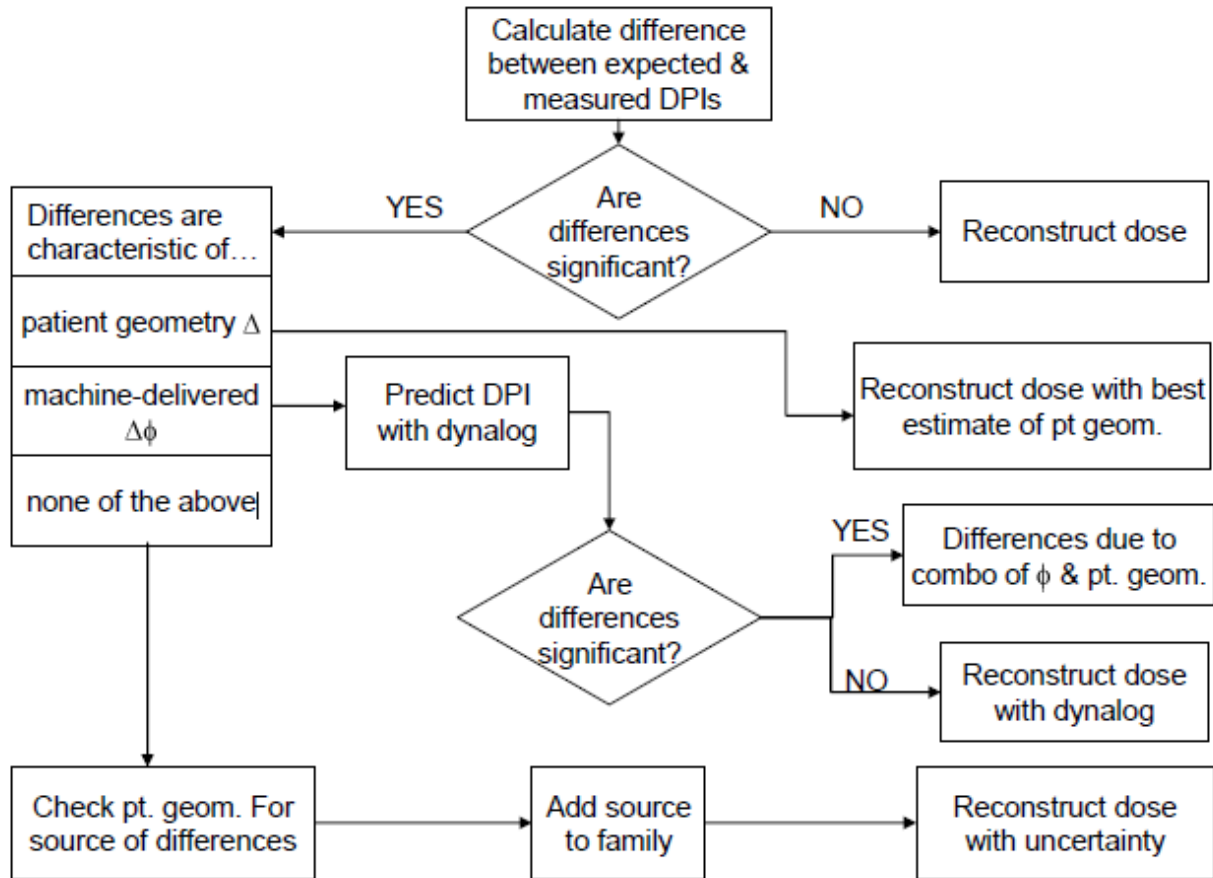


Figure 29: Decision tree showing how to process DPI deviations. If the differences are insignificant, dose reconstruction is performed to achieve delivery verification. If the differences are significant, the source of the differences is determined by comparing the deviation map with a bank of known deviations. This comparison will show whether the differences were caused by changes in the patient geometry, changes in the machine-delivered fluence, or a combination of the two.

To address this, a decision tree for how to deal with DPI deviations was developed and is shown in Figure 29. The process begins with simple comparison of the measured and expected DPIs. If significant differences do not exist, then patient dose reconstruction may be performed if the physicist desires to analyze DVHs. If significant differences do exist between the measured and expected DPIs, further action is required. The process continues with classification of the deviation according to its source by comparison with respect to a library of previously-known deviation maps and

probably sources of error. When the comparison shows that the deviations were caused by changes in the machine-delivered fluence, then the expected DPI should be re-simulated using the entrance fluence formed by the MLC leaf positions which were recorded during treatment (in files called “dynalogs”). When the deviation is attributed to patient anatomical changes, a better estimate of the patient geometry is necessary, either by re-imaging the patient or adjusting the prior image before dose evaluation. If the deviation map is dissimilar to any in the library of known deviations, the patient geometry should be examined to find the sources of the differences. Once the source is determined, it will be added to the library of known deviation maps for future matching purposes. The patient dose may then be reconstructed with a known uncertainty. If the uncertainty is significant, then dose reconstruction-based delivery verification will not be performed.

Correlation between DPI and DVH deviations must be further examined to obtain a more accurate predictor of treatment delivery failure. In this work, the only predictor examined was frequency of DPI pixel deviations greater than 5%, which resulted in an ROC curve showing accuracy of only 0.63. To increase this accuracy, combinations of other DPI deviation characteristics should be examined, such as greater or lower DPI deviation thresholds, or areas of DPI deviations. An increase in predictor accuracy is necessary for DPI-based dose verification to be effective.

This study was limited to the prostate site, where typical patient anatomy variations include bladder and rectal filling. Correlation between DPI and DVH deviations should also be examined at different sites such as H/N and lungs, where heterogeneity is more prevalent, leading to a higher variation in patient attenuation.

DPI-based verification should detect shrinkage of H/N tumors over the treatment course, as well as changes in the target size and shape in lung tumors over the treatment course.

The final step of closing the loop of IGART is development of a system which calculates the DPI deviations, evaluates whether the deviations are within tolerance, and recommends how to proceed. This system should be located in the treatment control room, where the user will be able to monitor the reported deviations and have the option of stopping treatment if necessary. The development of this tool is discussed in the following chapter.

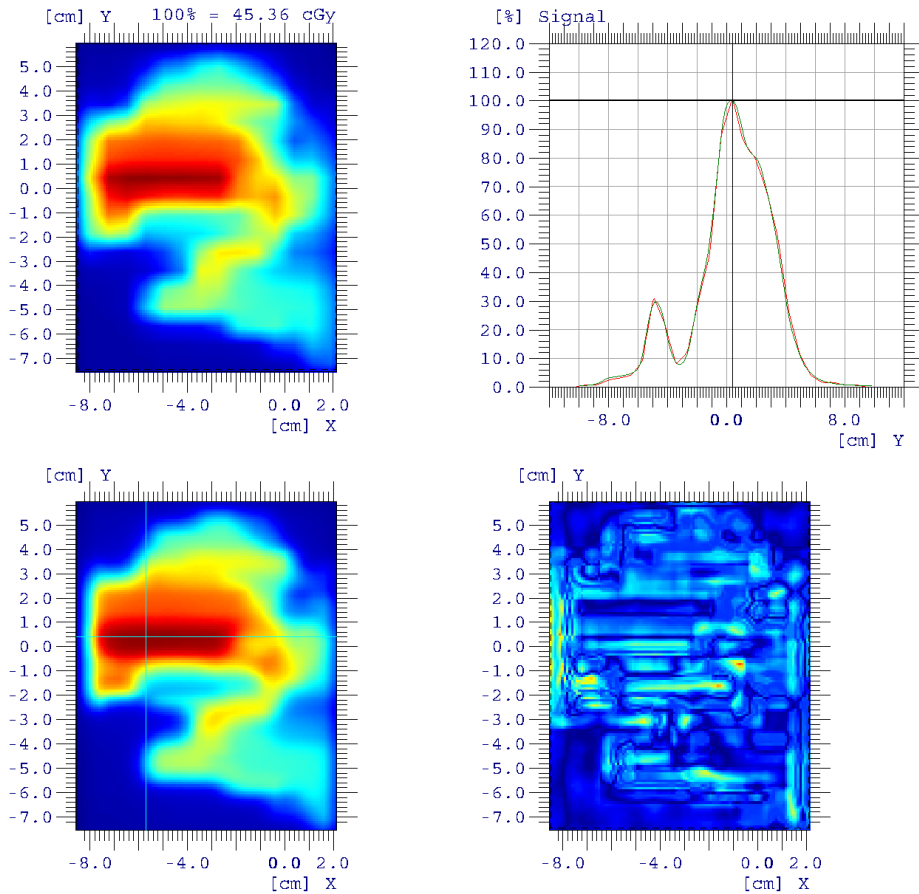
5. Dose Verification Graphical User Interface

Although there are several commercial EPID-based dose verification products, no existing product met the specific needs of this research study. For example, Varian (Palo Alto, CA) offers a 'PortalVision' tool whose image prediction algorithm is based on Van Esch's work (Van Esch, Depuydt et al. 2004). PortalVision allows for comparison of measured and simulated portal images; however, it is limited to pretreatment verification (i.e. no patient in the beam) and bases its image analysis on Low's gamma metric (Low and Dempsey 2003). Another product is available from Standard Imaging (Middleton, WI); however, it utilizes pretreatment fluence measurements to reconstruct dose on the patient's planning image. Deconvolution of the portal image yields the incident fluence, which is then used to simulate the delivered patient dose on the planning patient geometry. Verification is achieved when this 'delivered' patient dose is compared to and agrees with the planned patient dose within tolerance. In addition to commercial products available, several institutions have produced in-house verification tools for their own clinics (van Zijtveld, Dirkx et al. 2006; Mans, Wendling et al. 2010). The goal of this work is to provide our clinic with an in-house EPID-based verification tool, to be used for both pretreatment and, eventually, during-treatment delivery verification.

5.1. Current Clinical Practice

IMRT treatments were implemented at VCU in 1998. The original method used for pretreatment IMRT QA was purely radiographic film-based. Starting in 2000, an independent MC calculation was also performed. Film was replaced with the EPID in 2003, while MC simulation continued. This previous EPID-based system was qualitative in nature—the physicist would simply use a naked-eye determination of whether the field was adequately delivered. Starting in 2009, the EPID-based system was replaced with one using an I'mRT Matrixx (IBA Dosimetry America, Bartlett, TN) two-dimensional array of ionization chambers. This device has 1020 ionization chambers spaced out over an area of $24.4 \times 24.4 \text{ cm}^2$, providing a resolution of 0.8 cm. During pretreatment verification, the Matrixx is placed on the treatment couch to capture the measured beams. The measured images are then automatically imported to a verification GUI, which compares measured and expected images using the gamma metric (3%, 3 mm). Since the DTA tolerance is less than the resolution of the Matrixx, the measured images are interpolated for gamma calculations. For each field the GUI shows both the measured and expected image, a profile through the images, and the resulting gamma comparison image. A printout is obtained from the GUI containing these images along with the gamma statistics, treatment and patient information, and appropriate signature lines (see Figure 30).

VCU Medical College of Virginia
QA.opw



<p>Field (data set 1): matrix 1.1 Linac: 21EX Radiation Type: Photons Energy: 6.0 MV</p>	<p>Comment: Patient Name: Total number of pixels: 14445 Minimum Signal: 0.00 Maximum Signal: 1.62 Average Signal: 0.37 Standard Deviation: 0.23 Pixels in Ranges: 0.00 to 1.00 : 14200 (= 98.30 %) 1.00 to 1.62 : 245 (= 1.70 %) Result: Gamma, 3.0 %, 3.0 mm</p>	<p>Administrative: Date: _____ Signature: _____ Name: DZ</p>
<p>Field (data set 2): Imported Fluence 001 Linac: Trilogy Radiation Type: Photons Energy: 0.0 MV</p>		

VCU Medical College of Virginia



 IBA Dosimetry, OmniPro I'mRT
 Modified: 2010-02-18, 12:15:07

Figure 30: Sample printout from the I'mRT Matrixx verification system. The expected and measured fields are displayed on the left side, while the right side shows both a user-selected profile across both images, as well as the gamma comparison image. Treatment plan information is displayed at the bottom along with gamma results and appropriate signature lines.

Utilizing the Varian aS1000 EPID instead of the Matrixx allows for improvements in delivery verification in several areas. Physically, the EPID has a detection area that is twice as large ($40 \times 30 \text{ cm}^2$) as the Matrixx, and a resolution that is up to twenty times higher (0.04 cm). The EPID is also attached to the gantry, and may be automatically positioned and retracted from the control room, avoiding the time required to manually position the Matrixx for each verification session and allowing QA to be performed using treatment settings (e.g. gantry angle, collimator angle, etc...). The motivation for changing to an EPID-based verification system is to allow QA of larger treatment fields, detection of smaller treatment delivery errors (due to the higher resolution), and ideally implementation of a speedier process.

5.2. GUI-based Tool

Both a clinical and an expert/research version of the delivery verification tool were created using MATLAB (MathWorks, Natick, MA). For the clinical version, emphasis was placed on simplicity of the user interface and speed, qualities which would be both necessary and beneficial to improve efficiency in the clinical verification process. For the research version, more options are available to the user for preprocessing of the images as well as more comparison metrics to allow for judgment of verification.

5.2.1. Clinical Version

The interface for the clinical version of the tool is shown in Figure 31. When operating the clinical version of the verification GUI, the user first selects the directories for both the calculated expected images and the measured images. Once the directories have

been selected, all images are automatically detected in each directory. The GUI is able to import several image formats:

- DICOM (Digital Imaging and Communications in Medicine) – The record and verify system used at our clinic exports measured images in this format.
- dxf (Drawing Interchange Format) – Another format for exported measured images through our record and verify system.
- hna – The format used when acquiring images in the service mode with IAS Monitor.
- binary MC – our in-house MC system simulates EPID images which use this binary storage format.

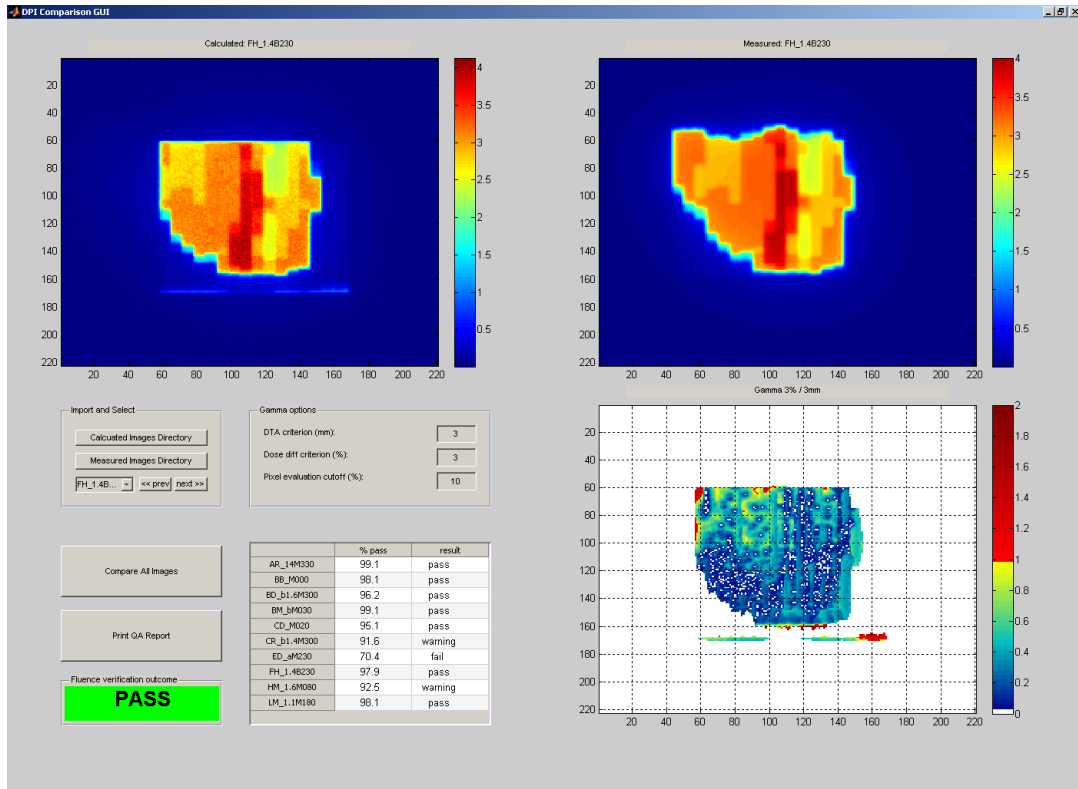


Figure 31: EPID-based delivery verification GUI designed for clinical use. The expected image is displayed in the upper left panel, while the measured image is displayed in the upper right panel. The resulting gamma comparison image is displayed in the lower right panel. Buttons in the lower left panel allow for scrolling among all of the fields for a given patient, as well as printing out the QA report. The table shows the gamma results for each field, as well as whether the field passed or failed the given criteria (in this case, a 3 mm distance-to-agreement and a 3% dose difference).

Ideally, for every measured image in the measured directory, there is a corresponding calculated image in the calculated directory. If this is not the case, the GUI reports that image(s) are missing from the appropriate location(s). The GUI then populates a list of all images that are located in both directories and imports them. The user may then scroll through and visualize each pair of images. The GUI uses header information from each image to automatically adjust for imager location and resolution.

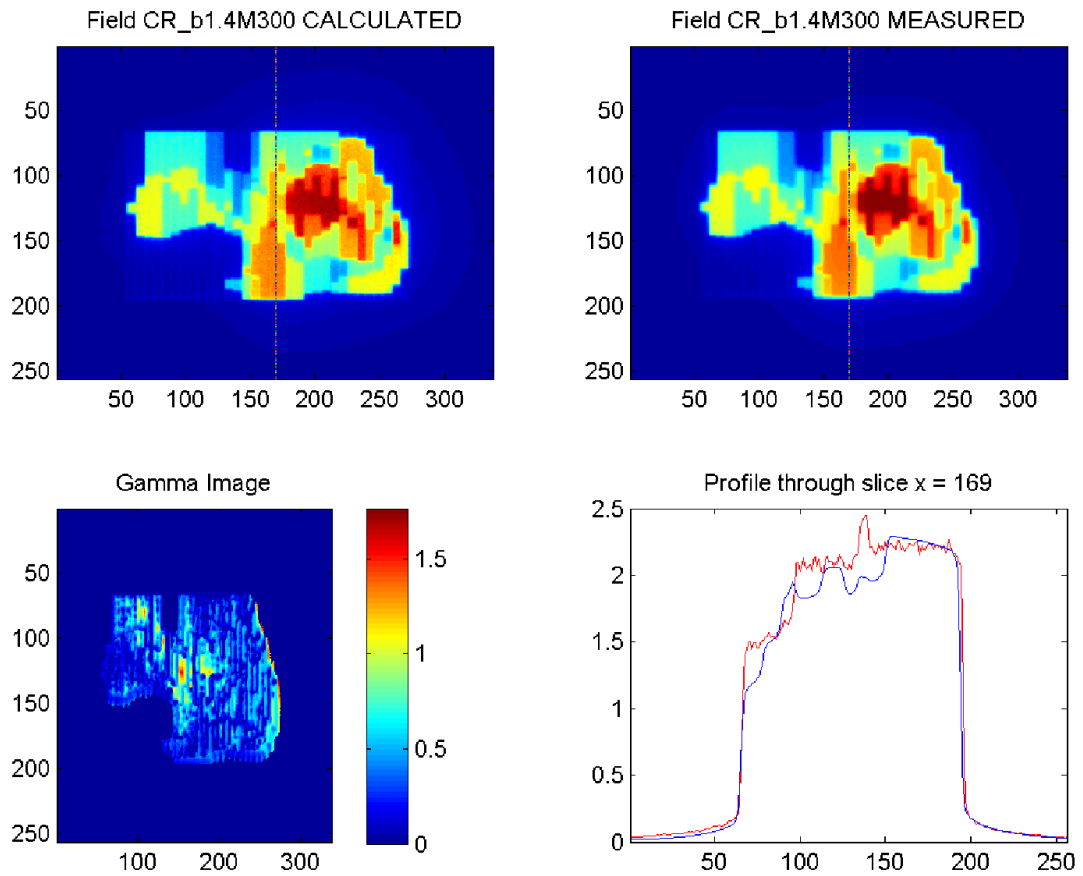
The next step of the verification process is for the user to click the “Compare All Images” button, which performs a gamma comparison between the two images. The default criteria for passing gamma at our clinic is

$$P_{\gamma_{3,3} < 1, 20\%} \geq 90$$

Where P is the percentage of pixels with gamma values less than 1 (i.e. passing gamma) for criteria of 3 mm distance-to-agreement and 3% dose difference. Gamma values are only calculated for pixels with intensity greater than 20% of maximum pixel intensity. The gamma calculation requires approximately five seconds per field. After the calculations are finished, the gamma image is displayed next to the corresponding measured and calculated images. The user may scroll through each field to visualize where any significant differences occur. The gamma results are also displayed in table form on the GUI. As the user scrolls through each field, the verification result is highlighted on the GUI as well. If 95% of the pixels pass gamma (3%, 3 mm), a large “PASS” is displayed with a green background. If the images fail the gamma criteria, a large “FAIL” is displayed with a red background. If the percentage of pixels passing gamma is between 90% and 95%, a large “WARNING” is displayed with a yellow background, and the user is advised to manually inspect the differences.

VCU Medical College of Virginia

QA.opw



Field: CR_b1.4M300
Energy: 18 MV

Gamma criteria: 3% / 3 mm
Gamma pass %: 97.8
Gamma mean, max: (0.08, 1.77)

Date: _____
Signature: _____
Name: _____

Figure 32: Sample QA printout that is auto-generated by the clinical DPI comparison GUI. The calculated and measured fields are shown, as well as the corresponding 3 mm / 3% gamma image and a profile comparison image. Field information is shown at bottom as well as a signature line for the verification.

The final step of the clinical process is to print the QA report for the treatment plan. As seen in Figure 32, the printout was designed to reflect the same information that was produced in the Matrixx QA printout: images of the fields, profiles through the fields, the gamma image, and plan information and signature lines. For each field in the plan, a soft-copy QA report is saved to disk (in html format) and a hard-copy is sent to the local printer. When the user is finished with verification for a specific patient, the verification results are automatically copied to a research database, allowing for further future analysis.

5.2.2. Research Version

Beyond the clinical mode, this tool provides an excellent framework for analysis of images. Therefore, a research version of the interface was also designed which allowed for more manipulation of images as well as various comparison metrics besides the gamma metric. The research interface is shown in Figure 33. Similar to the clinical interface, the first step is for the user to select the directories for the reference and test images. The user is then required to select the individual images for comparison from each directory, as the research version was designed for comparison of single images, not groups of images.

Prior to comparison, each image may be preprocessed in a number of ways. If image noise is a concern, a boxcar filter of user-chosen size may be applied. Output normalization may be performed between the two images. The normalization is calculated by multiplying the test image by the ratio of the sum of all pixels greater than 10% maximum intensity in the reference image divided by the same pixels in the test image.

A sub-pixel fast-Fourier-based rigid registration (Guizar-Sicairos, Thurman et al. 2008) was also coded into the GUI as an option. To test the accuracy of the registration, a reference field was randomly rotated and translated to form one hundred test images, which were then registered back to the reference image. For every test image, the registration was found to be accurate within half of a pixel and half of a degree. Since the registration algorithm did not account for scaling (i.e. differences in the zoom between the two images), an optional zoom factor correction was coded into the GUI as well. The zoom factor also incorporated the inverse-square law for adjusting the intensity of the image. The intensity adjustment assumes that differences in the zoom factor between two images are due to differences in the location of the imager in the z-plane.

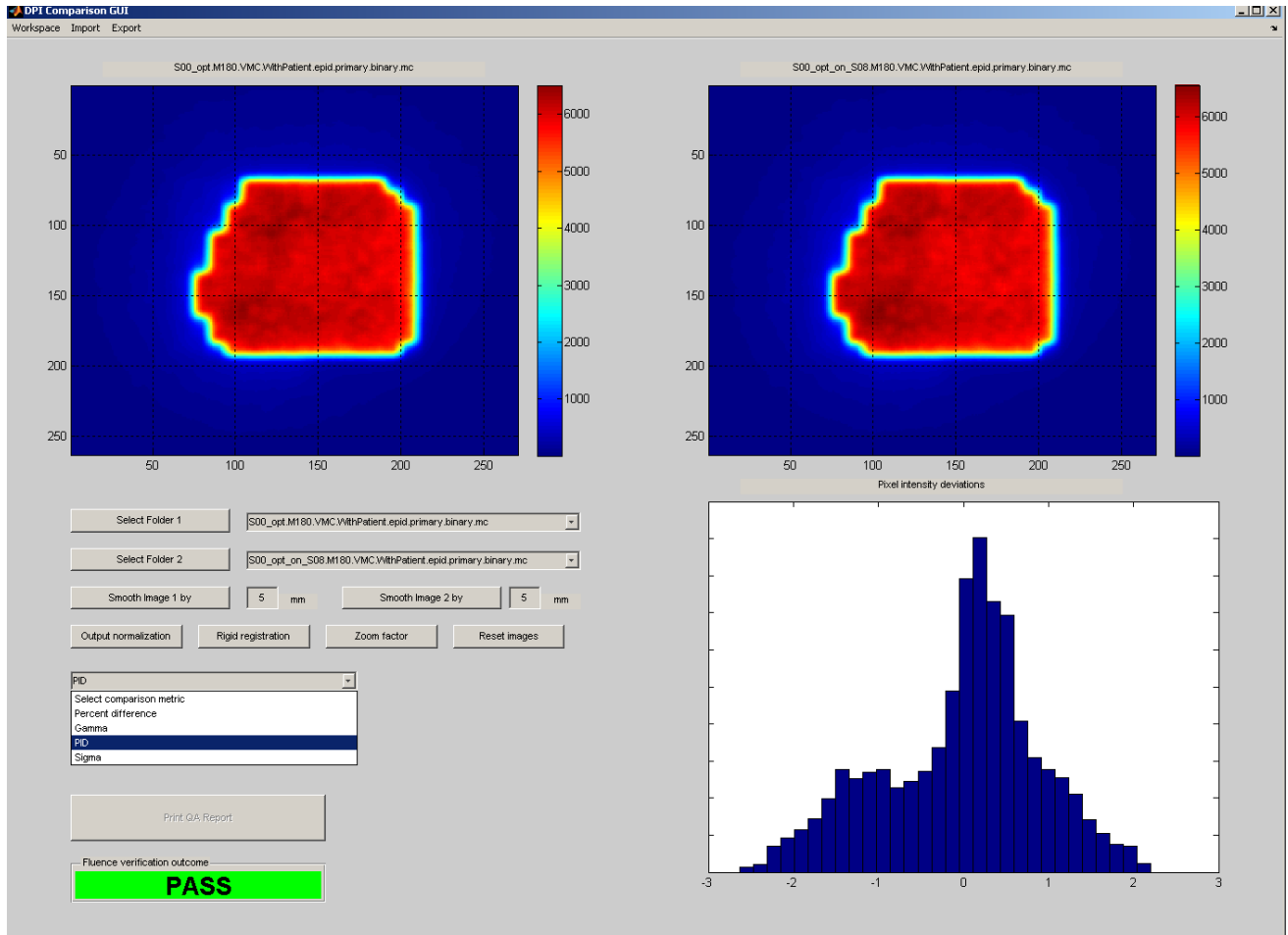


Figure 33: EPID-based delivery verification GUI for research purposes. The two imported images are displayed in the top panels, and the comparison image is displayed in the bottom right panel. Comparison metrics available are a percent difference image, a gamma image, and a pixel intensity deviation (PID) histogram. The result of the comparison is shown in the lower left corner (in this case, the test image passed the accepted tolerance).

The research version of the verification tool also provides several other comparison metrics in addition to the gamma metric, which allows for more comprehensive analysis of image deviations:

- A simple percent difference image can be calculated and displayed. The pixel-by-pixel histogram of the percent difference image, termed the pixel intensity distribution (PID), can also be displayed. The PID comparison metric was published in Medical Physics (Gordon, Gardner et al. 2012).

- If the user desires to analyze a series of images, and not just one single image against another, there is capability to calculate a series sigma image. In this calculation, the GUI finds all images located in the selected directory, and, for each pixel of the images, calculates the standard deviation of the pixel intensity over all of the images. This analysis is useful to reveal problematic areas of delivery in a field, whether caused by machine-related sources of deviation (e.g. jaw location uncertainty) or patient-related sources of uncertainty (e.g. presence of air pockets in the rectum).
- If two MC images are being compared, and the corresponding uncertainty images exist, then a “Kawrakow-Fippel” (KF) comparison may be performed (Kawrakow and Fippel 2000). This analysis reveals areas that differ significantly between the two images with respect to their corresponding pixel uncertainties. The user may display the KF image or the histogram of KF pixel values.

All analysis results can be saved to disk as image files or pdf files.

5.3. Future Improvements

Implementation of the verification tool into our clinic will start with several test QA cases, where past patient treatment information will be used both to calculate and measure portal images for several patients. The appropriate staff will then be trained in how to use the GUI to import these images and then perform verification.

The next step in automation of the verification process is to implement automatic generation of calculated images into the treatment planning process, as well as automatic placement of the calculated and measured images. The tool will be further

developed so that it will regularly automatically search for new calculated and measured images in the appropriate directories. When matching images are detected, it will perform the comparison automatically in the background. This process allows for a more efficient final manual review for each patient QA. The user can view several patient comparison results consecutively, instead of waiting for the comparison calculations to be performed between viewing of each set of patient fields.

During-treatment QA in the verification process is also desired. The goal of during-treatment verification is to avoid gross errors in treatment delivery. Instead of waiting to perform verification until after the treatment fraction is complete, during-treatment cine images will automatically be imported into the GUI, and compared to the predicted images, all while the patient is being treated. These comparisons will inherently incorporate errors due to assumptions made about the unknown patient geometry, however, gross deviations (e.g. wrong field, jaw settings, MU, etc...) between the measured and calculated images will still be detectable, and the delivery may be stopped mid-treatment.

6. Conclusion

The EPID is a useful tool for treatment QA due to its dosimetric stability and convenient positioning on the linac gantry arm. The aim of this work was to improve upon EPID-based dose verification for ART.

Software was developed which improved our institution's ability to simulate expected DPs. The ability to separate the primary and scatter portions of DPs was implemented. Also, exit fluences can now be outputted as well as DPs. A basic backprojection component was added to our MC system, allowing for backprojection-based dose reconstruction in instances where it is deemed appropriate.

The basic assumption of backprojection-based dose reconstruction, that variation in exit fluence is caused by machine-related variability, was tested and found to be erroneous. Interfractional changes in the patient anatomy caused significantly larger deviations in exit fluence than the inherent variation in the machine-delivered fluence. Exit fluence deviations must not simply be attributed to entrance fluence deviations, allowing for a potentially faulty patient dose reconstruction for delivery verification. Without knowledge of the during-treatment patient anatomy, dose reconstruction could potentially result in a worse estimate of the delivered dose than the planned dose itself. Therefore caution is recommended whenever dose reconstruction is desired.

Correlation between DPI deviations and DVH deviations was observed, and false positives and negatives were examined. Although positive correlation was found, further work must be performed to achieve a higher accuracy in using DPI deviations as a predictor for DVH deviations. A decision tree was proposed detailing when DPI-based delivery verification must be sufficient, and when dose reconstruction-based delivery verification is permissible. Potential DPI deviation tolerances were examined which predict when there are significant differences between the planned and delivered dose. Also, failure to meet tolerance could dictate that the patient anatomy should be re-imaged.

A semi-automated dose verification tool was developed for implementation at this institution, both for clinical and research purposes. The clinical tool allows for comparison of pretreatment or during treatment DPIs, and provides a measurement of treatment delivery success. The research tool includes several other means of comparison of two or more DPIs, and allows the user to manipulate the images throughout the comparison. Currently, the tool will determine if any egregious delivery errors have occurred, and report to the user whether the delivery passed within tolerance. The framework for implementation of an EPID-based dose verification system at this institution was completed, which will result in both a more efficient and more accurate verification process than the current system.

7. References

- Bailey, D. W., L. Kumaraswamy, M. Bakhtiari, H. K. Malhotra and M. B. Podgorsak (2012). "EPID dosimetry for pretreatment quality assurance with two commercial systems." J Appl Clin Med Phys **13**(4): 3736.
- Berger, M. J., Hubbell, J. H., Seltzer, S. M., Chang, J., Coursey, J. S., Sukumar, R., and Zucker, D. S. (1998). "XCOM: Photon cross sections database." NIST Standard Reference Database **8**: 87-3597.
- Cheung, J., J. F. Aubry, S. S. Yom, A. R. Gottschalk, J. C. Celi and J. Pouliot (2009). "Dose recalculation and the Dose-Guided Radiation Therapy (DGRT) process using megavoltage cone-beam CT." Int J Radiat Oncol Biol Phys **74**(2): 583-592.
- Ezzell, G. A., J. W. Burmeister, N. Dogan, T. J. LoSasso, J. G. Mechalakos, D. Mihailidis, A. Molineu, J. R. Palta, C. R. Ramsey, B. J. Salter, J. Shi, P. Xia, N. J. Yue and Y. Xiao (2009). "IMRT commissioning: multiple institution planning and dosimetry comparisons, a report from AAPM Task Group 119." Med Phys **36**(11): 5359-5373.
- Fix, M. K., M. Stampanoni, P. Manser, E. J. Born, R. Mini and P. Ruegsegger (2001). "A multiple source model for 6 MV photon beam dose calculations using Monte Carlo." Phys Med Biol **46**(5): 1407-1427.
- Gardner, J., J. Siebers and I. Kawrakow (2007). "Dose calculation validation of Vmc++ for photon beams." Med Phys **34**(5): 1809-1818.
- Gardner, J. K., L. Clews, J. J. Gordon, S. Wang, P. B. Greer and J. V. Siebers (2009). "Comparison of sources of exit fluence variation for IMRT." Phys Med Biol **54**(19): N451-458.
- Gardner, J. K., J. V. Siebers and I. Kawrakow (2007). "Comparison of two methods to compute the absorbed dose to water for photon beams." Phys Med Biol **52**(19): N439-447.
- Gordon, J. J., J. K. Gardner, S. Wang and J. V. Siebers (2012). "Reliable detection of fluence anomalies in EPID-based IMRT pretreatment quality assurance using pixel intensity deviations." Med Phys **39**(8): 4959-4975.

- Greer, P. B. and C. C. Popescu (2003). "Dosimetric properties of an amorphous silicon electronic portal imaging device for verification of dynamic intensity modulated radiation therapy." Med Phys **30**(7): 1618-1627.
- Guizar-Sicairos, M., S. T. Thurman and J. R. Fienup (2008). "Efficient subpixel image registration algorithms." Opt Lett **33**(2): 156-158.
- Kawrakow, I. (2001). VMC++, electron and photon Monte Carlo calculations optimized for Radiation Treatment Planning. Advanced Monte Carlo for Radiation Physics, Particle Transport Simulation and Applications: Proceedings of the Monte Carlo 2000 Meeting, Lisbon, Springer, Berlin.
- Kawrakow, I. and M. Fippel (2000). "Investigation of variance reduction techniques for Monte Carlo photon dose calculation using XVMC." Phys Med Biol **45**(8): 2163-2183.
- Kroonwijk, M., K. L. Pasma, S. Quint, P. C. Koper, A. G. Visser and B. J. Heijmen (1998). "In vivo dosimetry for prostate cancer patients using an electronic portal imaging device (EPID); demonstration of internal organ motion." Radiother Oncol **49**(2): 125-132.
- Letourneau, D., R. Wong, D. Moseley, M. B. Sharpe, S. Ansell, M. Gospodarowicz and D. A. Jaffray (2007). "Online planning and delivery technique for radiotherapy of spinal metastases using cone-beam CT: image quality and system performance." Int J Radiat Oncol Biol Phys **67**(4): 1229-1237.
- Louwe, R. J., E. M. Damen, M. van Herk, A. W. Minken, O. Torzsok and B. J. Mijnheer (2003). "Three-dimensional dose reconstruction of breast cancer treatment using portal imaging." Med Phys **30**(9): 2376-2389.
- Louwe, R. J., M. Wendling, M. B. van Herk and B. J. Mijnheer (2007). "Three-dimensional heart dose reconstruction to estimate normal tissue complication probability after breast irradiation using portal dosimetry." Med Phys **34**(4): 1354-1363.
- Low, D. A. and J. F. Dempsey (2003). "Evaluation of the gamma dose distribution comparison method." Med Phys **30**(9): 2455-2464.
- Mans, A., M. Wendling, L. N. McDermott, J. J. Sonke, R. Tielenburg, R. Vijlbrief, B. Mijnheer, M. van Herk and J. C. Stroom (2010). "Catching errors with in vivo EPID dosimetry." Med Phys **37**(6): 2638-2644.
- McCurdy, B. M., K. Luchka and S. Pistorius (2001). "Dosimetric investigation and portal dose image prediction using an amorphous silicon electronic portal imaging device." Med Phys **28**(6): 911-924.
- McCurdy, B. M. and S. Pistorius (2000). "A two-step algorithm for predicting portal dose images in arbitrary detectors." Med Phys **27**(9): 2109-2116.

- McDermott, L. N., R. J. Louwe, J. J. Sonke, M. B. van Herk and B. J. Mijnheer (2004). "Dose-response and ghosting effects of an amorphous silicon electronic portal imaging device." Med Phys **31**(2): 285-295.
- McDermott, L. N., M. Wendling, J. Nijkamp, A. Mans, J. J. Sonke, B. J. Mijnheer and M. van Herk (2008). "3D in vivo dose verification of entire hypo-fractionated IMRT treatments using an EPID and cone-beam CT." Radiother Oncol **86**(1): 35-42.
- Mohan, R., C. Chui and L. Lidofsky (1985). "Energy and angular distributions of photons from medical linear accelerators." Med Phys **12**(5): 592-597.
- Murphy, M. J. and D. A. Todor (2005). "Demonstration of a forward iterative method to reconstruct brachytherapy seed configurations from x-ray projections." Phys Med Biol **50**(11): 2715-2737.
- Mutanga, T. F., H. C. de Boer, V. Rajan, M. L. Dirx, M. J. van Os, L. Incrocci and B. J. Heijmen (2012). "Software-controlled, highly automated intrafraction prostate motion correction with intrafraction stereographic targeting: System description and clinical results." Med Phys **39**(3): 1314-1321.
- Nelms, B. E., H. Zhen and W. A. Tome (2011). "Per-beam, planar IMRT QA passing rates do not predict clinically relevant patient dose errors." Med Phys **38**(2): 1037-1044.
- Nijsten, S. M., W. J. van Elmpt, M. Jacobs, B. J. Mijnheer, A. L. Dekker, P. Lambin and A. W. Minken (2007). "A global calibration model for a-Si EPIDs used for transit dosimetry." Med Phys **34**(10): 3872-3884.
- Pacilio, M., D. Aragno, R. Rauco, S. D'Onofrio, M. C. Pressello, L. Bianciardi and E. Santini (2007). "Monte Carlo dose calculations using MCNP4C and EGSnrc/BEAMnrc codes to study the energy dependence of the radiochromic film response to beta-emitting sources." Phys Med Biol **52**(13): 3931-3948.
- Parent, L., J. Seco, P. M. Evans, A. Fielding and D. R. Dance (2006). "Monte Carlo modelling of a-Si EPID response: the effect of spectral variations with field size and position." Med Phys **33**(12): 4527-4540.
- Pasma, K. L., B. J. Heijmen, M. Kroonwijk and A. G. Visser (1998). "Portal dose image (PDI) prediction for dosimetric treatment verification in radiotherapy. I. An algorithm for open beams." Med Phys **25**(6): 830-840.
- Siddon, R. L. (1985). "Fast calculation of the exact radiological path for a three-dimensional CT array." Med Phys **12**(2): 252-255.
- Siebers, J. V., P. J. Keall, J. O. Kim and R. Mohan (2002). "A method for photon beam Monte Carlo multileaf collimator particle transport." Phys Med Biol **47**(17): 3225-3249.

- Siebers, J. V., J. O. Kim, L. Ko, P. J. Keall and R. Mohan (2004). "Monte Carlo computation of dosimetric amorphous silicon electronic portal images." Med Phys **31**(7): 2135-2146.
- Smitsmans, M. H., F. J. Pos, J. de Bois, W. D. Heemsbergen, J. J. Sonke, J. V. Lebesque and M. van Herk (2008). "The influence of a dietary protocol on cone beam CT-guided radiotherapy for prostate cancer patients." Int J Radiat Oncol Biol Phys **71**(4): 1279-1286.
- Steciw, S., B. Warkentin, S. Rathee and B. G. Fallone (2005). "Three-dimensional IMRT verification with a flat-panel EPID." Med Phys **32**(2): 600-612.
- Talamonti, C., M. Casati and M. Bucciolini (2006). "Pretreatment verification of IMRT absolute dose distributions using a commercial a-Si EPID." Med Phys **33**(11): 4367-4378.
- van Elmpt, W., S. Nijsten, B. Mijnheer, A. Dekker and P. Lambin (2008). "The next step in patient-specific QA: 3D dose verification of conformal and intensity-modulated RT based on EPID dosimetry and Monte Carlo dose calculations." Radiother Oncol **86**(1): 86-92.
- van Elmpt, W. J., S. M. Nijsten, R. F. Schiffeleers, A. L. Dekker, B. J. Mijnheer, P. Lambin and A. W. Minken (2006). "A Monte Carlo based three-dimensional dose reconstruction method derived from portal dose images." Med Phys **33**(7): 2426-2434.
- Van Esch, A., T. Depuydt and D. P. Huyskens (2004). "The use of an aSi-based EPID for routine absolute dosimetric pre-treatment verification of dynamic IMRT fields." Radiother Oncol **71**(2): 223-234.
- Van Esch, A., B. Vanstraelen, J. Verstraete, G. Kutcher and D. Huyskens (2001). "Pre-treatment dosimetric verification by means of a liquid-filled electronic portal imaging device during dynamic delivery of intensity modulated treatment fields." Radiother Oncol **60**(2): 181-190.
- van Zijtveld, M., M. L. Dirkx, H. C. de Boer and B. J. Heijmen (2006). "Dosimetric pre-treatment verification of IMRT using an EPID; clinical experience." Radiother Oncol **81**(2): 168-175.
- van Zijtveld, M., M. L. Dirkx, H. C. de Boer and B. J. Heijmen (2007). "3D dose reconstruction for clinical evaluation of IMRT pretreatment verification with an EPID." Radiother Oncol **82**(2): 201-207.
- Walters, B. R., I. Kawrakow and D. W. Rogers (2005). DOSXYZnrc users manual, NRC. **Report PIRS-794 (rev B)**.

- Wang, S., J. K. Gardner, J. J. Gordon, W. Li, L. Clews, P. B. Greer and J. V. Siebers (2009). "Monte Carlo-based adaptive EPID dose kernel accounting for different field size responses of imagers." Med Phys **36**(8): 3582-3595.
- Wendling, M., R. J. Louwe, L. N. McDermott, J. J. Sonke, M. van Herk and B. J. Mijnheer (2006). "Accurate two-dimensional IMRT verification using a back-projection EPID dosimetry method." Med Phys **33**(2): 259-273.
- Wendling, M., L. N. McDermott, A. Mans, J. J. Sonke, M. van Herk and B. J. Mijnheer (2009). "A simple backprojection algorithm for 3D in vivo EPID dosimetry of IMRT treatments." Med Phys **36**(7): 3310-3321.
- Yan, D., F. Vicini, J. Wong and A. Martinez (1997). "Adaptive radiation therapy." Phys Med Biol **42**(1): 123-132.
- Yan, G., C. Liu, T. A. Simon, L. C. Peng, C. Fox and J. G. Li (2009). "On the sensitivity of patient-specific IMRT QA to MLC positioning errors." J Appl Clin Med Phys **10**(1): 2915.

8. Appendix I

NOTE

Comparison of sources of exit fluence variation for IMRT

Joseph K Gardner^{1,5}, Luke Clews^{2,3}, J James Gordon¹, Song Wang¹, Peter B Greer^{2,4} and Jeffrey V Siebers¹

¹ Department of Radiation Oncology, Virginia Commonwealth University Medical Center, Richmond, VA, USA

² Radiation Oncology Department, Calvary Mater Newcastle Hospital, Newcastle, New South Wales, Australia

³ Royal Melbourne Institute of Technology, Melbourne, Victoria, Australia

⁴ University of Newcastle, Newcastle, New South Wales, Australia

E-mail: gardnerjk@vcu.edu

Received 13 January 2009, in final form 3 August 2009

Published 4 September 2009

Online at stacks.iop.org/PMB/54/N451

Abstract

The fluence exiting a patient during beam delivery can be used as treatment delivery quality assurance, either by direct comparison with expected exit fluences or by backprojection to reconstruct the patient dose. Multiple possible sources of measured exit fluence deviations exist, including changes in the beam delivery and changes in the patient anatomy. The purpose of this work is to compare the deviations caused by these sources. Machine delivery-related variability is measured by acquiring multiple dosimetric portal images (DPIs) of several test fields without a patient/phantom in the field over a time period of 2 months. Patient anatomy-related sources of fluence variability are simulated by computing transmission DPIs for a prostate patient using the same incident fluence for 11 different computed tomography (CT) images of the patient anatomy. The standard deviation (SD) and maximum deviation of the exit fluence, averaged over 5 mm × 5 mm square areas, is calculated for each test set. Machine delivery fluence SDs as large as 1% are observed for a sample patient field and as large as 2.5% for a picket-fence dMLC test field. Simulations indicate that day-to-day patient anatomy variations induce exit fluence SDs as large as 3.5%. The largest observed machine delivery deviations are 4% for the sample patient field and 7% for the picket-fence field, while the largest difference for the patient anatomy-related source is 8.5%. Since daily changes in patient anatomy can result in substantial exit fluence deviations, care should be taken when applying fluence back-projection to ensure that such deviations are properly attributed to their source.

(Some figures in this article are in colour only in the electronic version)

⁵ Author to whom any correspondence should be addressed.

1. Introduction

The use of intensity-modulated radiation therapy (IMRT) and image-guided radiation therapy (IGRT) in radiotherapy results in the delivery of complex fluence distributions to the patient, which necessitates two- or three-dimensional quality assurance. The electronic portal imaging device (EPID) has been shown to be an accurate and reproducible dosimeter for measuring the machine-delivered 2D fluence via comparisons with the expected/planned fluence (Greer and Popescu 2003, Van Esch *et al* 2004). It has been used extensively without the patient in the beam for pre-treatment verification purposes (Siebers *et al* 2004, Van Esch *et al* 2004, Steciw *et al* 2005, Talamonti *et al* 2006, van Elmpt *et al* 2006, 2008, van Zijtveld *et al* 2006, 2007, Nicolini *et al* 2008). With the patient in the beam, it has been used for during treatment verification via comparison of exit fluences (Kroonwijk *et al* 1998, Pasma *et al* 1998, McCurdy and Pistorius 2000, McCurdy *et al* 2001, van Elmpt *et al* 2005), comparison of back-projected entrance fluences (Vieira *et al* 2004) and back-projection-based dose reconstruction (Partridge *et al* 2002, Louwe *et al* 2003, Jarry and Verhaegen 2007, McDermott *et al* 2008). The EPID has also been used during treatment with edge-detecting algorithms to detect leaf-positioning deviations from desired or logged positions. (Sonke *et al* 2004, Mohammadi and Bezak 2007, Lee *et al* 2008b).

When used as an exit fluence dosimeter, there are several potential sources for measured exit fluence deviations, including changes in the entrance fluence, changes in detector response and changes in the patient position, orientation or geometry which result in differential attenuation of the incident fluence. The relative magnitudes of these potential exit fluence deviation sources have not been documented. Knowledge of the relative contributions is important since the blind application of fluence back-projection, in which all measured output fluence deviations are attributed to changes in the incident fluence, could mistakenly attribute deviations to an incorrect source and result in erroneous patient dose reconstructions. The purpose of this work is to test the basic assumption of back-projection-based dose reconstruction, that all exit fluence deviations are due to entrance fluence deviations, by quantifying the exit fluence variability caused both by entrance fluence variation and patient geometry variation.

2. Materials and methods

This study consists of two facets (1) measuring delivery device output fluence variability and (2) simulating the effect of patient-induced exit fluence variability. In measurements of the delivery output fluence deviations, no patient or phantom geometry is placed in the beam, so that observed differences cannot be attributed to changes in the patient anatomy. To assess patient anatomy-related sources of exit fluence deviations, simulated dosimetric portal images (DPIs) with identical incident fluences are used so that observed differences cannot be attributed to delivery fluence variations.

The delivery system used in the test is a Varian 2300 CD accelerator equipped with a Varian 120-leaf Millennium multileaf collimator (MLC) and an amorphous silicon Varian aS1000 EPID. This EPID has an active detection area of $30 \times 40 \text{ cm}^2$ divided into 1024×768 pixels of $0.4 \times 0.4 \text{ mm}^2$. The EPID positioning support arm was the E-arm type.

2.1. Machine-related sources of fluence variability

Measurements for machine-related sources of fluence variability are taken over two time scales: (1) immediate successive imaging to separate out short-term instrumentation variations and

(2) daily imaging (60 measurements over ~2 months) to measure variations over a time period longer than a typical treatment course time scale.

For all measurements, the EPID is extended to a source-to-detector distance (SDD) of 105 cm, since this is the distance at which pretreatment IMRT QA is performed at our institution. Each image is calibrated using the standard flood field and dark field calibration:

$$I_{x,y} = \frac{I_{x,y}^{raw} - DF_{x,y}}{FF_{x,y} - DF_{x,y}} \times FF_{mean}$$

where, for each pixel, $I_{x,y}$ is the normalized intensity, $I_{x,y}^{raw}$ is the uncorrected intensity, $DF_{x,y}$ is the dark field intensity and $FF_{x,y}$ is the flood field intensity. The $DF_{x,y}$ and $FF_{x,y}$ measurements are taken immediately prior to the acquisition of all DPIs. Although calibration fields are not usually acquired previous to each treatment fraction in the clinic, acquiring them in this method allowed for explicit analysis of changes in each tested input variable. Each DPI is acquired using 100 MU at a dose rate of 300 MU min⁻¹. At our institution, 1 MU corresponds to a dose of 1 cGy at the depth of maximum dose for a 10 × 10 cm² field size and 100 cm source-to-surface distance.

Daily QA measurements performed on the treatment machine verify that the accelerator output varies by <2%. Daily DPIs are acquired over 2 months for a flood field (28 × 38 cm²), both with and without the DF/FF calibration. Variations in measurements made without the calibration are the combination of accelerator output variation and detector response variation, and are quantified using the FF images, which only had the DF correction applied. Measurement variations with daily FF detector calibration are smaller than those made without calibration, since accelerator output variation is almost completely removed. Images are acquired at beam accelerating potentials of 6 MV and 18 MV. The center portion of each DPI is averaged to yield a metric for accelerator output. The effect of the size and shape of the averaged area is varied to determine if the calculated average is dependent on either of these factors.

The effects of jaw and EPID positioning variations on fluence deviations are examined. Jaw positioning variations result in fluence deviations near the field edges, and EPID positioning variations result in deviations in high gradient areas (as well as possible minor output variations due to changes in SDD). For each study, 100 consecutive DPIs of a 10 × 10 cm² field are acquired. For the jaws study, between each image acquisition the jaws are automatically moved to a 20 × 20 cm² field setting and then returned to their original location. Over 1 min of dead time elapsed between acquisitions so that detector ghosting would not have a significant effect. Jaw position variation is calculated by measuring the variation in the location of the 50% of maximum intensity line on each field edge. For the EPID positioning study, between each image acquisition the EPID was automatically retracted to the accelerator base (home position) and then repositioned to its original SDD. The variation in the EPID position is observed by calculating the variation in the field edge locations. For both studies, the standard deviation of pixel intensity is calculated for all pixels within ±2 mm of the field edge.

For IMRT delivery, inter-treatment variations in the MLC leaf positions and velocities potentially result in deviations in the composite fluence delivered to the patient. MLC leaf positioning tolerances reduce the potential fluence delivery deviations, and for the tested dynamic MLC fields, tolerance is set to 0.2 mm. DPIs are acquired for two modulated test fields: (1) a picket-fence field, which formed 1 mm wide regions of high intensity every 3 cm, and (2) a complex prostate patient dynamic MLC (dMLC) IMRT field that previously agreed poorly with clinical portal dosimetry prediction algorithms. The picket-fence field presents a challenging scenario with large dose gradients. The patient field presents a reasonably difficult

clinical field, which would incorporate all standard machine-related fluence variability sources into one field. Over the span of 2 months, 58 DPIs of the picket-fence field and 60 DPIs of the patient field are acquired. For each set of images, the per-pixel relative standard deviation (SD) image intensity is computed, as well as the largest difference between any two measured DPIs. Prior to analysis, each pixel is averaged with respect to the surrounding $5 \times 5 \text{ mm}^2$ area to remove deviations caused by dead pixels. The SD is calculated as a relative SD with respect to maximum intensity in the entire image. The SD calculations are performed after rigidly aligning each image, as well as scaling for different accelerator output intensities. Image alignment allowed for separation of fluence deviations caused by set-up errors from those caused by systematic MLC leaf positioning errors.

2.2. Patient anatomy-related sources of fluence variability

To examine potential effects of changes in patient anatomy on the exit fluence, a dataset consisting of 12 CTs acquired over the treatment course of a single prostate patient from the Netherlands Cancer Institute is utilized. The CTs are rigidly registered using bony anatomy in the Syntegra module of the Pinnacle³ treatment planning system. A hypothetical 14-beam (seven split beams) dMLC treatment plan is generated using 18 MV photons. For each beam, the exit fluence is simulated through each patient geometry. The Monte Carlo-based DPI prediction simulation is performed using a source model (Fix *et al* 2004), an in-house algorithm to transport the particles through the MLC (Siebers *et al* 2002), a modified version of VMC++ (Kawrakow 2001) to calculate patient dose and produce the exit fluence and an in-house convolution algorithm to simulate the DPI (Li *et al* 2006). For each patient geometry, each beam sampled identical particles from the source model, so that differences in the DPIs could be attributable to patient anatomy changes and not to entrance fluence deviations—the incident fluence is identical. Sufficient source particles are sampled to yield a nominal statistical precision of 1% to the dose maximum for each DPI. Differences and per-pixel SDs are computed in similar fashion as the previous section between the simulated DPIs generated through each of the patient CTs for each beam.

3. Results

3.1. Machine-related sources of fluence variability

The SD of the central axis value of the flood field is 1.9% for both accelerating potentials, quantifying the variation in the machine output/detector system. The SD of the DF/FF-calibrated flood field is 0.3%, indicating that daily calibration effectively removes output variations. No dependence is found on the size or shape of the averaged central area from 1 cm^2 to 100 cm^2 .

The measured uncertainty in jaw positioning is less than 0.2 mm (1 SD) in each direction, which is less than half the size of an aS1000 pixel. The average SD of the pixels around the field edge is 1.4%, with a maximum SD of 2.3%. The uncertainty due to EPID repositioning is less than half the size of a pixel. The average SD of the pixels around the field edge is 0.8%, with a maximum SD of 1.3%.

DPIs of the two test fields, their corresponding pixel SDs and the largest difference between two DPIs are shown in figure 1. The largest calculated pixel SDs for the picket-fence fields are 2.1% (6 MV) and 2.3% (18 MV), while those for the patient IMRT fields are 1.0% (6 MV) and 1.1% (18 MV). The largest percent difference of any pixel between any two picket-fence fields is 9.8% (6 MV) and 8.4% (18 MV), while that between any two patient

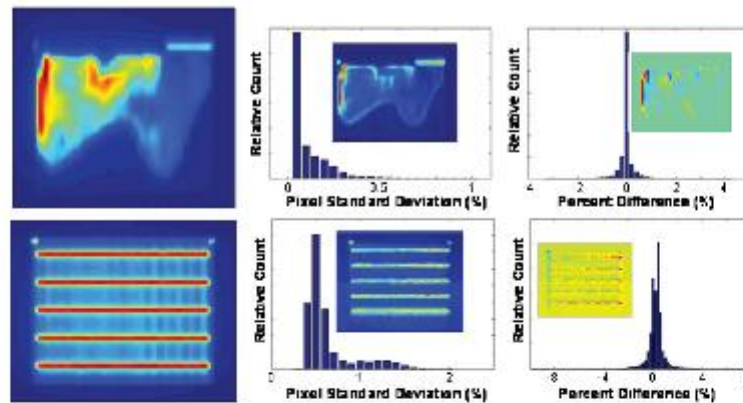


Figure 1. Patient dMLC IMRT field and picket-fence MLC test pattern shown in the left column. Pixel standard deviation maps calculated over ~60 images over the span of 2 months shown in the middle column. The worst difference between any two images is shown in the right column.

fields is 4.2% (6 MV) and 3.5% (18 MV). After image alignment and normalization, the largest pixel SDs for the picket-fence fields are 1.6% (6 MV) and 1.8% (18 MV), while those for the patient IMRT fields are 0.8% (6 MV) and 0.9% (18 MV).

3.2. Patient anatomy-related sources of fluence variability

A DPI of one of the patient fields, the corresponding pixel SDs and the largest difference between two DPIs simulated through different patient geometries are shown in figure 2. For each field, the largest pixel SDs and exit fluence deviations are shown in figure 3. Per-pixel percent differences greater than 3% existed in 78 of 154 simulated DPIs and greater than 5% existed in 16 fields. The largest calculated pixel SD is 2.5%, and the largest pixel percent difference between any two fields is 8.6%. Visual inspection of the patient CT data shows that the primary source of exit fluence deviations is changes in the patient geometry, which result in different pathlengths through the patient, especially due to the presence of the gas in the rectum.

4. Discussion

Exit fluence deviations caused by patient anatomy-related sources are found to be slightly larger than those caused by delivery-related sources, within the limits of this study. The magnitude of exit fluence deviations caused by machine-related sources (up to 4%) and patient-related sources (up to 9%) seemingly agree with the deviations in patient dose (up to 3% and 10%, respectively) reported in the literature (Lee *et al* 2008a). However, the present work does not address patient dose, so the agreement is not completely justified. During real treatment delivery, there is no a priori knowledge of whether exit fluence deviations are due to changes in machine output or due to changes in patient geometry. Tests with our delivery system indicate that per-delivery fluence variations are within the acceptable tolerances expected for

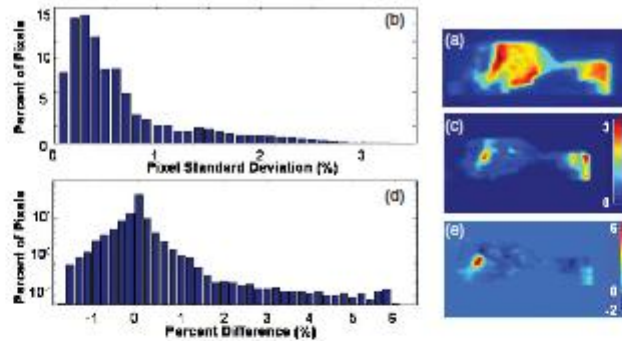


Figure 2. Data for through-patient exit fluence variability. Sample field exit fluence intensity map shown in (a). Histogram of pixel standard deviations (SDs) for the sample field shown in (b), with the corresponding SD map shown in (c). The area of large SDs on the left side of the image is due to the presence of rectal gas in some patient geometries, while the area of large SDs on the right side of the image is due to changes in the patient geometry, which resulted in different pathlengths through the patient. Histogram of exit fluence deviations observed between two sample DPIs generated through two different instances of the patient geometry shown in (d), with the corresponding map of differences shown in (e).

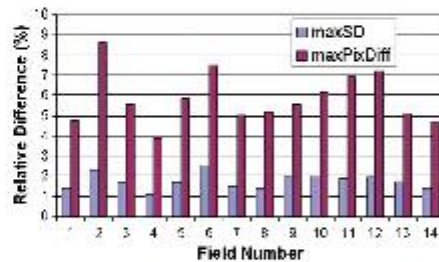


Figure 3. Maximum pixel difference and maximum pixel standard deviation for each field calculated over 12 patient geometry instances.

patient treatment. For our system, blind application of back-projection to determine incident fluence is not justified. Doing so would likely attribute patient geometry-related sources of exit fluence deviations to incident fluence deviations—the wrong source. Dose recalculation based on this false incident fluence could potentially result in a poorer prediction of the patient dose than making no correction at all.

The use of pre-treatment imaging, such as offered by cone-beam CT, (CBCT) should reduce the magnitude of exit fluence deviations since there would be less opportunity for the patient geometry to change between imaging and treatment delivery. However, acquiring a CBCT for every fraction increases treatment times and imaging dose to the patient. If the patient geometry remains relatively stable, then generating DPIs through a previous instance

of the patient geometry should suffice for treatment verification. A possible use for exit fluence dosimetry is to set tolerance levels for exit fluence deviations to determine when re-imaging of the patient should be performed.

This work is a limited prospective study of detecting and measuring exit fluence deviations. Therefore, several other possible machine-related sources of fluence variability have perhaps gone unmeasured. The delivery of each test field is performed at a gantry angle of 0° , so gantry sag effects are not examined. From fraction to fraction, however, these effects should remain constant. Also, since each source of deviation is isolated as much as possible, it is possible that some deviations caused by the combination of several sources went undetected. The inclusion of the complex patient IMRT field aided in examining how the various sources of machine-based deviations (such as output variation and jaw-, MLC leaf-, and EPID-positioning) contribute in a clinical situation. A retrospective analysis of multiple patient fields would yield more comprehensive results of machine-related sources of deviations; however, the intent of this work was not to completely describe every source of deviations, but to show the potential weakness of the back-projection assumption made in dose reconstruction.

5. Conclusions

For the treatment system and patient geometries tested, exit fluence deviations caused by patient anatomy-related sources are greater than those caused by machine-related sources. Therefore, for our clinic it is not a safe assumption that deviations are always the result of the machine's inability to produce the correct entrance fluence. In general, evidence-based decisions should be made as to when patient dose reconstruction is beneficial and when exit fluence variations are significantly different from those expected from realistic delivery errors.

Acknowledgments

This research was supported in part by Varian Medical Systems. The authors would like to thank Dr Jan-Jakob Sonke and the NKI for the CT images used in this study.

References

- Fix M K, Keall P J, Dawson K and Siebers J V 2004 Monte Carlo source model for photon beam radiotherapy: photon source characteristics *Med. Phys.* **31** 3106–21
- Greer P B and Popescu C C 2003 Dosimetric properties of an amorphous silicon electronic portal imaging device for verification of dynamic intensity modulated radiation therapy *Med. Phys.* **30** 1618–27
- Jarry G and Verhaegen F 2007 Patient-specific dosimetry of conventional and intensity modulated radiation therapy using a novel full Monte Carlo phase space reconstruction method from electronic portal images *Phys. Med. Biol.* **52** 2277–99
- Kawrakow I 2001 VMC++, electron and photon Monte Carlo calculations optimized for radiation treatment planning *Advanced Monte Carlo for Radiation Physics, Particle Transport Simulation and Applications: Proc. of the Monte Carlo 2000 Meeting (Berlin)* pp 229–36
- Kroonwijk M, Pasma K L, Quint S, Koper P C, Visser A G and Heijmen B J 1998 *In vivo* dosimetry for prostate cancer patients using an electronic portal imaging device (EPID): demonstration of internal organ motion *Radiother. Oncol.* **49** 125–32
- Lee L, Le Q T and Xing L 2008a Retrospective IMRT dose reconstruction based on cone-beam CT and MLC log-file *Int. J. Radiat. Oncol. Biol. Phys.* **70** 634–44
- Lee L, Mao W and Xing L 2008b The use of EPID-measured leaf sequence files for IMRT dose reconstruction in adaptive radiation therapy *Med. Phys.* **35** 5019–29
- Li W, Siebers J V and Moore J A 2006 Using fluence separation to account for energy spectra dependence in computing dosimetric a-Si EPID images for IMRT fields *Med. Phys.* **33** 4468–80

- Louwe R J, Damen E M, van Herk M, Minken A W, Torzsok O and Mijnheer B J 2003 Three-dimensional dose reconstruction of breast cancer treatment using portal imaging *Med. Phys.* **30** 2376–89
- McCurdy B M, Luchka K and Pistorius S 2001 Dosimetric investigation and portal dose image prediction using an amorphous silicon electronic portal imaging device *Med. Phys.* **28** 911–24
- McCurdy B M and Pistorius S 2000 A two-step algorithm for predicting portal dose images in arbitrary detectors *Med. Phys.* **27** 2109–16
- McDermott L N, Wendling M, Nijkamp J, Mans A, Sonke J J, Mijnheer B J and van Herk M 2008 3D *in vivo* dose verification of entire hypo-fractionated IMRT treatments using an EPID and cone-beam CT *Radiother. Oncol.* **86** 35–42
- Mohammadi M and Bezak E 2007 Evaluation of MLC leaf positioning using a scanning liquid ionization chamber EPID *Phys. Med. Biol.* **52** N21–33
- Nicolini G, Fogliata A, Vanetti E, Clivio A, Vetterli D and Cozzi L 2008 Testing the GlaaS algorithm for dose measurements on low- and high-energy photon beams using an amorphous silicon portal imager *Med. Phys.* **35** 464–72
- Partridge M, Ebert M and Hesse B M 2002 IMRT verification by three-dimensional dose reconstruction from portal beam measurements *Med. Phys.* **29** 1847–58
- Pasma K L, Heijmen B J, Kroonwijk M and Visser A G 1998 Portal dose image (PDI) prediction for dosimetric treatment verification in radiotherapy: I. An algorithm for open beams *Med. Phys.* **25** 830–40
- Siebers J V, Keall P J, Kim J O and Mohan R 2002 A method for photon beam Monte Carlo multileaf collimator particle transport *Phys. Med. Biol.* **47** 3225–49
- Siebers J V, Kim J O, Ko L, Keall P J and Mohan R 2004 Monte Carlo computation of dosimetric amorphous silicon electronic portal images *Med. Phys.* **31** 2135–46
- Sonke J J, Ploeger I S, Brand B, Smitsmans M H and van Herk M 2004 Leaf trajectory verification during dynamic intensity modulated radiotherapy using an amorphous silicon flat panel imager *Med. Phys.* **31** 389–95
- Steciw S, Warkentin B, Rathes S and Fallone B G 2005 Three-dimensional IMRT verification with a flat-panel EPID *Med. Phys.* **32** 600–12
- Talamonti C, Casati M and Bucciolini M 2006 Pretreatment verification of IMRT absolute dose distributions using a commercial a-Si EPID *Med. Phys.* **33** 4367–78
- van Elmpt W, Nijsten S, Mijnheer B, Dekker A and Lambin P 2008 The next step in patient-specific QA: 3D dose verification of conformal and intensity-modulated RT based on EPID dosimetry and Monte Carlo dose calculations *Radiother. Oncol.* **86** 86–92
- van Elmpt W J, Nijsten S M, Mijnheer B J and Minken A W 2005 Experimental verification of a portal dose prediction model *Med. Phys.* **32** 2805–18
- van Elmpt W J, Nijsten S M, Schiffeleers R F, Dekker A L, Mijnheer B J, Lambin P and Minken A W 2006 A Monte Carlo based three-dimensional dose reconstruction method derived from portal dose images *Med. Phys.* **33** 2426–34
- Van Esch A, Depuydt T and Huyskens D P 2004 The use of an aSi-based EPID for routine absolute dosimetric pre-treatment verification of dynamic IMRT fields *Radiother. Oncol.* **71** 223–34
- van Zijtveld M, Dirix M L, de Boer H C and Heijmen B J 2006 Dosimetric pre-treatment verification of IMRT using an EPID: clinical experience *Radiother. Oncol.* **81** 168–75
- van Zijtveld M, Dirix M L, de Boer H C and Heijmen B J 2007 3D dose reconstruction for clinical evaluation of IMRT pretreatment verification with an EPID *Radiother. Oncol.* **82** 201–7
- Vieira S C, Dirix M L, Heijmen B J and de Boer H C 2004 SIPT: a method to verify the IMRT fluence delivered during patient treatment using an electronic portal imaging device *Int. J. Radiat. Oncol. Biol. Phys.* **60** 981–93

9. Appendix II

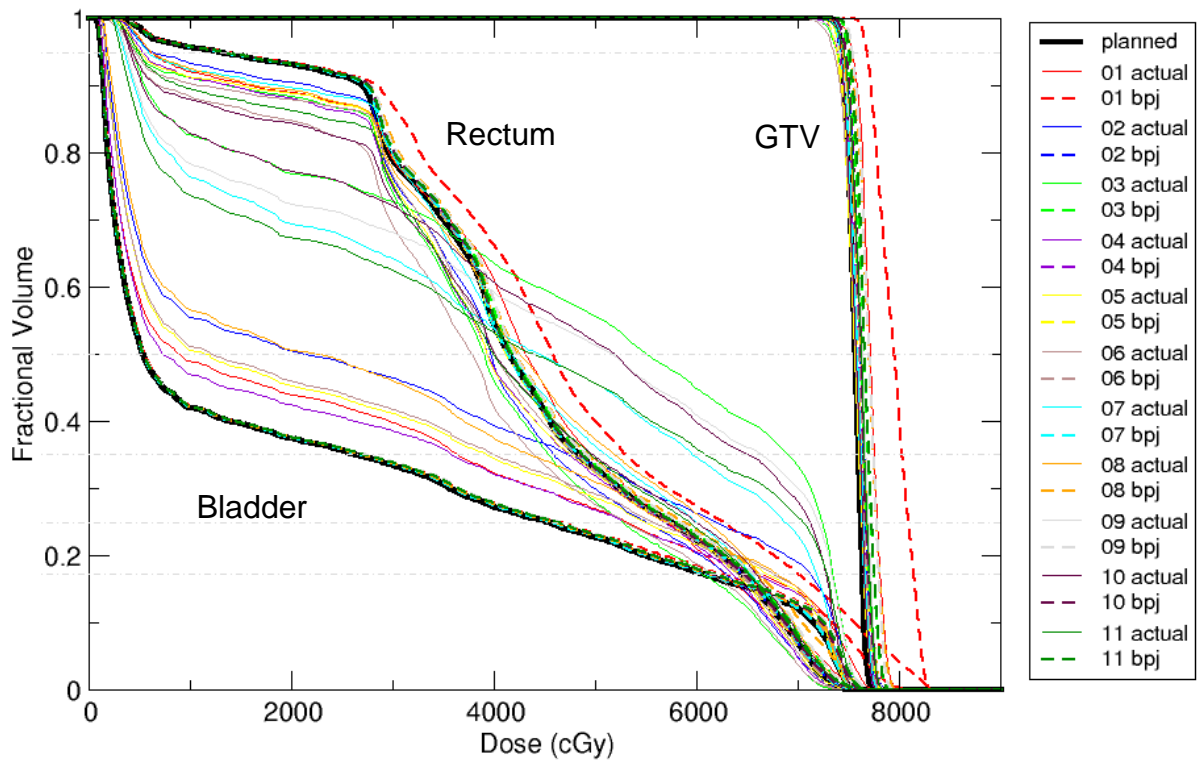


Figure 34: GTV, rectum, and bladder DVHs for patient poses [01, 02 ...] for patient 1. The planned doses are shown as the bolded black solid lines. For each simulated treatment fraction, both the delivered doses (thin solid lines) and reconstructed doses (dashed lines) are shown. Beam energy for this patient was 6 MV.

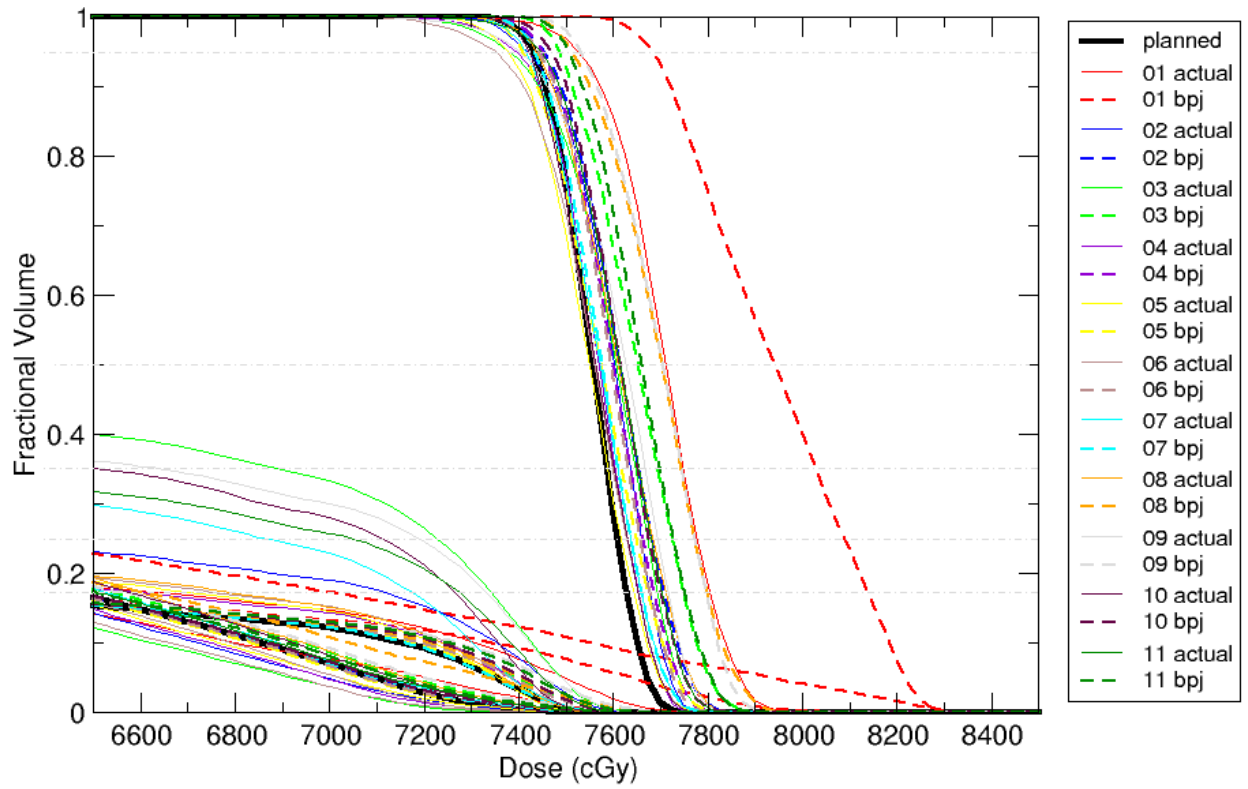


Figure 35: GTV DVHs for patient poses [01, 02 ...] for patient 1. The planned dose is shown as the bolded black solid line. For each simulated treatment fraction, both the delivered doses (thin solid lines) and reconstructed doses (dashed lines) are shown. Beam energy for this patient was 6 MV.

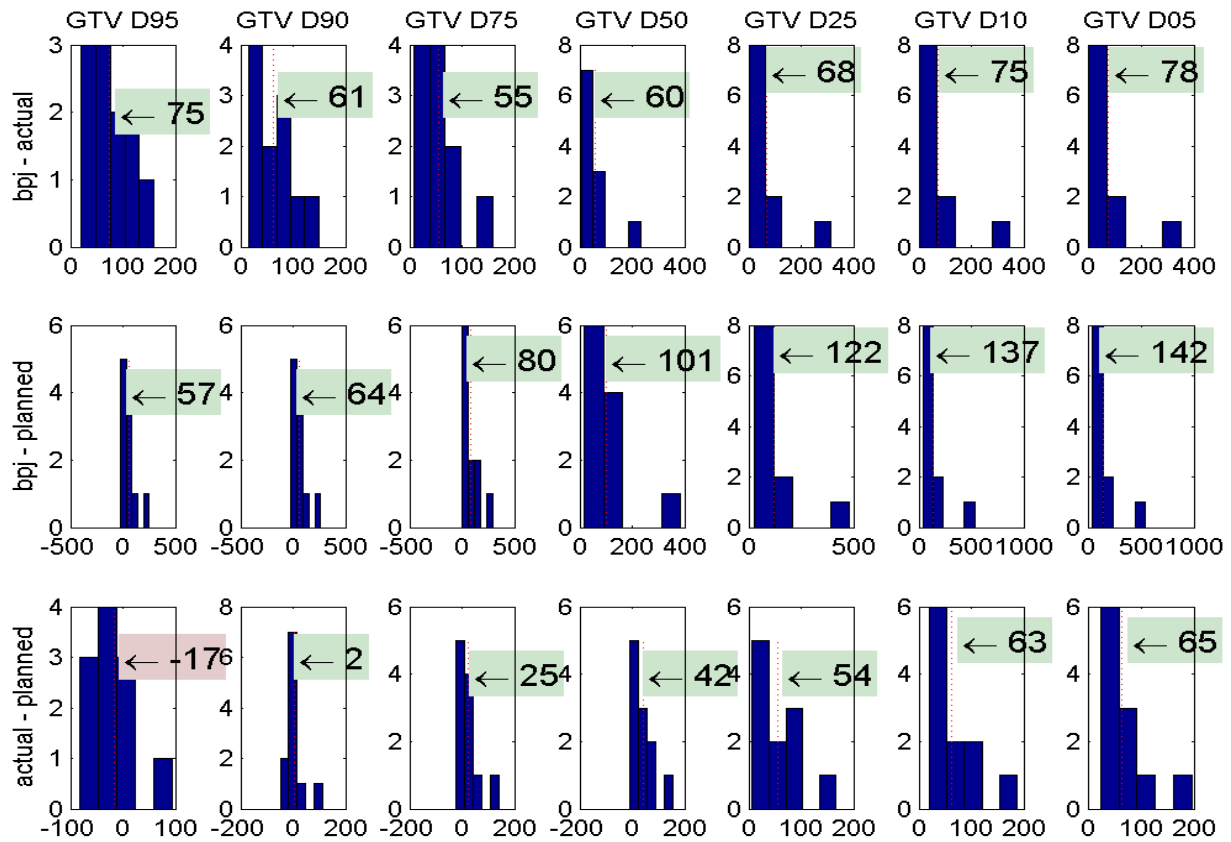


Figure 36: Histograms of the differences between planned, actual, and backprojected GTV dose indices for patient 1. The x-axes represent the dose difference in units of cGy. The numbers in the red/green boxes represent the mean differences. For the D₉₅ values, the average delivered dose is 75 cGy greater than the average reconstructed dose. Beam energy for this patient was 6 MV.

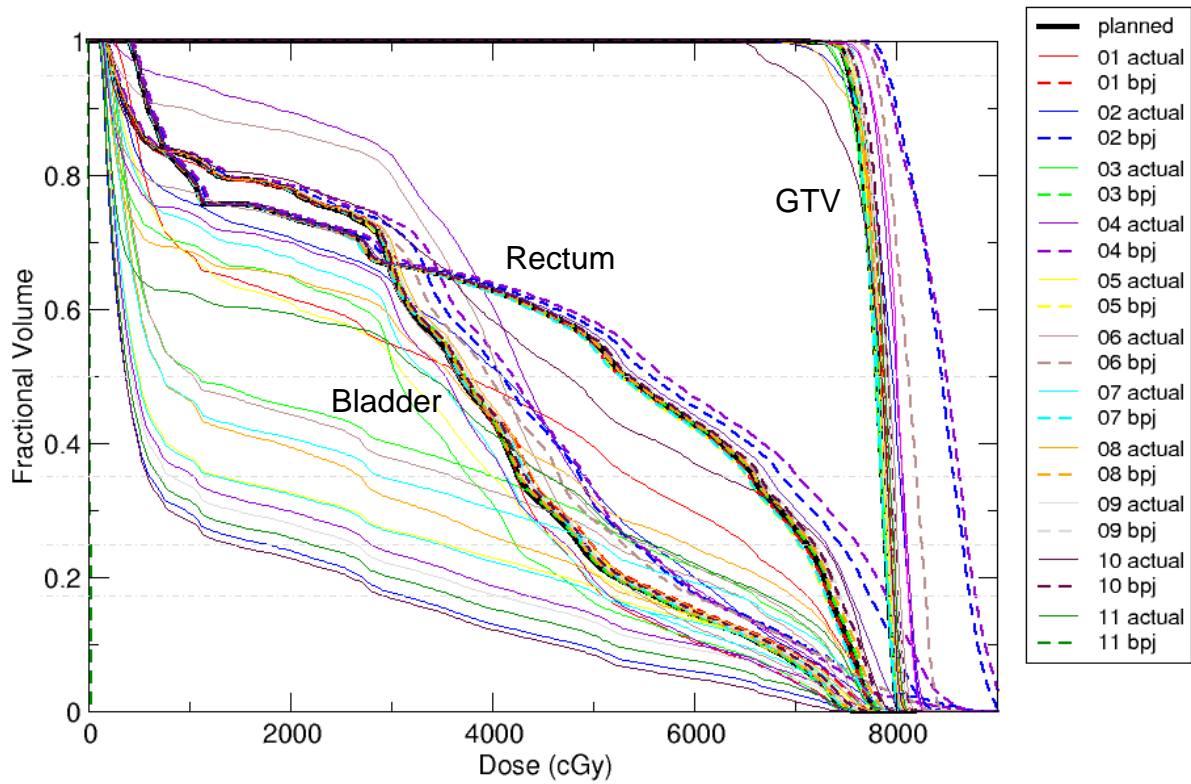


Figure 37: GTV, rectum, and bladder DVHs for patient poses [01, 02 ...] for patient 2. The planned doses are shown as the bolded black solid lines. For each simulated treatment fraction, both the delivered doses (thin solid lines) and reconstructed doses (dashed lines) are shown. Beam energy for this patient was 6 MV.

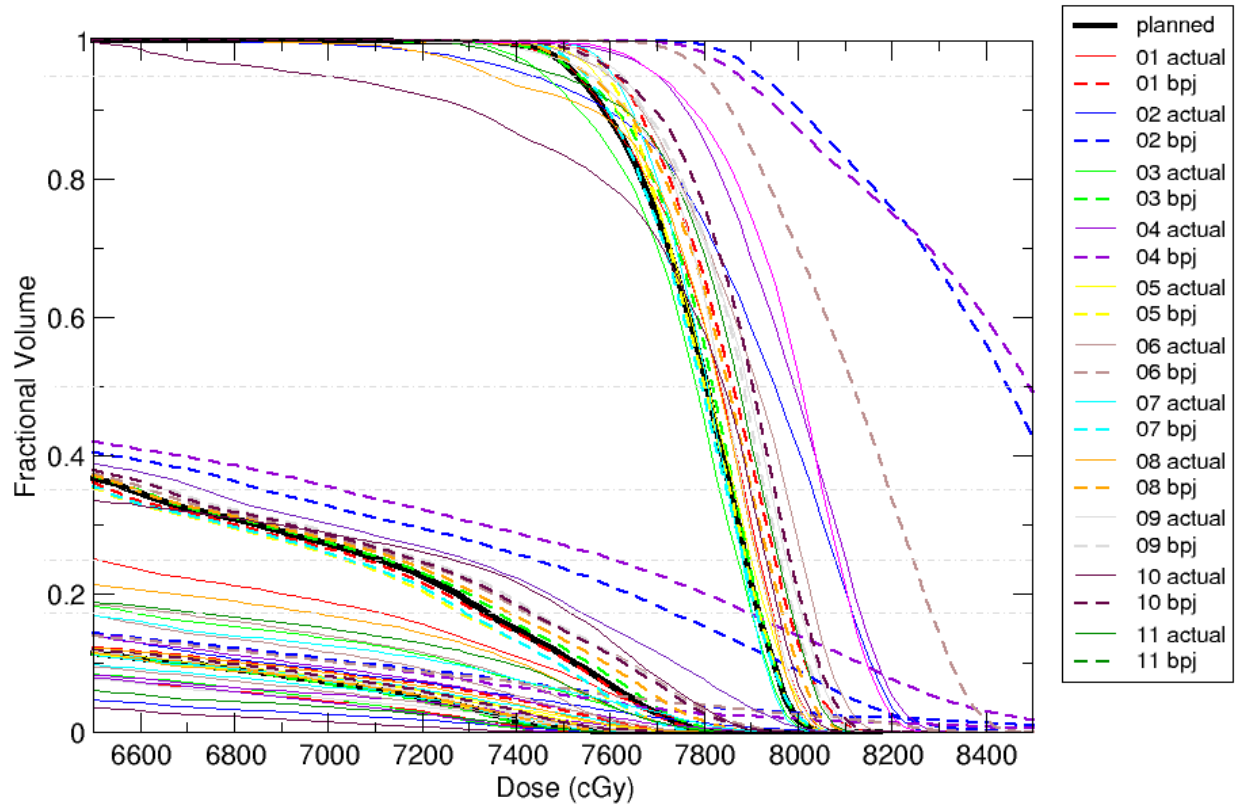


Figure 38: GTV DVHs for patient poses [01, 02 ...] for patient 2. The planned dose is shown as the bolded black solid line. For each simulated treatment fraction, both the delivered doses (thin solid lines) and reconstructed doses (dashed lines) are shown. Beam energy for this patient was 6 MV.

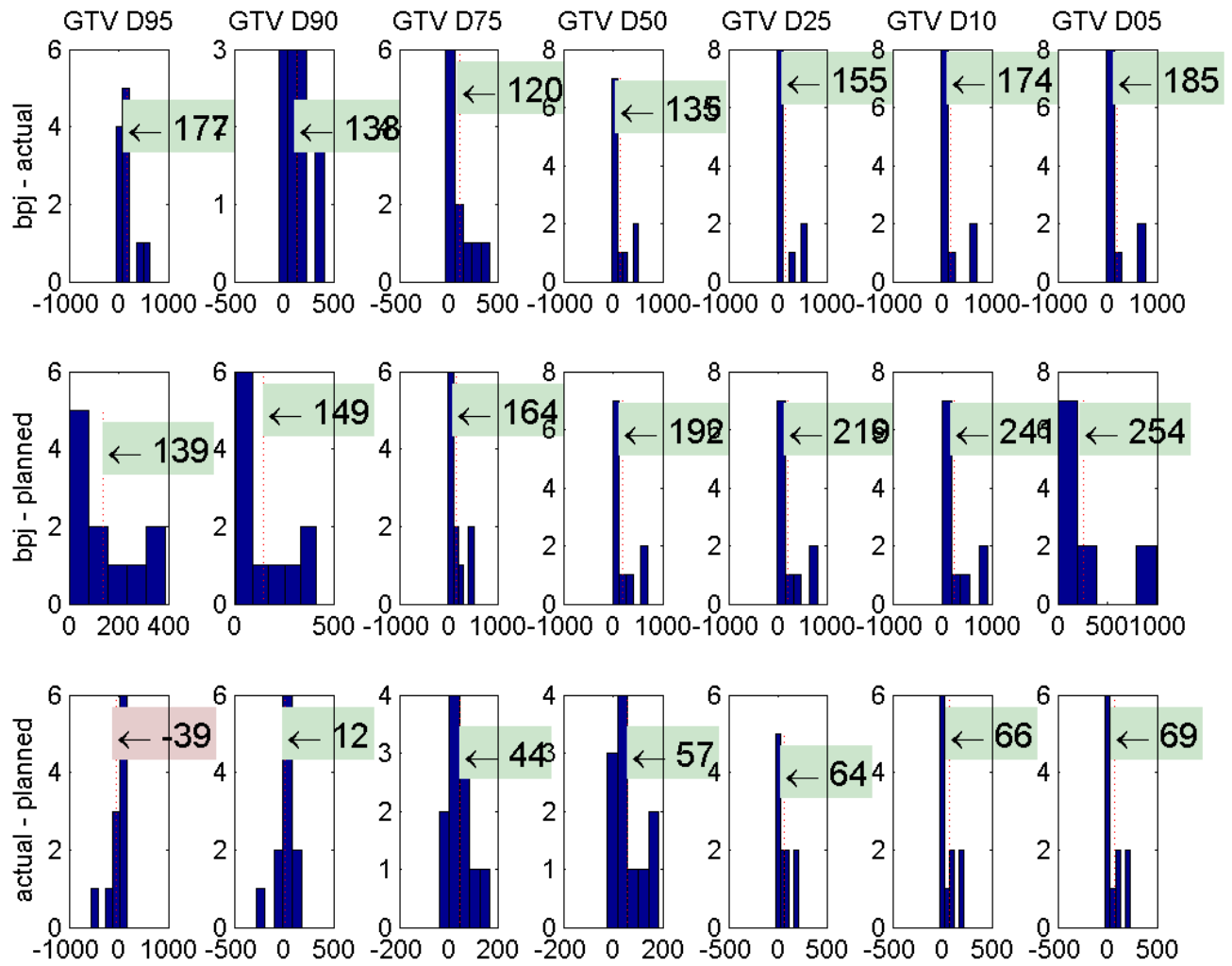


Figure 39: Histograms of the differences between planned, actual, and backprojected GTV dose indices for patient 2. The x-axes represent the dose difference in units of cGy. The numbers in the red/green boxes represent the mean differences. For the D₉₅ values, the average delivered dose is 177 cGy greater than the average reconstructed dose. Beam energy for this patient was 6 MV.

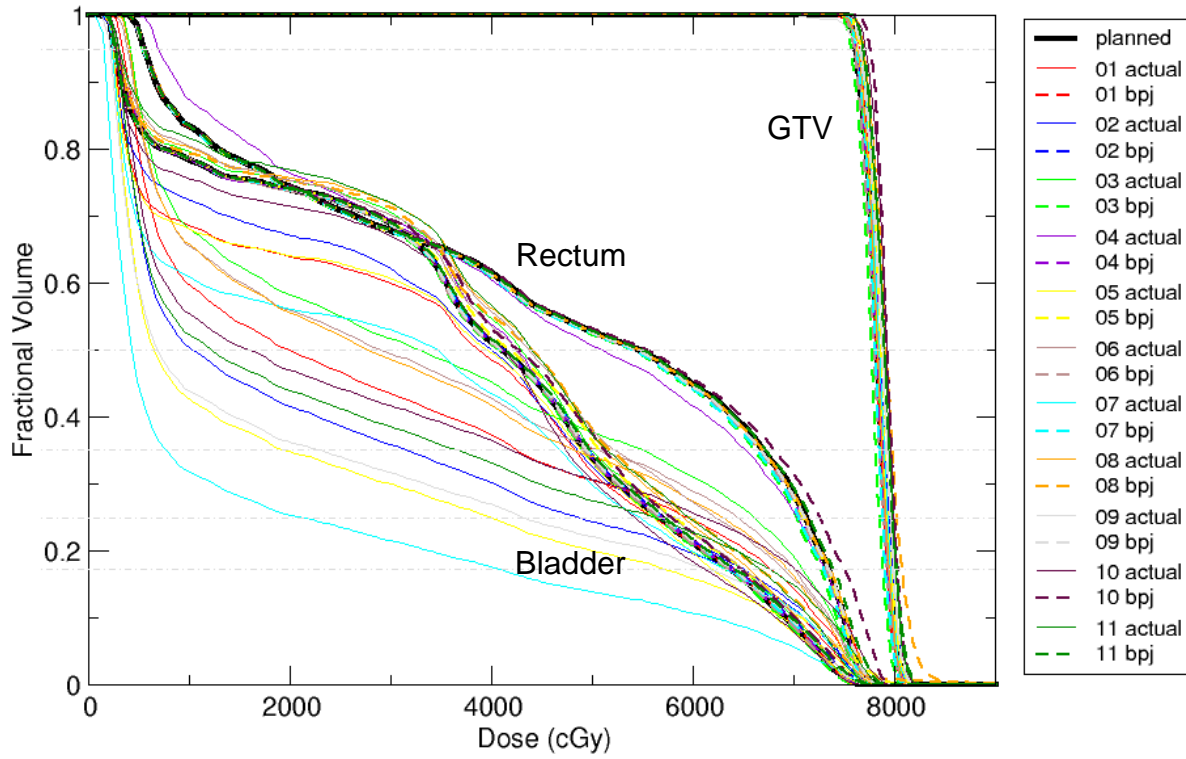


Figure 40: GTV, rectum, and bladder DVHs for patient poses [01, 02 ...] for patient 3. The planned doses are shown as the bolded black solid lines. For each simulated treatment fraction, both the delivered doses (thin solid lines) and reconstructed doses (dashed lines) are shown. Beam energy for this patient was 6 MV.

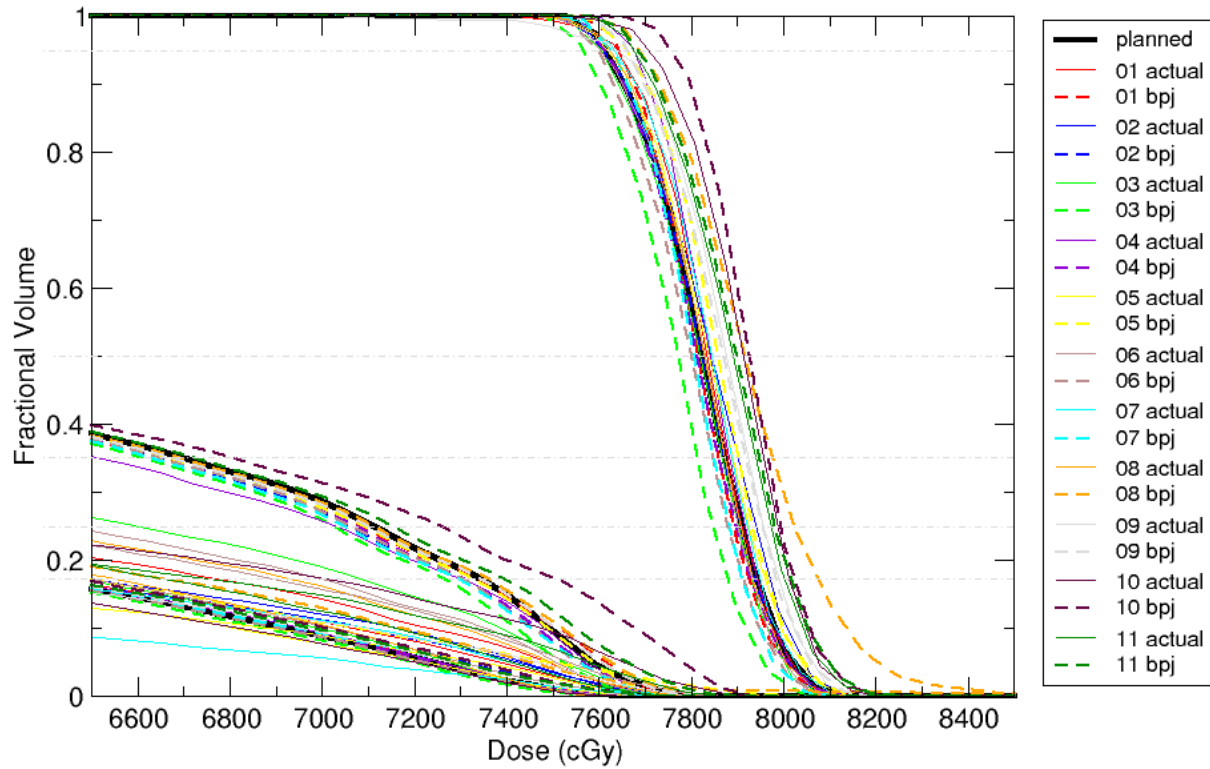


Figure 41: GTV DVHs for patient poses [01, 02 ...] for patient 3. The planned dose is shown as the bolded black solid line. For each simulated treatment fraction, both the delivered doses (thin solid lines) and reconstructed doses (dashed lines) are shown. Beam energy for this patient was 6 MV.

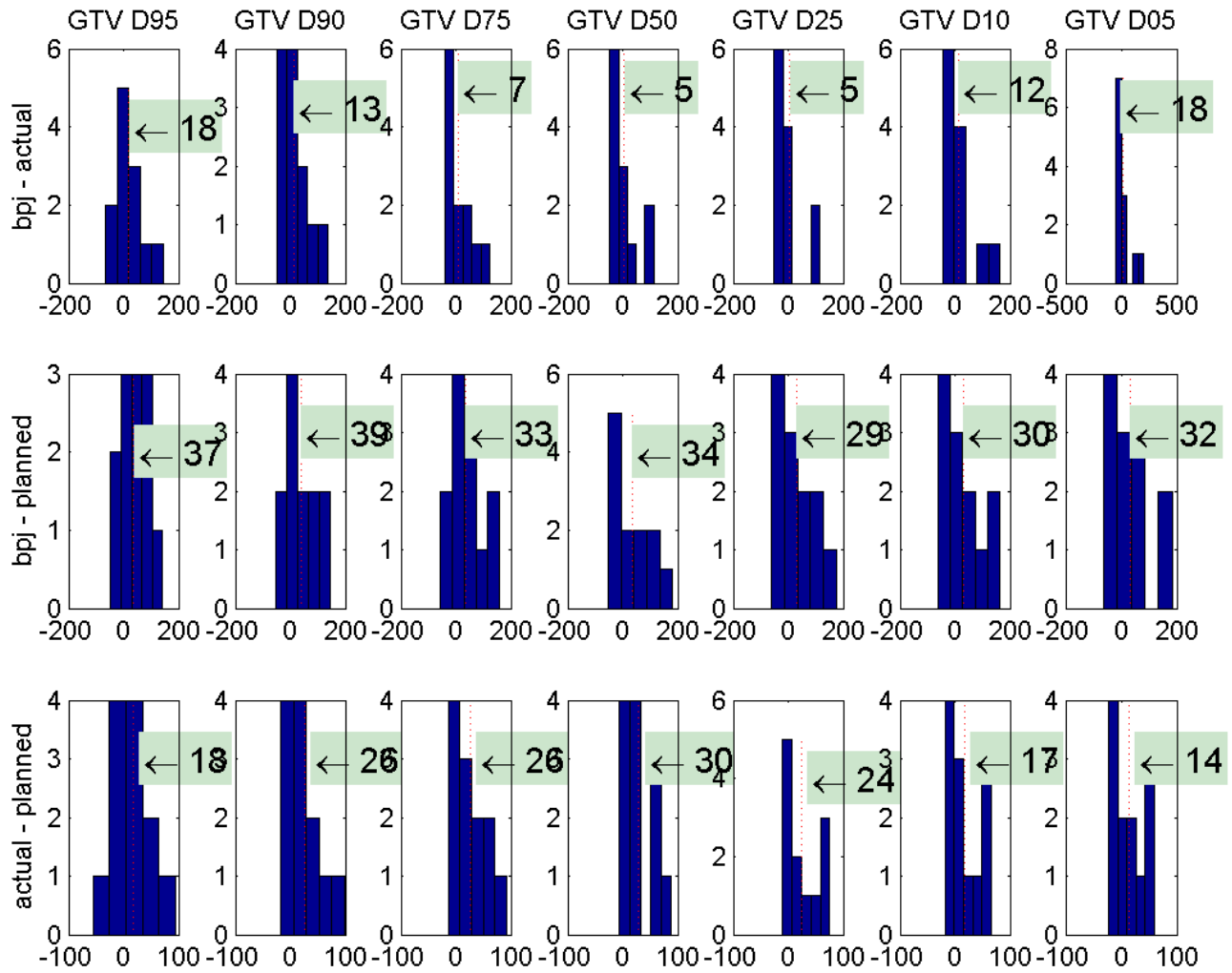


Figure 42: Histograms of the differences between planned, actual, and backprojected GTV dose indices for patient 3. The x-axes represent the dose difference in units of cGy. The numbers in the red/green boxes represent the mean differences. For the D₉₅ values, the average delivered dose is 18 cGy greater than the average reconstructed dose. Beam energy for this patient was 6 MV.

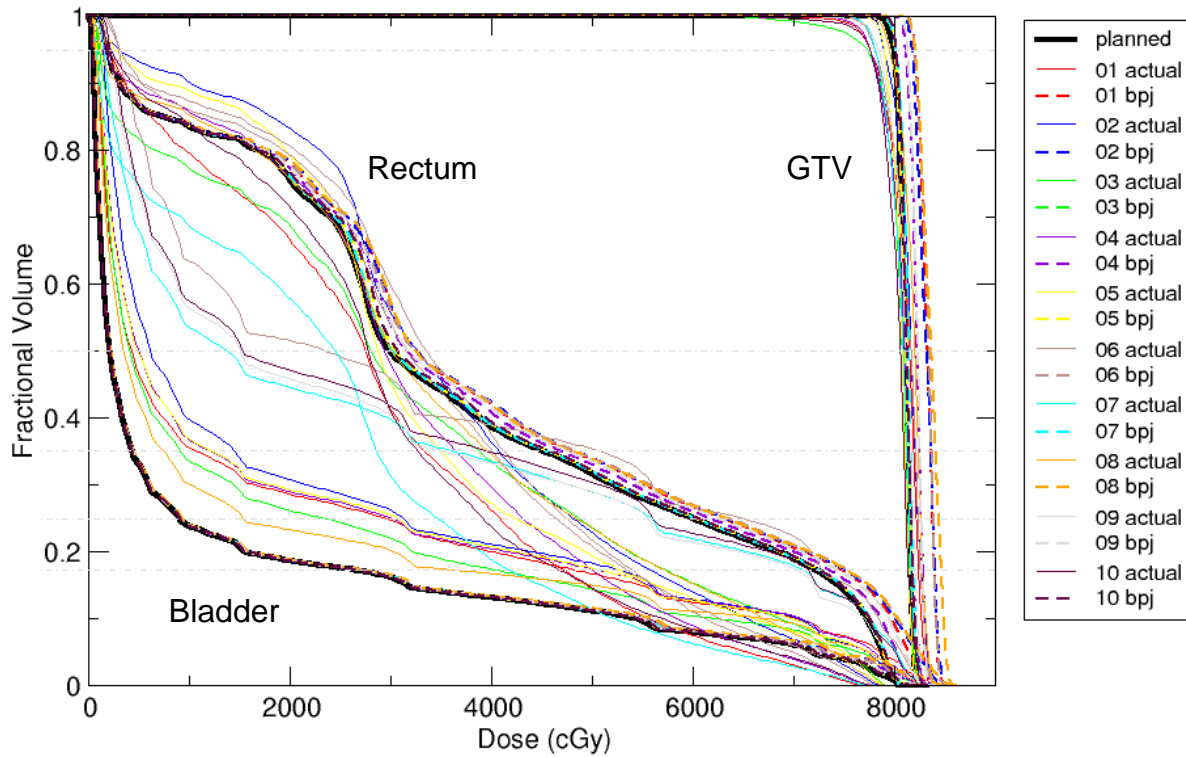


Figure 43: GTV, rectum, and bladder DVHs for patient poses [01, 02 ...] for patient 4. The planned doses are shown as the bolded black solid lines. For each simulated treatment fraction, both the delivered doses (thin solid lines) and reconstructed doses (dashed lines) are shown. Beam energy for this patient was 18 MV.

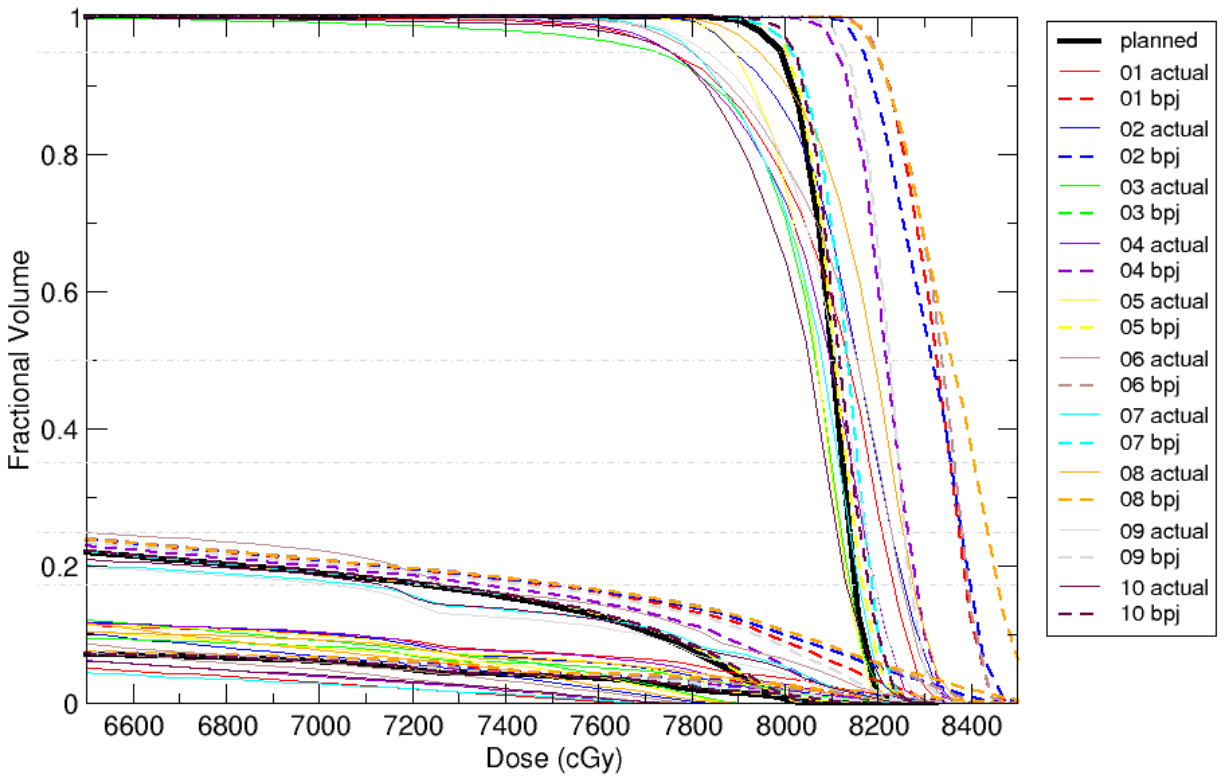


Figure 44: GTV DVHs for patient poses [01, 02 ...] for patient 4. The planned dose is shown as the bolded black solid line. For each simulated treatment fraction, both the delivered doses (thin solid lines) and reconstructed doses (dashed lines) are shown. Beam energy for this patient was 18 MV.

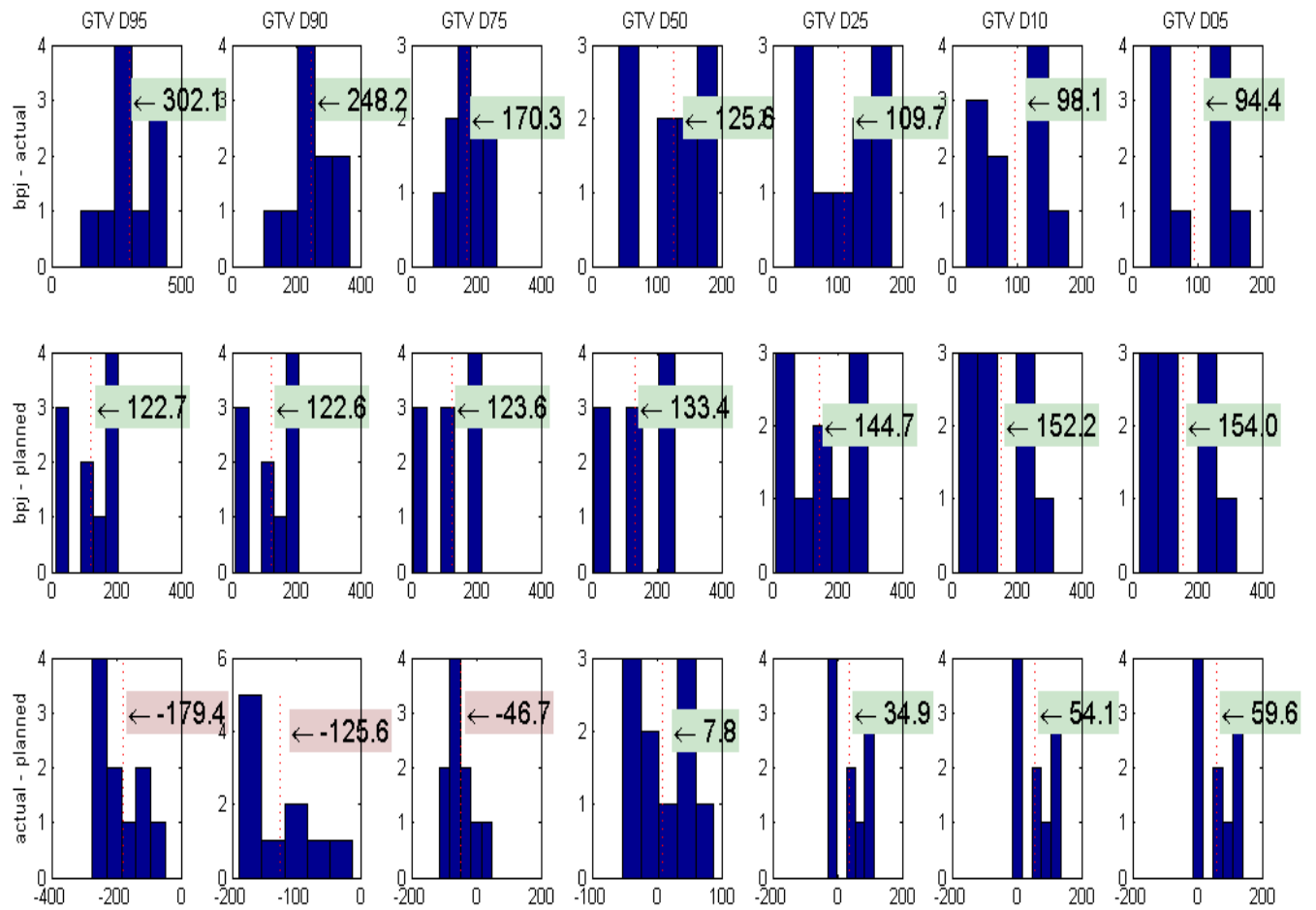


Figure 45: Histograms of the differences between planned, actual, and backprojected GTV dose indices for patient 4. The x-axes represent the dose difference in units of cGy. The numbers in the red/green boxes represent the mean differences. For the D_{95} values, the average delivered dose is 302 cGy greater than the average reconstructed dose. Beam energy for this patient was 18 MV.

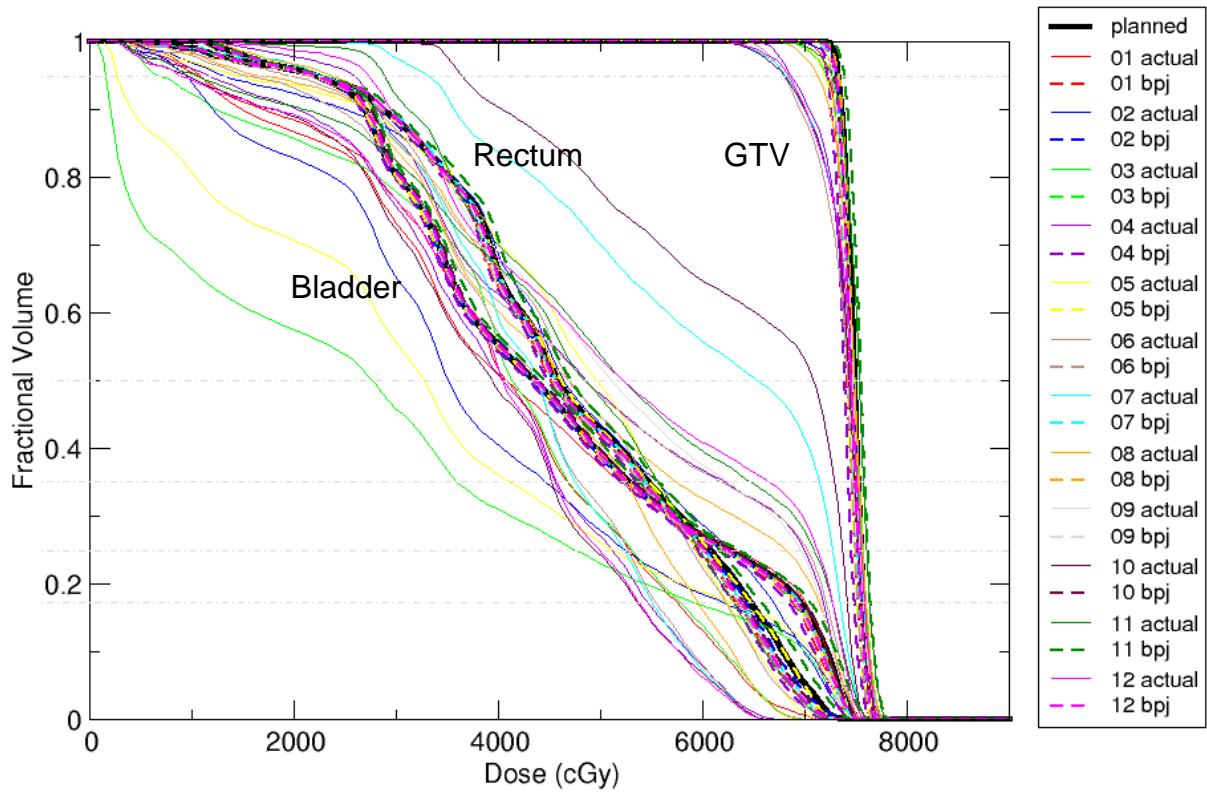


Figure 46: GTV, rectum, and bladder DVHs for patient poses [01, 02 ...] for patient 5. The planned doses are shown as the bolded black solid lines. For each simulated treatment fraction, both the delivered doses (thin solid lines) and reconstructed doses (dashed lines) are shown. Beam energy for this patient was 6 MV.

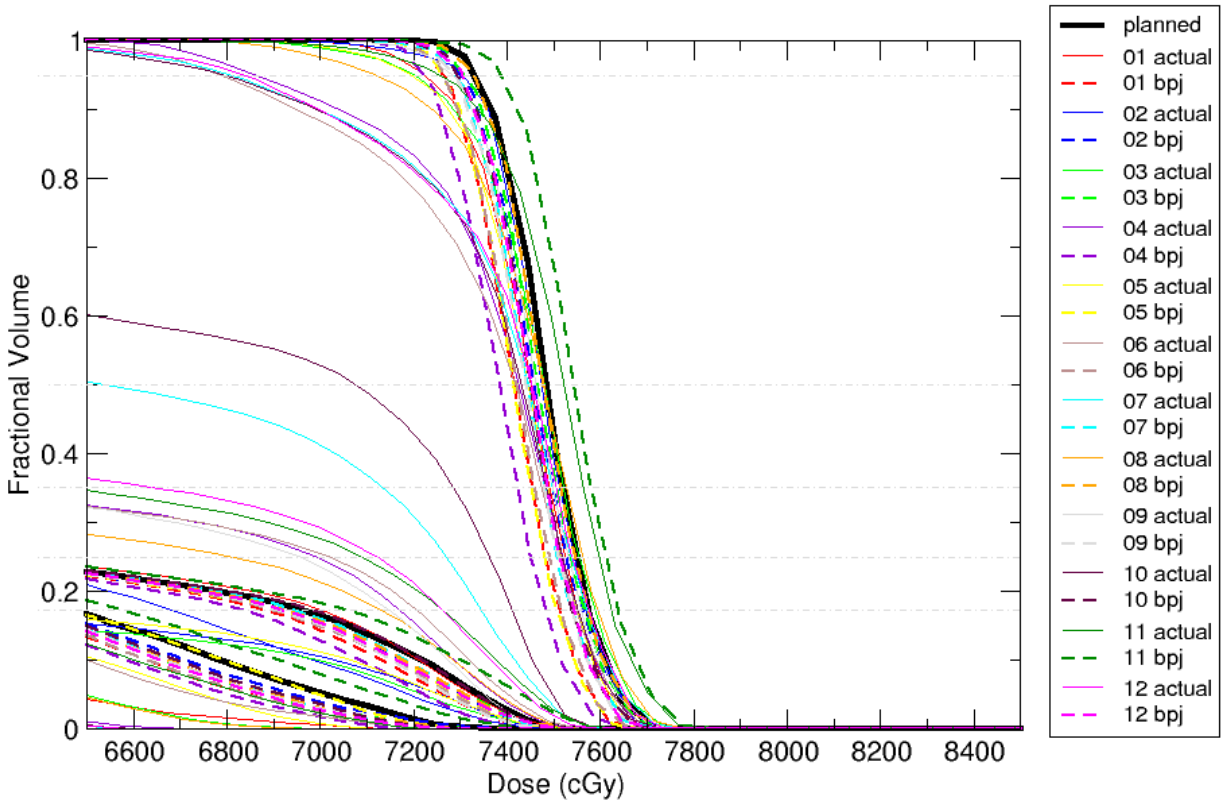


Figure 47: GTV DVHs for patient poses [01, 02 ...] for patient 5. The planned dose is shown as the bolded black solid line. For each simulated treatment fraction, both the delivered doses (thin solid lines) and reconstructed doses (dashed lines) are shown. Beam energy for this patient was 6 MV.

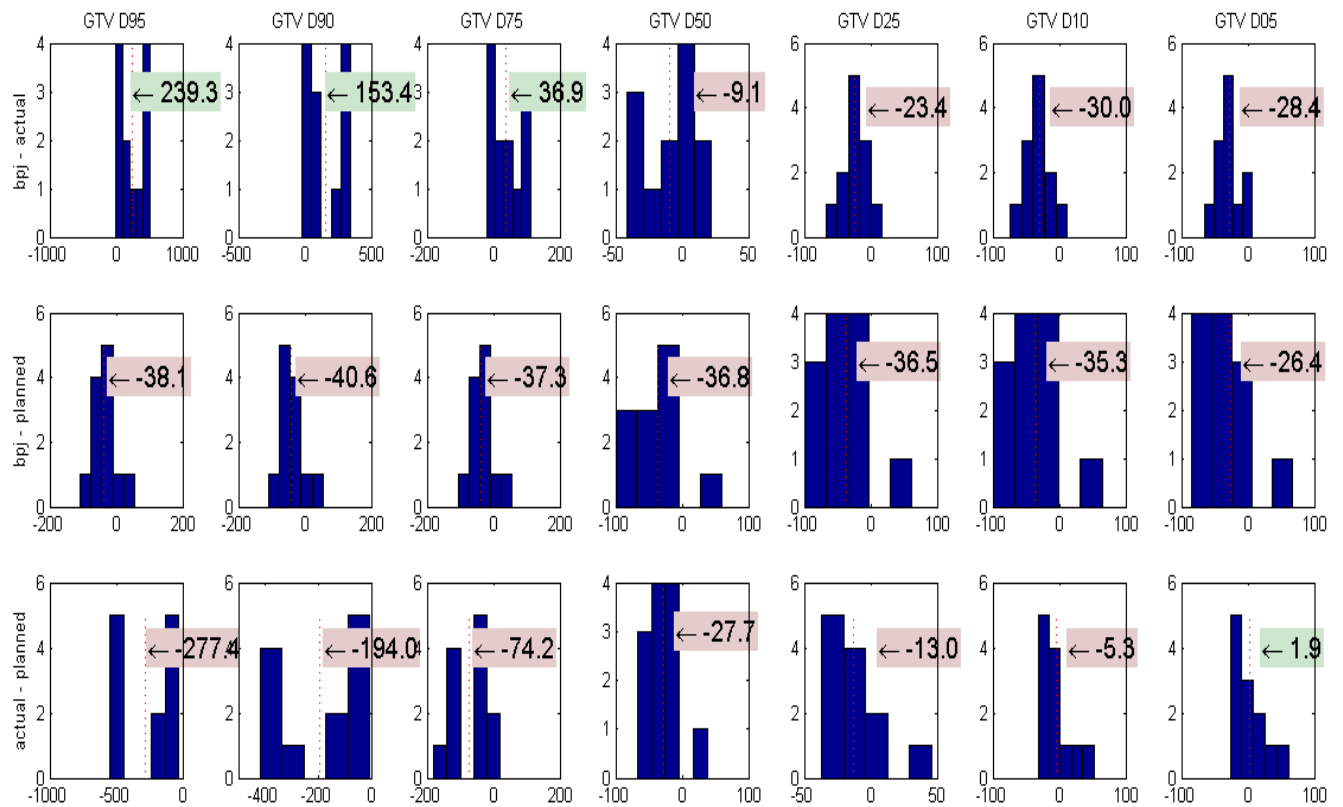


Figure 48: Histograms of the differences between planned, actual, and backprojected GTV dose indices for patient 5. The x-axes represent the dose difference in units of cGy. The numbers in the red/green boxes represent the mean differences. For the D_{95} values, the average delivered dose is 239 cGy greater than the average reconstructed dose. Beam energy for this patient was 6 MV.

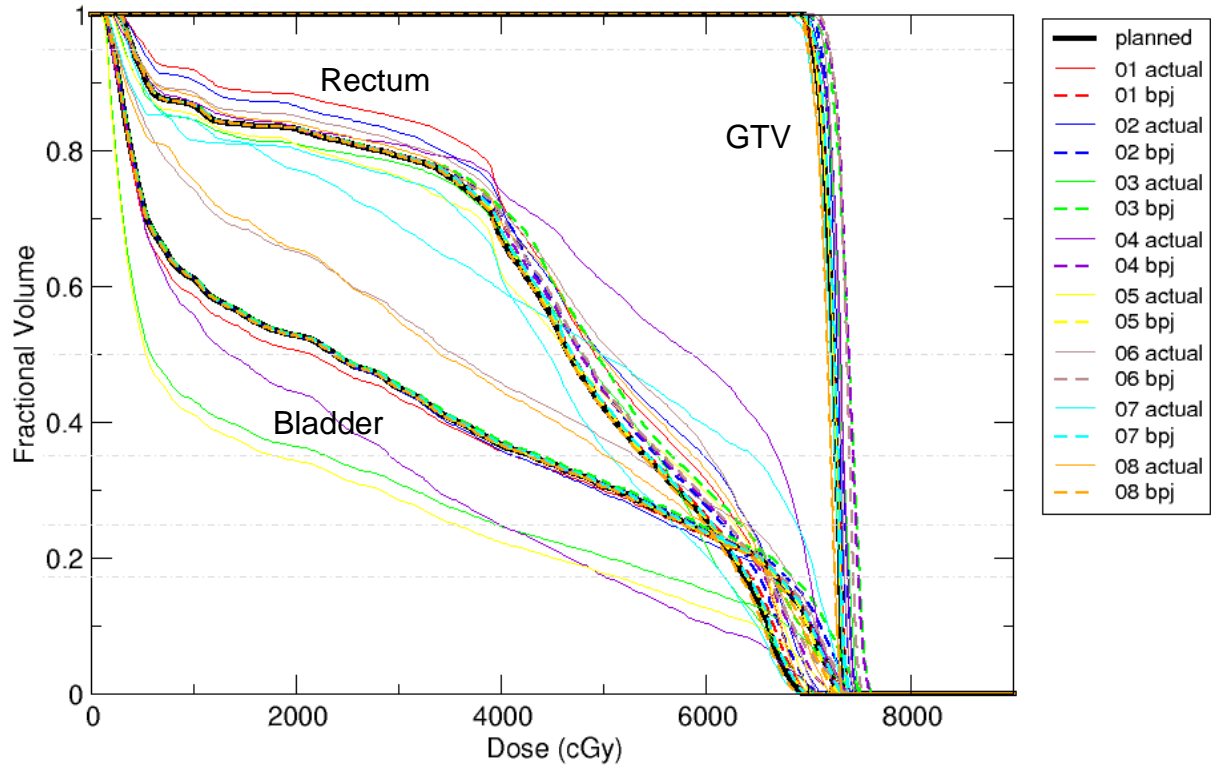


Figure 49: GTV, rectum, and bladder DVHs for patient poses [01, 02 ...] for patient 6. The planned doses are shown as the bolded black solid lines. For each simulated treatment fraction, both the delivered doses (thin solid lines) and reconstructed doses (dashed lines) are shown. Beam energy for this patient was 6 MV.

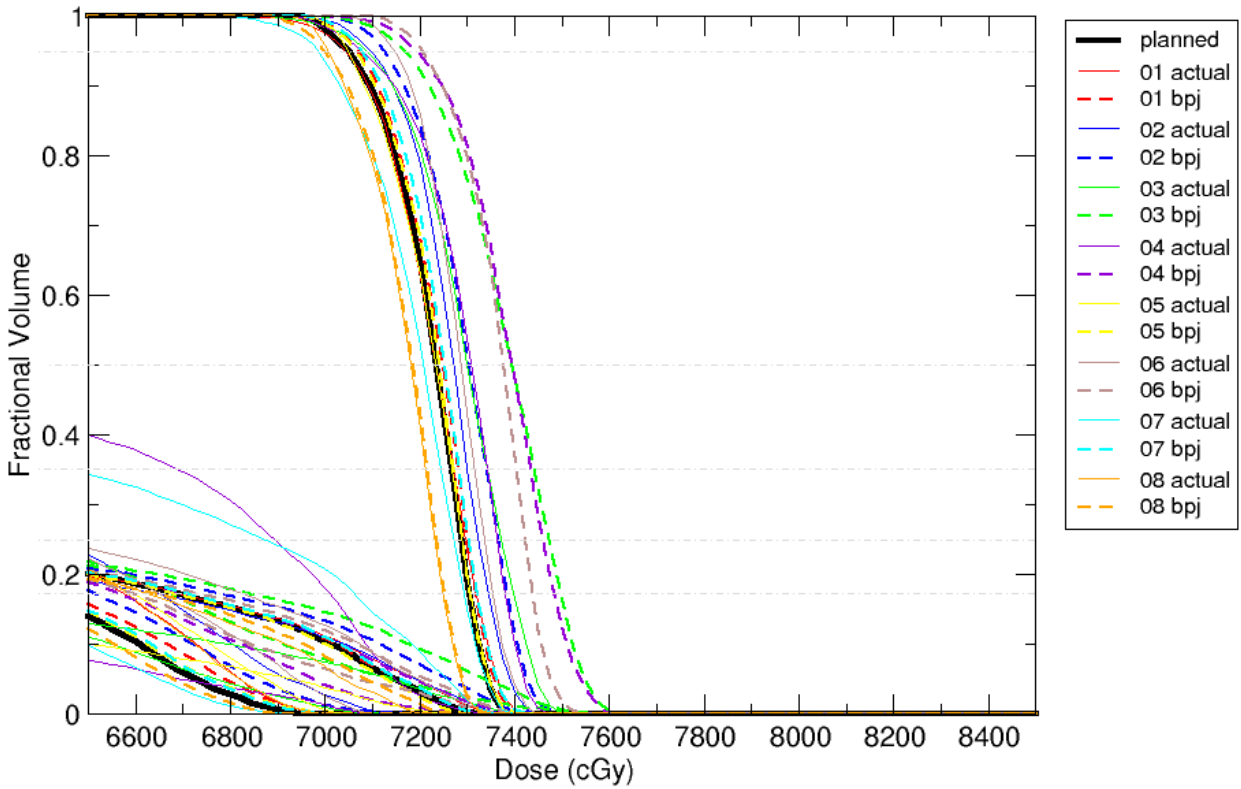


Figure 50: GTV DVHs for patient poses [01, 02 ...] for patient 6. The planned dose is shown as the bolded black solid line. For each simulated treatment fraction, both the delivered doses (thin solid lines) and reconstructed doses (dashed lines) are shown. Beam energy for this patient was 6 MV.

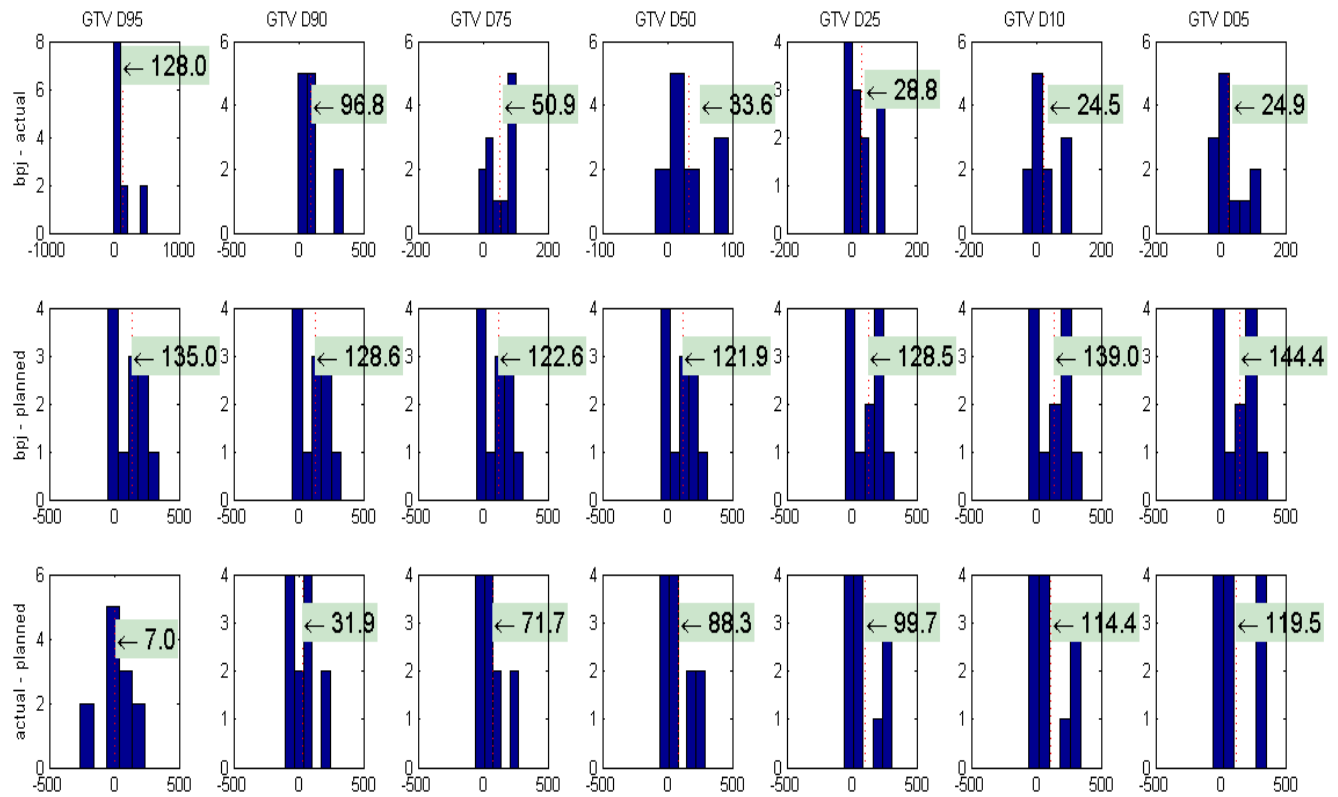


Figure 51: Histograms of the differences between planned, actual, and backprojected GTV dose indices for patient 6. The x-axes represent the dose difference in units of cGy. The numbers in the red/green boxes represent the mean differences. For the D_{95} values, the average delivered dose is 128 cGy greater than the average reconstructed dose. Beam energy for this patient was 6 MV.

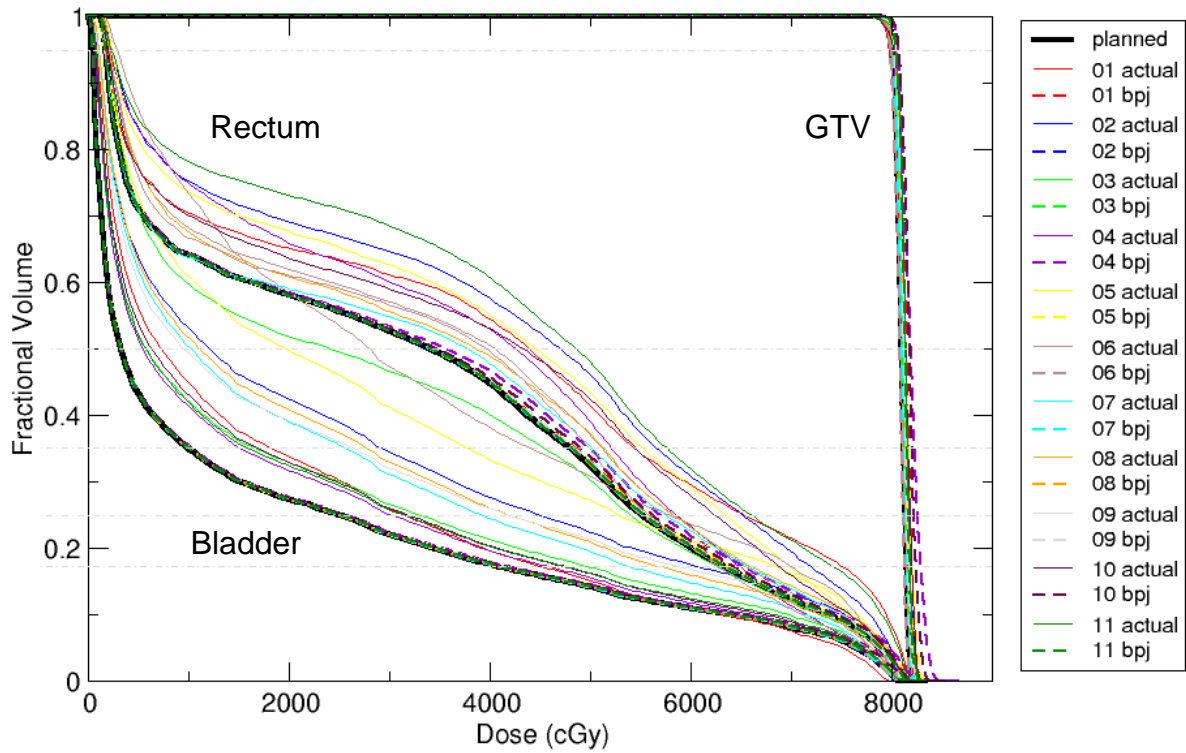


Figure 52: GTV, rectum, and bladder DVHs for patient poses [01, 02 ...] for patient 7. The planned doses are shown as the bolded black solid lines. For each simulated treatment fraction, both the delivered doses (thin solid lines) and reconstructed doses (dashed lines) are shown. Beam energy for this patient was 18 MV.

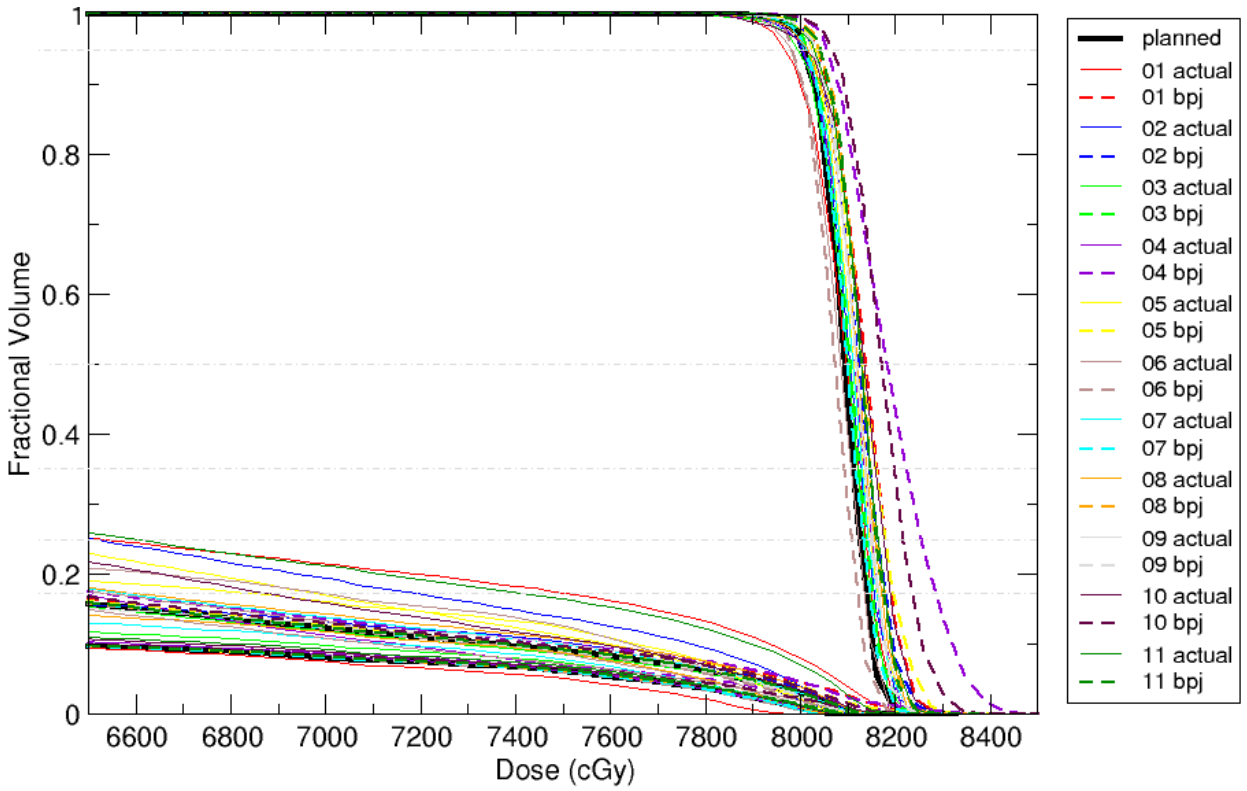


Figure 53: GTV DVHs for patient poses [01, 02 ...] for patient 7. The planned dose is shown as the bolded black solid line. For each simulated treatment fraction, both the delivered doses (thin solid lines) and reconstructed doses (dashed lines) are shown. Beam energy for this patient was 18 MV.

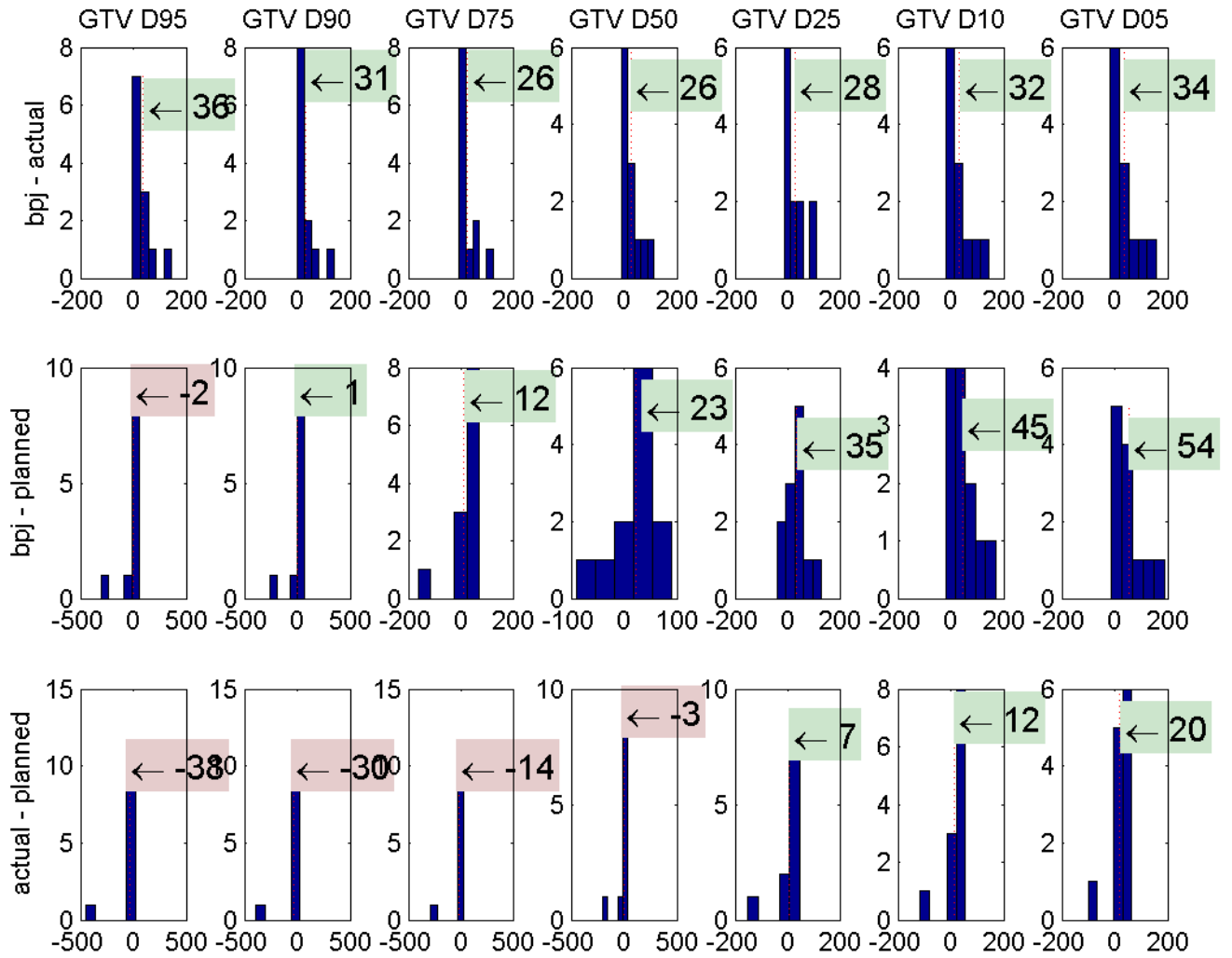


Figure 54: Histograms of the differences between planned, actual, and backprojected GTV dose indices for patient 7. The x-axes represent the dose difference in units of cGy. The numbers in the red/green boxes represent the mean differences. For the D₉₅ values, the average delivered dose is 36 cGy greater than the average reconstructed dose. Beam energy for this patient was 18 MV.

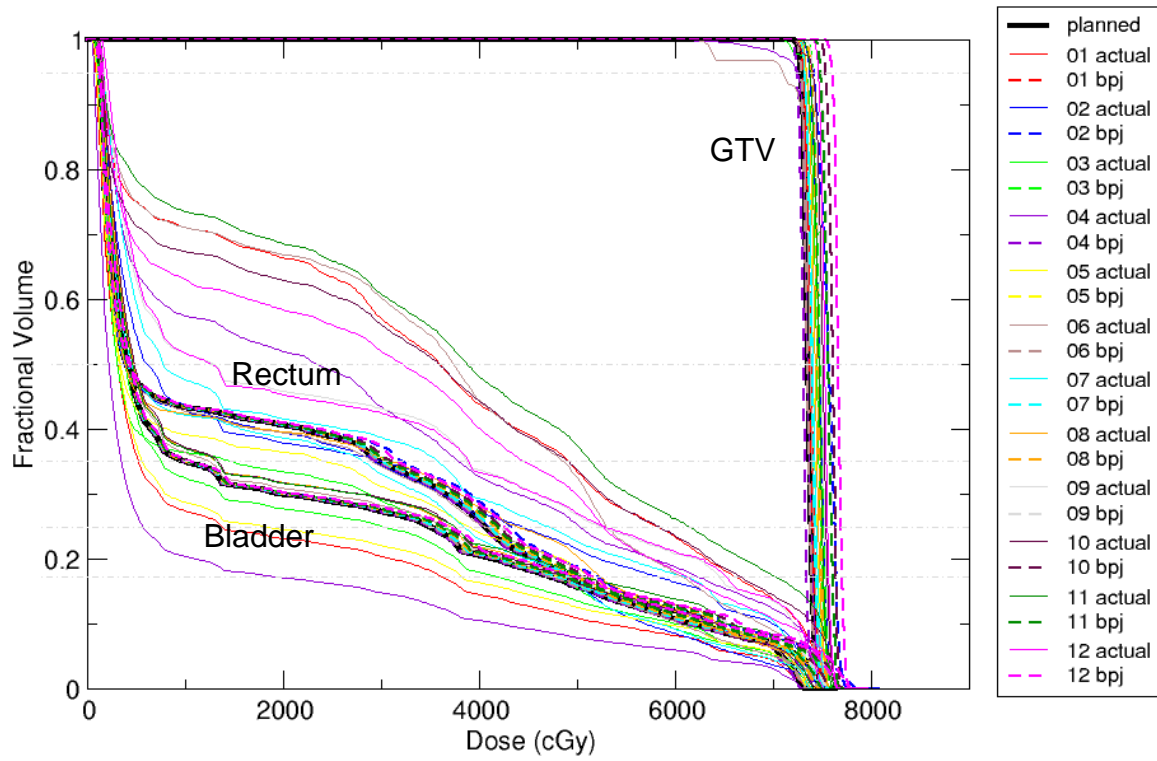


Figure 55: GTV, rectum, and bladder DVHs for patient poses [01, 02 ...] for patient 8. The planned doses are shown as the bolded black solid lines. For each simulated treatment fraction, both the delivered doses (thin solid lines) and reconstructed doses (dashed lines) are shown. Beam energy for this patient was 6 MV.

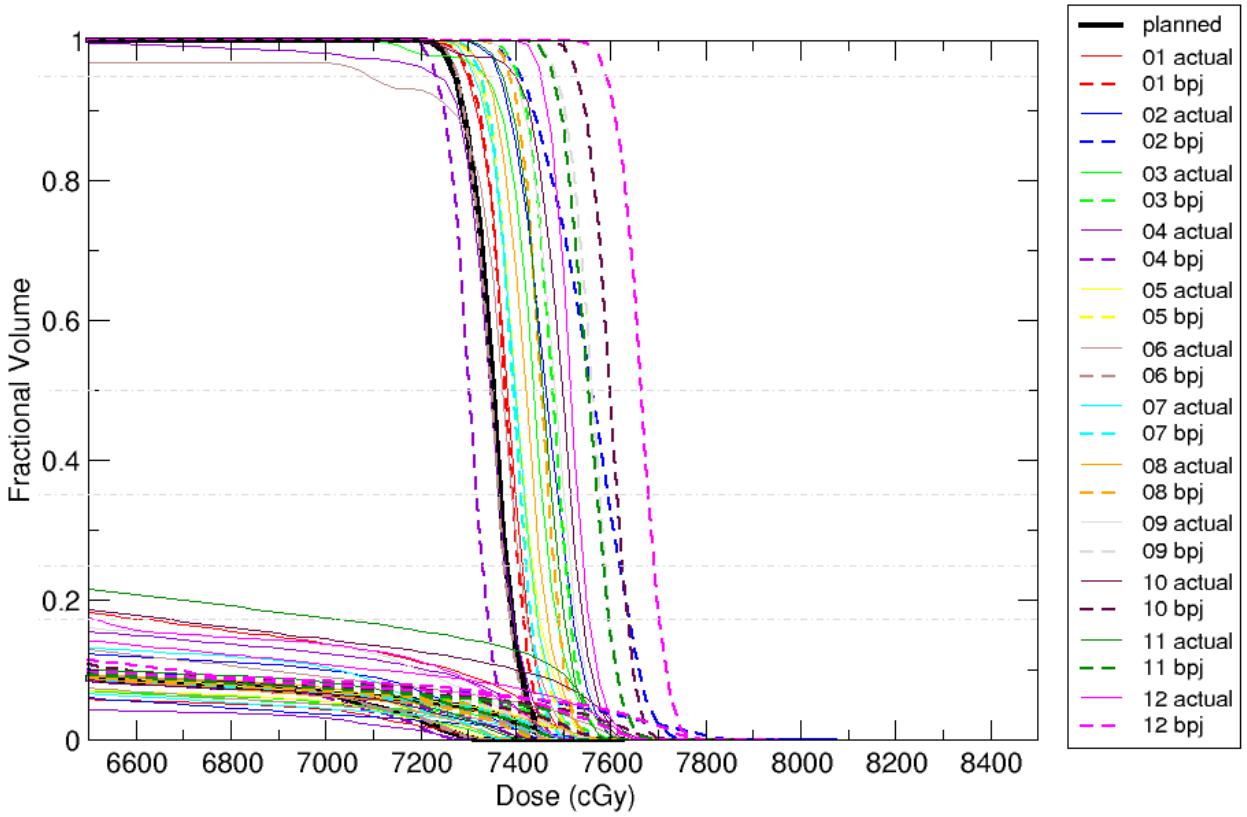


Figure 56: GTV DVHs for patient poses [01, 02 ...] for patient 8. The planned dose is shown as the bolded black solid line. For each simulated treatment fraction, both the delivered doses (thin solid lines) and reconstructed doses (dashed lines) are shown. Beam energy for this patient was 6 MV.

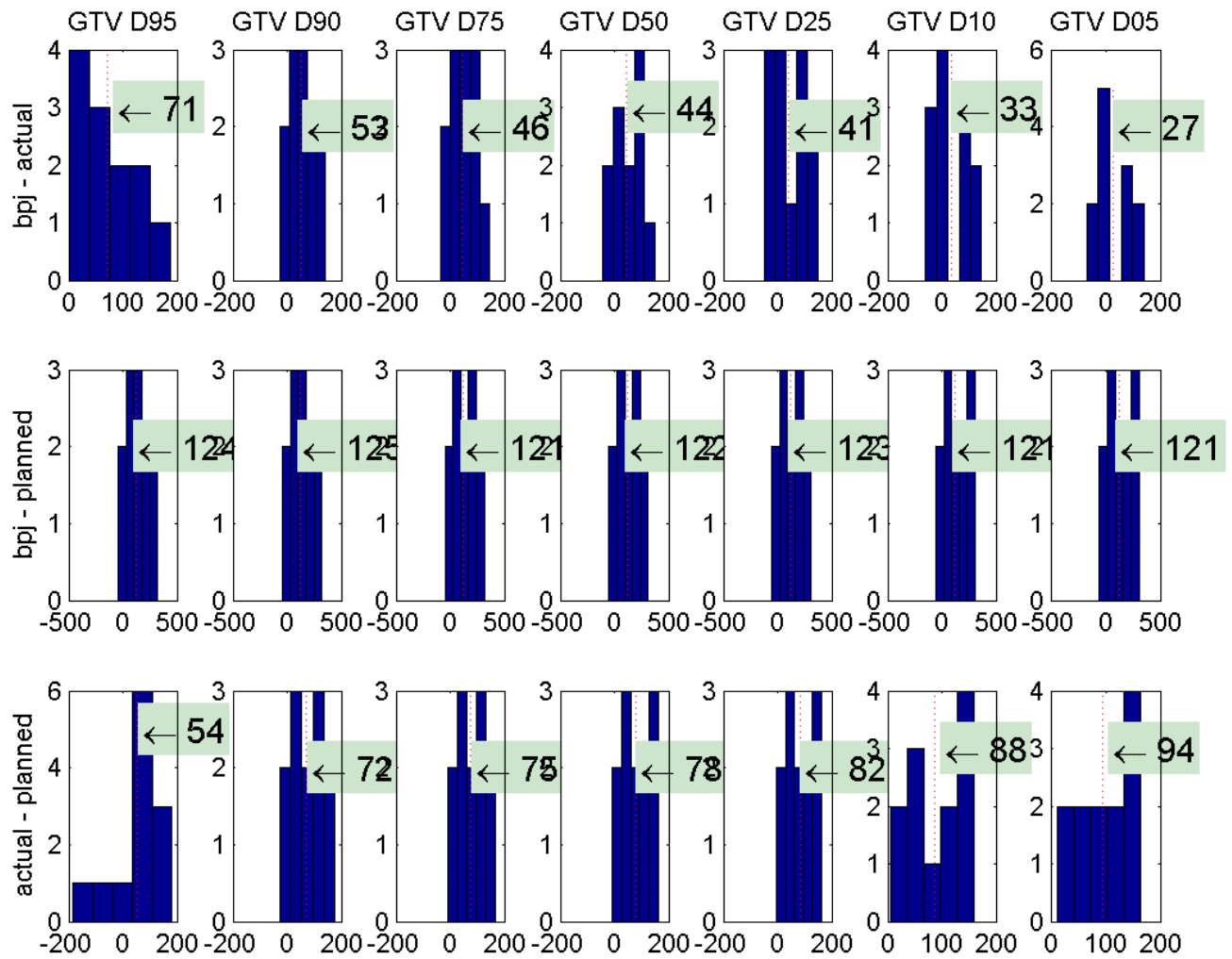


Figure 57: Histograms of the differences between planned, actual, and backprojected GTV dose indices for patient 8. The x-axes represent the dose difference in units of cGy. The numbers in the red/green boxes represent the mean differences. For the D₉₅ values, the average delivered dose is 71 cGy greater than the average reconstructed dose. Beam energy for this patient was 6 MV.

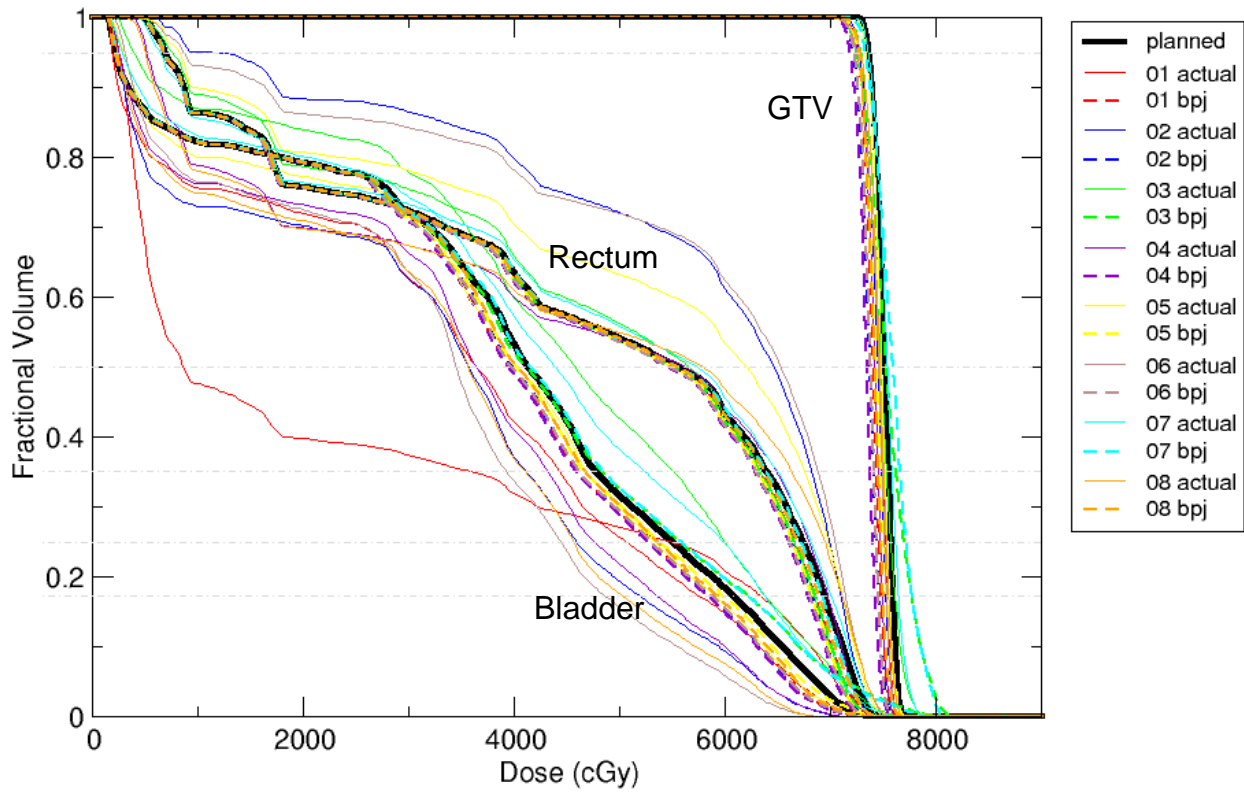


Figure 58: GTV, rectum, and bladder DVHs for patient poses [01, 02 ...] for patient 9. The planned doses are shown as the bolded black solid lines. For each simulated treatment fraction, both the delivered doses (thin solid lines) and reconstructed doses (dashed lines) are shown. Beam energy for this patient was 6 MV.

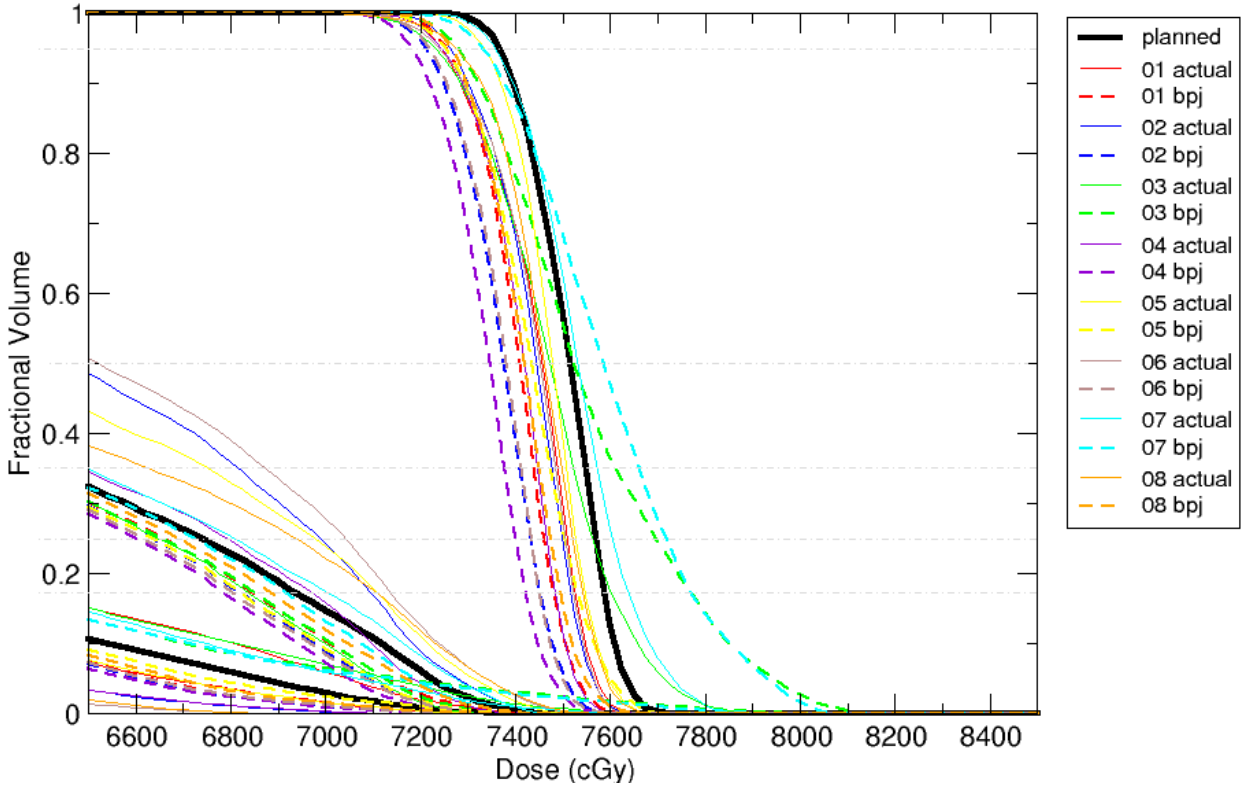


Figure 59: GTV DVHs for patient poses [01, 02 ...] for patient 9. The planned dose is shown as the bolded black solid line. For each simulated treatment fraction, both the delivered doses (thin solid lines) and reconstructed doses (dashed lines) are shown. Beam energy for this patient was 6 MV.

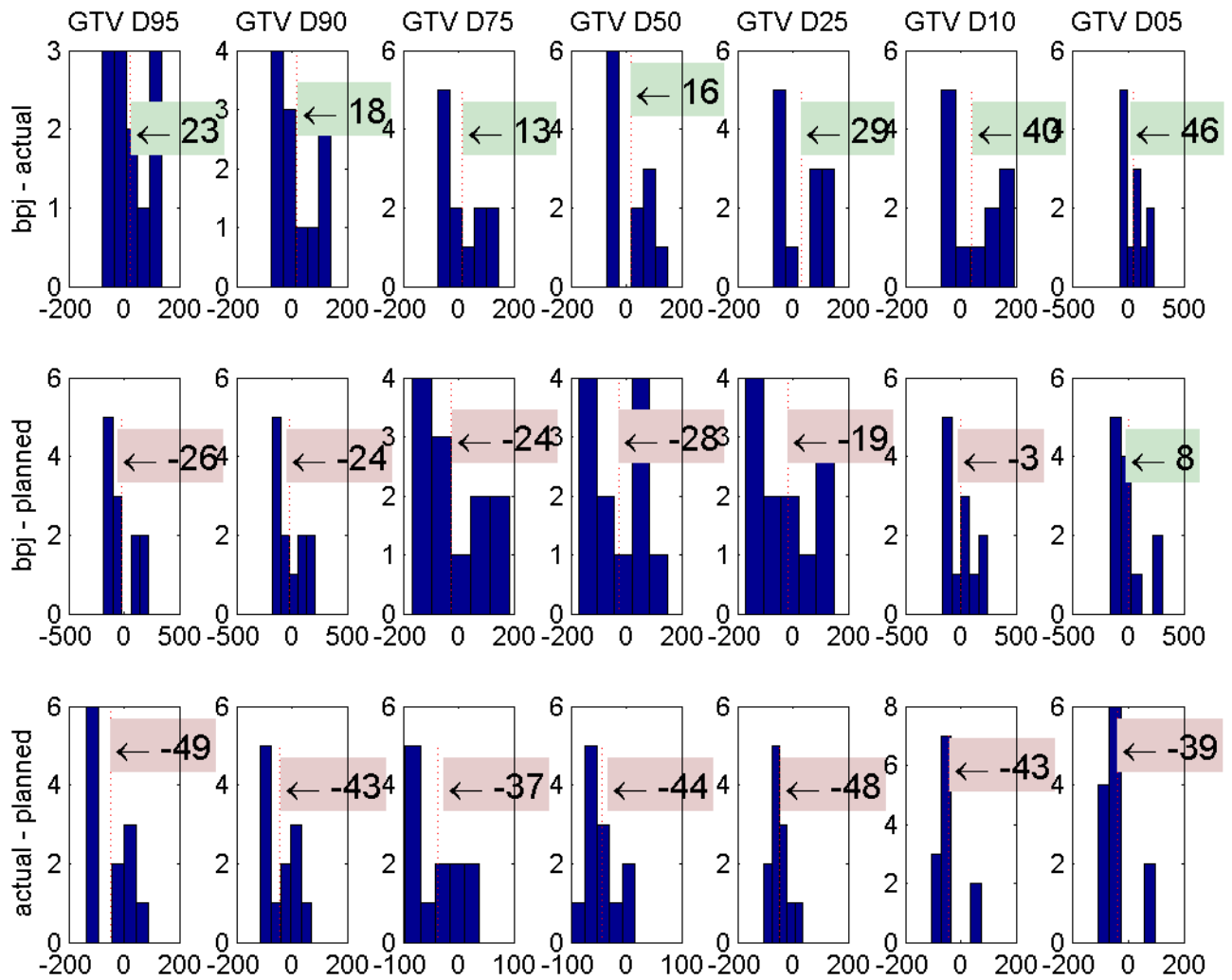


Figure 60: Histograms of the differences between planned, actual, and backprojected GTV dose indices for patient 9. The x-axes represent the dose difference in units of cGy. The numbers in the red/green boxes represent the mean differences. For the D_{95} values, the average delivered dose is 23 cGy greater than the average reconstructed dose. Beam energy for this patient was 6 MV.

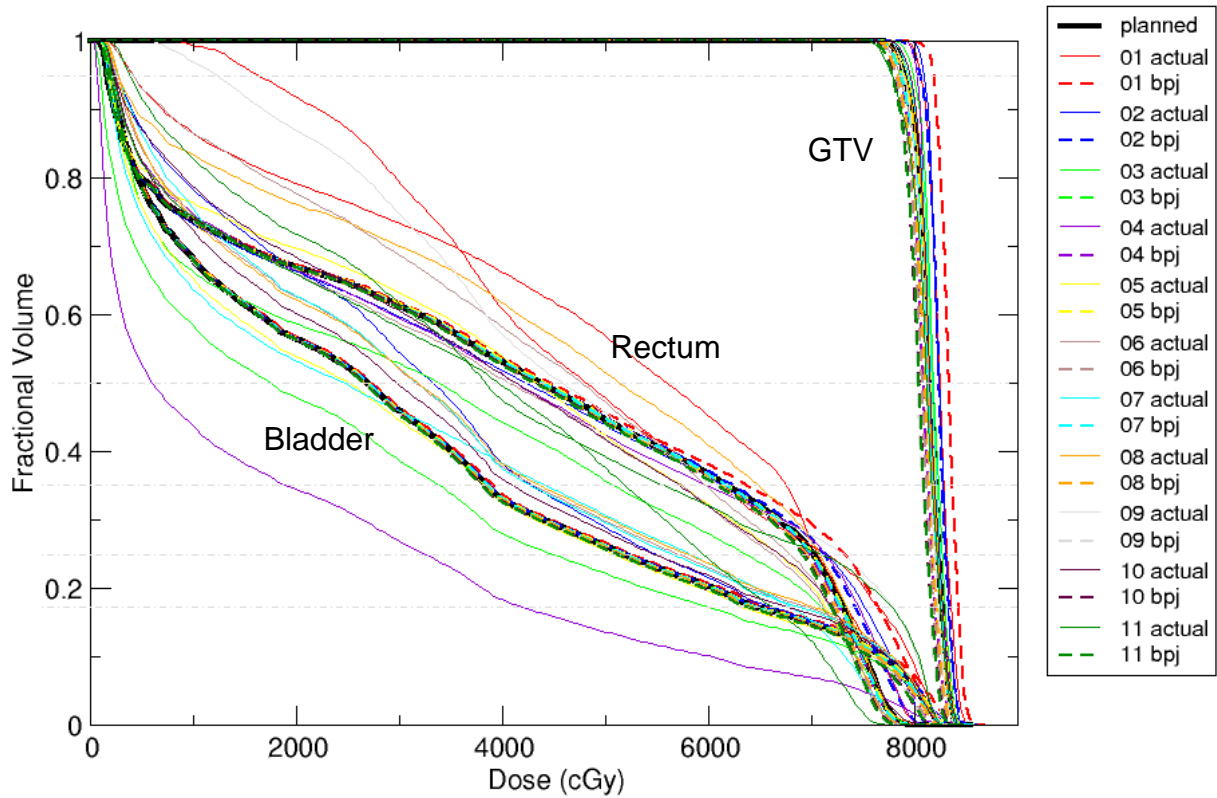


Figure 61: GTV, rectum, and bladder DVHs for patient poses [01, 02 ...] for patient 11. The planned doses are shown as the bolded black solid lines. For each simulated treatment fraction, both the delivered doses (thin solid lines) and reconstructed doses (dashed lines) are shown. Beam energy for this patient was 18 MV.

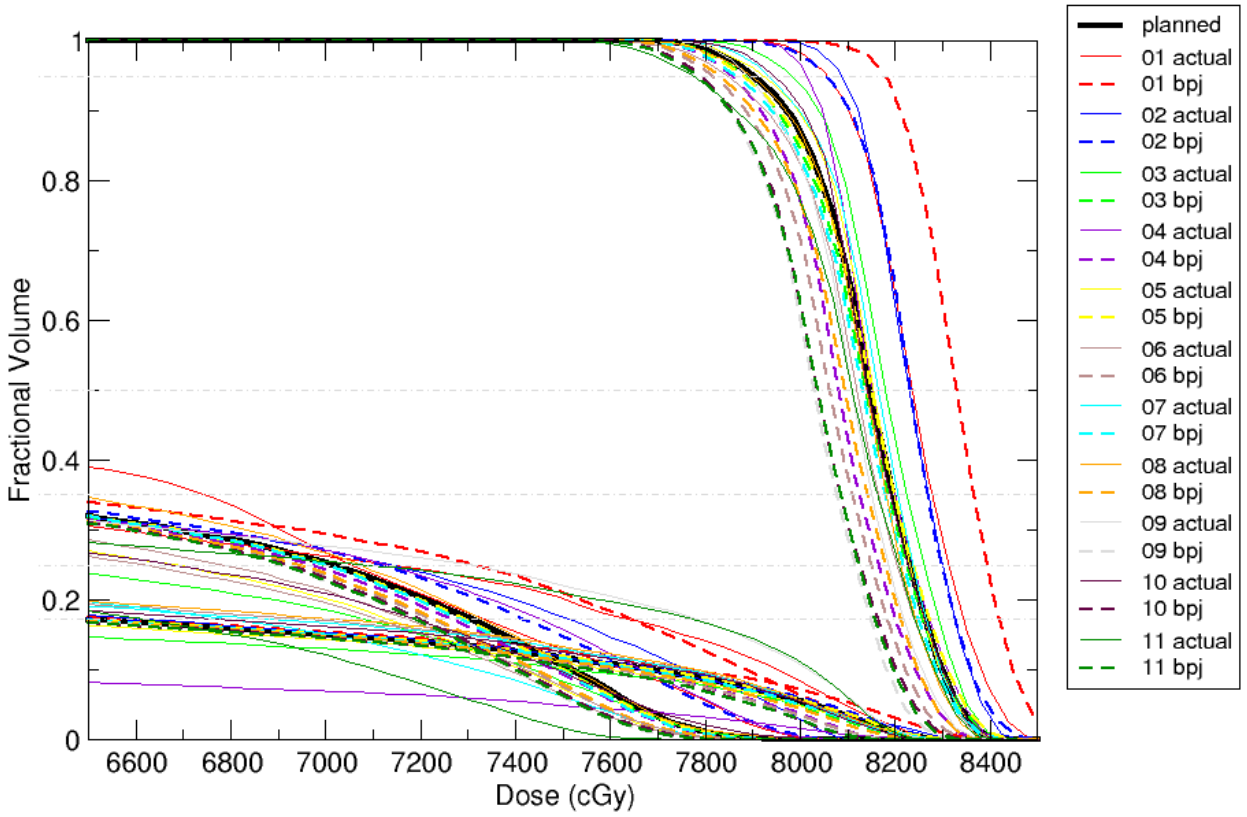


Figure 62: GTV DVHs for patient poses [01, 02 ...] for patient 11. The planned dose is shown as the bolded black solid line. For each simulated treatment fraction, both the delivered doses (thin solid lines) and reconstructed doses (dashed lines) are shown. Beam energy for this patient was 18 MV.

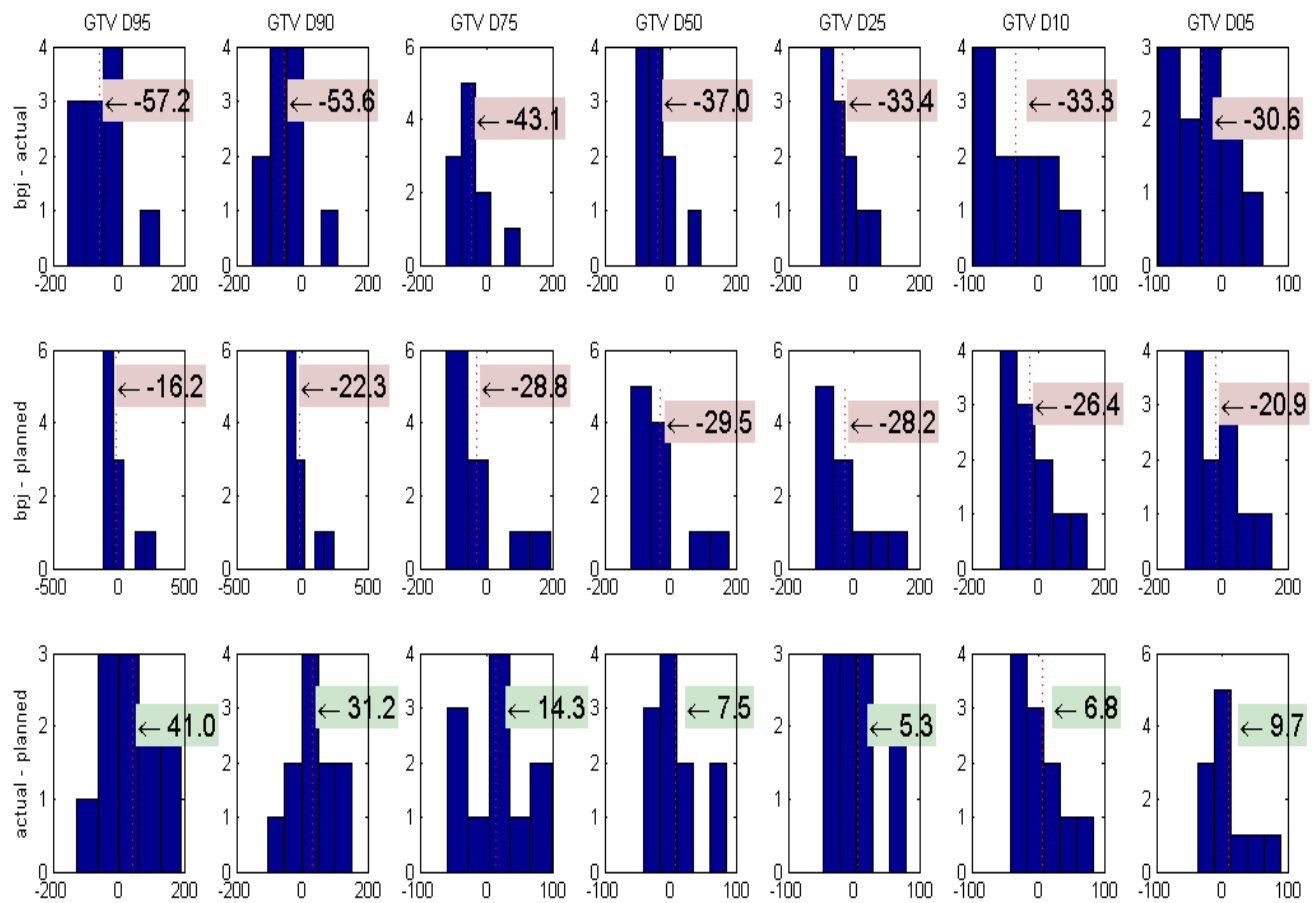


Figure 63: Histograms of the differences between planned, actual, and backprojected GTV dose indices for patient 11. The x-axes represent the dose difference in units of cGy. The numbers in the red/green boxes represent the mean differences. For the D₉₅ values, the average delivered dose is 57 cGy less than the average reconstructed dose. Beam energy for this patient was 18 MV.

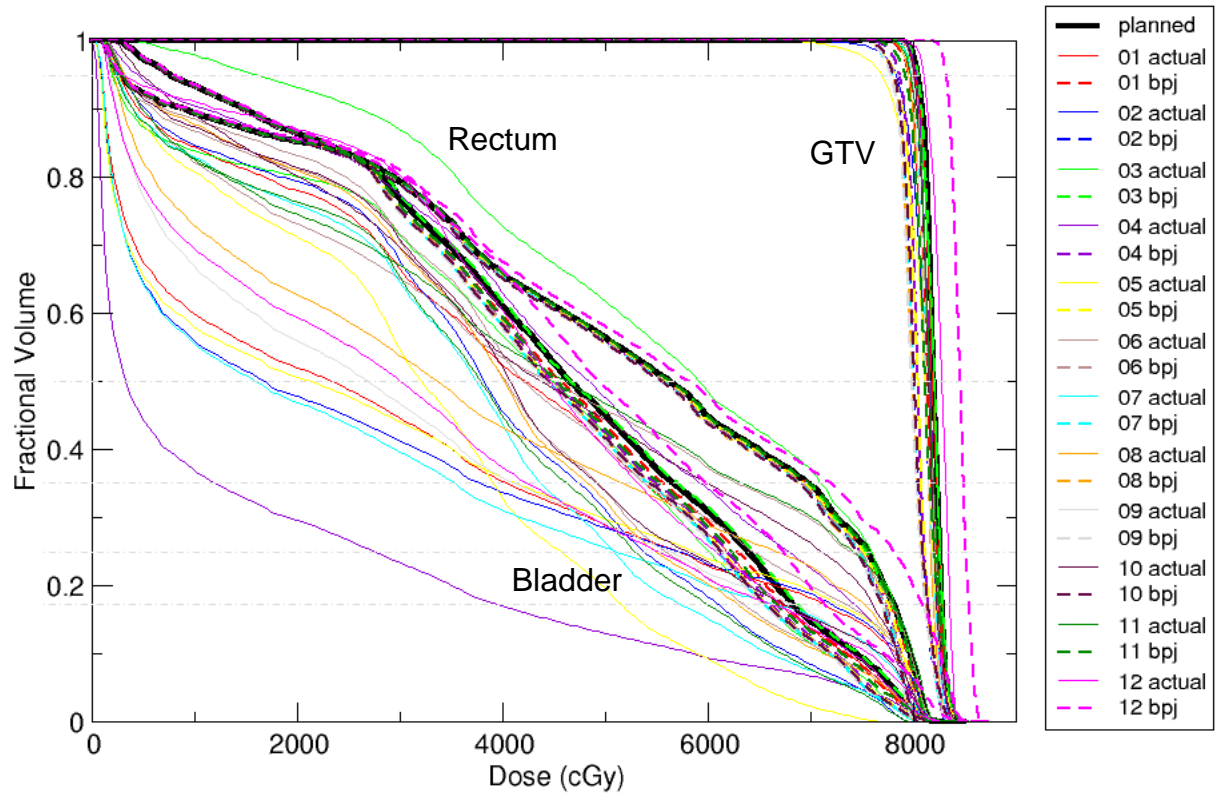


Figure 64: GTV, rectum, and bladder DVHs for patient poses [01, 02 ...] for patient 12. The planned doses are shown as the bolded black solid lines. For each simulated treatment fraction, both the delivered doses (thin solid lines) and reconstructed doses (dashed lines) are shown. Beam energy for this patient was 18 MV.

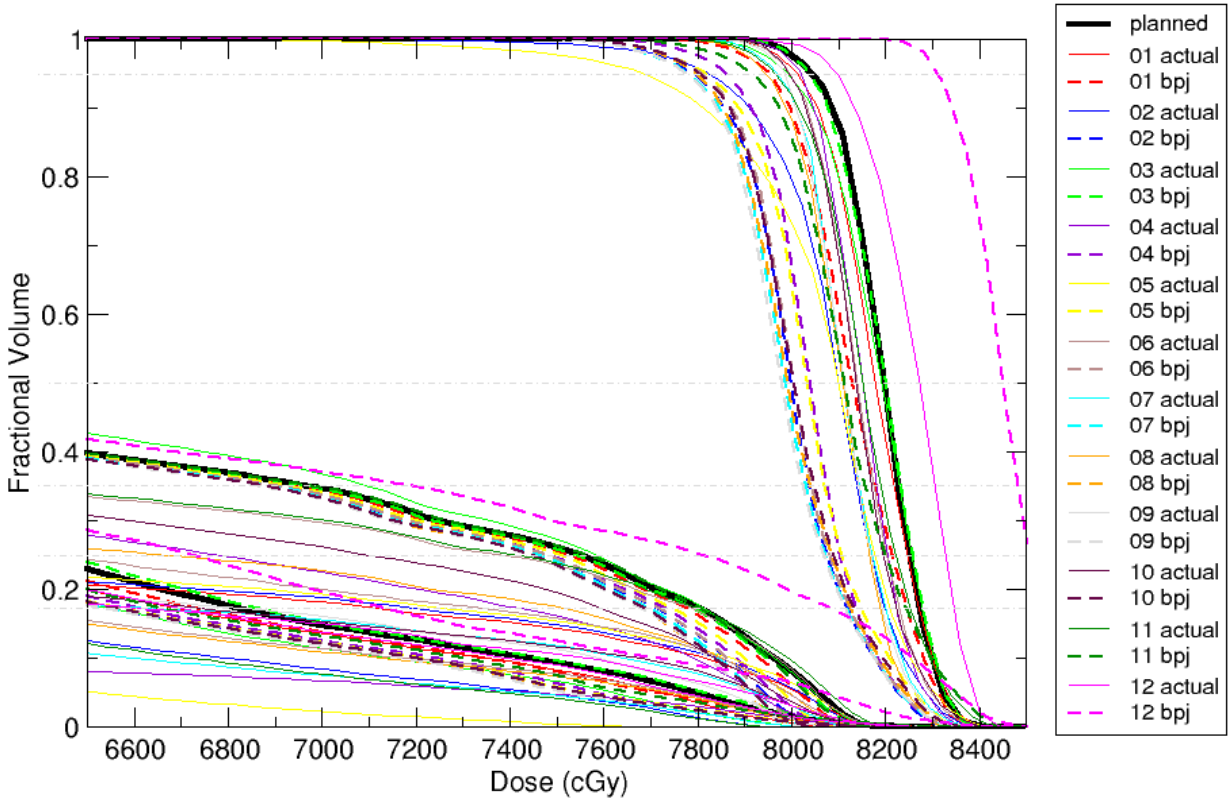


Figure 65: GTV DVHs for patient poses [01, 02 ...] for patient 12. The planned dose is shown as the bolded black solid line. For each simulated treatment fraction, both the delivered doses (thin solid lines) and reconstructed doses (dashed lines) are shown. Beam energy for this patient was 18 MV.

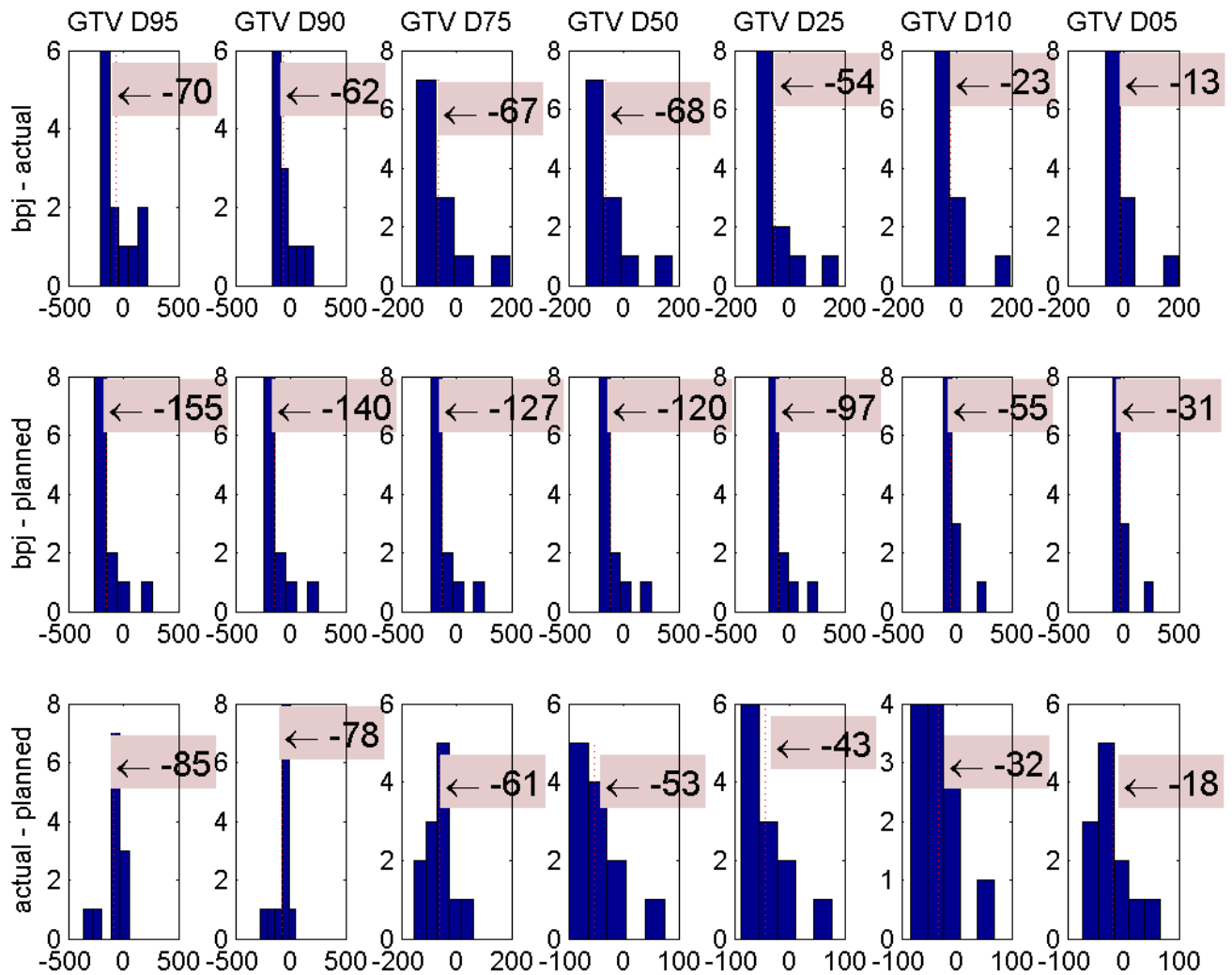


Figure 66: Histograms of the differences between planned, actual, and backprojected GTV dose indices for patient 12. The x-axes represent the dose difference in units of cGy. The numbers in the red/green boxes represent the mean differences. For the D_{95} values, the average delivered dose is 70 cGy less than the average reconstructed dose. Beam energy for this patient was 18 MV.

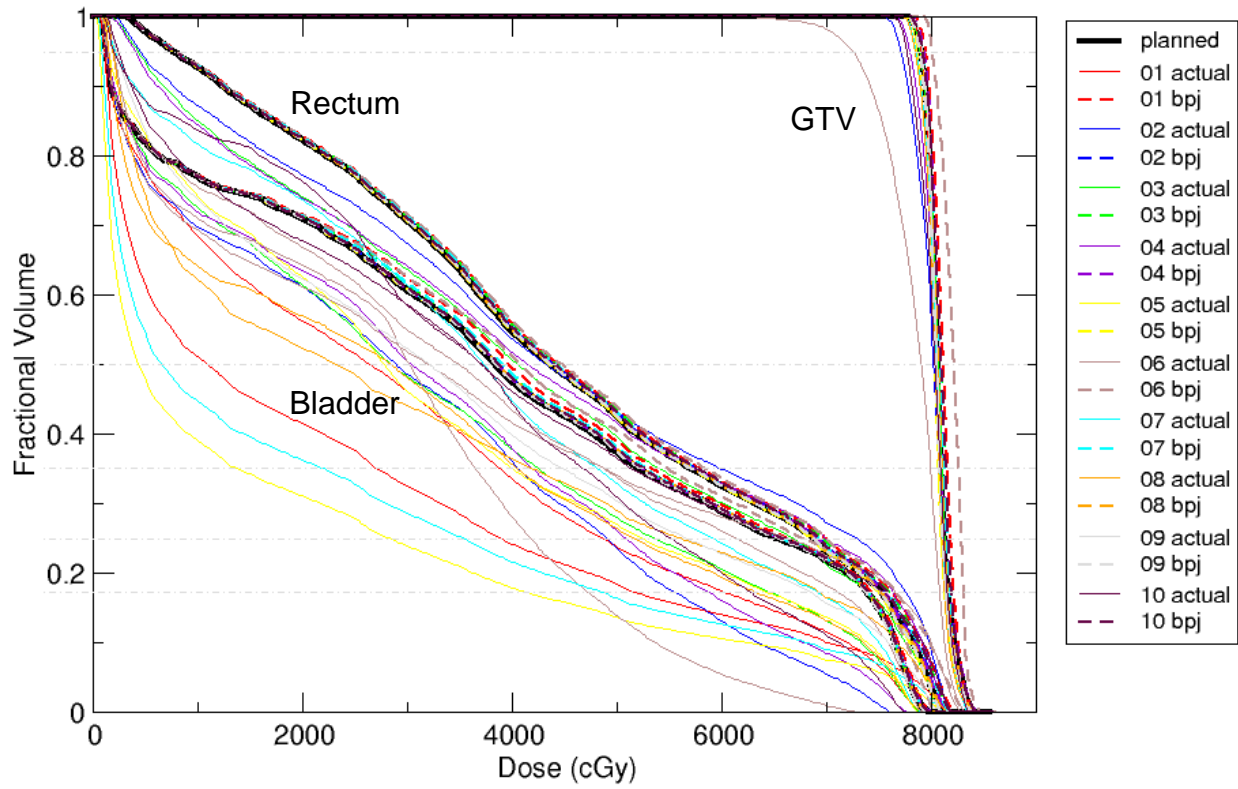


Figure 67: GTV, rectum, and bladder DVHs for patient poses [01, 02 ...] for patient 13. The planned doses are shown as the bolded black solid lines. For each simulated treatment fraction, both the delivered doses (thin solid lines) and reconstructed doses (dashed lines) are shown. Beam energy for this patient was 18 MV.

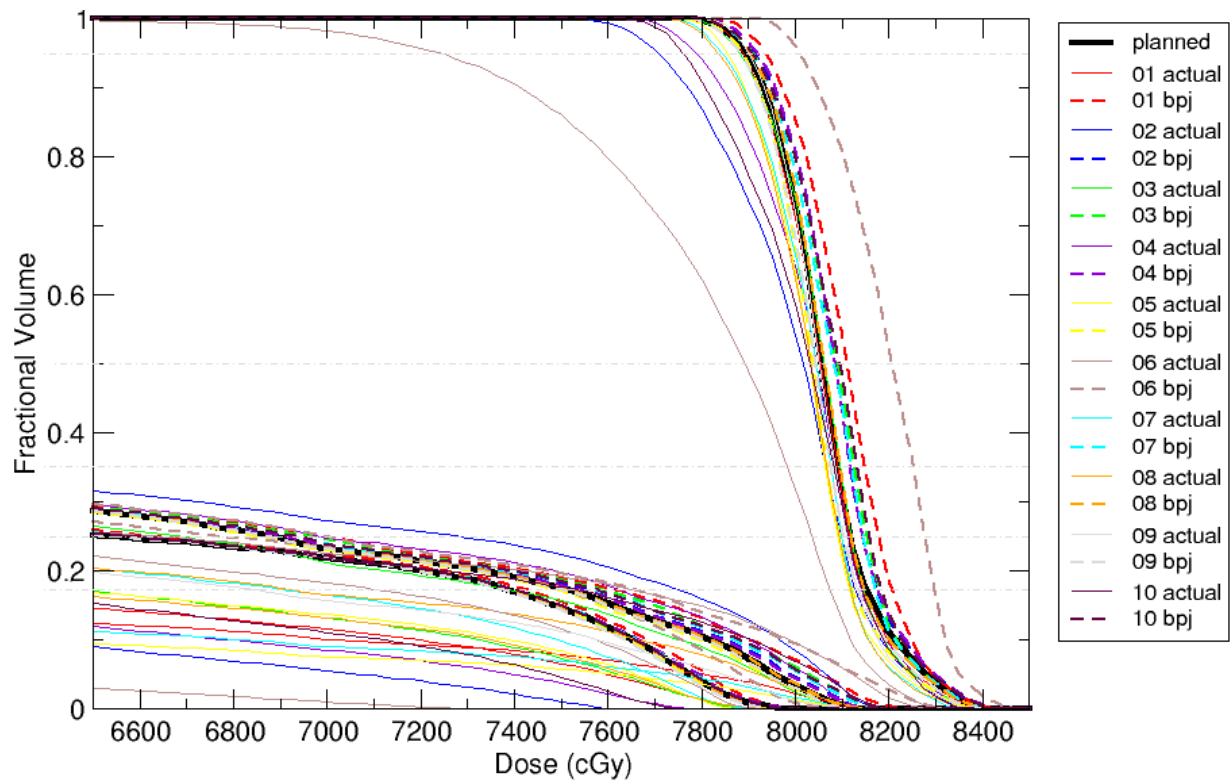


Figure 68: GTV DVHs for patient poses [01, 02 ...] for patient 13. The planned dose is shown as the bolded black solid line. For each simulated treatment fraction, both the delivered doses (thin solid lines) and reconstructed doses (dashed lines) are shown. Beam energy for this patient was 18 MV.

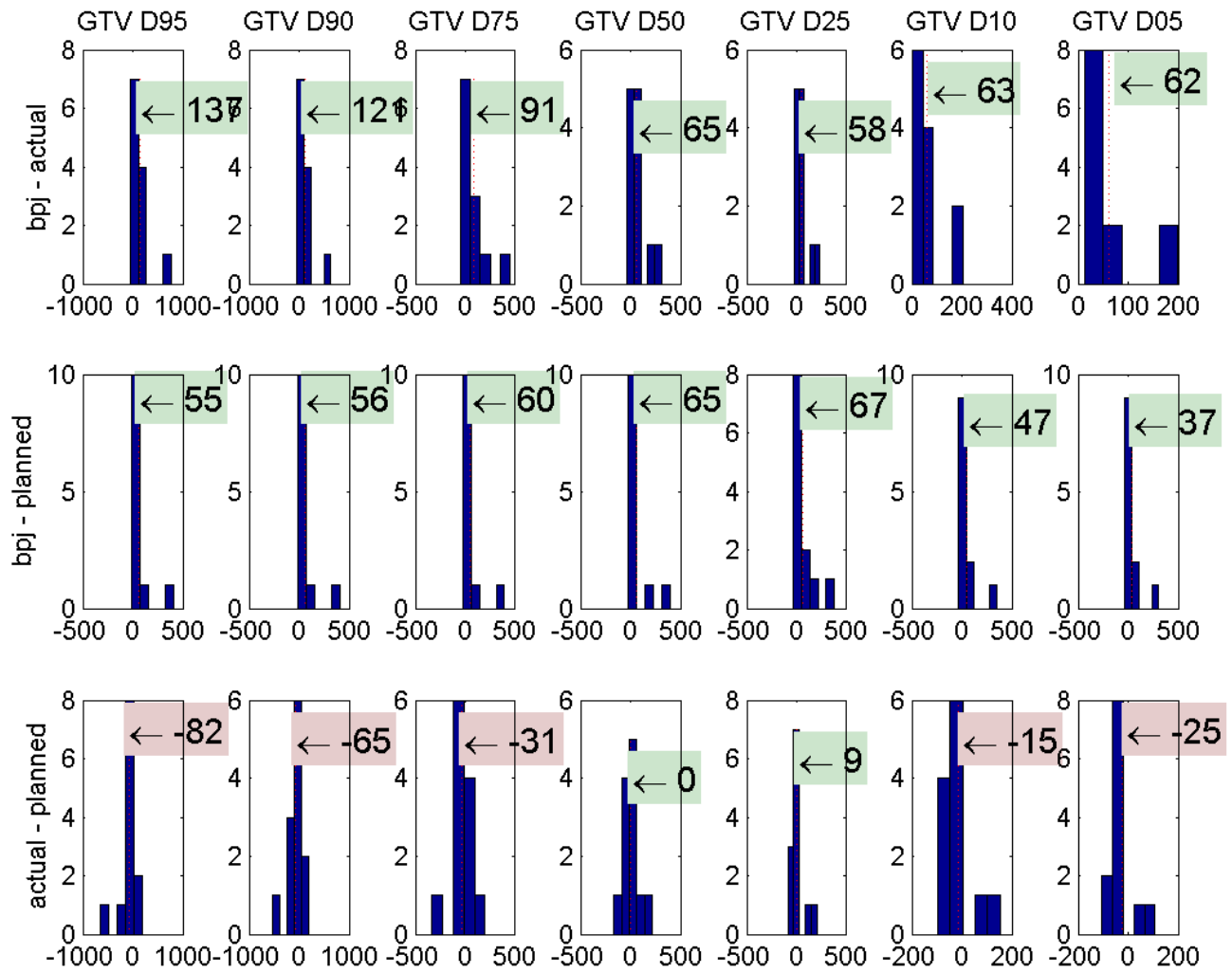


Figure 69: Histograms of the differences between planned, actual, and backprojected GTV dose indices for patient 13. The x-axes represent the dose difference in units of cGy. The numbers in the red/green boxes represent the mean differences. For the D_{95} values, the average delivered dose is 137 cGy greater than the average reconstructed dose. Beam energy for this patient was 18 MV.

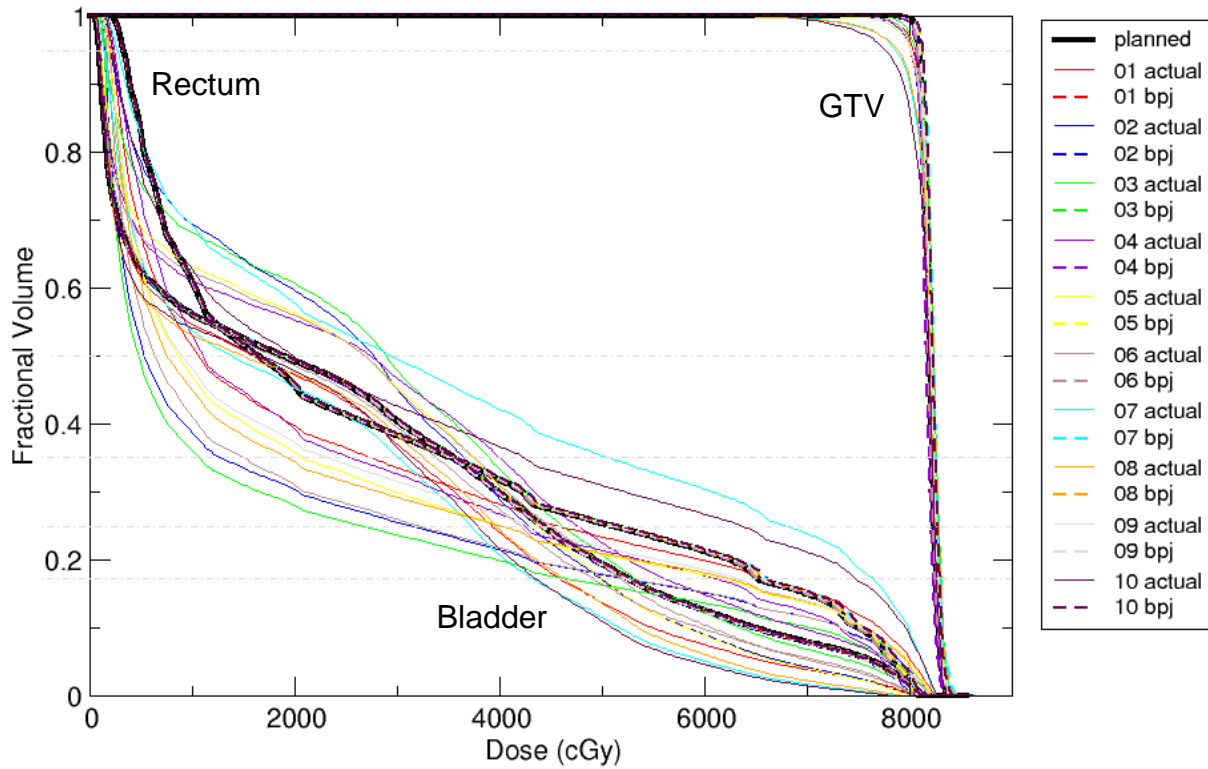


Figure 70: GTV, rectum, and bladder DVHs for patient poses [01, 02 ...] for patient 14. The planned doses are shown as the bolded black solid lines. For each simulated treatment fraction, both the delivered doses (thin solid lines) and reconstructed doses (dashed lines) are shown. Beam energy for this patient was 18 MV.

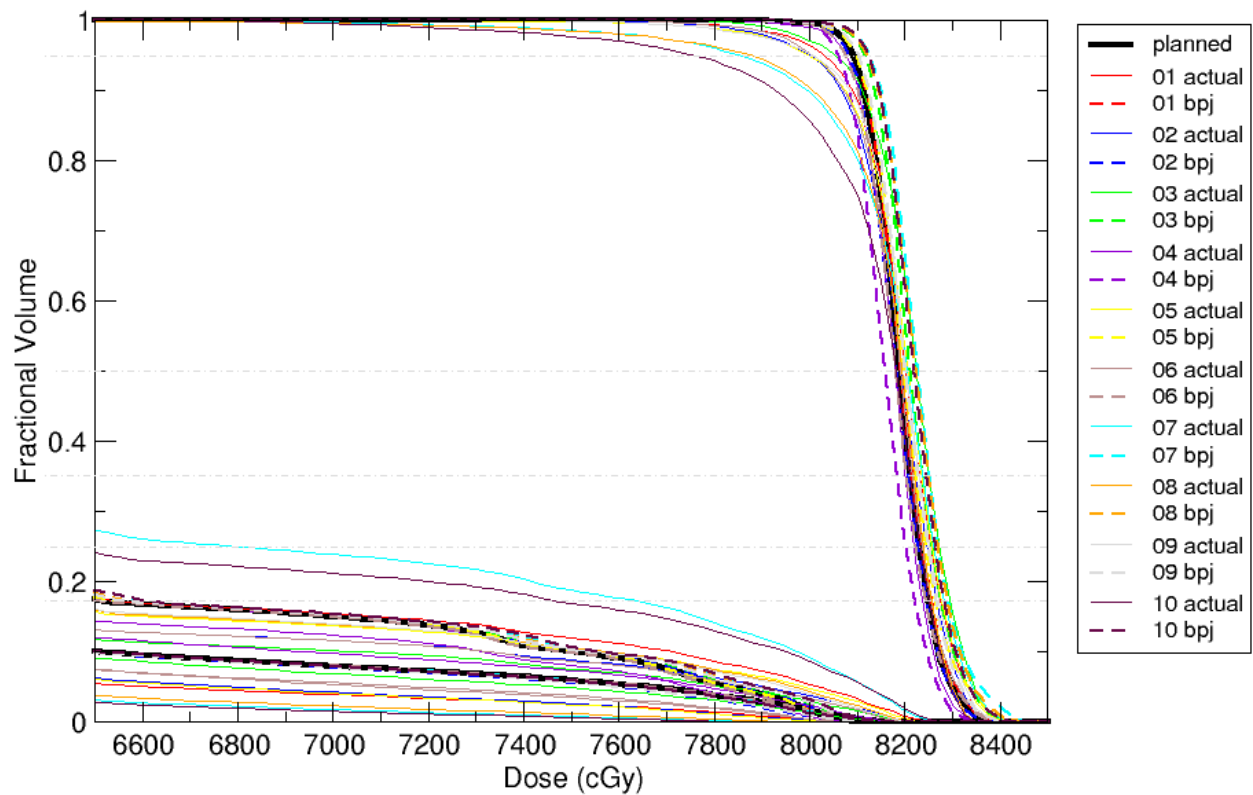


Figure 71: GTV DVHs for patient poses [01, 02 ...] for patient 14. The planned dose is shown as the bolded black solid line. For each simulated treatment fraction, both the delivered doses (thin solid lines) and reconstructed doses (dashed lines) are shown. Beam energy for this patient was 18 MV.

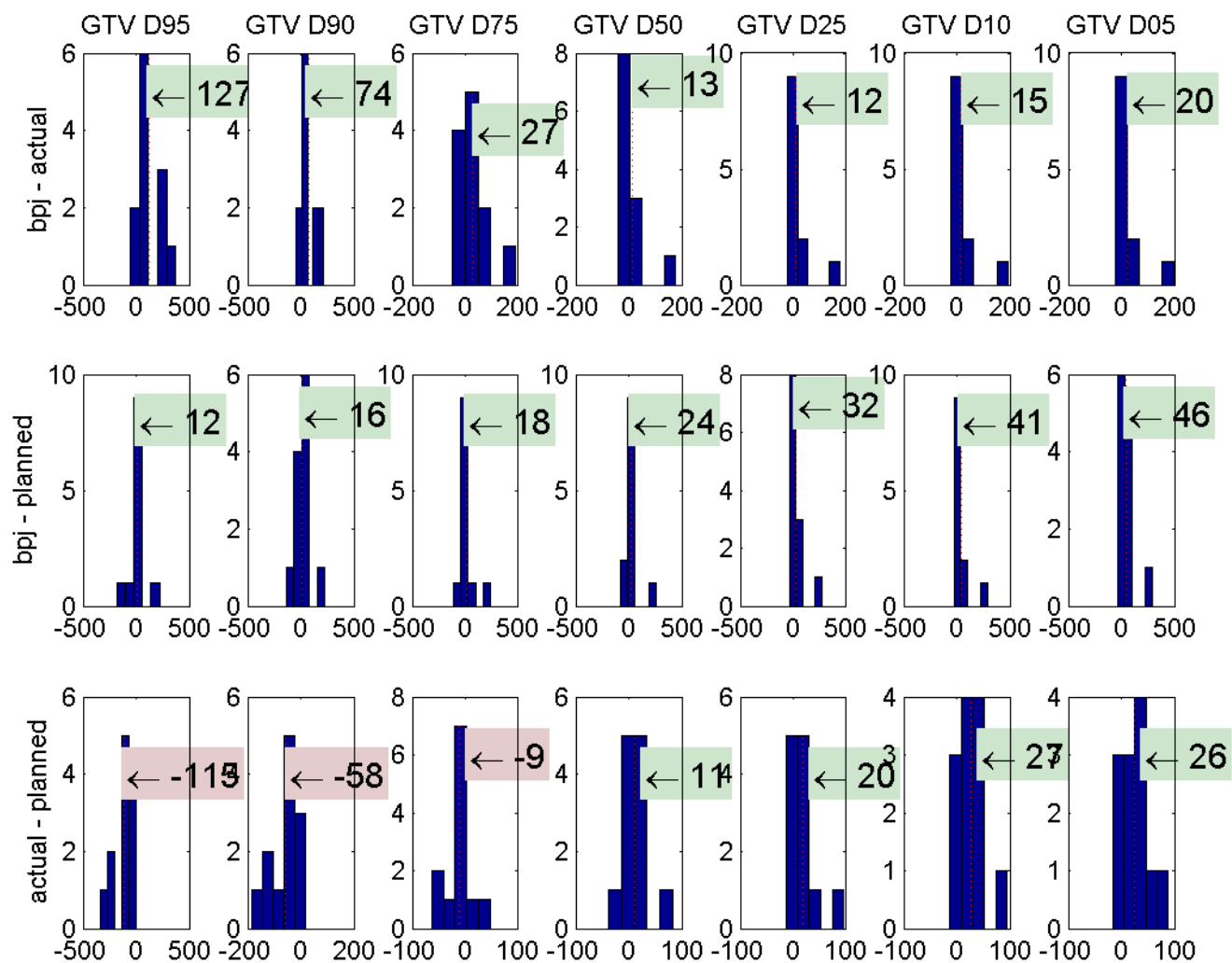


Figure 72: Histograms of the differences between planned, actual, and backprojected GTV dose indices for patient 14. The x-axes represent the dose difference in units of cGy. The numbers in the red/green boxes represent the mean differences. For the D₉₅ values, the average delivered dose is 127 cGy greater than the average reconstructed dose. Beam energy for this patient was 18 MV.

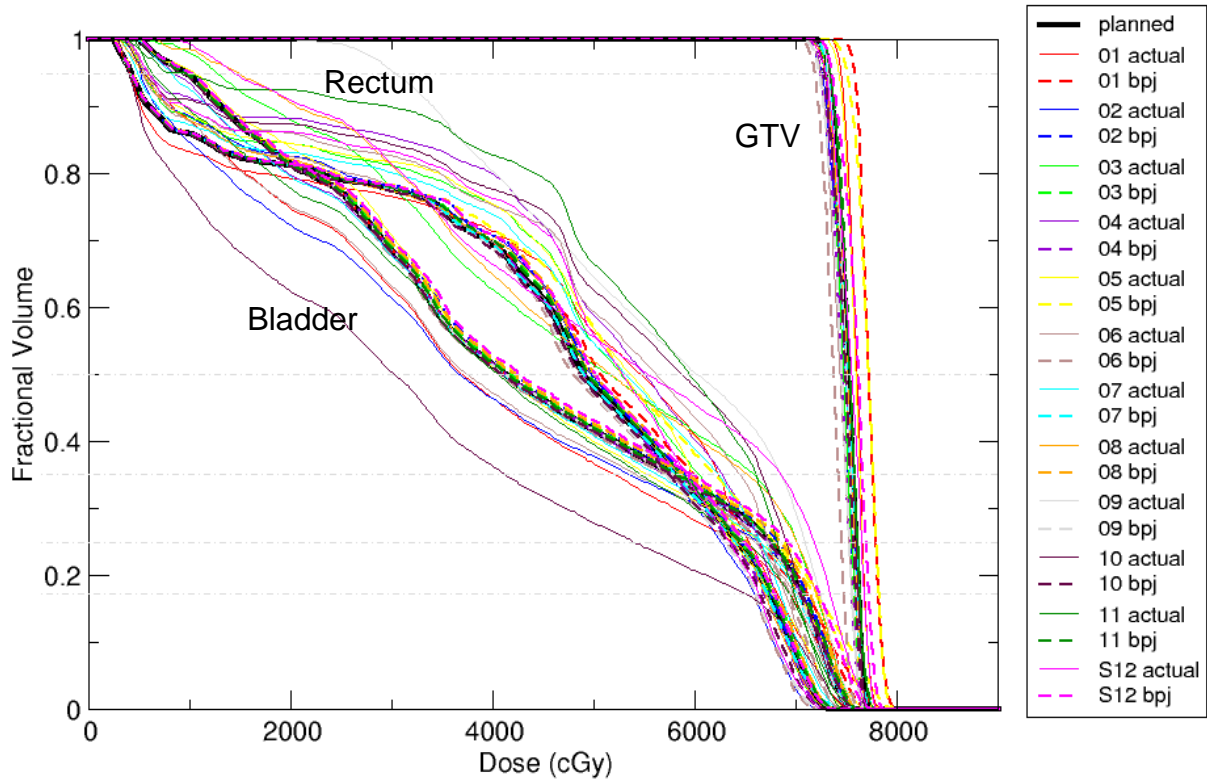


Figure 73: GTV, rectum, and bladder DVHs for patient poses [01, 02 ...] for patient 16. The planned doses are shown as the bolded black solid lines. For each simulated treatment fraction, both the delivered doses (thin solid lines) and reconstructed doses (dashed lines) are shown. Beam energy for this patient was 6 MV.

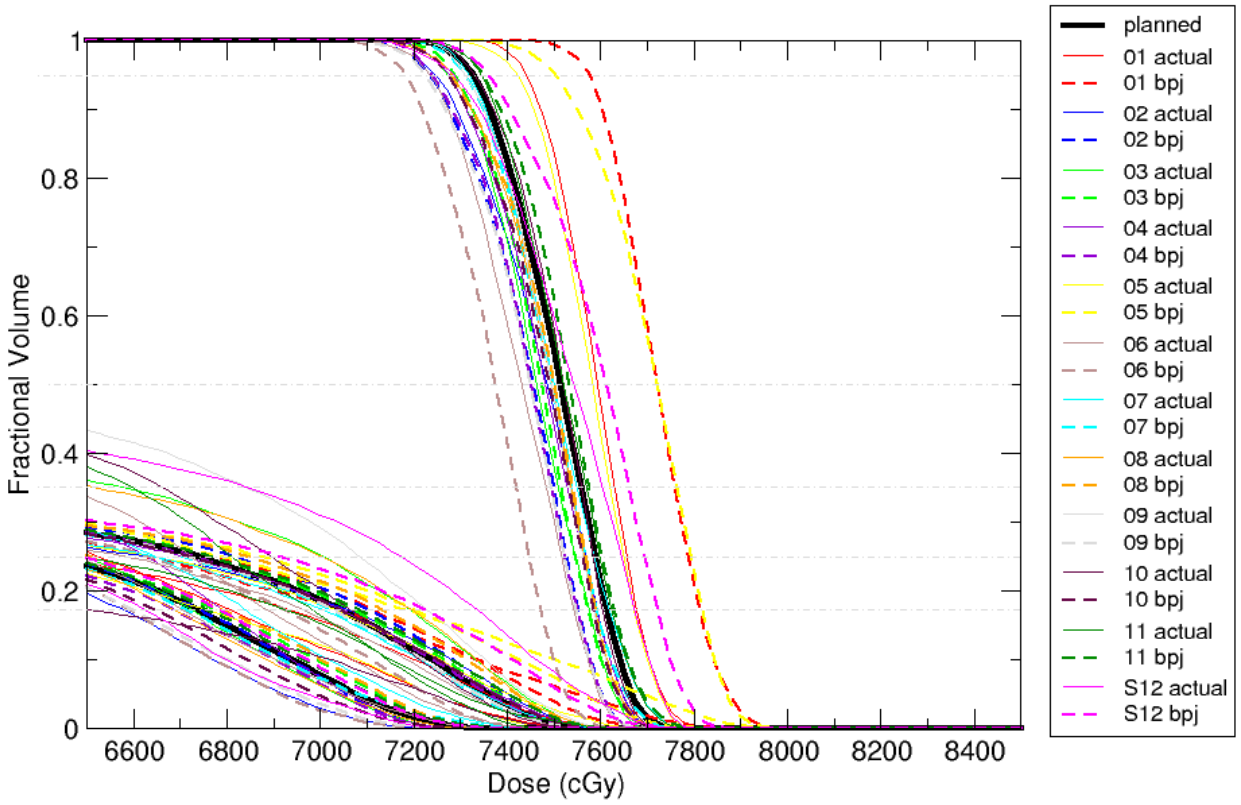


Figure 74: GTV DVHs for patient poses [01, 02 ...] for patient 16. The planned dose is shown as the bolded black solid line. For each simulated treatment fraction, both the delivered doses (thin solid lines) and reconstructed doses (dashed lines) are shown. Beam energy for this patient was 6 MV.

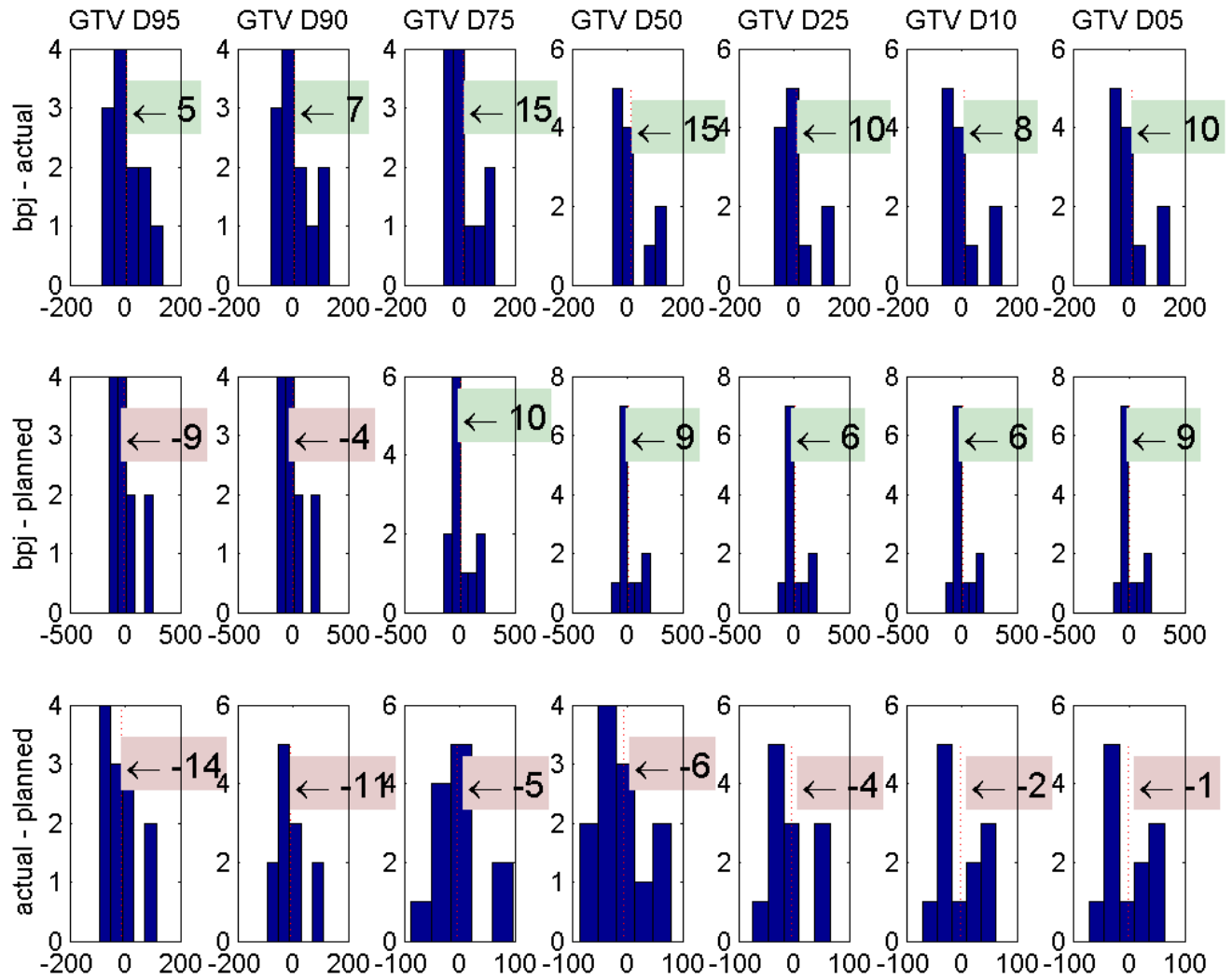


Figure 75: Histograms of the differences between planned, actual, and backprojected GTV dose indices for patient 16. The x-axes represent the dose difference in units of cGy. The numbers in the red/green boxes represent the mean differences. For the D_{95} values, the average delivered dose is 5 cGy greater than the average reconstructed dose. Beam energy for this patient was 6 MV.

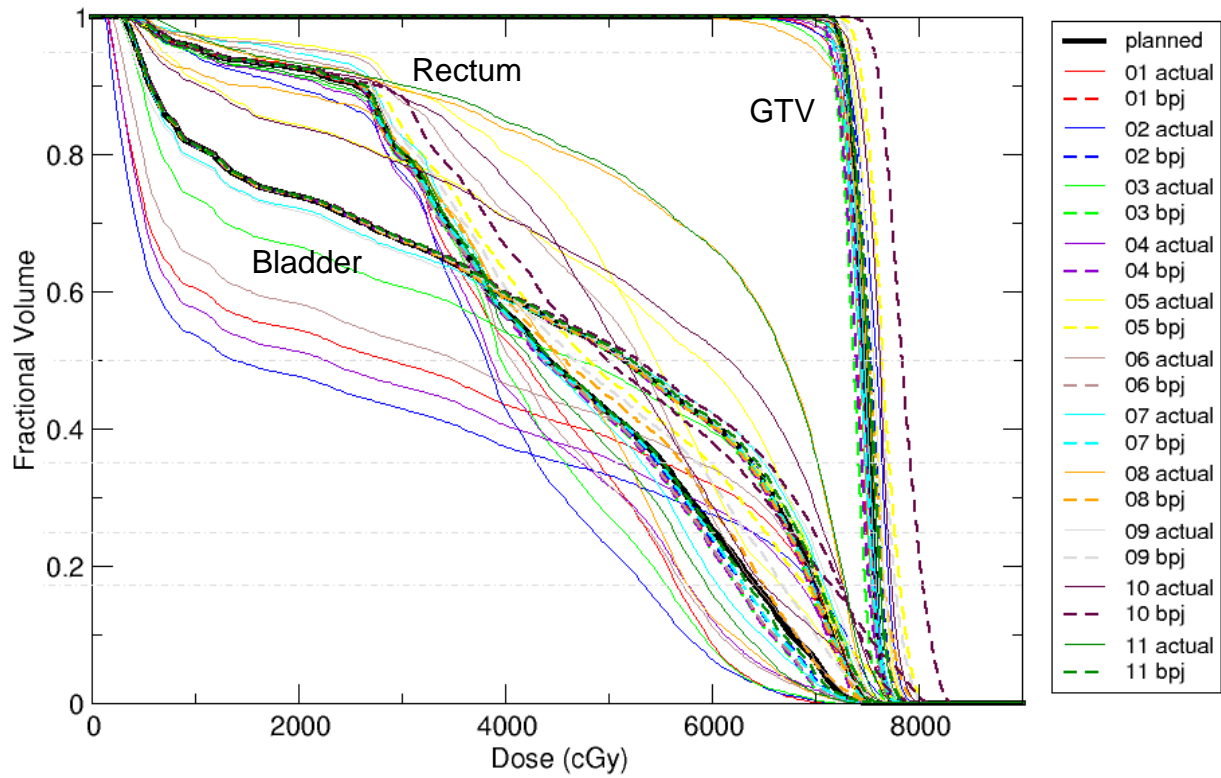


Figure 76: GTV, rectum, and bladder DVHs for patient poses [01, 02 ...] for patient 18. The planned doses are shown as the bolded black solid lines. For each simulated treatment fraction, both the delivered doses (thin solid lines) and reconstructed doses (dashed lines) are shown. Beam energy for this patient was 6 MV.

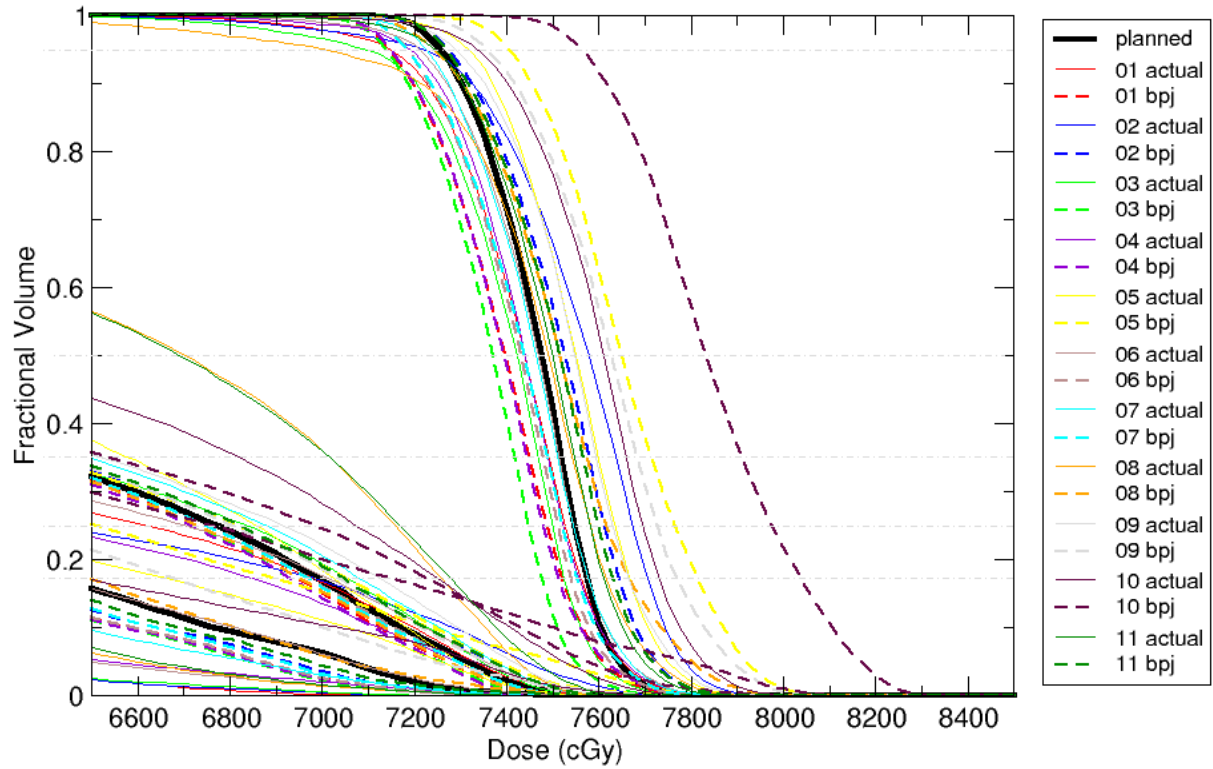


Figure 77: GTV DVHs for patient poses [01, 02 ...] for patient 18. The planned dose is shown as the bolded black solid line. For each simulated treatment fraction, both the delivered doses (thin solid lines) and reconstructed doses (dashed lines) are shown. Beam energy for this patient was 6 MV.

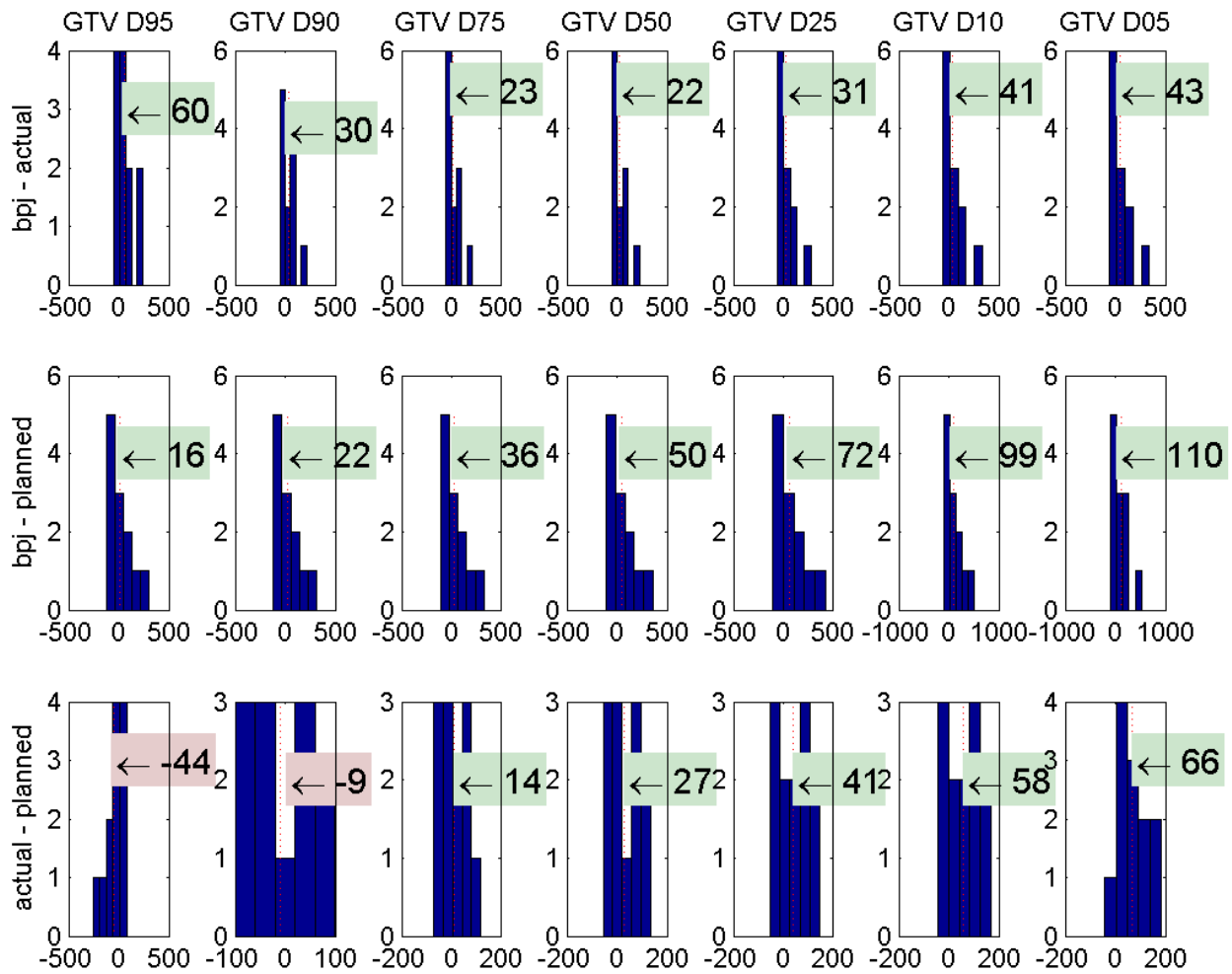


Figure 78: Histograms of the differences between planned, actual, and backprojected GTV dose indices for patient 18. The x-axes represent the dose difference in units of cGy. The numbers in the red/green boxes represent the mean differences. For the D_{95} values, the average delivered dose is 60 cGy greater than the average reconstructed dose. Beam energy for this patient was 6 MV.

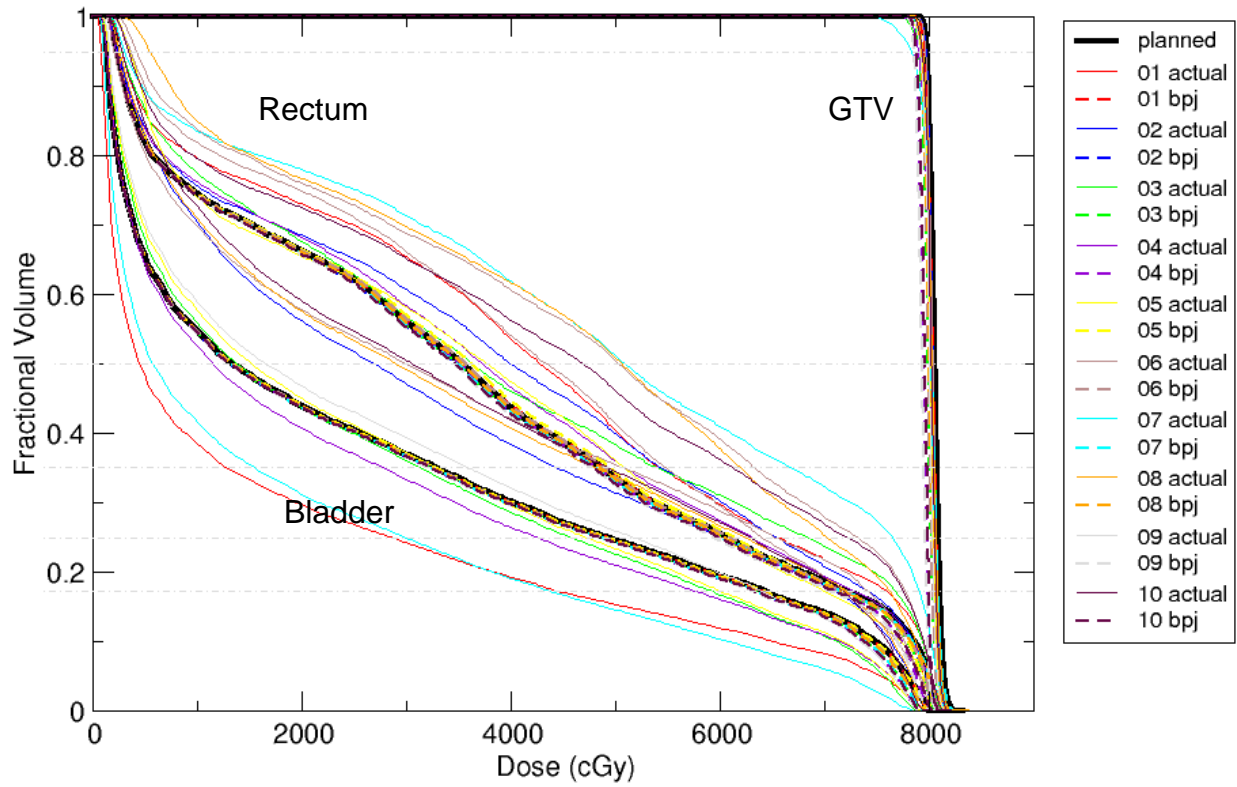


Figure 79: GTV, rectum, and bladder DVHs for patient poses [01, 02 ...] for patient 19. The planned doses are shown as the bolded black solid lines. For each simulated treatment fraction, both the delivered doses (thin solid lines) and reconstructed doses (dashed lines) are shown. Beam energy for this patient was 18 MV.

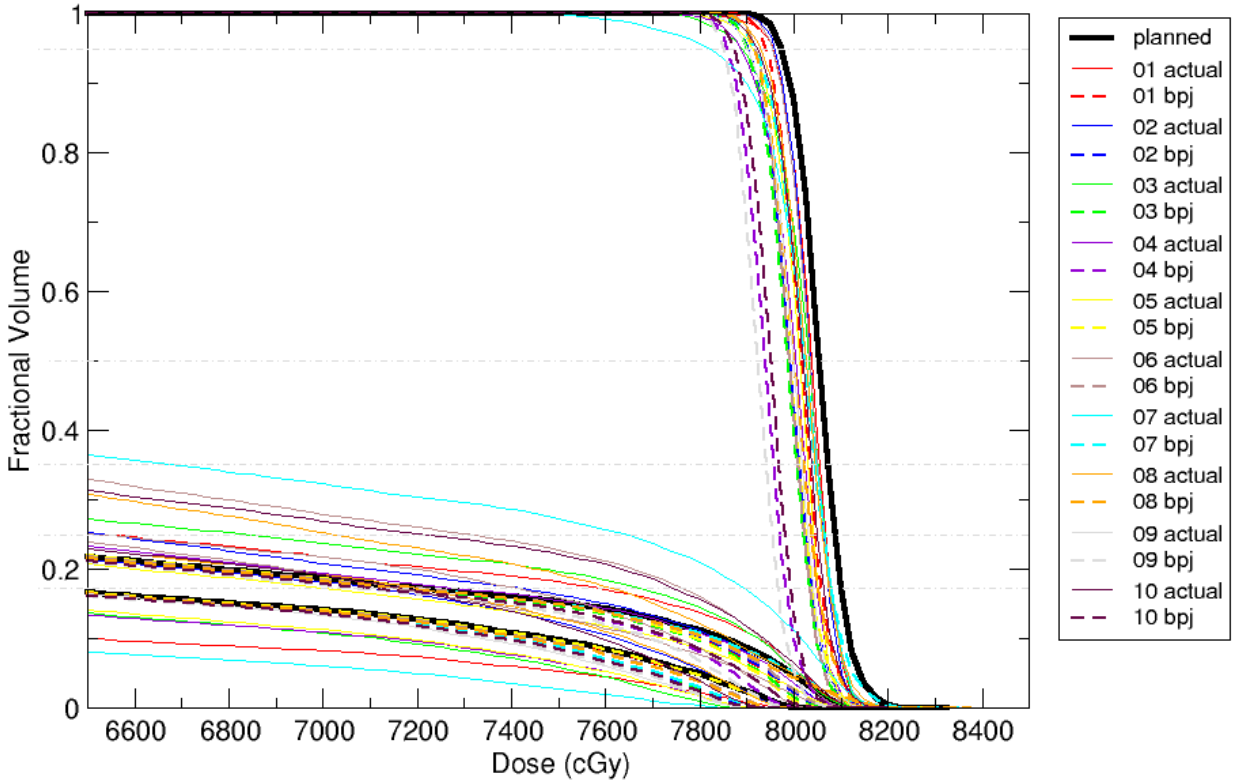


Figure 80: GTV DVHs for patient poses [01, 02 ...] for patient 19. The planned dose is shown as the bolded black solid line. For each simulated treatment fraction, both the delivered doses (thin solid lines) and reconstructed doses (dashed lines) are shown. Beam energy for this patient was 18 MV.

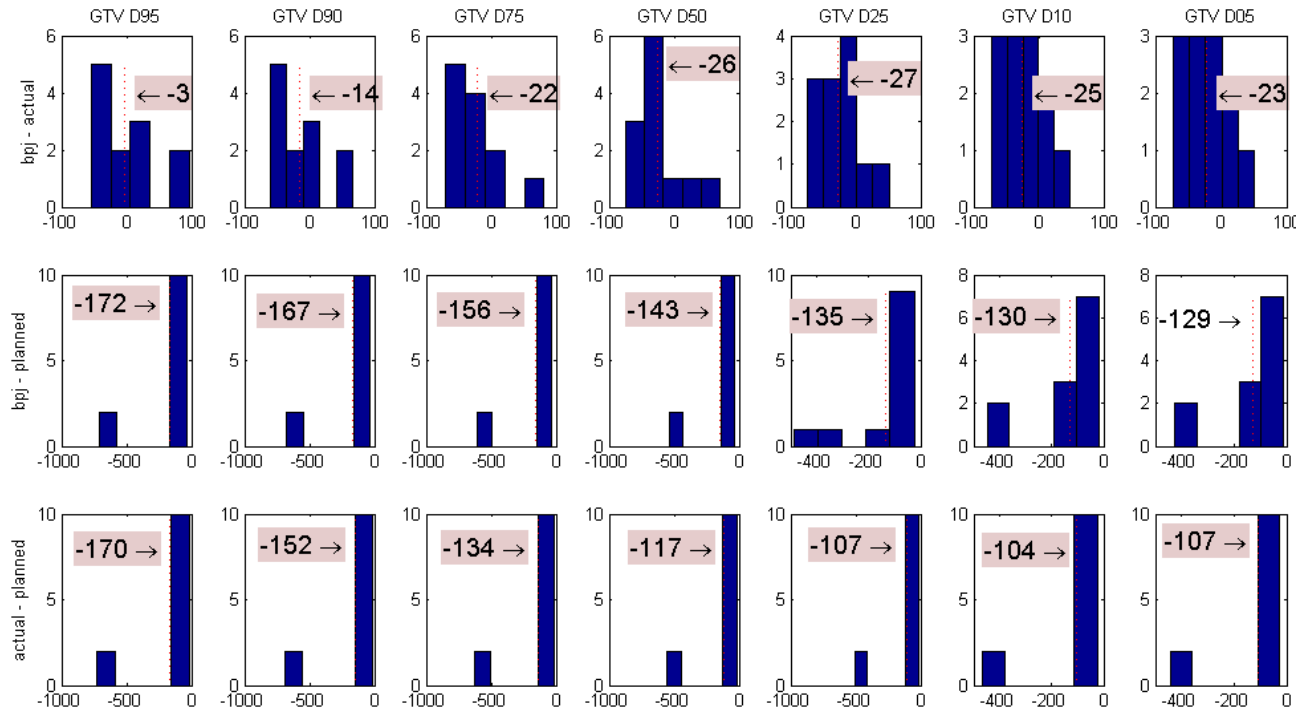


Figure 81: Histograms of the differences between planned, actual, and backprojected GTV dose indices for patient 19. The x-axes represent the dose difference in units of cGy. The numbers in the red/green boxes represent the mean differences. For the D_{95} values, the average delivered dose is 3 cGy greater than the average reconstructed dose. Beam energy for this patient was 18 MV.

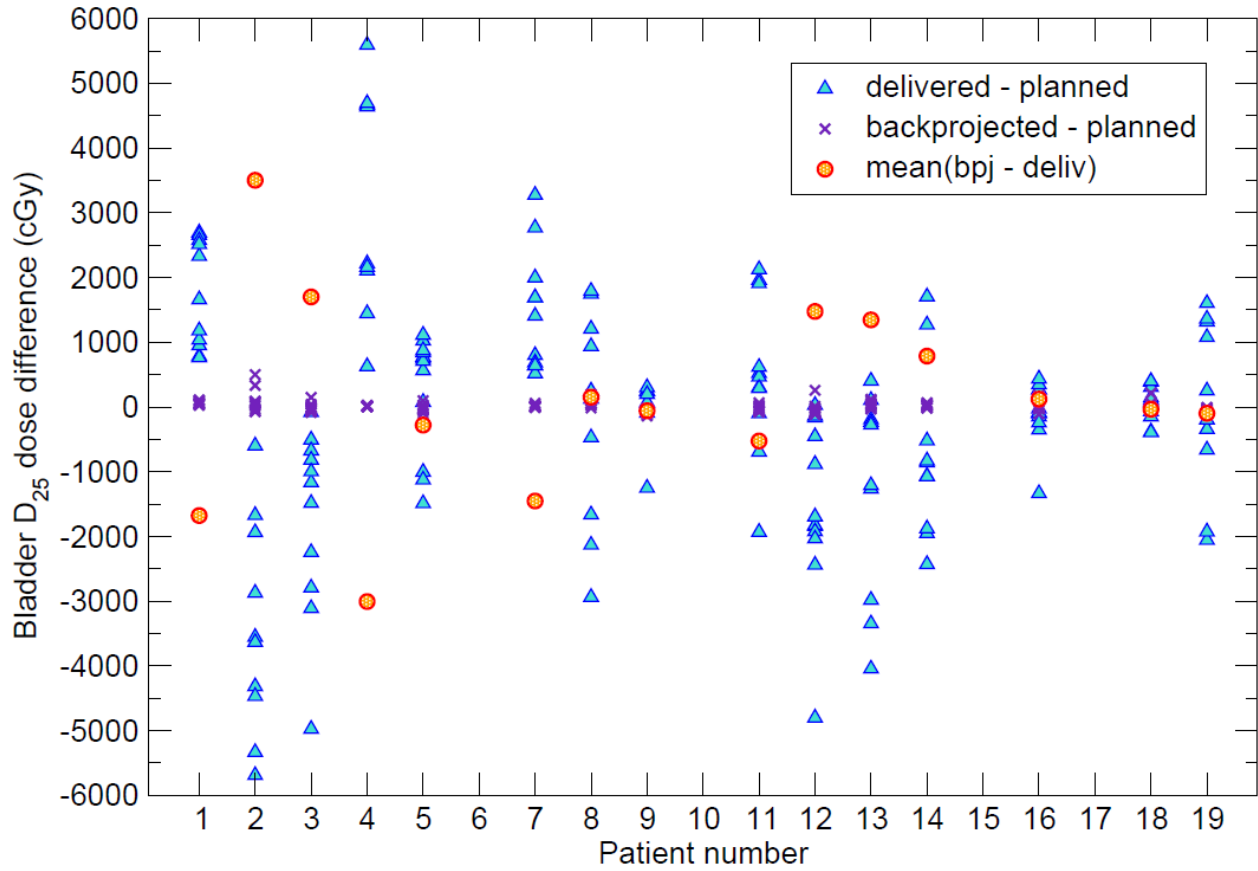


Figure 82: Distribution of bladder D₂₅ deviations for each patient. Delivered versus planned deviations are shown by the blue triangles. Backprojected versus planned deviations are shown by the purple x's. The mean deviations between backprojected and delivered dose are shown by the orange circles.

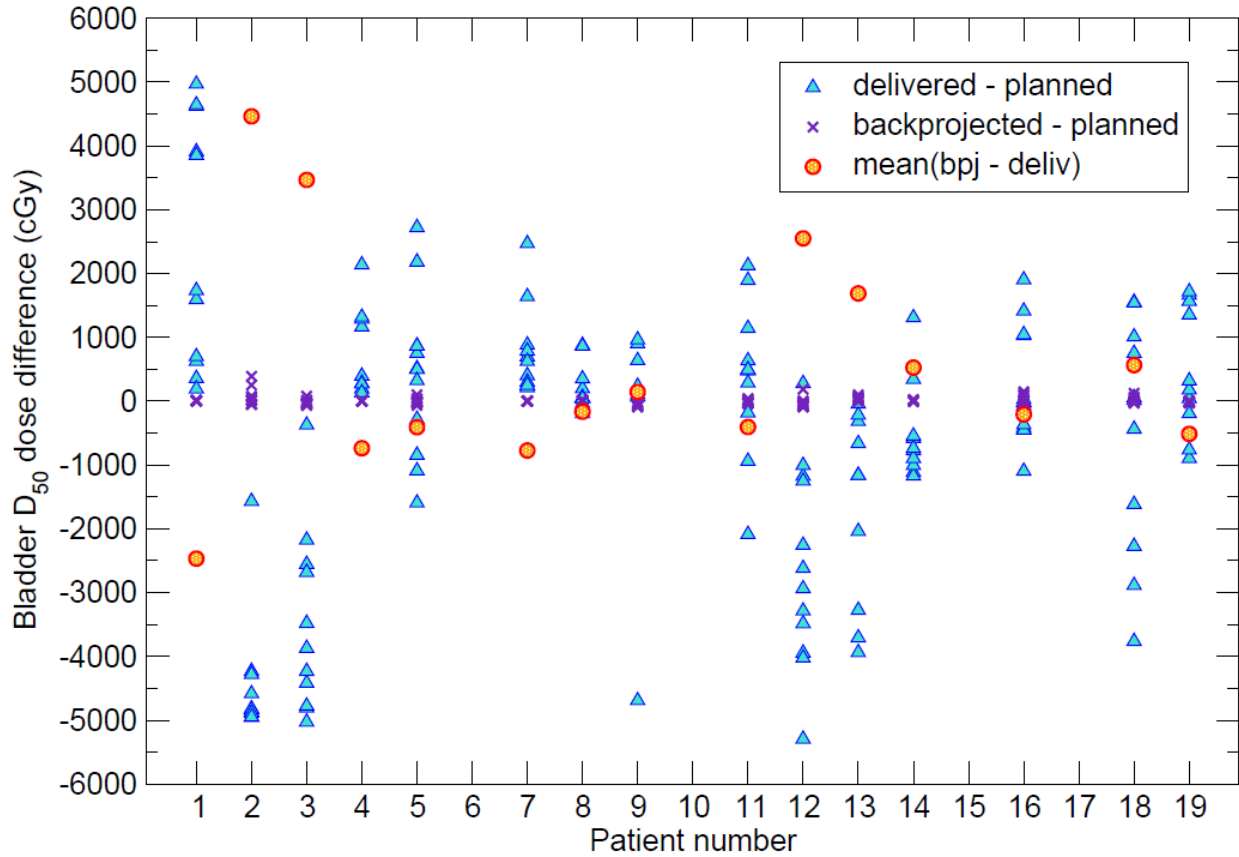


Figure 83: Distribution of bladder D₅₀ deviations for each patient. Delivered versus planned deviations are shown by the blue triangles. Backprojected versus planned deviations are shown by the purple x's. The mean deviations between backprojected and delivered dose are shown by the orange circles.

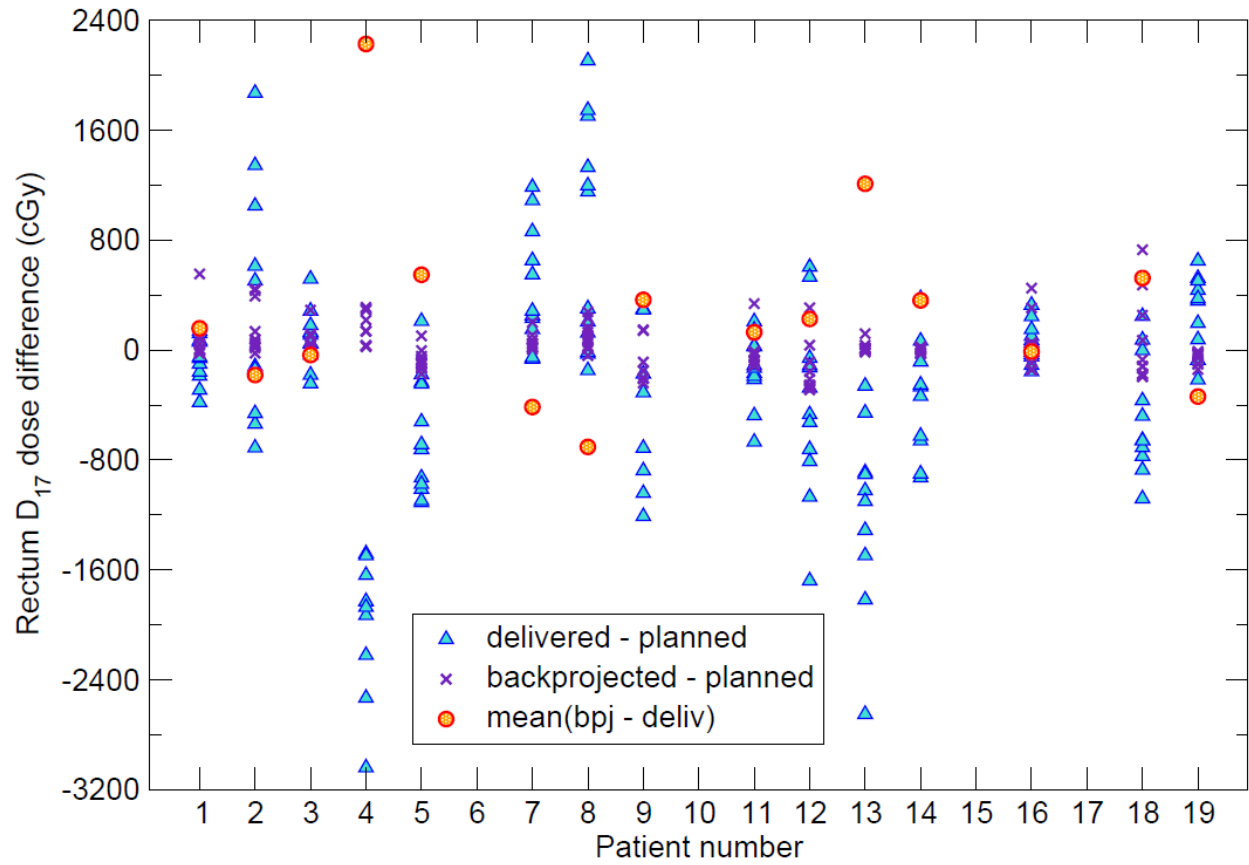


Figure 84: Distribution of rectum D₁₇ deviations for each patient. Delivered versus planned deviations are shown by the blue triangles. Backprojected versus planned deviations are shown by the purple x's. The mean deviations between backprojected and delivered dose are shown by the orange circles.

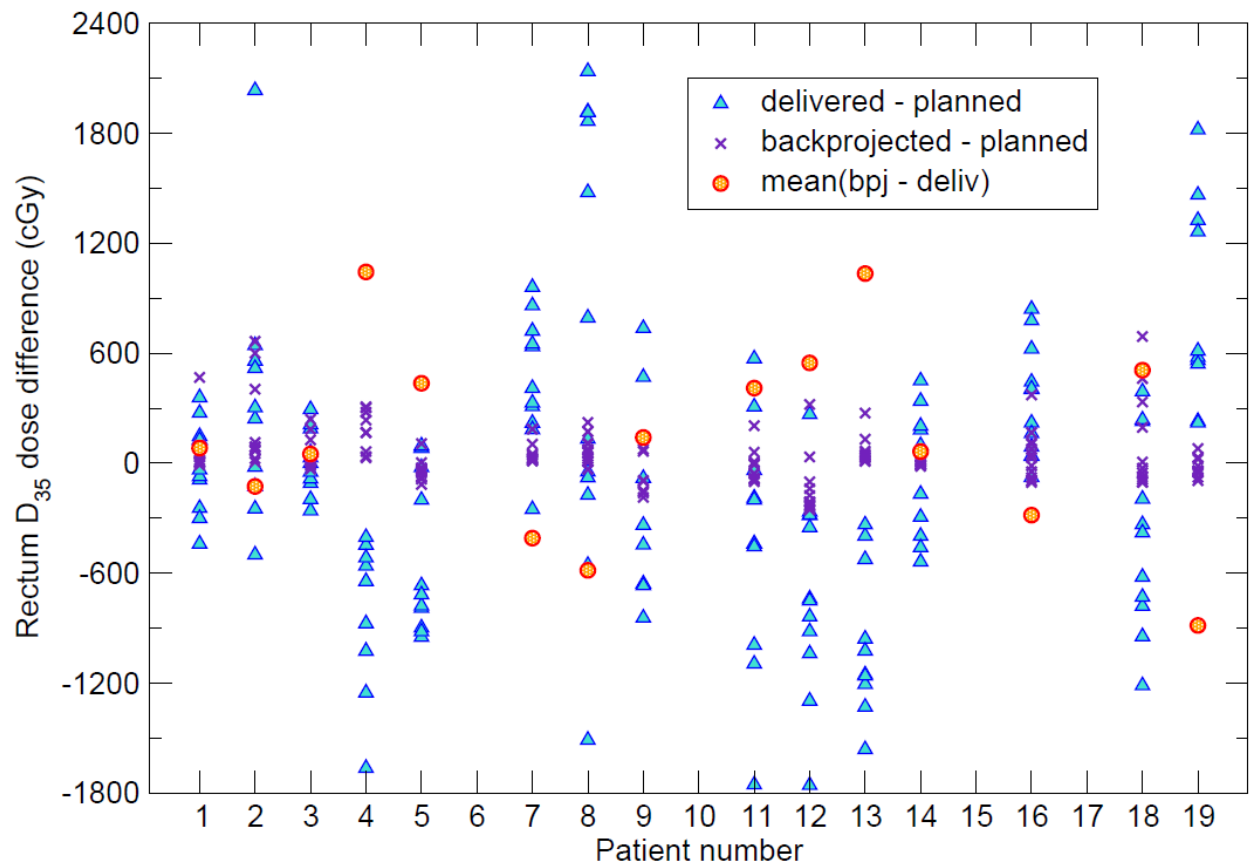


Figure 85: Distribution of rectum D₃₅ deviations for each patient. Delivered versus planned deviations are shown by the blue triangles. Backprojected versus planned deviations are shown by the purple x's. The mean deviations between backprojected and delivered dose are shown by the orange circles.

Vita

Joseph Kingsley Gardner was born on October 15, 1979, in Atlanta, Georgia, and is an American citizen. He graduated from Baylor High School, Chattanooga, Tennessee in 1997. He received his Bachelor of Science in Physics from the University of Richmond, Richmond, Virginia in 2001. He received his Master of Science in Applied Physics from Virginia Commonwealth University in 2005.

Papers and Presentations:

- Gordon, J. J., J. K. Gardner, S. Wang and J. V. Siebers (2012). "Reliable detection of fluence anomalies in EPID-based IMRT pretreatment quality assurance using pixel intensity deviations." Med Phys **39**(8): 4959-4975.
- Gardner, J. K., L. Clews, J. J. Gordon, S. Wang, P. B. Greer and J. V. Siebers (2009). "Comparison of sources of exit fluence variation for IMRT." Phys Med Biol **54**(19): N451-458.
- Wang, S., J. K. Gardner, J. J. Gordon, W. Li, L. Clews, P. B. Greer and J. V. Siebers (2009). "Monte Carlo-based adaptive EPID dose kernel accounting for different field size responses of imagers." Med Phys **36**(8): 3582-3595.
- "Acceptance Criteria for pretreatment QA EPID images". Talk given at AAPM Mid-Atlantic Conference, 2008.
- "Quantification of sources of fluence variation incident on an EPID" variation for IMRT". Talk given at EPI2k8 conference, 2008.
- Gardner, J., J. Siebers and I. Kawrakow (2007). "Dose calculation validation of Vmc++ for photon beams." Med Phys **34**(5): 1809-1818.
- Gardner, J. K., J. V. Siebers and I. Kawrakow (2007). "Comparison of two methods to compute the absorbed dose to water for photon beams." Phys Med Biol **52**(19): N439-447.